



UNIVERSITAT DE LES ILLES BALEARS
DEPARTAMENT DE FÍSICA

Polymer depletion-driven colloids and polymer-surface interactions.

*Tesi presentada per Joan Josep Cerdà, en el
Departament de Física de la Universitat de
les Illes Balears, per optar al grau de Doctor
en ciències Físiques.*

Mallorca, Maig 2005

El director de tesi Tomás M. Sintés Olives Titular d'Escola Universitaria de la universitat de les Illes Balears certifica que aquesta tesi doctoral ha estat realitzada pel Sr. Joan Josep Cerdà Pino, i perquè quedi constància escrita firma

a Palma 18 de Maig de 2005.

Tomás M. Sintés Olives

*Als meus pares Maria Magdalena i Rafel,
als qui dec tot el que sóc.*

Resum

Un dels aspectes més significatius de la Física és l'estudi de totes les interaccions existents a la naturalesa. No seria massa agosarat afirmar que l'enorme progrés tecnològic sofert per la humanitat al llarg dels darrers segles es deu indubtablement a la millora substancial del coneixement sobre les interaccions i propietats de la matèria. Els polímers i els col·loides són un clar exemple de com un enteniment cada volta millor de les seves interaccions i propietats ha redundat en una millora de la qualitat de vida al llarg dels darrers dos segles. Tot i que els polímers i col·loides han estat estudiats durant tant de temps, els nous avanços en els camps de la química i el disseny molecular han obert la porta a nous tipus de polímers i partícules col·loïdals amb aplicacions difícils d'imaginar anys enrera. Com exemple hom podria citar el cas dels liposomes estabilitzats amb cadenes polimèriques els quals poden transportar medicament anticancerós i que tenen diversos avantatges respectes a altres vies de lluita contra el càncer. La natura també ens ofereix molts exemples de sistemes polimèrics i col·loïdals dels quals tenir-ne un coneixement de les seves propietats ens és vital com ara l'ADN, les proteïnes o els liposomes i superfícies cel·lulars. Per tant, una millora del coneixement sobre polímers i col·loides no només ens ajudarà a millorar i optimitzar les aplicacions de les noves molècules producte de les síntesis sinó que també ens servirà per a entendre millor el funcionament i les propietats dels sistemes biològics.

Tot i la gran quantitat de coneixements de que ja es disposa sobre dits sistemes, hom pot considerar de fet que encara s'està lluny d'un coneixement absolut de les propietats i interaccions dels col·loides i els polímers. Així per exemple, al dia d'avui només tenim un coneixement molt parcial de com controlar i modificar les interaccions en aquests sistemes, i de fet, alguns aspectes molt bàsics romanen encara sense una explicació quantitativa adequada.

Per aquesta raó, la present tesi s'ha realitzat amb el propòsit de contribuir en la mesura del possible a una millora del coneixement que tenim en alguns d'aquests aspectes bàsics però encara no entesos del tot. El contingut de la tesi s'ha dividit en onze capítols dels quals els tres primers estan dedicats a donar una introducció bàsica amb la intenció de facilitar una millor comprensió dels capítols posteriors

en els que s'exposa la recerca duita a terme. El primer capítol de la introducció presenta les principals característiques dels sistemes polimèrics, mentre que el segon capítol introdueix els trets més rellevants que emprarem en aquesta tesi associats a la física dels polímers. El tercer i darrer capítol d'aquesta introducció exposa les principals característiques dels mètodes numèrics usats en la recerca que hem fet.

L'exposició de la recerca duita a terme comença amb els capítols 4 i 5 on s'estudien les transformacions de fase en sistemes col·loïdals (en dues dimensions) induïdes per unes forces d'origen entròpic anomenades *forces de minvament*, conegudes també pel seu nom en anglès com a '*depletion forces*'. En els següents dos capítols (6 i 7) es presenta l'estudi duit a terme sobre les propietats d'un tipus de partícules col·loïdals conegudes amb el nom de *raspalls esfèrics polimèrics* ('*spherical polymer brushes*'). En particular, l'estudi es centra en caracteritzar el comportament d'aquells raspalls esfèrics en els quals els efectes induïts per la curvatura de la superfície són substancials. En el capítol 6 es presenta la caracterització de la força existent entre dos d'aquests raspalls esfèrics, mentre que en el capítol 7 s'estudia el cas de raspalls esfèrics encapsulats dins d'una cavitat esfèrica. Per altra banda, els següents tres capítols (8 a 10) estudien la conducta de cadenes polimèriques sotmeses a lligadures no trivials. Així, en el capítol 8 es determina l'efecte que tenen les interaccions de volum exclòs en cadenes polimèriques semiflexibles confinades sobre superfícies esfèriques. En el capítol 9, hom estudia els processos d'adsorció de copolímers de bloc semiflexibles quan s'adsorbeixen sobre superfícies homogènies. Finalment, en el capítol 10 s'estudien els processos d'adsorció i reconeixement de cadenes homopolimèriques quan es troben pròximes a superfícies que presenten un patró consecutiu de vetes adsorbents i no adsorbents. La tesi finalitza amb un capítol onzè en el que es recullen les principals conclusions obtingudes en els capítols de recerca.

Tots els anteriors estudis s'han duit a terme mitjançant simulacions numèriques en les que s'han emprat les tècniques de *Monte-Carlo* i la *Dinàmica Browniana*. La Dinàmica Browniana s'ha emprat en els capítols 4 i 5 per a l'estudi de les transformacions de fase en els sistemes col·loïdals amb forces de minvament. Mentre que les tècniques de Monte Carlo s'han usat en la resta de capítols per a la modelització de les cadenes polimèriques. Les simulacions numèriques presenten diversos avantatges respecte la recerca tradicional duita a terme en laboratoris. Per una banda, les simulacions numèriques ens permeten dur a terme l'estudi de sistemes en els que altrament seria molt difícil la caracterització bé per problemes inherents a la preparació de les mostres en la forma adequada per dur a terme dit estudi; bé per motius relacionats amb dur a terme mesures difícils d'obtenir amb les tècniques disponibles en el laboratori. Com exemple, podríem esmentar que

les simulacions numèriques ens permeten evitar fàcilment els problemes relacionats amb la presència del camps gravitatoris durant els processos d'agregació col·loïdal. Un altre exemple seria el fet que les simulacions numèriques permeten estudiar amb tant de detall com es vulgui les primeres passes dels processos d'agregació. Circumstància que pot ser de gran utilitat en aquells processos en els que les cinètiques siguin massa ràpides com per a poder ésser seguides amb detall en el laboratori. Tot i aquest seguit d'avantatges, el principal problema que es presenta al dia d'avui quan hom es decideix a dur a terme un estudi mitjançant simulacions numèriques és la limitada potència dels ordinadors, la qual ens obliga a treballar amb sistemes de grandària reduïda i models físics força simplificats.

Els principals resultats i conclusions obtingudes al llarg de la present tesi es resumeixen en els següents paràgrafs:

- L'estudi dels sistemes col·loïdals bidimensionals exposat en els capítols 4 i 5 mostra una transició des d'una fase col·loïdal dispersa cap a una regió en la que coexisteixen dues fases: una formada per partícules en forma dispersa i l'altra fase constituïda per agregats col·loïdals cristal·lins. Dita transició s'observa al incrementar la fondària del pou del potencial d'interacció entre les partícules col·loïdals. Si es segueix incrementant la fondària del pou del potencial, aleshores s'observa com els agregats passen de tenir una naturalesa compacta a fractal. Aquests agregats fractals tenen una estructura híbrida en el sentit que presenten un empaquetament hexagonal compacte a escales de longitud curtes, mentre que semblen objectes fractals quan són observats a longituds d'escala majors. Per a pous de potencial prou fondos, hom recupera la conducta observada en els models DLCA en termes del valor de la dimensió fractal, el valor de l'exponent cinètic z i la forma d'escalament que presenta la distribució de grandàries dels agregats. Per a pous de potencial de poca fondària, però encara dins de la regió de coexistència de les dues fases, la cinètica observada per al creixement dels agregats presenta diverses similituds amb la cinètica associada a les separacions de fases en mescles binàries a temps mitjos. En el cas de pous de potencials prou petits en els quals només existeix la fase dispersa, hom observa que la cinètica d'agregació concorda força bé amb el model de camp-mig desenvolupat per Sorensen, Zhang, and Taylor (SZT) [71] per a sistemes en que la fragmentació dels agregats juga un paper primordial.
- L'estudi sobre la veracitat o no de la hipòtesis d'escalament dinàmic per al factor d'estructura $S(q)$ en la separació de fases dels sistemes col·loïdals amb forces de minvament (capítol 5) ens mostra que efectivament existeix un vertader escalament dinàmic per a pous de potencial amb poca fondària

però que es troben dins de la regió de coexistència de les dues fases. Els resultats mostren que en aquests casos, després d'un període inicial transitori, existeix una única longitud característica en el sistema que és condició necessària per a tenir un vertader escalament dinàmic. El període transitori inicial compren la fase de nucleació dels agregats i la fase inicial de creixement en la que els agregats creixen bàsicament per mitjà de la incorporació de monòmers i petits agregats als nuclis que van creixent. En aquest règim, la distància entre agregats i el radi de gir evolucionen de forma diferent amb el temps i l'escalament dinàmic és impossible. No obstant, després del període transitori inicial, el mecanisme de creixement predominant és la col·lisió entre els grans agregats amb la subseqüent reorganització de les seves superfícies amb l'objectiu de reduir la seva tensió interfacial. Els processos de creixement que romanen actius després del període transitori inicial induïxen a la distància entre agregats i al radi de gir a una evolució temporal semblant. Per aquest motiu, després del període inicial sí que s'observa una única longitud d'escala en el sistema.

En el cas de pous de potencial fondos, els processos de creixement induïxen la formació d'agregats de naturalesa fractal. En aquest cas els resultats proven que el sistema està controlat per dues longituds característiques que evolucionen de forma diferent amb el temps. Aquest darrer fet implica que no és possible tenir un vertader escalament dinàmic en el sistema. Tot i això, els resultats mostren un escalament aparent de les dades durant un cert període de temps degut a que dins de dita finestra de temps, les dues longituds característiques tenen valors comparables. Els resultats obtinguts s'han comparat amb les prediccions teòriques de Huang-Oh-Sorensen (HOS) [166]. Dits autors assumeixen que en sistemes monodispersos el factor d'estructura se pot escriure com un producte del factor d'estructura associat als centres de masses dels agregats multiplicat per un factor d'estructura associat a les partícules que conformen un d'aquests agregats. Cadascun d'aquests dos factors d'estructura té les seves pròpies longituds característiques. La comparació mostra una concordança parcial amb les prediccions de HOS, per una banda s'observa que dita teoria pot explicar l'origen del pic observat en el factor d'estructura per a pous de potencial poc fondos. En canvi, les prediccions de HOS no permeten explicar adequadament l'origen del pic en el cas de pous de potencial fondos. Una explicació plausible per aquesta falta de concordança per a potencials fondos és que en aquest cas els grans agregats mostren una polidispersió major.

- Els estudis duits a terme al llarg dels capítols 4 i 5 demostren clarament la importància de l'ús de la Dinàmica Browniana en l'estudi de l'agregació col·loïdal, i més generalment en l'estudi de sistemes que presentin transicions en les que el sistema evoluciona des d'una fase dispersa cap a una fase sòlida. Els resultats mostren que és possible estudiar amb la dinàmica Browniana sistemes d'agregats que evolucionen des d'una morfologia cristal·lina compacte a una morfologia fractal just canviant el valor d'un simple paràmetre.
- En els capítols 6 i 7 ens hem concentrat en l'estudi dels anomenats raspalls esfèrics (partícules col·loïdals que contenen polímers enganxats a la seva superfície) en aquells casos on els efectes de la curvatura juguen un paper primordial. Així, en el capítol 6 hem mesurat la força d'interacció entre dos raspalls esfèrics. Els resultats mostren que és possible descriure el perfil de forces mitjançant dos règims. A distàncies curtes, la teoria de Witten and Pincus [169] proporciona una descripció adequada de la força. Mentre que a distàncies més llargues la interacció es pot explicar en termes d'una extensió a la teoria de Flory per a dissolucions diluïdes de polímers. Els resultats mostren que la conducta global s'ajusta qualitativament bé (excepte en el règim de distàncies curtes) mitjançant la teoria fenomenològica de Doroszkowski and Lambourne [170] sempre i quan els raspalls tinguin una densitat de cadenes polimèriques enganxades sobre la seva superfície prou elevada. Els resultats també indiquen que la grandària radial característica dels raspalls no pertorbats segueix la mateixa relació d'escala respecte de la longitud de les cadenes N i el nombre de cadenes enganxades f que els polímers d'estrella $R_0 \sim N^{3/5} f^{1/5}$. Els resultats obtinguts s'han comparat amb els formalismes de camp-mig autoconsistent (SCF) de Wijmans-Leermakers-Fleer [202] i Lin-Gast [210]. S'han observat grans discrepàncies entre els resultats SCF i els resultats de Monte-Carlo en sistemes amb gran curvatura. Els mètodes SCF sobreestimen la interacció entre raspalls esfèrics a distàncies curtes degut a que no poden tenir en compte, de forma adequada, les correlacions existents entre monòmers.
- En el capítol 7 es presenten els resultats obtinguts per a raspalls esfèrics confinats dins de cavitats esfèriques. La densitat de monòmers i la pressió dins de la cavitat han estat mesurades. A més de les tècniques de Monte-Carlo, en aquest estudi s'ha fet un ús directe de la llei de recurrència de la funció de densitat de probabilitat per al propagador $G_N(r, r')$, evitant d'aquesta manera les aproximacions involucrades en els càlculs autocon-

sistents de camp mig que empren equacions tipus Schrödinger. Una comparació directa entre els mètodes de SCF usats i els resultats obtinguts mitjançant simulacions MC mostra que l'ús de la llei de recurrència i per tant de l'aproximació de camp-mig és una bona alternativa en el cas de raspalls lliures o dèbilment comprimits. En el cas de sistemes força comprimits, es proposa un extensió de la teoria de Flory per solucions polimèriques. Els resultats via Monte-Carlo concorden força bé amb l'extensió proposada a la teoria de Flory, amb l'avantatge addicional de que l'extensió proposada no implica cap cost computacional. En el règim de compressions molt elevades, s'ha trobat que la fracció volumètrica de monòmers v segueix un escalament amb la pressió P , $P \sim v^\alpha$. Els resultats SCF donen $\alpha = 2.15 \pm 0.05$, pròxim a la llei de *des Cloiseaux* ($\alpha = 9/4$), mentre que les simulacions de Monte-Carlo indiquen $\alpha = 2.73 \pm 0.04$. La diferència entre els valors d' α trobats mitjançant MC i SCF es pot atribuir al fet que els càlculs SCF no tenen en compte de forma adequada les correlacions existents entre monòmers.

- En el capítol 8 es presenten els resultats obtinguts per a cadenes flexibles i semiflexibles confinades sobre superfícies esfèriques. Els resultats es comparen amb les prediccions teòriques per a cadenes ideals de Mondescu and Muthukumar (MM) [267], y Spakowitz and Wang (SW) [268]. S'ha trobat que en tots els casos estudiats les prediccions de SW concorden força millor amb els resultats obtinguts mitjançant simulacions de Monte-Carlo que amb les prediccions de MM. Les conformacions de cadenes de longitud L , i longitud de persistència l_p restringides a moure's sobre una esfera de radi R poden ésser descrites de manera raonable mitjançant el formalisme de SW en el règim $L/(2\pi) < R < 2l_p$. Per a $R/l_p > 2$, la distància quadràtica mitja entre els finals de cadena, evoluciona en funció de la longitud de la cadena des d'un valor semblant a un camí autoevitant de dimensió dos, fins a un valor de saturació. En el límit de cadenes curtes i amb gran rigidesa s'observa una conducta similar al cas límit d'una barra rígida. A diferència de les cadenes ideals, les cadenes amb efectes d'exclusió de volum que es troben confinades sobre esferes de radi prou gran mostren una transició des d'un estat desordenat a un estat helicoidal quan s'incrementa prou la rigidesa de la cadena. Dita transició ha estat caracteritzada per mitja de la funció de correlació orientacional dels enllaços. Els resultats reflecteixen un balanç entre l'energia associada al vinclament de la cadena i les interaccions de volum exclòs.

- L'estudi dels processos d'adsorció de cadenes polimèriques semiflexibles sobre superfícies planes s'ha duit a terme en els capítols 9 i 10. Així, en el capítol 9 es presenten els resultats per a l'adsorció de polímers-bloc sobre superfícies homogènies. Concretament, s'han estudiat i comparat entre si diversos tipus d'estructures copolimèriques, tals com ara homopolímers, diblocs, copolímers tipus $(A_\alpha B_\alpha)$, i heteropolímers amb estructura aleatòria. En tots els casos estudiats s'ha observat que els processos d'adsorció es troben afavorits amb un increment de la rigidesa de la cadena. En particular, s'ha observat que l'adsorció completa d'estructures dibloc és de fet un procés que té lloc en dues passes a temperatures d'adsorció diferents que depenen de la rigidesa de la cadena, la longitud de la cadena i les energies d'adsorció de cada tipus de monomer amb la superfície ϵ_A and ϵ_B . Aquest procés observat per diblocs gradualment reverteix cap a un procés únic en el cas de copolímers de grandària de bloc α reduïda. Els resultats mostren que cada bloc de les cadenes copolimèriques rígides satisfà, independentment, les lleis d'escalament clàssic per a cadenes flexibles, en canvi, s'ha trobat que l'exponent de l'escalament ϕ depèn de la rigidesa de la cadena i de les energies d'adsorció. Per a cadenes rígides prou llargues, el radi de gir exhibeix una conducta típica d'una cadena polimèrica composta de N/l_p unitats on la seva longitud de persistència canvia com $l_p \sim (\kappa/k_B T)^{0.5}$.
- El capítol 10 presenta un estudi sobre el procés d'adsorció de cadenes homopolimèriques sobre una superfície construïda a base d'un patró periòdic de vetes adsorbents i no adsorbents. La conducta de les cadenes en funció de la rigidesa de la cadena, l'energia d'interacció i l'amplada de les vetes ha estat estudiada en detall. S'observa que el procés consta de dues etapes: *i*) la cadena s'adsorbeix de forma bastant isotròpica sobre la superfície a una temperatura característica T_c , i, *ii*) cal una nova reducció de la temperatura per davall de T_c per a que la cadena sigui reconeguda per a la superfície i s'ajusti al patró especificat. La reorganització de la cadena adsorbida sobre la superfície al abaixar la temperatura s'ha estudiat mitjançant la determinació del grau d'estirament, Q , i de la no-asfericitat de la cadena, A . Els resultats mostren que existeix una amplada de les vetes òptima que maximitza l'estirament de les cadenes. S'ha introduït un criteri per estimar la temperatura característica a la qual té lloc el reconeixement del patró per part de la cadena $T_r < T_c$. La dependència d'aquesta temperatura de reconeixement T_r amb els paràmetres associats a la cadena i a la superfície ha estat també estudiada en detall.

Desig que els materials exposats al llarg de la present tesi siguin a més d'una contribució a la clarificació de certs aspectes relacionats amb la física dels polímers i els col·loides, una aportació de valor per aquells que volen començar la seva recerca en aquest camp i a més a més seveixi per a estimular nous estudis tant teòrics com experimentals.

Joan J. Cerdà.
Palma de Mallorca, Maig 2005.

Agraïments

Deia en Newton que si ell havia tingut l'oportunitat de veure més enllà que la majoria dels homes era gràcies a haver muntat sobre les espatlles de gegants. Jo he de dir que si he tingut l'oportunitat de trobar algun que altre còdol a la vorera de la mar i finalitzar aquesta tesi és gràcies al recolzament de moltes persones que tot i no ser gegants, sens dubte han contribuït a fer possible que després d'un parell (mallorquí) d'anys¹, avui pugui estar aquí escrivint aquestes línies.

En primer i en el més destacat dels llocs vull agrair la confiança i el suport incondicional dels meus pares al llarg de tots aquests anys, i als qui vull dedicar aquesta tesi.

Voldria també agrair el suport rebut per part de les persones amb les quals he treballat durant aquests anys: en Tomàs Sintès, qui m'ha acompanyat i ha sofert en primera persona els despropòsits d'un servidor al llarg de la travessia pel desert. En Raúl Toral, amb qui durant els primers anys vàrem treballar les interaccions en raspalls polimèrics i que sempre que ha pogut ens ha donat quelcom més que una mà amb la logística i els assumptes pecuniaris. Agrair també el suport, la confiança i les ensenyances de n'Amit Chakrabarti amb qui he col·laborat estretament durant aquests darrers anys. En aquest cas voldria fer extensiu el meu agraïment a la família de n'Amit, Leena, Mohana i Meg que em varen acollir durant les meves estades a Kansas com un més de la família (*'the big child'*). També agrair a n'Emilio Hernández la seva disposició per ajudar-nos en les qüestions pecuniàries.

També vull mencionar en aquestes línies el meu agraïment al departament de Física Interdisciplinar de l'IMEDEA així com a tots els seus membres per la paciència i els recursos que han posat al meu abast, quelcom més que meritori si es té en compte tot el temps que han hagut d'aguantar a un servidor i a les seves quasi eternes simulacions que en més d'una ocasió han aclaparat més de la meitat dels recursos informàtics del departament. Expressar també el meu agraïment

¹Per aquells de fora de l'illa, una definició aproximada del que és un parell mallorquí seria: un nombre major que 2 i menor que $6 \cdot 10^{23}$.

al Departament de Física de la UIB que m'ha permès durant aquests dos darrers anys gaudir d'una plaça d'ajudant al departament. Vull agrair també al Col·legi Arcàngel Sant Rafel de Palma, i en especial a la seva directora Margalida Moyà, les facilitats que me donaren quan hi vaig estar treballant per a que pogués compaginar docència, estudis i recerca al mateix temps.

I com no, també vull esmentar la meva gratitud al trio calavera: Mr. Pep Mulet, Mr. Pep Batle i Mr. Mariano Cara els quals han sofert els efectes secundaris d'estar exposats a la radiació del *bitxo gros* durant anys i més anys, i que m'han ajudat en no menys de $(n - 1)$ ocasions. Els agraïments no podrien estar complets si no fes també menció a la gent de l'antic grup *d'Excursions Dominicales* i a la gent *d'Excursions On-Line* els quals varen sofrir i molts d'ells encara avui en dia sofreixen a la *sargantana rampante* i les seves entremaliadures.

And last but not least, no puc concloure aquest agraïments sense lloar la creativa, imaginativa i difícilment igualable política científica d'ajut i suport als que es volen iniciar en els camins de la ciència duta a terme per part dels successius governs espanyols, de la Comunitat Autònoma de les Illes Balears, i del Consell Insular de Mallorca. Polítiques que m'han permès aprendre a valorar *le savoir faire* de dites institucions, així com adquirir les habilitats i coneixements necessaris per el dia de demà emplenar impresos i sol·licituds de forma diligent i metòdica.

Seriosament, a tots els que han fet possible la consecució d'aquesta tesi, expressar-los la meva més sincera gratitud.

J. J.

Firò era i no era temps enrera
un al·lotet que havia nom Juanet que
s'encaperrotà a fer una tesi. Es posà
a la feina dia i nit, nit i dia. Caminà tot
plegat Set dies i Set nits, Sempre dins el
llevant, tresca qui tresca i mira qui mira
ben arreu per veure si guiparia Senya de
res . . .

Idò heu de creure i pensar i pensar i
creure que, un dia, devers es beil, la tesi
fonc acabada . . .

L'am contà la Sargantana de'n Juanet.

Preface

When somebody begins to read a thesis about colloids and polymers, two quite natural key questions arise:

- (a) Why should polymers and colloids matter to physicists?
- (b) After approximately two centuries of hard studies about the nature and behavior of colloidal and polymeric systems: There is still something interesting to be done in this area?

In my opinion the answer to the above questions is dealt in an excellent way by Daoud and Williams in their book about soft-matter physics². Therefore an adapted answer to the above issues based upon Daoud-Williams statements could be

- (a) One of the main topics in physics should be the study and understanding of all the interactions present in nature. The study and the subsequent understanding of the matter properties and behaviors have reported in the past two centuries many improvements and benefits to humanity. Polymers and colloids are a clear example of how their study has become in a large progress and a better life quality. In addition, the study of such systems has contributed and it still contributes to broaden our notion of how matter can behave: self-organization in the space, flow and carrier properties, superconducting materials, etc.
- (b) Although colloids and polymers has been object of scientific research for a very long time, the advances in synthetic chemistry have opened the door to a vast, new and mainly unexplored region in the field. It is not very daring to claim that we are still in the first stages. The shaping and control of the interactions in the polymeric and colloidal systems is not still full understood. In this context, some very basic aspects of colloid and polymer science still remain without a successful quantitative explanation. Therefore the field is still plenty of room for new and fresh research.

²Daoud, M.; and Williams, C. E., *Soft Matter Physics*; Springer-Verlag: Berlin, 1999.

In fact, the purpose of the present thesis is to give an insight about several still non rather well understood issues in polymeric and colloidal systems. The thesis is divided into eleven chapters from which the three first constitute a brief introduction to the basic knowledge needed for a better understanding of the following chapters. Thus, Chapter 1 is devoted to an introduction to colloidal systems, whereas Chapter 2 deals with the basic characteristics of polymeric systems, and Chapter 3 ends the general introduction by summarizing the main features of the numerical methods used along the thesis. Research exposition begins with Chapters 4 and 5 devoted to the study and characterization of the phase transformations in two-dimensional depletion driven colloids. On the other hand Chapters 6 and 7 deal with the properties of a particular but very important kind of colloidal particles known as *spherical polymer brushes*. The pair-wise interaction of spherical brushes when curvature effects are important is studied in Chapter 6, whereas Chapter 7 focuses on the behavior of a spherical brush encapsulated inside a spherical cavity. The three following chapters (8 to 10) are devoted to the study of the behavior of polymer chains with non trivial constraints. In Chapter 8 a study about the excluded volume effects on polymer chains confined to spherical surfaces is presented. Chapter 9 is devoted to the characterization of the adsorption process of semiflexible block-copolymers on homogeneous surfaces. Finally, Chapter 10 studies the processes of adsorption and recognition of homopolymer chains close to pattern-stripped surfaces. The thesis ends with a chapter in which the main conclusions obtained along Chapters 4 to 10 are highlighted.

All the above topics have been addressed by using Monte-Carlo and Brownian-Dynamics numerical techniques. Numerical simulations have become nowadays a basic tool in the study of complex systems, otherwise difficult to prepare in the lab, giving the possibility of measuring properties with an accuracy in some cases not available with current lab tools. They can be used to test ideas concerning the behavior of experimental systems and to pose well defined problems for theoretical analysis. In this way, they provide a valuable bridge between theory and experiment. As an example, numerical simulations allow us to bypass easily the problems related to the presence of gravity during colloidal aggregation in experiments. In the same direction, numerical studies allow us to observe the very early stages of the aggregation phenomena, specially useful when one deals with fast kinetics difficult to characterize in lab. On the other hand, the main handicap of current numerical simulations is the limited amount of power calculus of present computers which forces us to the study of small sized systems.

In addition to make a contribution intended to clarify several aspects in colloidal and polymeric systems, I hope the material herein presented would be a valuable reference for those who want to start a research in the field of the physics

of polymers and colloids. In turn, I hope the thesis would stimulate further fresh theoretical and experimental studies.

Joan J. Cerdà
May 2005

Acknowledgments

Newton said that if he had seen further than most men, it was because he had stood on the shoulders of giants. I have to state that if I have had the opportunity to find some smoother pebble playing on the sea-shore and end up this thesis, it is thanks to the support of many people. Although they are not giants, they have contributed, without doubt, to make possible that after a (Majorcan) couple of years³ I could be here writing these lines.

First of all, and in the most outstanding position, I want to thank the unconditional support of my parents during all these years, and I want to dedicate the present thesis to them.

I also want to thank the support I have received from the people with whom I have been working during these years: Tomàs Sintes, who has accompanied me throughout my journey in the desert, and who in addition has suffered in first person all my nonsense during these years. Thanks to Raúl Toral, with whom we have been working during the first years in the interactions with polymeric brushes, and who whenever possible gave me support for logistic and funding issues. I want also to thank the support and the lessons that Amit Chakrabarti have given me during these last years in which we have been working closely. In this case, I also want to extent my gratefulness to Amit's family, Leena, Mohana and Meg which welcome me like one more in the family (*'the big child'*) during my stays in Kansas. Also, thanks to Emilio Hernández for his help concerning funding issues.

I also want to mention in these lines my gratefulness to the IMEDEA cross-disciplinary physics department, as well as to all its members for the patience and resources they made me available. Something more than meritorious if one takes into account how long they are suffering me and my almost eternal simulations. Simulations that, in many cases, have monopolized most than the half of the computational resources of the department. I also want to thank the Physics

³For those from outside the island, an approximate definition of what is a Majorcan couple is: a number larger than two and smaller than $6 \cdot 10^{23}$.

Department of the UIB which have allowed me to hold an assistant instructor position at this Department for the last two years. Thanks also to the Col·legi Arcàngel Sant Rafel of Palma, and specially to its principal Margalida Moyà, for the facilities given that made me possible to arrange teaching, research and studies during those years.

Of course, I also want to thank my gratefulness to the *calavera trio*: Mr. Pep Mulet, Mr. Pep Batle i Mr. Mariano Cara which have suffered the aftereffects of being exposed to the *big bug* radiations for so many years, and who have helped me in not less than $(n - 1)$ occasions. My gratefulness could not be complete without mentioning the people of the former group of *Excursiones Dominicales* and also the people of *Excursions On-Line* which suffered and are still nowadays suffering the *sargantana rampante* and its pranks.

And last but not least, I can't finish this section devoted to the acknowledgment without praising the creative, imaginative and hard to equal scientific policies of aid to the beginners in science carried out by the successive Spanish governments, the Balearic Islands local governments, and the Majorcan Insular Council. Policies that have allow me to value *le savoir faire* of such institutions, and that also have allowed me to acquire the necessary abilities and knowledge in order to fill up forms and requests with diligence and in a methodical way.

Seriously, to all the people who have make possible the attainment of this thesis, my best sincere gratitude.

J. J.

Contents

1	An introduction to colloids	1
1.1	Brownian Motion and diffusion	2
1.2	Stability of colloidal systems	4
1.2.1	The DLVO model	10
1.2.2	Addition of polymers to colloidal systems	12
1.2.3	Colloid stabilization using grafted polymers	16
1.3	The colloidal aggregation process	18
1.3.1	Fractals	18
1.3.2	Measuring Fractal dimensions of colloidal aggregates	21
1.3.3	Irreversible cluster-cluster aggregation kinetics	23
1.3.4	Reversible cluster-cluster aggregation kinetics	30
1.4	Scattering by aggregates	33
1.4.1	Typical structure factors for fractal aggregates	37
2	Basic principles of polymer physics	41
2.1	What is a polymer?	41
2.2	Conformations of a polymer chain	44
2.3	Characterization of a single polymer chain	47
2.3.1	The mean square end-to-end distance, and the Kuhn segment length	47
2.3.2	The Radius of gyration of the chain	48
2.3.3	The asphericity and non-sphericity parameters	49
2.3.4	The bond-angle correlation function (BAC) and the persistence length l_p	49
2.3.5	The bond orientational correlation function (BOC)	50
2.4	Models for ideal chains	50
2.4.1	The freely jointed chain model	51
2.4.2	The Gaussian chain model	52

2.4.3	The freely rotating chain model	53
2.4.4	The worm like chain model	53
2.5	Real chains: the effect of long-range interactions	54
2.6	Polymer solutions	57
2.6.1	Other theoretical approaches to polymer solutions: the virial expansion, the Flory-Huggins theory, and the des Cloizeaux Law	60
2.7	Polymers near surfaces. The adsorption process	62
3	Numerical Simulations: Basic features of the Stochastic methods	65
3.1	Monte Carlo simulations in the canonical ensemble	68
3.1.1	The Metropolis algorithm: general scheme	69
3.1.2	The Metropolis algorithm applied to the canonical collectivity	70
3.1.3	Statistics from a sequence of correlated states	72
3.1.4	Monte Carlo simulations of polymer chains: basic features	74
3.2	Brownian dynamics	76
3.2.1	Algorithms for Brownian Dynamics simulations	79
4	Kinetics of phase transformations in depletion-driven colloids	87
4.1	Introduction	87
4.2	Cluster Morphology	90
4.3	Comparison with Traditional Models of Aggregation and Phase Separation	94
4.3.1	Fractal Dimension	94
4.3.2	Growth Kinetics	94
4.4	Concluding remarks	100
5	Structure factor scaling in colloidal phase separation	103
5.1	Introduction	103
5.2	General Features of the Structure Factor	106
5.3	Scaling of the Structure Factor and Various Length Scales in the System	108
5.3.1	Growth of Compact Clusters	108
5.3.2	Growth of Fractal Clusters	112
5.4	Origin of the Peak in the Structure Factor	115
5.5	Concluding remarks	119

6	Spherical polymer brushes I: The pair-wise interaction	121
6.1	Introduction	122
6.2	Theoretical review	125
6.2.1	Self-Consistent Field theories	125
6.2.2	Other related theories to the study of spherical brushes .	132
6.3	Previous experimental findings	135
6.4	Interaction between two spherical brushes	138
6.4.1	Numerical Model	140
6.4.2	Computing the force between spherical brushes	141
6.4.3	Results and Discussion	144
6.5	Concluding remarks	149
7	Spherical polymer brushes II: Encapsulated brushes	153
7.1	Numerical models	153
7.1.1	Monte Carlo method	153
7.1.2	Self Consistent Field method	155
7.2	Results and discussion	157
7.2.1	Density profiles	157
7.2.2	Cavity pressure and force profiles	158
7.3	Summary and concluding remarks	165
8	Polymer chains confined to spherical surfaces	167
8.1	Introduction	167
8.2	Theoretical Review	169
8.2.1	The Mondescu-Muthukumar Theory	169
8.2.2	The Spakowitz-Wang theory	169
8.3	Numerical model	170
8.4	Results and discussion	171
8.4.1	Mean square end-to-end distance	171
8.4.2	Transition from disordered to helicoidal conformations .	179
8.5	Concluding remarks	183
9	Adsorption of stiff copolymers on homogeneous flat surfaces	185
9.1	Introduction	185
9.2	Numerical Model	187
9.3	Results and Discussion	188
9.3.1	Diblock chains	188
9.3.2	Block copolymer chains	194

9.4 Concluding remarks	198
10 Stiff polymer adsorption onto striped surfaces	201
10.1 Introduction	201
10.2 Numerical Model	202
10.3 Results and Discussions	202
10.3.1 Degree of stretching	204
10.3.2 Non-sphericity	207
10.4 Summary and Conclusions	209
11 General conclusions	211
Bibliography	217
Erratum	231
Addenda	233
Curriculum Vitae	i

Chapter 1

An introduction to colloids

Physics is becoming so unbelievably complex that it is taking longer and longer to train a physicist. It is taking so long, in fact, to train a physicist to the place where he understands the nature of physical problems that he is already too old to solve them.
Eugene P. Wigner; (1902-1995)

Well, let's try to make it easier for the sake of the next generations . . .

This chapter is intended to provide a short summary of the main topics related to the world of colloids. As we will see in brief, colloids comprise a huge area with applications in many, an sometimes unsuspected, areas.

A colloidal system can be defined as a diphasic medium in which one of the phases is very finely dispersed in the other phase. In this definition no restriction is made on the chemical nature or the physical state of the constituents. The characteristic length scale of the domains of the dispersed phase ranges usually between $1nm$ and $1000nm$. Historically, the term *colloid* was coined in 1861 by the British chemist Thomas Graham from the Greek word *kolla* for glue, to label a supposed characteristic of some chemical class of products that do not go through a wall of parchment.

Colloids far from being a weird phenomena in nature are almost omnipresent in our every day life (Table 1.1). The large variety of colloidal systems and their useful properties have overspread the use of colloids in many areas ranging from chemical and food industry to nanotechnology and medicine. Examples of the use of colloids in current technological devices are the electrophoretic image displays¹ (EPIDs), and the superheated-superconducting colloid detectors of elemental particles² (SSCD's).

¹The EPID or electrophoretic image display contain submicron-size particles of pigments dispersed in a liquid along with a dye that provides contrast. When an electrical potential is applied to the system, pigment particles are driven to the interface between the suspending liquid and a viewing plate. EPIDs might be used in the design of new TV flat panel devices. Nowadays, EPID's are used for instance in the manufacture of the so-called e-paper.

²Superheated-superconducting colloid detectors (SSCD's) are devices in which superconduct-

Continuous medium	Dispersed phase		
	Solid	Liquid	Gas
Liquid	Suspensions Inks	Emulsions Mayonnaise	Foams Whipped cream
Gas	Solid aerosols smoke	Liquid aerosols fog	
Solid	Solid dispersions Composite materials	Solid emulsions Butter	Solid foams Polyurethane foams

Table 1.1. Some examples of colloidal systems classified in function of the physical state of the constituents.

Disciplines that use colloids have improved their performances thanks to the knowledge about colloids acquired during the XX-th century. However, despite the huge efforts done, not all the aspects about colloids are perfectly understood at present. Some basic questions about colloidal systems remain still unsolved or are only partially understood. For instance, the interaction among colloids in certain systems is still poorly understood. Another weak point is related to the understanding of how the initial conditions, interparticle potentials and flow properties influence the creation of mesoscopic structures in colloidal systems. Also the rheology of colloidal suspensions is still a battle horse in many labs around the world.

Part of the work done in this thesis is devoted to improve our knowledge on some of the weak points concerning colloidal systems. However, before we face up such effort we will review some basic facts about colloids.

1.1 Brownian Motion and diffusion

In 1828 Robert Brown reported the erratic movement of pollen particles floating in quite water which seemed to jump randomly in any direction. The same behavior was observed by Brown when pollen was replaced with very fine mineral

ing colloids of a few micrometers in diameter are embedded in a dielectric material, and placed in a magnetic field. The grains are maintained just below their superconducting transition temperature. The device is used to detect fundamental particles: when the fundamental particle collides with the colloid, it deposits a small amount of energy enough to promote a transition in the grain from superconductor to the normal state in which the magnetic flux can penetrate into the colloid. This change of phase of the colloid particle produces a detectable electromagnetic signal. See for instance, Drukier, A. Z.; Freese, K. F.; and Spergel, D. N., *Phys. Rev. D*, **33**, 3495, (1986).

particles. Brown concluded from these observations that the random motion occurred independently of the origin and composition of the particles. What Brown observed in 1828 was in fact the typical motion of colloidal particles. In 1905, Einstein [1] proposed the following theory to explain the Brownian (colloidal) motion: the displacement $\vec{x}(t)$ of a colloidal particle of mass m is governed by the equation

$$m \frac{d^2 \vec{x}}{dt^2} = -\frac{1}{\mu} \frac{d\vec{x}}{dt} - \nabla U + \vec{f}_{random}(t) \quad (1.1)$$

that assumes that three forces act onto the particle: the first term on the right side states for a friction force due to the viscosity of the fluid. The second term are the forces due to external potentials like the gravity. The third term stands that the constant buffeting of a colloidal particle by solvent molecules can be described through a force that fluctuates randomly in time but with zero mean. If we assume that the motion is over-damped because the viscous term usually dominates the inertial one, then $\frac{d^2 \vec{x}}{dt^2} = 0$, and the above equation reduces to the *Langevin equation*

$$\frac{d\vec{x}}{dt} = -\mu \nabla U + \vec{\eta}(t) \quad (1.2)$$

where $\vec{\eta}(t) = \mu \vec{f}_{random}(t)$ is a stochastic velocity with zero mean $\langle \vec{\eta}(t) \rangle = 0$. If we assume that the probability distribution of $\vec{\eta}(t)$ is Gaussian with variance $2D$ (we will see later the meaning of D)

$$P[\vec{\eta}(t)] \sim e^{-\int d\tau \frac{\vec{\eta}^2(\tau)}{4D}} \quad (1.3)$$

then the covariance of the noise at two times t and t' is

$$\langle \eta(t) \eta(t') \rangle = 2D \delta(t - t') \quad (1.4)$$

When $U = 0$ the separation $\vec{x}(t) - \vec{x}(0)$ has a variance given by

$$\langle (\vec{x}(t) - \vec{x}(0))^2 \rangle = 6Dt \quad (1.5)$$

In fact, it is possible to show that the parameter D is the diffusion coefficient of particles in the fluid when $U = 0$. Furthermore, it is possible to show that Einstein's relation connecting the fluctuations of noise to the dissipation in the medium

$$D = k_B T \mu \quad (1.6)$$

must be satisfied in the Brownian motion.

Experiments show that the use of the Langevin equation with a noise satisfying the above constraints is an adequate approach to describe the Brownian

motion of a colloidal particle. However, in a colloidal system there are many particles so a formalism which gives a global description of the system is desirable. It is possible to describe a whole system of colloidal particles in terms of the particle concentration $c(\vec{x}, t)$ (rather than particle per particle) using the *Smoluchowski equation* [2],

$$\frac{\partial c}{\partial t} = \mu \nabla \cdot (k_B T \nabla c + c \nabla U) \quad (1.7)$$

Another approach is the description of the Brownian motion in terms of the temporal distribution function of the position \vec{x} and velocity \vec{v} of particles $f(\vec{x}, \vec{v}; t)$. It is possible to obtain an equation for such distribution function if we assume the next hypothesis: (i) the fluid evolves on a much shorter time-scale than the particle, and a Markov assumption can be made for the variables associated to the particles; (ii) only small jumps occur, and the transition probabilities between two states of the particle is sharply peaked around a mean value. Under these assumptions, the time evolution of $f(\vec{x}, \vec{v}; t)$ reduces to a Fokker-Plank (or Kramers-Klein) equation:

$$\frac{\partial f(\vec{x}, \vec{v}; t)}{\partial t} = \nabla_{\vec{v}} \cdot \left[\left(\frac{\vec{v}}{\mu m} - \frac{F(\vec{x}, t)}{m} + \frac{k_B T}{m^2 \mu} \nabla_{\vec{v}} \right) f(\vec{x}, \vec{v}; t) \right] - \nabla_{\vec{x}} \cdot (\vec{v} f(\vec{x}, \vec{v}; t)) \quad (1.8)$$

where F is the force derived from U . The Fokker-Plank equation can also be deduced starting from the Liouville equation, the advantage of deriving it from Liouville equation is that in such case we can bypass the stochastic assumptions assumed in the phenomenological description of the Brownian motion [3,4]. Kramers-Klein and Smoluchowski descriptions for a colloidal system are in fact analogous, a rigorous proof of this relation was established by Wilemski in 1976 [5].

The use of a single scalar μ to deal with friction in the Brownian motion (Rouse Model) is just an approximation to the real motion of colloidal particles. It is possible to go further in the description of the Brownian movement, but μ should be replaced by a mobility matrix which accounts for the hydrodynamic interactions between all the particles.

1.2 Stability of colloidal systems

The colloidal particles present in a system can suffer several types of attractive and repulsive forces. These forces can arise directly from the interaction with other colloidal particles or as an effect due to the special characteristics of the medium in which colloids are dispersed. If the net force acting upon colloidal particles is repulsive we will have an stable system. However, if the net force

among colloids is attractive the system is unstable and the colloids tend to form mesoscopic domains called aggregates. In fact, the tuning of the colloidal interactions has been used by the humanity since the ancient times. For instance, when we pour an acid such as vinegar or citric acid into milk, it is possible to obtain cheese, white glue (the casein glue used by painters), or a plastic material depending on the type of milk and the subsequent treatment. The acid is responsible for a change in the interactions between casein proteins³ usually found in milk forming micelles (a type of colloidal particle).



Figure 1.1. When an acid such as vinegar is added to milk, casein proteins coagulate leading to cheese, glue or plastic depending on the procedure.

The stability, instability or metastability of a colloidal system depends on the type of interactions present in each colloidal system. Colloidal particles interact with other colloidal particles as well as with the molecules of the medium in

³The addition of small amounts of acid to the milk promotes the denaturalization of casein proteins and its coagulation. It is a similar process to the produced by bacteria which convert the lactose of the milk in acid lactic. In natural milk, casein proteins (80% of milk proteins) are known to form negatively charged micelles, the electrical charge contribute to the stabilization of such micelles. When acid is added to milk, casein micelles reduce their electric charge and eventually become unstable in the suspension. Usually micelles start an aggregation process due to hydrophobic interactions (milk is a 88% water). When whole milk is used, the colloidal fat particles present in the milk are drag along with the casein proteins leading to the formation of cheese. When skim milk is used, the visible white clumps contain mainly casein protein. If casein clumps are separated from the whey, diluted with a little of water an neutralized with sodium bicarbonate (baking soda), we get a white glue: the casein glue. The optional use of heat when adding the acid has a twofold effect: it helps to denaturalize the proteins, and it promotes the reactions of polymerization among proteins. The heating of Casein clumps, depending on the conditions, may eventually lead to plastic matter that behaves like rubber and it hardens with time. A harder plastic can be obtained if casein reacts with formaldehyde.

which colloids are dispersed. Colloidal interactions can be described in terms of the basic interactions of molecules or atoms that form the colloidal particles. The number and nature of the interactions is extremely diverse but a rough classification of the main interactions is depicted in Figure 1.2.

Concerning the *electrostatic forces*, a colloidal particle can acquire a net charge due to several processes: adsorption of charged species from the medium, chemical equilibria of dissociating groups in the particles (like Casein proteins in milk), or desorption of lattice ions. However, electro-neutrality must be satisfied, and consequently a layer of counter ions must form around the colloidal particles. This layer is usually called the electrostatic double layer, and the interactions are of complex nature. However, the force can be roughly approximated as an exponential decaying force

$$F_{\text{double layer}} \sim e^{-\kappa R} \quad (1.9)$$

where R is the distance among the surface particles, and $1/\kappa$ is a characteristic length called the *Debye length* that, in general, ranges from 30nm for very low concentrations of polyelectrolytes to 0.1nm for high concentrations. A deeper study of double layer effects can be found in Evans-Wennerström [6] and Israelachvili [7]. Keesom, Debye and London forces are generally referred as van der Waals forces (vdW)⁴. Besides vdW forces are not as strong as hydrogen-bond and covalent interactions (see Table 1.2), vdW forces play a main role in the stability of neutral colloidal suspensions as we will see later. In the non-retarded

Force	Associated strength (KJ/mol)	
	From	To
Keesom	0.5	20
Debye	0.02	0.5
London	0.5	30
H-bond	4	50
covalent	100	800

Table 1.2. A rough estimation of range of strengths associated to several types of intermolecular forces.

approximation⁵, the leading terms of the three contributions to the vdW forces

⁴We adopt here a restrictive definition of the van der Waals forces accordingly to the IUPAC criteria [IUPAC Compendium of Chemical Terminology, 2nd Edition, 1997]. The term 'van der Waals forces' is sometimes used loosely for the totality of nonspecific attractive or repulsive intermolecular forces.

⁵At separations larger than a few nanometers retardation effects become significant. There is a

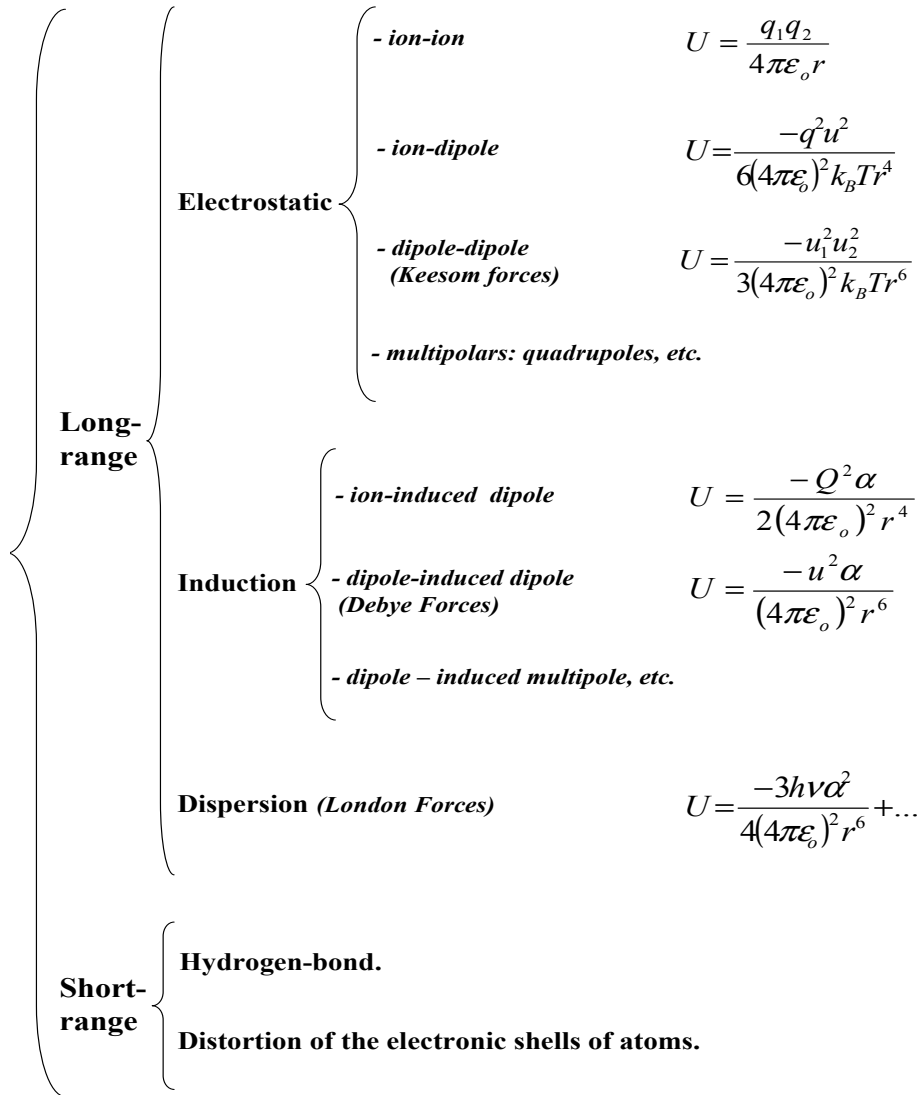


Figure 1.2. A rough classification of the main interactions that exist among molecules that form colloidal particles. Interaction energies (in SI units) have been written in the scheme for those cases where expressions of the energy are simple and general. The notation is: q stands for the electric charge, u is the electric dipole moment, α is the electric polarizability, r is the distance between particles, k_B is the Boltzmann constant, T absolute temperature, h Planck's constant, ν is the electronic adsorption (ionization) frequency, and ϵ_0 is the permittivity of the vacuum.

exhibit a characteristic dependence $1/r^7$. This similarity can be used to model an effective attractive potential between molecules proportional to $-1/r^6$. However, each colloidal particle is usually formed of many molecules or atoms which make vdW interactions among large bodies (colloidal particles) non trivial. If we assume colloidal particles to be monodisperse spheres of diameter D , then the net contribution of the molecular forces $\sim 1/r^6$ is⁶ [8],

$$V_{vdW}(r) = \frac{-A}{12} \left[\frac{D^2}{r^2 - D^2} + \frac{D^2}{r^2} + 2 \ln \left(1 - \frac{D^2}{r^2} \right) \right] \quad (1.10)$$

where the Hamaker constant A is a measure of the strength of the vdW forces between the colloidal aggregates ($A \approx 10^{-20} - 10^{-18} J$). In the limit $D \gg r$ Eq. 1.10 behaves as $V_{vdW}(r) \sim -AD/r$, whereas in the limit $D \ll r$ the dependence $V_{vdW}(r) \sim -AD^6/r^6$ is recovered.

In addition to vdW forces, a repulsive force arises at very small separations between neutral colloids. This repulsive short ranged force has a quantum nature and it is due to the distortion of the clouds of electrons of the atoms when they are very close. The interaction is complex, and a general and simple expression for such type of interactions is not available. In practice, we assume an arbitrary but convenient representation (an effective potential) for this repulsive interaction at short distances. The most rough model represents the interaction as a hard-core potential,

$$V(r_{ij}) = \begin{cases} 0, & \text{for } |\mathbf{r}_i - \mathbf{r}_j| > \sigma, \\ \infty, & \text{for } |\mathbf{r}_i - \mathbf{r}_j| < \sigma. \end{cases} \quad (1.11)$$

where σ is a parameter determining the range of the repulsive interaction. The hard-core potential is, in fact, the limiting case ($n \rightarrow \infty$) of a power-law model,

$$V(r_{ij}) = \left(\frac{\sigma}{r} \right)^n \quad (1.12)$$

The power-law model represents a more realistic approach than the hard-core because electron clouds are to some extent penetrable. However, a power-law dependence is usually more expensive in computer time than a hard-core potential. Another representation of the repulsive force is the exponential-potential

finite time taken for the changes in the electromagnetic field to travel from one particle to a second particle and its effects come back because electromagnetic fields do not propagate instantaneously. Retardation effects occur when such delay in time becomes comparable to the period of the fluctuating field itself. Non-retarded van der Waals forces are a simplification of the true phenomena.

⁶Hamaker method assumes pair-wise additivity of the molecular vdW forces which constitutes a rough approximation. A more accurate alternative is to use the continuum theory of Lifshitz [7, 9, 10] which leads to power-law dependences close to those obtained with the Hamaker method.

$V(r_{ij}) \sim \exp(-r_{ij}/\sigma)$ but usually its calculation is more expensive in computer time.

In order to overcome the complex nature of the interactions present in colloidal systems, the use of effective potentials has become a natural way to try to explain the stability or instability of colloidal suspensions. When the double-layer electrostatic phenomena is not considered (neutral colloids), a commonly used effective potential between the molecules forming colloidal aggregates is the *Lennard-Jones potential*⁷,

$$U_{LJ} = 4\epsilon \left(\frac{\sigma^{12}}{r^{12}} - \frac{\sigma^6}{r^6} \right) \quad (1.13)$$

where ϵ is equal to the absolute value of the maximum depth of the potential. If we suppose the colloidal aggregates are monodisperse spheres of radius R , and diameter D , then the net contribution of the components $1/r^6$ to the large body interactions is given by Eq. 1.10, whereas the components $1/r^{12}$ have a contribution [11],

$$V_{LJ_{12}}(r) = \frac{A\sigma^6}{37800} \frac{1}{r} \left[\frac{r^2 - 14Rr + 54R^2}{(r - 2R)^7} + \frac{r^2 + 14Rr + 54R^2}{(r + 2R)^7} - 2 \frac{r^2 - 30R^2}{r^7} \right] \quad (1.14)$$

When a molecular LJ potential is used, the Hamaker constant is $A = 4\pi^2\epsilon\sigma^6\rho^2$, where ρ is the density of molecules or atoms in a colloidal particle.

Once we have a rough approximation to the interaction between colloids, a first crude approach to the study of the stability of colloidal suspensions can be done. Figure 1.3 shows the effective interaction among colloidal particles $V_{model} = V_{LJ_{12}} + V_{vdW}$. The combination of a repulsive and an attractive force leads to the existence of a short-ranged potential-well which, in principle, will force neutral colloidal particles to aggregate. Figure 1.3 makes clear that other repulsive forces (electrostatic or steric) will be needed usually in order to make a colloidal suspension stable.

The study of the colloidal stability-instability phenomena through the previous potential is a rough approximation to the simplest colloidal suspension in which the dispersing medium does not play any role. We will study the stability-instability phenomena in more complex scenarios where the dispersing medium modifies substantially the nature of the colloid-colloid interactions.

⁷The Lennard-Jones potential contains a term $-1/r^6$ to take into account the vdW forces, and a term $1/r^{12}$ to describe the force that arises from the distortion of the electronic atomic shells. The $1/r^{12}$ dependence is arbitrary but it has been observed to lead to reasonable results. A historical reason to set the repulsive term as $1/r^{12}$ is that it is straight to calculate once $1/r^6$ is known.

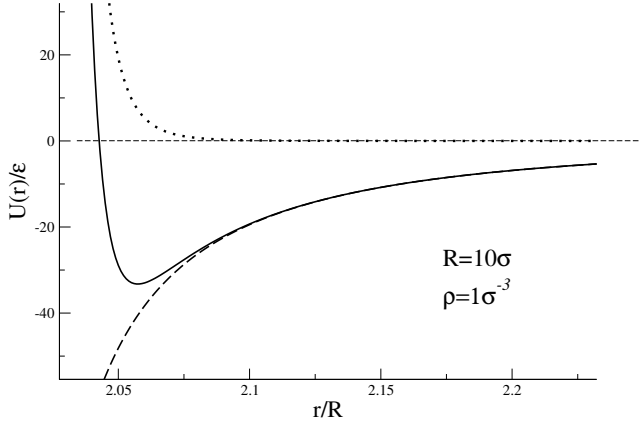


Figure 1.3. The effective potential $V_{model} = V_{LJ12} + V_{vdW}$ in rescaled units of ϵ and the radius of the colloidal particles R . The two contributions to the potential are plotted with dotted (V_{LJ12}) and dashed lines (V_{vdW}). The potential has been computed for particles of size $R = 10\sigma$. The density of molecules inside the colloidal particles is set to $\rho = (\sigma)^{-3}$.

1.2.1 The DLVO model

One of the former theories intended to explain the existence of both stable and unstable suspensions was the DLVO theory developed in the 40's independently by Derjaguin-Landau [12] in Russia, and Verwey-Overbeek [13] in the Netherlands. The theory assumes that the presence of charged particles in the medium leads to the formation of a double-layer surrounding the colloidal particles [7]. The presence of the double-layer implies the existence of an exponentially decaying repulsive force (Eq. 1.9). When the size of the objects is small enough gravitational effects can be neglected, and it is possible to consider the stability of a suspension due to the combination of attractive van der Waals forces and the repulsive electrostatic effects. The theory predicts that vdW forces become increasingly important when the interparticle distance is reduced, whereas the electrostatic double layer interactions dominate at large separations. For instance, the DLVO theory predicts the following potential for monodisperse spherical aggregates of diameter $D = 2R$, and total charge $-Ze$ suspended in a simple 1 : 1 electrolyte solution [14],

$$V_{DLVO}(r) = V_{SC} + V_{vdW} + \frac{Z^2 e^2}{\epsilon} \left(\frac{\exp(\kappa R)}{1 + \kappa R} \right)^2 \frac{\exp(-\kappa r)}{r} \quad (1.15)$$

where ϵ is the dielectric constant, V_{vdW} is given by Eq. 1.10, and V_{SC} represents the core steric repulsion. As it is shown in Figure 1.4(a), when the electrostatic repulsive term is large enough, an energy barrier prevents the suspension from suffering spontaneous aggregation. When the concentration of electrolytes increases the double layer becomes thinner and the electrostatic force is weaker. By tuning the concentration of electrolytes a secondary minimum can exist (Figure 1.4(b)). This second minimum usually is rather shallow with a depth of the order

of few $k_B T$'s. If the energetic barrier separating the primary from the secondary minimum is large when compared to $k_B T$ the aggregation occurs only through the secondary minima. The resulting aggregates often can be redispersed by merely shaking the sol. Nonetheless, aggregation through secondary or shallow minima leads to very interesting aggregation kinetics and cluster morphology. Aggregates formed through secondary minimum are, in fact, meta-stable because colloids will tend to reach the thermodynamic equilibrium state reaching the primary minimum. The knowledge about how long a colloidal suspension would remain in the meta-stable state is of fundamental interest for pharmaceutical and chemical industries because it is a main factor to determine the shelf-life of their products. By tuning adequately the interactions products can last for years. For instance some gold colloids prepared by Faraday 130 years ago are still conserved.

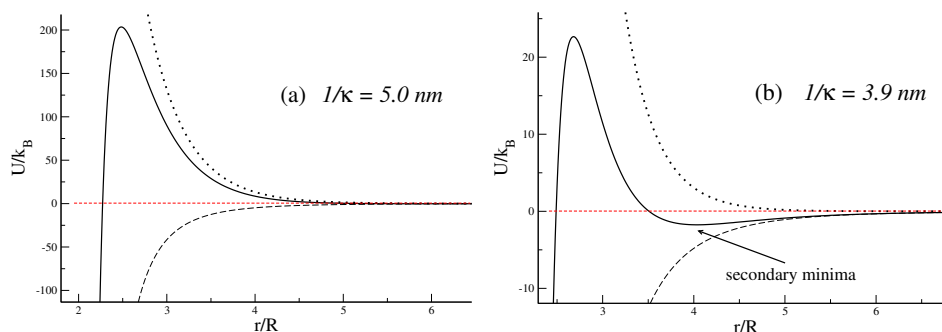


Figure 1.4. Electrostatic forces can induce the formation of energy barriers (a), and secondary minima (b). Potentials have been obtained accordingly to Eq. 1.15 with $Z = 10$, $\epsilon = 80\epsilon_o$, $A=10^{-19} J$, and $R = 10nm$.

Although the DLVO theory explains roughly the stability of many charged colloidal systems, it is an old theory and does not account for a large list of interactions like Hofmeister⁸ effects, hydrogen bonding, or hydration forces⁹ among

⁸The Hofmeister effect is known since 1888 when Franz Hofmeister demonstrated that the amount of salt required to precipitate hen-egg-white protein depends on the choice of the background salt. Since then, similar effects have been observed in nature as, for instance, in the foaminess of ocean waves that depends on the background salt [Craig, V. S. J.; Ninham, B. W.; Pashley, R., *Nature*, **364**, 317, (1993).]. Hofmeister effect has been also found in a large number of biological systems, for instance, the permeability of red blood cells also depends on the type of background salt.

⁹The DLVO theory is based on the assumption that water is a continuum fluid described by its bulk properties. At separations of the order of the molecular size, this is no longer the case. The specific interactions of water with the surface of the colloidal particles leads to the solvation or hydration forces. Water binds strongly to chemical surface groups like phosphates, sulphates, or hydroxylic groups. When two particles try to get closer, water molecules must be removed with

others that are known to play a significant role in some colloidal systems. For a review about the break up of DLVO forces see Boström-Williams-Nimham [15] and Grasso et al [16], also the book of Israelachvili [7] deals with some "non-DLVO" forces.

1.2.2 Addition of polymers to colloidal systems

The presence of polymers in the colloidal suspension is another interesting scenario in the study of the stability of colloidal particles. The introduction of polymer chains in a colloidal dispersion can promote either the stabilization or the aggregation and sedimentation of the colloidal particles.

The twofold nature of polymers in colloidal suspensions is known and used since ancient times. Ancient Chinese people knew (and European people rediscovered in the middle ages) a fine suspension of carbon no longer sediments out when Arabic gum (a natural polymer obtained as an exudate from a bush) is added to the mixture. This stabilized suspension is called *Indian Ink*. Also examples of stabilization of colloids using short organic chains are found in our every day life, for instance the emulsifier lecithin (common name for the phosphatidylcholine, PC) is used in chocolate and mayonnaise to prevent them from forming agglomerates. An example in the opposite direction comes from wine. In order to clear wine of impurities we can pour a watered-down egg white inside the wine. In this case polymers cause colloids in suspension to aggregate forming agglomerates large enough to sediment out and wine comes clear.

These two opposite effects can be explained as follows. If we add a solution of some neutral polymer of very high molecular weight to a dispersion of particles, the first adsorbed chains create a thin adsorbed layer (see Figure 1.5(a)). Since the chain conformation is highly flattened, polymers have a small effect in the system behavior. As we increase the polymer concentration, links can be established between particles, aggregates may form and precipitate (see Figure 1.5(b)). This phenomena is known as *bridging flocculation*. When we increase furthermore the polymer concentration, the surface particles saturate with polymers and then one particle repel each other via steric effects. In this case, a partial redissolution is possible (Figure 1.5(c)).

If we use a solution of polymers of low molecular weight (figure 1.5(d)), usually from 3000 to 10000 Daltons ¹⁰, as soon as the colloidal particles are saturated with polymers, a repulsive force appears at short distances. In such cases,

a subsequent energetic cost. The energetic cost of removing water molecules close to the surfaces can be understood as an effective repulsive hydration or solvation force among particles.

¹⁰Dalton is a unit of mass equal to the weight of an hydrogen atom, (1.657×10^{-24} g). The weight of proteins and other macromolecules are often measured in Daltons.

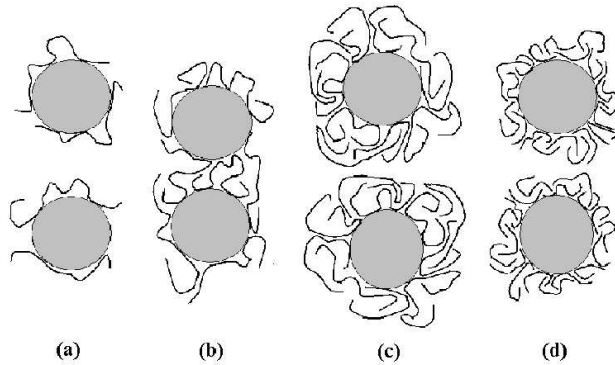


Figure 1.5. Schematic representation of four possible situations when polymer chains are added to a dispersion of colloidal particles. Plots (a-c) represents cases of long polymer chains with increasing polymer concentration. Plot (d) represents the case of short chains.

the steric effect generated by the adsorbed polymer chains dominates the attractive van-der Waals forces between uncoated particles, furthermore, the possibility of creating links between adsorbed chains over different particles is reduced due to the low molecular weight of the chains.

All the above examples are related to polymers that adsorb onto the surface of the colloidal particles. Although at first sight could be surprising, non-adsorbing polymers can modify the properties of colloidal solutions as well. The presence of such non-adsorbing polymers in solution leads to net attractive forces among colloidal particles called *depletion forces*, that produce the *depletion flocculation* phenomenon. The range of the attraction is directly related to the radius of gyration of the polymer, whereas the strength is proportional to the polymer concentration (osmotic pressure). The origin of the depletion forces can be explained as follows. As it is shown in Figure 1.6-(a), the surface of the particles can be assumed to be impenetrable walls. Therefore, polymers close to the surface have some of their conformations forbidden what is an entropic penalty. In order to minimize the loss of entropy the polymer concentration near the particles (the so called depletion zone) decreases. Nonetheless, the existence of zones depleted of polymers also have an entropic penalty so the colloids tend to reduce the net area exposed to the polymers. A way to reduce the exposed area is that colloidal particles approach each other, (Figure 1.6-(b)). If the attractive force created by the depletion effects is large enough to overcome the repulsive forces, the colloidal particles eventually aggregate. This attractive force can be also interpreted as if it arises from an unbalanced osmotic pressure when the polymers are expelled from the gap between two colloids.

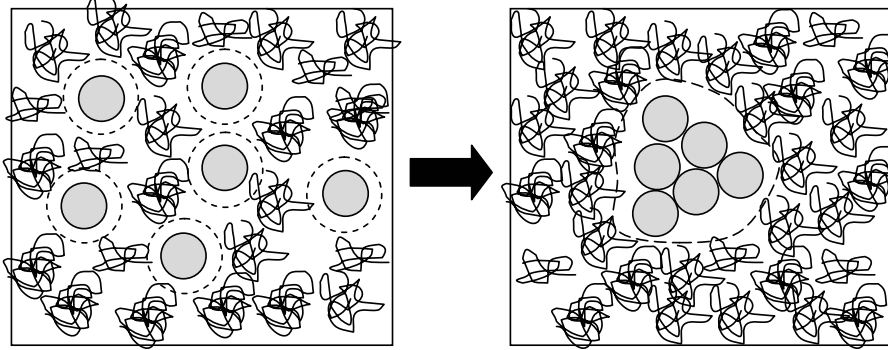


Figure 1.6. Colloids tend to approach in order to reduce the volume excluded to polymers. This phenomena can be modeled in terms of a depletion force among colloids.

1.2.2.a Modeling the presence of non-grafted polymers in colloidal systems

The statistical mechanics of colloid-polymers mixtures goes back to the pioneering studies of Asakura and Oosawa [17, 18] (AO) in the 50's. AO showed that when two large bodies are immersed in a solvent containing small macromolecules, an effective attractive interaction is induced between the two bodies. AO obtained an explicit expression for the depletion force between two colloids immersed in an ideal solution of macromolecules. In the 70's Vrij [19] went an step further by writing down an explicit one-component Hamiltonian model widely used in subsequent studies about colloid-polymer mixtures. The model is known today as the AO model or Asakura-Oosawa-Vrij model. The genuine AO model is an extreme non-additive binary hard-sphere model in which the colloids are treated as hard-spheres with diameter σ_c , and the polymers have a double character: polymer chains do not interact among them and cannot penetrate the colloidal particles. For a colloid, a polymer looks in the AO model as a hard-sphere of diameter $\sigma_p = 2R_g$, R_g being the radius of gyration of the polymer (see Chapter 2). The pairwise potentials colloid-colloid (V_{cc}), colloid-polymer (V_{cp}), and polymer-polymer (V_{pp}) are:

$$V_{cc}(r_{ij}) = \begin{cases} 0, & \text{for } |\mathbf{r}_i - \mathbf{r}_j| > \sigma_c, \\ \infty, & \text{for } |\mathbf{r}_i - \mathbf{r}_j| < \sigma_c. \end{cases} \quad (1.16)$$

$$V_{cp}(r_{ij}) = \begin{cases} 0, & \text{for } |\mathbf{r}_i - \mathbf{r}_j| > (\sigma_c + \sigma_p)/2, \\ \infty, & \text{for } |\mathbf{r}_i - \mathbf{r}_j| < (\sigma_c + \sigma_p)/2. \end{cases} \quad (1.17)$$

$$V_{pp}(r_{ij}) = 0 \quad (1.18)$$

These potentials are a good approximation for sterically stabilized particles, and also for charged colloids dissolved in a solvent with a high ionic concentration where the screening length is short. The assumption that the polymers do not interact among them is only valid for low polymer concentrations and polymers in a θ -solvent (see Chapter 2). The question about the importance of the degree of deformation of ideal polymers when they are mixed with colloids in the AO model was addressed in the pioneering Monte Carlo simulations of Meijer and Frenkel [20]. In their work a comparison of simulations of colloid-polymer mixtures using the AO model with simulations using ideal polymers onto lattices was done. The results showed that if $\sigma_p < 0.7\sigma_c$ the AO worked remarkable well.

The AO model can be worked at several levels. Direct computer simulations [21, 22] where polymers and colloids are explicitly in the system are not straightforward due to slow equilibration and non-ergodicity. A second approach is the effective one-component Hamiltonian in which an effective Hamiltonian is obtained for one of the components by integrating out the the degrees of freedom of the other component. The effective one-component Hamiltonian is an exact map of the binary solution to a single effective-component when $\zeta = \frac{\sigma_p}{\sigma_c} < 2/\sqrt{3} - 1 \sim 0.1547$. For $\zeta < 0.1547$ geometrical considerations ensure that there is no triple overlap of exclude volume regions, even when three colloids are in simultaneous contact. The effective pair potential can be written as

$$V^{eff}(r; z_p) = V_{cc}(r) + V_{AO}(r; z_p) \quad (1.19)$$

where V_{cc} is the pairwise potential among two colloids, and V_{AO} is the Asakura-Oosawa pair depletion potential,

$$\beta V_{AO}(r_{ij}; z_p) = \begin{cases} 0, & \text{for } s > 1 + \zeta, \\ -\eta (1 + \zeta^{-1})^3 \left(1 - \frac{3s}{2(1+\zeta)} + \frac{s^3}{2(1+\zeta)^3} \right), & \text{for } 1 < s < 1 + \zeta. \end{cases} \quad (1.20)$$

where $\eta = \frac{\pi}{6}\sigma_p^3 z_p$, $s = \frac{r_{ij}}{\sigma_c}$, $\zeta = \frac{\sigma_p}{\sigma_c}$, and z_p is the fugacity of the polymers.

When $\zeta > 0.1547$ the one-component Hamiltonian becomes inexact because three-body and higher-body terms are also present. We want to point out that in our simulations on polymer depletion driven colloids $\zeta \leq 0.1$ so the mapping between the one effective component and the binary liquid is exact. The phase behavior of the AO model is of fluid-solid type for small ζ 's, whereas for large ζ 's stable gas-liquid phase separations occurs because many-body interactions become important. In fact, the phase behavior of the AO model for $\zeta > 0.1547$ is only partially understood. Gast et al [23] predicted (using thermodynamic perturbative theories) at large ζ 's a stable colloidal liquid phase that resemble those of simple atomic fluids for $\zeta > 0.6$. A critique to the Gast predictions was done

in the sense that the contribution of many-body interactions are not necessarily small, and a reasonable doubt exist about the usefulness of perturbative methods in this case. Another alternative to the one-component Hamiltonian at large ζ 's is the so-called free-volume theory of Lekkerkerker et al [24]. This theory accounts for some of the many-body effects and predicts a stable colloidal gas-liquid transition for $\zeta > 0.32$. The phase diagrams estimated through the free-volume theory shows similar trends than in the Meijer Monte Carlo lattice simulations [20]. Another method used to deal with phase behavior at large ζ 's is the density functional theory (DFT) specifically designed for the AO model [25] which has predicted new interfacial phenomena in the liquid-gas interface.

The presence of many-body effects is not the only problem present in the AO model for large ζ values. Potentials used during the study of the kinetics of depletion interactions are often treated as instantaneous potentials. But depletion interactions need time to build up because particles need a time to collide among them. Vliegthart and Schoot [26] have reported substantial fluctuations of the depletion force respect to the value obtained using instantaneous potentials do exist for large ζ values.

The AO model is not the only model that exists to mimic colloid-polymer mixtures. For instance, models based on liquid-state integral equations are also available [27]. Before concluding this section devoted to the presence of polymers in the suspension, we want to point out that an interesting topical review about experiments in real polymer-colloids mixtures has been recently written by Poon [28].

1.2.3 Colloid stabilization using grafted polymers

Another way of using polymers to stabilize colloidal systems consist on grafting polymer chains by one edge directly onto the surface of the colloidal particles rather than coating the colloid with an adsorbed polymer layer. As it is shown in Figure 1.7, when the density of grafted chains is large enough, a brush like effect occurs (see Chapter 2).

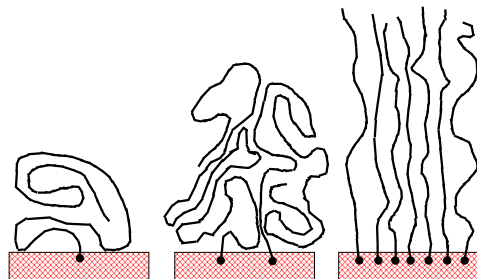


Figure 1.7. The brush-like effect can be observed by increasing the density of chains grafted onto a planar surface.

The polymer brushes provide a particularly effective steric protection for the colloidal particles. The end-grafted polymer stabilized colloids have been found useful in many applications of special relevance. For instance, the sterically stabilization of liposome have been used to improve in a large extent the colloidal and biological properties of anticancer drugs¹¹. Another important area in which sterically stabilized colloids play a main role is in nanotechnology where they are used in the quantum dot assembly¹². Also grafted polymer particles like grafted polystyrene colloids have been used to take up contaminants such as toluene, chloroform or naphthalene from water.

The use of the brush effect as stabilizer of colloids is not only limited to polymers attached through chemical bonds by one end to the surface. Mixed-monomer macromolecules whose chains contain two blocks (diblock polymers) are also of interest. In the diblock molecules, one of the blocks has a strong affinity for the solvent, whereas the other has a strong affinity for the surface. This duality leads to an anchor/buoy system with remarkable stabilization capacity.

It is worthwhile to point out that besides the relevance of such systems and their many potential applications, the pair-wise interaction potential between two of such particles has not been studied for the case of colloids having a size of the same order than the characteristic size of the chains. One of the aims of this thesis is the study of the interaction between two polymer-brush colloids in this regime.

¹¹Electrostatic stabilization cannot provide adequate stability to liposomes in *in vivo* applications where blood proteins and enzymes can disintegrate them easily. Conventional liposomes are in most of cases cleared by macrophages in the liver and spleen, so a large amount of drugs are released there. In contrast, liposomes with surface-grafted polymers have a more prolonged circulation in the body and its biodistribution is different from the usual liposomes. Grafted-polymer liposomes tend to accumulate in tumors, infections and inflammations that are characterized by leaky capillaries. The sterically stabilized liposomes are finally destroyed by macrophages in these sites. Due to the capacity to evade the defenses of the immune systems for a long time and to concentrate in specific areas, the sterically stabilized polymers have been used as ideal vehicles for anticancer drugs. Packing the drug into such special liposomes, the drug reaches in a large extent the target tissue, allowing a reduction in the systemic concentrations needed. The reduction of systemic concentrations reduces the toxicity of the drug and therefore its secondary effects on patients. For a good review on the novel applications of liposomes see Lasic, Dan D., *Tibitech*, **16**, 307, (1998).

¹²At nanoscopic level the properties of small particles change with the size of the particle due to the important change in the surface/volume ratio of the particles. As an example small CdSe crystals exhibit different colors depending on the particle size black ($\sim 10nm$), red ($\sim 4.5nm$), or yellow ($\sim 1.2nm$). In the bottom-up technique, organic chains that became grafted onto the particles surface are used to avoid the natural tendency of small crystals to aggregate and form larger crystals with ordinary macroscopic properties.

1.3 The colloidal aggregation process

In the previous sections we have commented that unstable colloid solutions tend to form colloidal aggregates that in presence of a gravitatory field tend to precipitate out of the solution when they are large enough. The study of the formation of colloidal aggregates is interesting for many reasons. Aggregation process leads to the formation of very different morphologies depending on the strength and range of the colloidal interactions. The particular morphology of an aggregate is of interest because it may influence, for instance, their suitability as a catalyzer or a molecular adsorber as well as influence other properties of the aggregate. Furthermore, colloidal aggregation brings an excellent opportunity for a better understanding of crystallization and nucleation processes (see Chapters 4 and 5).

The kinetics and the cluster morphology are fundamental aspects in the study of the aggregation. The aggregation kinetics has been studied since the beginnings of the XX-th century. For instance, Smoluchowski developed his famous kinetic equation as early as in 1916. In reference to the cluster morphology, as long as the beginnings of the XX-th century people knew that aggregates obtained through an slow aggregation process were apparently compact, whereas aggregates obtained in a fast aggregation process had very weird ramified structures. The cluster morphology was at that time considered as too complicated to have a quantitative description. Only since the late 70's with the introduction of the mathematical concept of *fractal structure* it has been possible to go an steep beyond and do a quantitative investigation of the cluster morphology and kinetics of such disordered aggregates. A general review about the role of fractals in the aggregation phenomena can be found in Jullien-Botet [29].

1.3.1 Fractals

The concept of Fractal was introduced in the 70's by Benoit Mandelbrot [30]. A fractal can be defined as a rugose object in which rugosities are present at any length scale. Therefore no tangent line or tangent point can be defined on its surface or contour. An example of fractal is shown in Figure 1.8 where the aggregation of carbon soot (colloidal particles made of carbon) leads to a ramified fractal structure.

One should keep in mind that in Nature do exist a below and an upper characteristic length scale within which a real object can be considered to have a fractal structure. For fractal colloidal aggregates the natural cutoff lengths are the size of a single colloidal particle, that is usually compact, and the whole size of the aggregate.

The term Fractal includes several classes of objects: self-similar fractals, ran-

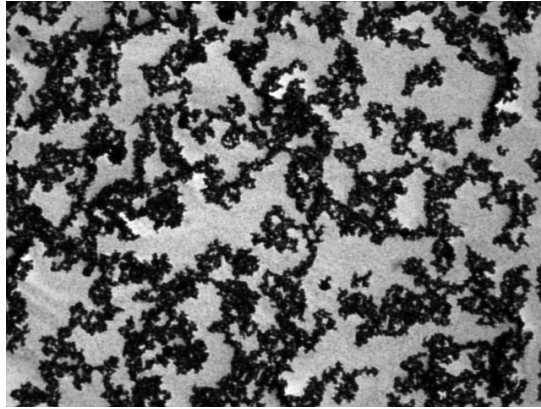


Figure 1.8. Ramified structures that resemble a fractal can be obtained when carbon soot aggregates. Taken from NASA web page, fact sheet number: FS-2002-03-56-MSFC.

dom self-similar fractals, non-similar fractals, and multi-fractals. Self-similar fractals are those whose structure is invariant under a change of scale, that is, the fractal looks identical whatever scale we choose to observe it. However, real objects often do not have regular shapes and usually have some randomness. Thus, for real objects, the best we can expect is a self-similarity property in a statistical sense. We can still use the tools used to characterize self-similar fractals to describe random fractals by doing a little of statistics.

In contrast, non-similar fractals are more difficult to characterize¹³. An example of non-similar fractal could be an object in which the growth or building rules are different when we consider different directions in the space. A multi-fractal set can be roughly defined as an infinite number of interpenetrating fractal subsets, where each subset has its own morphology and growth rules. Reviews on multifractality can be found in the books of Vicsek [31] and Meakin [32].

Fractals can be classified with several parameters, from which the most common is the *fractal dimension*.

1.3.1.a Parameters used to characterize fractal objects

The *fractal dimension* is one of the main parameters used to characterize a fractal object. There are several definitions of the fractal dimension, the most general and, at the same time, the most complex definition is the Hausdorff-Besicovitch dimension [33] D_{HB} . Consider the fractal object as a mathematical set of points

¹³Non-similar fractals cannot be described through a single fractal dimension like in self-similar fractals. The number of parameters needed depends on the degree of anisotropy and complexity associated to the growth rules. When the number of parameters needed to describe the object in a proper way becomes infinity, we call such object a multi-fractal.

in a metric space E , and $A \subset E$. We define the d -dimensional Hausdorff measure $H_d(A)$ as the infimum of positive numbers a_i such that, for whatever $r > 0$, A can be covered by a countable family of closed sets of diameter less than r such that the sum of the d -th powers of their diameters is less than a_i . The value of $H_d(A)$ can range from 0 to ∞ depending on the value of d we choose. We now define the Hausdorff-Besicovitch dimension D_{HB} of A as the infimum of d_i such that $H_{d_i}(A) = 0$. In a mathematical sense, a set is called *fractal* when its Hausdorff-Besicovitch dimension is greater than its topological dimension.

A most simple definition of fractal dimension is the Minkowski-Bouligand dimension D_{MB} , which is often identical to the Hausdorff-Besicovitch dimension D_{HB} . If we cover all the object using a minimum number N_l of spheres of diameter l , in the limit $l \rightarrow 0$ we expect the power-law

$$N_l \sim l^{-D_{MB}}$$

to be satisfied. It is conjectured that $D_{MB} \geq D_{HB}$, and only for strictly self-similar fractals, $D_{MB} = D_{HB}$.

Other power-law relationships can be used in order to describe a fractal. In some cases these alternative measures lead to results similar to D_{MB} or D_{HB} , in other cases, they measure intrinsic different properties of the fractal. For instance, we can measure the mass contained in a sphere of radius r centered at a given point of the object, the mass $m(r)$ is expected to follow the power-law:

$$m(r) \sim r^D$$

where D is often called the self-similarity exponent since if one multiplies all lengths by β , masses should be multiplied by β^D . Another name for the exponent D is the *mass dimension*. For strictly self-similar fractals, the mass dimension coincides with the Hausdorff-Besicovitch dimension. It is worthwhile to remark that the mass distribution is related to the probability of finding a particle at distance r from another particle, and this is by definition the correlation function $C(r)$, therefore, in a fractal object we must expect the correlation function to obey a power law given by

$$C(r) \sim r^{-(d-D)}$$

where d is the dimension of the smallest Euclidean space embedding the whole object.

Another parameter we can define using a power law relationship is the *Spreading dimension* d_s of a fractal. If we carry out walks of length L by visiting a sequence of points inside the object and sum the mass of all visited points $m(L)$, we expect $m(L)$ to follow

$$m(L) \sim L^{d_s}$$

Notice that if we could deform the object without breaking the connections among the points that form it, we would be able to change the fractal dimension but not the spreading dimension.

Another exponent of interest is the *tortuosity* λ . If we choose two points inside the object separated by a distance l , and the length of the minimal path entirely contained in the object is l_{min} , we define the tortuosity λ as,

$$l_{min} \sim l^\lambda$$

due to the definitions of D and d_s , the following relation is expected to hold $\lambda = D/d_s$.

It is remarkable that the concept of fractal far from being a tool of exclusive use for mathematicians and physicists, it has also found many application in biology and medicine [34,35]. From the anatomical outline of neuronal cells, vascular and airway systems to the detection of some cancers via the determination of the fractal dimension of cell membranes ¹⁴.

1.3.2 Measuring Fractal dimensions of colloidal aggregates

In the above section we have summarized the main issues related to fractal objects, among them the use of the fractal dimension as a descriptor of the fractal. We found that basically there are two theoretical ways of defining the fractal dimension, the Hausdorff-Besicovitch dimension D_{HB} , and the more practical Minkowski-Bouligand dimension D_{MB} . Based on these definitions, several algorithms have been defined to compute the fractal dimension of a given object.

1.3.2.a The box-counting method

The method consist on covering the object with boxes of size r , and determining the number of boxes $N(r)$ we need to cover the object. The box-counting dimension D_b is determined through the relationship

$$N(r) = r^{-D_b}$$

In practice, when the object is formed by a set of discrete points, as in a colloidal fractal aggregate, the accuracy of the value of D_b is observed to depend on the number of points that form the object. For instance, if we measure the D_b of a compact 2d object that has been discretized in a regular lattice we observe

¹⁴The fractal concept have been used in the detection of some types of cancers in which cell membranes become altered. For instance, Hairy-cell leukemia is a form of lymphocytic neoplasia that produces lymphocytes with more pseudopods than normal lymphocytes.

that $D_b \cong 1.83$ for an object containing 1000 points, $D_b \cong 1.93$ if it contains 5000 points and $D_b \cong 1.96$ for a compact object discretized in 30000 points. This example tell us that we must be cautious with the D_b values obtained for small colloidal aggregates, and assign a reasonable range of error to them.

For fractals that do not have a multi-fractal nature, the dimension obtained by dilating a box centered on a given point (nested squares method, also known as the sand box method) is equivalent to the dimension obtained by covering the structure with boxes. One should be aware that a random placement of the origin in the nested squares method can lead to a breakdown of the method, typically the centroid of the aggregate is an usual choose to place the center of the boxes.

1.3.2.b The cluster-ensemble averaged fractal dimension

The averaged fractal dimension of a set of aggregates can be measured through the evaluation of their radius of gyration R_g . The radius of gyration is expected to behave as $R_g \sim N^{1/D_f}$ where D_f is the cluster-ensemble averaged fractal dimension and N the mass (number of units) of the aggregate. We have found in our studies that this method is more accurate than the box-counting method when fractal aggregates are not very large. This method constitutes a fast way in order to compute an averaged value of the fractal dimension of a set of aggregates resulting from an aggregation process. However, caution must be taken when the size distribution depends on the spatial direction where the hypothesis $R_g \sim N^{1/D_f}$ turns out to be incorrect.

Besides all, we have found this method to be the most reliable on computing the fractal dimension of the aggregates in our computer simulations.

1.3.2.c The density correlation function method

The correlation function of a fractal object can be defined as

$$C(\vec{r}) = \frac{1}{V} \sum_{\vec{r}^j} \rho(\vec{r} + \vec{r}^j) \rho(\vec{r}^j)$$

where \vec{r}^j stands for the positions of all the particles that form the fractal. If the fractal is spherically symmetric, then $C(r) = C(\vec{r})$. Self-similar fractals are expected to have a decaying correlation function

$$C(r) \sim r^{D_f-d}$$

This method can be used to determine the fractal dimension from a single aggregate or to obtain an averaged fractal dimension from a set of aggregates.

The use of the correlation method with a single cluster is not adequate when clusters are small because in that case the borders of the object influence strongly the correlation function.

1.3.3 Irreversible cluster-cluster aggregation kinetics

Irreversible cluster-cluster aggregation is expected when the attraction among particles is larger than few $k_B T$'s. Several approaches have been used to deal with the kinetics of the irreversible cluster-cluster aggregation. Direct analysis of the Smoluchowski equation [36, 37]; Friedlanders's theory of self-preserving spectra [38–40] also known as the Scaling theory; numerical works based on solving the *master equation*; and computer simulations of aggregation models [41, 43–45] (DLCA, RLCA, etc.).

1.3.3.a Analytical results from Smoluchowski equation

A key equation in the history of the studies about the kinetics of the irreversible particle aggregation is the *Smoluchowski equation*. Consider a process in which two aggregates of i and j particles join to form a larger aggregate of size $i + j$. The process can be represented as $A_i + A_j \rightarrow A_{i+j}$. Assume that the rate of such events per unit of volume and time is given by $K_{ij}c_i c_j$, where c_i and c_j are the concentration of clusters of size i and j respectively. K_{ij} would represent an intrinsic constant associated to the aggregation process. Notice that several strong assumptions are implicit in the above statements:

- Binary collisions between aggregates are assumed.
- Spatial fluctuations are neglected (mean-field approach). Therefore the transport of species cannot be a rate-limiting factor in the system because it leads to large spatial correlations.
- The rate of collisions between two aggregates is proportional to the product of their concentrations. This last hypothesis is a tough approximation, nonetheless it has been found to be in reasonable agreement with numerical simulations when concentrations are low [46].

Additionally, a cluster of size $i + j$ can disappear in a process $A_{i+j} + A_k \rightarrow A_{i+j+k}$. Therefore, by analogy to chemical kinetics equations, the equation giving the evolution of the concentration of aggregates of size k , c_k , should obey the following Smoluchowski equation,

$$\frac{dc_k}{dt} = \frac{1}{2} \sum_{i+j=k} K_{ij}c_i c_j - \sum_i K_{ik}c_i c_k \quad (1.21)$$

The Smoluchowski equation is often rewritten in terms of the number of aggregates n_k containing k particles, $n_k = Vc_k$, where V is the volume of the system, thus

$$\frac{dn_k}{dt} = \frac{1}{2} \sum_{i+j=k} k_{ij}n_in_j - \sum_i k_{ik}n_in_k \quad (1.22)$$

where $k_{ij} = K_{ij}/V$.

It is rather obvious that in order to go further in the kinetic study, some insight about the set of kinetic coefficients K_{ij} is needed. It is a common practice to refer the K_{ij} coefficients for all particles as the *aggregation kernel*. Although the Smoluchowski equation dates back to 1916, explicit forms of the K_{ij} based on microscopic details of the aggregation phenomena were not studied until the 50's and 60's. Even if we assume K_{ij} to be known, a system of infinitely many coupled non-linear rate equations must be solved.

Exact analytical solutions of the Smoluchowski equation are only available for simple functional forms of the aggregation kernel. However, Smoluchowski himself obtained an elegant solution for the case of an initial monodisperse system of N single particles ($n_1 = N, n_k = 0$ for $k > 1$), for a constant aggregation kernel $K_{ij} = \kappa$. Consider that the solution for n_k can be separated into the product of two independent time functions

$$n_k = \phi(t)[\psi(t)]^{k-1} \quad (1.23)$$

with the initial conditions $\phi(0) = N$ and $\psi(0) = 0$. Then, the solution to the Smoluchowski equation for a constant kernel $K_{ij} = \kappa$ is

$$n_k = N \frac{(\kappa N t / 2)^{k-1}}{(1 + \kappa N t / 2)^{k+1}} \quad (1.24)$$

Such expression predicts that the number of clusters of size k has a maximum at intermediate times followed by a asymptotical decrease with t^{-2} . For $t \gg 2/(kN)$, n_k can be written as an exponential decaying function

$$n_k = \frac{4}{k^2 \kappa^2 N} \left(\frac{k}{t}\right)^2 \exp\left(\frac{-2k}{\kappa N t}\right) \quad (1.25)$$

Other analytical solutions have been derived for a whole family of kernels that verify the homogeneity relation:

$$K_{\alpha i, \alpha j} = \alpha^\lambda K_{ij}$$

In principle one can differentiate two regimes: the *flocculation regime* in which $\lambda < 1$, and the *gelation regime* for $\lambda > 1$. It can be shown that in the flocculation

regime, the mean cluster size $\langle n \rangle$ at large times behave as

$$\langle n \rangle \sim t^z \quad (1.26)$$

with

$$z = \frac{1}{1 - \lambda}. \quad (1.27)$$

If we restrict to very large clusters ($k > \langle n \rangle$) and times, the reduced form for the size distribution function can be obtained [47],

$$n_k \sim k^{-\theta} f(k/\langle n \rangle) \quad (1.28)$$

with $\theta = 2$, and

$$f(x) = x^{-\lambda} \exp(-x(1 - \lambda)). \quad (1.29)$$

For $w < 0$ the distribution will exhibit a maximum at a finite k whereas for $0 < \lambda < 1$ the distribution is always decreasing. The gelation regime ($\lambda > 1$) is characterized by the fact that, after a typical finite time T , a cluster that spreads from one extreme to the other of the system appears. The mass of such aggregate diverges as the size of system is taken to infinity. This violation of the mass conservation by some kernels after a finite time T was first reported by Leod [48] in the 1960's. In the late 1970's meaningful solutions for times $t > T$ were found, and a physical interpretation in terms of "gelation transition" was given [49–51].

The value of the exponent z can be calculated easily for colloidal clusters that follow a Brownian motion. Smoluchowski showed that a reasonable kernel for three dimensional Brownian clusters was,

$$K_{ij} \sim (i^{1/3} + j^{1/3})(i^{-1/3} + j^{-1/3})$$

where the first term is related to the effective cross-section assumed to be proportional to the sum of the clusters radii. The second term is associated to the sum of the cluster diffusivities which are inversely proportional to the clusters radii (following Stokes-Einstein relation). The above kernel can be generalized to clusters in a d -dimensional space with a fractal dimension D_f . If we assume that the diffusivity of a cluster of size i , u_i , has a power law dependence $u_i \sim i^\gamma$ on the cluster size, then

$$K_{ij} \sim (i^{1/D_f} + j^{1/D_f})^{d-2} (i^\gamma + j^\gamma)$$

It is straightforward to check that this kernel is homogeneous with a homogeneity degree $\lambda = (d - 2)/D_f + \gamma$. If we combine this results with the previous one $z = 1/(1 - \lambda)$, we obtain that the exponent z for aggregates that follow a Brownian motion in an irreversible process is

$$z = \frac{1}{1 - \gamma - (d - 2)/D_f} \quad (1.30)$$

1.3.3.b The Scaling approach in the irreversible cluster aggregation

The analytical expressions 1.25 and 1.28 obtained for particular kernels contain the seed of what has turn out to be another successful approach to the study of the aggregation kinetics: *the scaling theory*. In fact, Scaling techniques have been proved to be useful even in circumstances where the Smoluchowski equation does not provide an adequate representation of the aggregation kinetics. An excellent review of this issue has been reported by Leyvraz [40].

It is possible to rewrite the Eq. 1.25 as

$$n_k = k^{-\theta} f(k/t^z) \quad (1.31)$$

with $\theta = 2$ and $z = 1$ for the case of a constant kernel. In this reduced form, the equation resembles to Eq. 1.28. This result suggests the possibility that other solutions for n_k may also be written in a similar way.

In the scaling theory we assume the solutions of interest can be written as in Eq. 1.31. In addition, we assume $f(x)$ to verify: (a) $f(x)$ is exponentially small for $x \gg 1$, and (b) $f(x) \sim x^\delta$ for $x \ll 1$, then it can be proved that the mean cluster size $\langle n \rangle$ must behave as $\langle n \rangle \sim t^z$ and the number of clusters N_c must follow the power-law $\langle N_c \rangle \sim t^{-z}$ provided that the next identities should be always satisfied:

$$\sum n_k = N_c \quad (1.32)$$

$$\sum kn_k = N \quad (1.33)$$

On the other hand, for small $\langle n \rangle/t^z$, Vicsek and Family [41] showed that the following scaling expression was also a plausible scaling form,

$$n_s(t) \sim t^{-w} s^{-\tau} F(s/t^z) \quad (1.34)$$

In this case, the function F is an explicit function of s and t . The scaling form 1.34 combined with the normalization condition

$$N = \sum kn_k \sim \int_1^\infty n_k(t) k dk \quad (1.35)$$

leads to

$$N \sim t^{-w+z(2-\tau)} \int_{t^z}^\infty x^{1-\tau} f(x) dx \quad (1.36)$$

Since the total mass of the system must be constant, the exponents w, τ and z are related as

$$w = (2 - \tau)z \quad (1.37)$$

Eq. 1.37 implies the inequality $\tau \leq 2$ because $w > 0$ and $z > 0$ in physical systems (where small aggregates join to form larger aggregates). Another consequence of Eq. 1.37 is that a comparison of Eq. 1.31 for $x \ll 1$ with Eq. 1.34 leads to $\theta = 2$. Notice that the result $\theta = 2$ was obtained initially for the particular case of a constant kernel. The result obtained now is, by far, more general. Furthermore, it is also possible to show that the scaling form given by Eq. 1.34 leads the same averaged aggregate size dependence with time,

$$\langle n \rangle \sim t^z \quad (1.38)$$

and the total number of clusters in the system behaves as [41]

$$N_c \sim \begin{cases} t^{-z}, & \text{for } \tau < 1, \\ t^{-w}, & \text{for } \tau > 1. \end{cases} \quad (1.39)$$

1.3.3.c The master equation in the irreversible cluster aggregation

All the approaches based in the Smoluchowski equation neglect spatial fluctuations. Results obtained from numerical simulations [52, 53] point out that irreversible aggregating systems with Euclidian dimension $d < d_c = 2$, show large spatial fluctuations that lead to kinetic exponents which depend on the dimension as well as to novel non-monotonic cluster size distributions. Smoluchowski equation, as well as rate-equations (their analogous in the continuum), assume that the time evolution of the population aggregates is deterministic. In some cases, random fluctuations can play a main role and lead to results that differ notoriously from those obtained using the Smoluchowski formalism.

An alternative to the deterministic Smoluchowski formalism are the stochastic approaches for modeling the kinetics, one of those is based on the use of *master equations*. The main element of the master equation formalism is the "grand probability function", $P(N_1, N_2, \dots, N_n; t)$ that represents the probability that in a volume V at time t there are N_1 "aggregates" of size 1, N_2 aggregates of size 2, ..., and N_n aggregates of size n . The master equation is the time-evolution equation for the grand probability function P , that in an irreversible system reads

$$\frac{dP(\vec{N}, t)}{dt} = \frac{1}{2V} \sum_{i,j} K_{ij} ((N_i+1)(N_j+1+\delta_{i,j})P(\vec{N}_{ij}^+, t) - N_i(N_j-\delta_{i,j})P(\vec{N}, t)) \quad (1.40)$$

where K_{ij} is the aggregation kernel, and \vec{N}_{ij}^+ stands for, $(N_1, \dots, N_i + 1, \dots, N_j + 1, \dots, N_{i+j} - 1, \dots, N_n)$ for $i \neq j$, and $(N_1, \dots, N_i + 2, \dots, N_{2i} - 1, \dots, N_n)$ for $i = j$. A breakthrough in the use of the master equation formalism was done in the 1970's when Gillespie [54,55] published a new and successful algorithm to solve

these equations. Since then, several authors have made use of the master equation formalism to study irreversible aggregation phenomena (see, for instance, Thorn et al [56], and Odriozola et al [57]).

1.3.3.d Numerical models in the irreversible cluster aggregation

The use of mean field equations constitutes a rough approach to real systems. An example of the limitations of the mean field is its break down when the rate-limiting factor is the transport of clusters. Therefore, it would be desirable to consider new approaches in which the transport mechanism and the reaction mechanism are explicitly specified.

In an effort to go beyond the mean field in the study of irreversible aggregation phenomena, several models of aggregation were proposed and tested by computer simulations. These models, although very primitive, are able to capture some of the basic features of colloidal aggregation phenomena. Two main classes can be considered: the models in which single particles stick to a single cluster (i.e. DLA [58], RLA, and Eden [59] models) and the models in which cluster-cluster aggregations are taken into account. Experience has shown that cluster-cluster models are a more suitable description of the aggregation processes among colloidal particles. A broad description of these models can be found in Vicsek [31].

Although multiple variants of cluster-cluster aggregation have been devised, most of the models are usually based in the following assumptions: move a cluster following Brownian or ballistic trajectories; when two clusters become nearest neighbors, they combine to form a new larger aggregate with probability $0 < p \leq 1$. Notice that fragmentation of the clusters formed in previous steps is not allowed, therefore, when aggregation occurs, it has an irreversible nature even if $p < 1$.

We may classify these models into two main families: *diffusion-limited cluster-cluster aggregation models* (DLCA) in which $p = 1$ (the first time they become together they aggregate), and *reaction-limited cluster-cluster aggregation models* (RLCA), in which $p < 1$.

DLCA

The former diffusion-limited models are due to the independent works of Meakin et al [60] and Kolb et al [61]. Clusters are assumed to undergo random walks. The diffusion coefficient D_s of a cluster of size s is assumed to depend on the cluster size as

$$D_s \sim s^\gamma$$

where γ is the diffusivity exponent. This can be justified by the fact that the mobility of a particle in a fluid is inversely proportional to its hydrodynamic radius. The classic DLCA considers $\gamma = 0$. If γ is non-zero, clusters are usually moved as follows: *i*) a random number $0 < \eta < 1$ is selected, and *ii*) the cluster is moved only if $\eta < D_s/D_{max}$ where D_s is the diffusion coefficient of the cluster, and D_{max} the largest diffusion coefficient in the system. Simulations of diffusion-limited models lead to the formation of clusters of fractal nature in which the fractal dimension is observed to depend on the diffusivity exponent γ . In 2d, if $\gamma < 1$, the fractal dimension is almost the same $D \cong 1.45$. For $\gamma > 1$, simulations show a continuous change from $D \cong 1.45$ to $D \cong 1.7$, for $\gamma = 2$. If $\gamma \geq 2$ the fractal dimension is constant and equal to the fractal dimension obtained in diffusive particle-cluster aggregation (DLA) $D = 1.7$. DLCA simulations also confirm that the exponents w , z , and τ , as well as the cluster size distribution function $n_k(t)$, depend on γ . In particular, numerical results show that $n_k(t)$ exhibits a crossover from a bell-shaped distribution in k for $\gamma < \gamma_c$ to a monotonic decreasing function when $\gamma > \gamma_c$. This crossover is also related to a change in the way in which cluster size distributions scale. If $\gamma > \gamma_c$, DLCA results scale as

$$n_k(t) \sim t^{-w} k^{-\tau} f(k/t^z) \quad (1.41)$$

where $f(x)$ is a cutoff function $f(x) \sim 1$ for $x \ll 1$ and $f(x) \ll 1$ for $x \gg 1$. For $\gamma < \gamma_c$, a scaling form

$$n_k(t) \sim k^{-2} F(s/t^z) \quad (1.42)$$

is still valid, but the cutoff function $F(x)$ is $F(x) = x^2 g(x)$. $g(x) \ll 1$ for $x \ll 1$, and also $g(x) \ll 1$ for $x \gg 1$ which give rise to a bell-shaped function. In addition, DLCA results for $\langle n \rangle$ and N_C agree with the usual power laws given in Eq. 1.38 and 1.39 respectively. This power laws are observed for any value of γ .

RLCA

In the reaction-limited cluster-cluster aggregation we can study the dynamical properties [62] through a diffusion-limited model with $p \ll 1$ [43]. If we assume the stick probability of two clusters of size i and j to be size dependent in the form,

$$P_{ij} = \begin{cases} p_o(ij)^\sigma, & \text{for } p_o(ij)^\sigma < 1, \\ 1, & \text{for } p_o(ij)^\sigma \geq 1. \end{cases}$$

where $p_o \leq 1$ is a constant. In this case, in addition to the crossover exponent γ_c , a second crossover exponent σ_c appears. When $\gamma > \gamma_c$ (or $\sigma > \sigma_c$) the scaling

law given by Eq. 1.41 applies. However, if $\gamma < \gamma_c$ (or $\sigma < \sigma_c$), the scaling form Eq. 1.41 is no longer valid, but Eq. 1.42 applies.

1.3.4 Reversible cluster-cluster aggregation kinetics

In many cases the aggregation process exhibit a certain degree of reversibility. Suppose a fragmentation processes $A_{i+j+k} \rightarrow A_{i+j} + A_k$ occurs with a rate of events per unit of volume and time given by $F_{ij} c_{i+j}$. Then, the generalized Smoluchowski equation reads,

$$\frac{dn_k}{dt} = \frac{1}{2} \sum_{i+j=k} (k_{ij} n_i n_j - F_{ij} n_{i+j}) - \sum_i (k_{ik} n_i n_k - F_{kj} n_{k+j}) \quad (1.43)$$

A general solution of the above equation is not available although the existence and uniqueness of mass-conserving solutions for such equations has been proved mathematically (Lamb [63], and references therein). As a difference to the irreversible case, the inclusion of fragmentation processes leads under some conditions to stable equilibrium solutions for the cluster mean size and the size distribution. Unlike the irreversible Smoluchowski equation (invalid for systems with dimensionality $d < 2$), the mean field reversible Smoluchowski equation can also be applied to systems with dimensionalities $d \geq 1$ [64]. It has been suggested the possibility that in the reversible case spatial fluctuations, that play a critical role in low dimensionality systems, are somehow compensated by the cluster fragmentation phenomena [64].

Blatz and Tobolsky [65] appears to be the first who obtained an analytical solution to the reversible Smoluchowski equation in 1945. They assumed the fragmentation and aggregation kernels to be constants $k_{ij} = \kappa_1$ and $F_{ij} = \kappa_2$. Since their pioneering work, analytical solutions have been restricted to a small number of kernel dependences [65–69].

Nonetheless, interesting results can be obtained for the reversible case when the fragmentation kernel has the form $F_{ij} = \kappa \Phi_{ij}$, where κ is a breakup constant and Φ_{ij} is an arbitrary function (with $\Phi_{1,1} = 1$) determining the dependence of the fragmentation rate on the cluster sizes. We expect that by increasing κ , the mean cluster size $\langle n(\kappa, t) \rangle$ will decrease. If the mean cluster size scales for $t \rightarrow \infty$ with κ , then $\langle n(\kappa, t) \rangle$ is expected to behave asymptotically as

$$\langle n(\kappa, \infty) \rangle \sim \kappa^{-y} \quad (1.44)$$

and the total number of clusters behave as

$$N(t \rightarrow \infty, \kappa) \sim \kappa^y \quad (1.45)$$

The value of the exponent y (independent of the system dimensionality) can be calculated in the mean field picture [64] if we assume: (a) the aggregation and fragmentation kernels are homogenous functions of degree λ and α respectively, (b) the generalized Smoluchowski equation is invariant under the transformations $\kappa \rightarrow a\kappa$ and $k \rightarrow a^{-y}k$. If such conditions are fulfilled, the exponent y is simply related to the degrees of homogeneity of the coagulation and fragmentation rate constants,

$$y = \frac{1}{\alpha - \lambda + 2} \quad (1.46)$$

1.3.4.a Scaling approaches to the reversible aggregation phenomena

If we assume that the scaling form for the irreversible aggregation also holds for the reversible case [64],

$$n_k(t, \kappa) \sim k^{-2} f(k/\langle n(t, \kappa) \rangle) \quad (1.47)$$

the scaling form for the cluster-size distribution at $t \rightarrow \infty$ is

$$n_k(t \rightarrow \infty, \kappa) \sim k^{-2} f(k\kappa^y) \quad (1.48)$$

The scaling function $f(x)$ is expected to behave [64] as

$$f(x) \sim x^{2-\tau} e^{-cx} \quad (1.49)$$

where the exponent τ and the constant c are expected to depend on the details of F_{ij} . These results have been confirmed with $\tau = \lambda - \alpha$ for aggregation kernels that, in addition of being homogenous, satisfy the detailed balance condition [70],

$$k_{ij}n_i n_j = F_{ij}n_{i+j} \quad (1.50)$$

These type of kernels allow an explicit determination of the scaling forms for their solutions.

The use of the scaling hypothesis for the reversible case (Eq. 1.47) can be used to obtain new results. Sorensen et al [71] have shown that if the scaling function Eq. 1.47 holds for all time, and the aggregation and fragmentation kernels are homogeneous functions, the mean cluster size $\langle n \rangle$ should obey the following differential equation

$$\frac{d\langle n \rangle}{dt} = a\langle n \rangle^\lambda - b\langle n \rangle^{\alpha+2} \quad (1.51)$$

where a and b are constants in the Sorensen deduction (which is true only in certain cases). If a and b are constants, the above equation can be rewritten in a scaled equation,

$$\frac{d\langle n^* \rangle}{dt^*} = \langle n^* \rangle^\lambda - \langle n^* \rangle^{\alpha+2} \quad (1.52)$$

in which $\langle n^* \rangle = \langle n \rangle / \langle n_o \rangle$ and $t^* = t/t_o$. $\langle n_o \rangle$ is the equilibrium value of $\langle n \rangle$ at long times, whereas t_o could be identified with a characteristic time scale to reach the equilibrium (when the solution leads to a steady state). The Eq. 1.52 becomes actually a worthwhile result because it allows us to compare numerical works against predictions from Smoluchowski mean field equation and, in turn, relate these results to the degrees of homogeneity of the kernels. Furthermore, Eq. 1.52 establishes a stability criteria for the solutions of the Smoluchowski equation. The kinetics is expected to yield a stable solution ($\langle n \rangle$ has a finite value at $t \rightarrow \infty$) if $\alpha + 2 - \lambda > 0$; otherwise solutions are expected to diverge. In the stable regime, if $\langle n^* \rangle \ll 1$ and $\lambda < 1$, then

$$\langle n^* \rangle \sim t^z \quad (1.53)$$

where $z = 1/(1 - \lambda)$. In the opposite extreme $\langle n^* \rangle \rightarrow 1$,

$$\langle n^* \rangle \sim (c - t/z')^{z'} \quad (1.54)$$

with $z' = -1/(1 + \alpha)$ and c as a constant value.

Unfortunately, Sorensen results are not as general as they could be thought at first sight. Vigil and Ziff [72] pointed out that the Sorensen formalism, although mathematically correct, could not warrant a and b to be constants for whatever choose of the aggregation and fragmentation kernels. Until now no work has established a general criteria to elucidate which type of kernels will lead a and b to be true constants. It is known that the Blatz-Tobolsky model satisfy such requirements. It is easy to show that models in which $\lambda = \alpha + 2$ will be also correctly described by Eq. 1.52. Another group of kernels that satisfy the above equations 1.53 and 1.54 are those kernels in which detailed balance is satisfied at equilibrium (see Eq. 1.50). Therefore, although Sorensen theory is not valid for all the kernels, it seems to have a wide range of kernels in which is applicable.

In addition to the remark of Vigil and Ziff, Meakin and Ernst [44] obtained the important result that the scaling distribution has two functional forms. At early times, when aggregation dominates, the scaling form is similar to the scaling used in the irreversible case. At large times, the scaling function $f(x)$ is expected to behave in a different way,

$$n_k(t, \kappa) \sim k^{-2} f(k\kappa^y, t\kappa^x) \quad (1.55)$$

where y is given by Eq. 1.46 and $x = y/z$. The transition from one scaling regime to the other is characterized by a typical time $\tau(\kappa)$, that is supposed to behave as $\tau(\kappa) \sim \kappa^{-x}$ for $\kappa \rightarrow 0$.

The results of Meakin-Ernst and Vigil-Ziff might in principle limit strongly the usefulness of Sorensen results. In order to elucidate to which extent Sorensen

results are valid, Elminyawi et al [73] integrated numerically the generalized Smoluchowski equation for several kernels. Numerical results show that limitations placed to the Sorensen results are not too severe. Theoretical predictions agree with the numerical solutions with a large degree of accuracy in most of cases. In addition, numerical results show that the crossover of $n_k(t)$ from the initial scaling form (exponential behavior) exist as predicted by Meakin and Ernst, but changes in the scaling form are observed for clusters of size $i \ll \langle n \rangle$. Nevertheless such small clusters have a small contribution to the parameters a and b in the Sorensen equation. Therefore, Sorensen results can be considered as a good approach to the solution of the Smoluchowski equation in many cases.

1.3.4.b Other approaches to the reversible aggregation phenomena

As in the previous irreversible aggregation process, the master equation formalisms can be applied to the reversible aggregation case. To do so, the following term should be added to the right hand side of the irreversible master equation (Eq. 1.40),

$$\frac{1}{2} \sum_{n=2}^{\infty} (N_n + 1) \sum_{i=1}^{n-1} F_{i,n-i} P(\vec{N}_{i,(n-i)}^-, t) - N_n \sum_{i=1}^{n-1} F_{i,n-i} P(\vec{N}, t) \quad (1.56)$$

where F_{ij} is the fragmentation kernel, and $\vec{N}_{i,j}^-$ stands for, $(N_1, \dots, N_i - 1, \dots, N_j - 1, \dots, N_{i+j} + 1, \dots, N_n)$ for $i \neq j$, and $(N_1, \dots, N_i - 2, \dots, N_{2i} + 1, \dots, N_n)$ for $i = j$. This formalism has been applied to the study of the kinetics in several particular reversible aggregation-fragmentation models [74–76].

As in the irreversible case, non-mean field approaches to the study of the reversible aggregation phenomena have been done. These alternative approaches will be presented in Chapter 4.

1.4 Scattering by aggregates

Scattering techniques are a very powerful tool for probing the structure and dynamics of the matter at microscopic level. Depending on the characteristic length scales of the object under study, we can use: light, X-ray, and neutron scattering techniques. The smallest length scale that can be resolved with a given technique is of the same order of magnitude of the wavelength associated to the beam: $\lambda \sim 0.1nm$ for Neutron and X-ray techniques, $\lambda \sim 500nm$ for light scattering. Any of the above methods have advantages and disadvantages depending on the characteristics of the sample. For instance, neutrons are scattered much

Technique	Typical λ (nm)	\mathbf{q} (nm^{-1})
Laser light scattering	500	$1 \cdot 10^{-3} - 4 \cdot 10^{-2}$
Small-angle x-ray scattering	0.15	$2 \cdot 10^{-2} - 4 \cdot 10^{-1}$
Small-angle neutron scattering	0.1	$7 \cdot 10^{-3} - 9 \cdot 10^{-1}$
Wide-angle neutron scattering	0.1	$1 \cdot 10^1 - 5 \cdot 10^1$

Table 1.3: Range covered by various scattering techniques.

more strongly than X-rays when the sample contains large amounts of light elements such as hydrogen. Atoms with large electronic structure produce a roughly similar scattering strength in X-ray and neutron techniques. Radiation at optical length scales is found to be scattered several orders of magnitude more strongly than X-rays. Light scattering is desired in colloids where the density of scatters is very low, but can also lead to the so-known multi-scattering phenomena (photons are scattered more than once as they pass through the sample). Multi-scattering is usually undesired because it complicates the scattering results, although the multi-scattering problem has been turned into an asset in certain techniques as the diffusing-wave spectroscopy [77]. Table 1.3 shows a comparison of the typical ranges covered by various scattering techniques.

Light scattering has proved to be very useful in the study of colloidal aggregation, because colloidal aggregates often develop structures whose fundamental length scales are comparable to optical length scales. The basic principles of the static and dynamic light scattering by aggregates has been reviewed recently in detail by several authors [78–81].

In this section we will give a short summary of the main facts related to the scattering of radiation by colloidal aggregates.

Consider a scalar electromagnetic field,

$$E(\vec{r}) \sim e^{i\vec{k}_i \cdot \vec{r}}$$

affecting two colloidal particles (Figure 1.9). Light is scattered towards the detector in the direction \vec{k}_s . Assuming the scattering to be elastic the wavelength of the scattered light is unchanged, $|\vec{k}_i| = |\vec{k}_s|$. In order to simplify the discussion, multi-scattering is neglected, and the refractive index of the medium is unity. The light scattered from both particles will travel a different distance

$$\Delta s = \left(\frac{\vec{k}_s}{k_s} \right) \cdot \Delta \vec{r} - \left(\frac{\vec{k}_i}{k_i} \right) \cdot \Delta \vec{r},$$

and therefore a phase difference $\Delta\phi$ is present when both waves arrive at the

detector. The relative phase is,

$$\Delta\phi = 2\pi/\lambda\Delta s = (\vec{k}_s - \vec{k}_i) \cdot \Delta\vec{r} = \vec{q} \cdot \Delta\vec{r}$$

where the scattering wave vector \vec{q} is defined as $\vec{q} = \vec{k}_s - \vec{k}_i$, of modulus

$$q = \frac{4\pi}{\lambda} \sin\left(\frac{\theta}{2}\right) \quad (1.57)$$

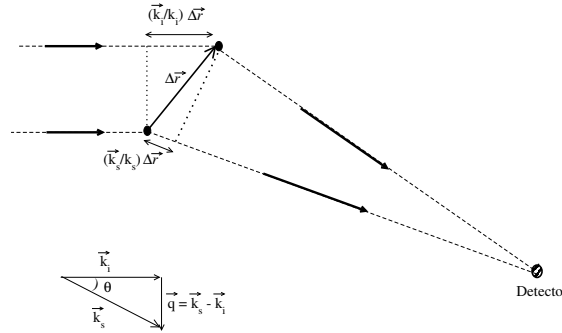


Figure 1.9: Scheme of the scattering of light from two particles.

The contribution to the scattered beam of a single particle j , located at position \vec{r}_j , at the detector position \vec{R} , can be written as

$$\vec{E}_j(\vec{q}, \vec{R}) \sim \vec{c}_j(\vec{q}) e^{i\vec{k}_s \cdot \vec{R}} e^{-i\vec{q} \cdot \vec{r}_j} \quad (1.58)$$

where $\vec{c}_j(\vec{q})$ is the amplitude factor of the scattered light associated to the particle j . The intensity associated to a system of N scatters is then

$$I(\vec{q}) \sim \left\langle \left| \vec{E}(\vec{q}) \right|^2 \right\rangle \sim \sum_{j=1}^N \sum_{k=1}^N \vec{c}_j(\vec{q}) [\vec{c}_k(\vec{q})]^* e^{-i\vec{q} \cdot (\vec{r}_j - \vec{r}_k)} \quad (1.59)$$

If the amplitude factors are all them similar as would be the case for identical spherical particles it is possible to rewrite the intensity as,

$$I(\vec{q}) \sim F(\vec{q})S(\vec{q}) \quad (1.60)$$

where $F(\vec{q})$ is the form factor which describes the structure of a single particle, and $S(\vec{q})$ is the structure factor that accounts for the spatial correlations among the positions of the center of masses of the scatters,

$$S(\vec{q}) = \sum_{j=1}^N \sum_{k=1}^N e^{-i\vec{q} \cdot (\vec{r}_j - \vec{r}_k)} = \left| \sum_{k=1}^N e^{-i\vec{q} \cdot \vec{r}_k} \right|^2 \quad (1.61)$$

The structure factor can be easily related to the particle number function

$$n(\vec{r}) = \sum_i^N \delta(\vec{r} - \vec{r}_i) \quad (1.62)$$

and to its self-convolute function (better known as the autocorrelation function)

$$g(\vec{r}) = \int n(\vec{r} - \vec{\zeta})n(\vec{\zeta})d\vec{\zeta} \quad (1.63)$$

through the equality

$$\sum_{k=1}^N e^{-i\vec{q}\cdot\vec{r}_k} = \int e^{i\vec{q}\cdot\vec{r}} n(\vec{r})d\vec{r} \quad (1.64)$$

and the convolution theorem of Fourier analysis. From Eq. 1.61 we obtain the following expressions for the structure factor,

$$S(\vec{q}) = \int g(\vec{r})e^{i\vec{q}\cdot\vec{r}} d\vec{r} \quad (1.65)$$

and

$$S(\vec{q}) = \left| \int n(\vec{r})e^{i\vec{q}\cdot\vec{r}} d\vec{r} \right|^2 \quad (1.66)$$

Under the assumption of isotropy, $S(\vec{q}) \sim S(q)$ and $g(\vec{r}) \sim g(r)$, Eq. 1.65 yields (for 3d)

$$S(\vec{q}) = 4\pi \int g(r) \frac{\sin(qr)}{qr} r^2 dr \quad (1.67)$$

In a pure liquid, (see Figure 1.10), the structure factor has the well known damped-oscillating shape that reflects the fact that particles inside a liquid have correlated positions, and that these correlations become weaker when the distance among the particles increases.

In order to measure the structure factor associated to the colloidal particles that form the aggregates in the suspension, we must subtract the profile of the pure medium (the liquid). In what follows we will assume the structure factor to be referred to the contribution of the colloidal particles only. The function $S(q)$ for large values of q is expected to give information about the interparticle correlations among neighboring colloidal particles, whereas at low q values will probe large scale correlations or inhomogeneities.

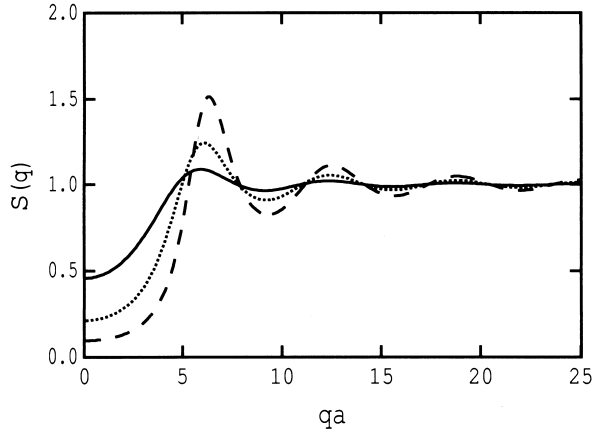


Figure 1.10. Static liquid structure factor for a liquid of hard spheres at three different volume fractions: $\phi = 0.1$ (solid line), $\phi = 0.2$ (dotted line), and $\phi = 0.3$ (dashed line).

1.4.1 Typical structure factors for fractal aggregates

Suspensions in which fractal aggregates are present usually exhibit a structure factor $S(q)$ in which at least three different regimes can be observed.

In the limit of very small $qR_g \ll 1$ we are in the Rayleigh regime. In this regime there is no interparticle interference because the probe lengths are much larger than whatever typical length in the system. The regions of that size are uncorrelated with each other and $S(q) \sim N^2$.

In the limit $qR_g < 1$ (lengths larger than the mean size of the aggregate), the structure factor can be written as

$$S(q) \sim N^2 \left(1 - \frac{1}{3} q^2 R_g^2 \right) + \dots \sim N^2 e^{-q^2 R_g^2 / 3} \quad (1.68)$$

where R_g denotes the radius of gyration of the aggregate. The above result is often called the *Guinier equation* [82–84] and can be obtained [29] by expanding the integrand of Eq. 1.67 and use the identity,

$$R_g^2 = \frac{1}{2} \int r^2 g(r) d\vec{r} \quad (1.69)$$

The Guinier equation allows to determine the size of the aggregates easily because it is independent of $g(r)$ and thus of the details such as the refractive index.

In this regime $qR_g > 1 > qr_o$ we observe lengths smaller or comparable to the size of the aggregate but still larger in comparison with the size of a single colloidal particle r_o . In order estimate $S(q)$ in this regime we need an explicit form for $g(r)$. Teixeira [84] showed that $g(r)$ is expected to scale as,

$$g(r) \sim r^{D_f - d} h(r/R) \quad (1.70)$$

where D_f is the fractal dimension of the aggregate, R is a characteristic length that represent the size of the aggregate, and $h(r/R)$ is a cutoff function that takes care of the finite character of the aggregate. $h(x)$ is approximately constant for $x < 1$ and it decreases faster than any power law for $x > 1$. This cutoff function is independent of the fractal nature of the aggregate and the structure factor can be written as

$$S(q) \sim \int_0^{\infty} h(r/R) r^{D_f-d} \sin(qr) / (qr) r^{d-1} dr \quad (1.71)$$

or,

$$S(q) \sim q^{-D_f} \int_0^{\infty} h(u/(qR)) u^{D_f-2} \sin(u) du \quad (1.72)$$

The nature of $h(x)$ insures the convergency of the above integral to a finite constant, thus the structure function of a fractal aggregate at large q -values is expected to behave as

$$S(q) \sim q^{-D_f} \quad (1.73)$$

It is possible to obtain the fractal dimension of an aggregate from the above result, as it has been done for several authors [85, 86].

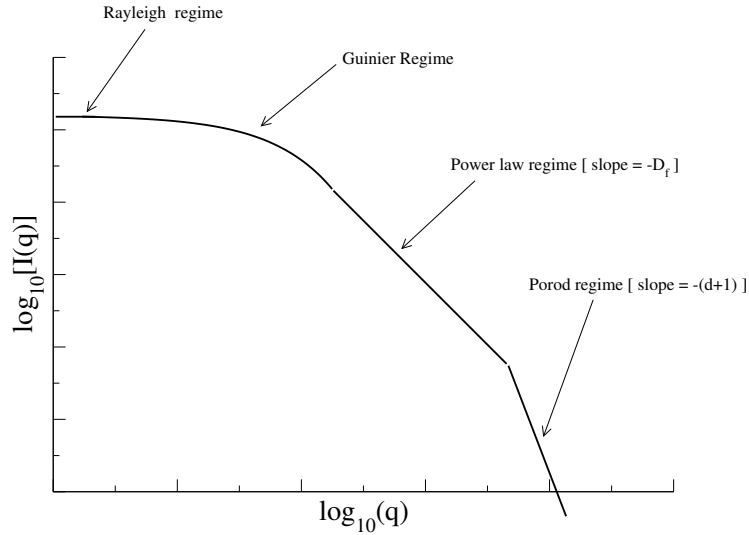


Figure 1.11. Schematic representation of the expected scattered light intensity $I(q)$ versus q from an ensemble of fractal aggregates. The four typical regimes are depicted.

For $qr_o \gg 1$ (q^{-1} becomes of the order of the size of the colloidal particles r_o) we enter the so called Porod regime. At this scale the fractal nature of the

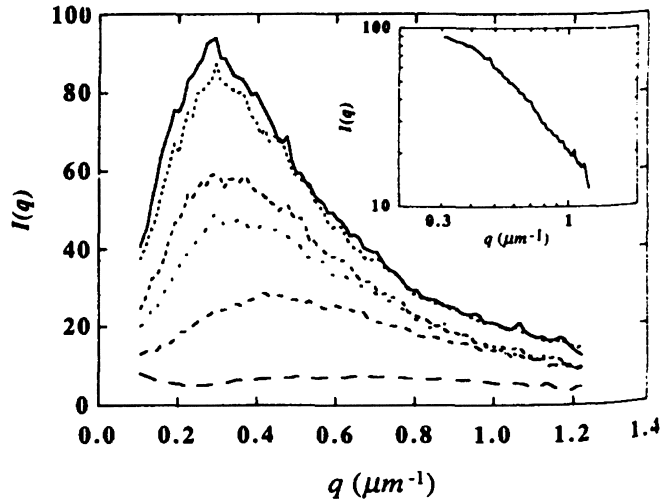


Figure 1.12. In some cases a peak at low angles appears in the scattering from an aggregating suspension. The evolving intensity pattern $I(q)$ is plotted versus q for an emulsion of droplets that suffer an aggregation process. The times are $t = 5, 90, 150, 240, 360,$ and 600 s (bottom to top) after the temperature quench. The inset shows a double logarithmic plot for high values of q . The plot have been taken from Bibette et al. [91].

aggregate is lost, unless primary particles by themselves have a fractal nature. In this regime the structure factor behaves as [83, 87–89],

$$S(q) \sim q^{-(d+1)} \quad (1.74)$$

In summary, the structure factor function for fractal systems is expected to exhibit four regimes (Figure 1.11): the Rayleigh regime, the Guinier regime, the regime ruled by D_f , and the Porod regime. This picture, although useful, is in some cases incomplete. Some aggregating systems exhibit a peak in the structure factor at small non-zero angles (small q -values) [80, 90, 91] (see Figure-1.12). Some authors have suggested that the presence of such peak at finite angle could be the characteristic mark of the formation of a mesoscopic structure in the system at the scale of tens of particles. Nonetheless, the origin and physical meaning of this peak is still partially understood. This issue will be later revised in Chapter 5.

Chapter 2

Basic principles of polymer physics

The aim of this chapter is to introduce some basic concepts related to polymer physics. A full statistical mechanics description of polymer physics is out of the scope of the thesis and can be found elsewhere [92–95], however, we will revise the main theoretical concepts and ideas related to the research studies carried out in this thesis. Additional references are given along the chapter for readers interested in a deeper study of the topics presented here.

2.1 What is a polymer?

A polymer can be roughly defined as a macromolecule made of a large sequence of chemical units (called monomers) linked by covalent bonds¹. A diagrammatic representation of a polymer molecule is shown in Figure 2.1 where A,B,C,... are monomer units and the dash symbols represent covalent bonds between monomers. The monomers that form a polymer could be in principle all chemically different, although usual polymers only contain few different kinds of monomers. The covalent bond that links a monomer unit with another is in most of cases a Carbon-Carbon bond, nonetheless there are notorious exceptions as proteins in which amino acids play the role of monomers which are linked by Carbon-Nitrogen (C-N) covalent bonds. DNA can also be considered as a polymer in which the monomers are the nucleotides. DNA monomers are linked

¹Nowadays, the concept of giant macromolecules seems to us very natural, but it has a long history. Prior to 1920's, the vast majority of scientists denied the existence of such molecules. It wasn't until 1927 that the organic chemist Hermann Staudinger demonstrated without refusal that polymers were made by a sequence of units linked by covalent bonds.

among them by phosphor-oxygen bonds ². A basic quantity related to a polymer molecule is the number of monomers N often called the *degree of polymerization*. Usually $N \gg 1$, for example, proteins have chain lengths of the order of $N \sim 10^2 - 10^4$ amino acids, whereas DNA (among the longest polymers) contains about $N \sim 10^9$ nucleotides.

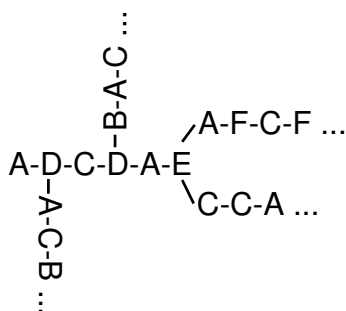


Figure 2.1. The most basic representation of a polymer molecule is a diagram showing how chemical monomer units are linked among them to form the primary structure of the macromolecule. Each letter in the diagram represents a different chemical monomer, and straight lines represent covalent bonds.

The most simple polymers are those based on a sequence of carbon and hydrogen atoms. Among them, the easiest is the well-known polyethylene that can be depicted by the formula $CH_3 - (CH_2)_n - CH_3$ (see Figure 2.2). A typical polyethylene molecule contains of the order of 10^5 monomer units ($-CH_2-$).

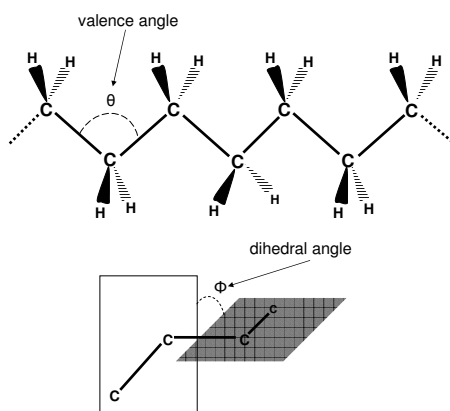


Figure 2.2. Chemical representation of a segment of a polyethylene molecule in which each $-CH_2-$ unit constitutes a chemical monomer. The angles θ and ϕ stand for the valence and the dihedral angles respectively.

Polyethylene is the stereotype of a *linear polymer* that can be defined as a polymer whose monomers are linked to other monomers through two and only

²Other polymers with covalent bonds between monomers different from carbon-carbon: polysilanes (Si-Si), Silicons (Si-O), polygermanes (Ge-Ge), polystannanes (Sn-Sn), and the polyphosphazenes (P-N).

two covalent bonds, except the monomers located at both ends that are linked by a single covalent bond to the remaining chain. Polymers in which there are monomers that share bonds with three or more monomers are called *ramified polymers*. The polymer depicted in Figure 2.1 is a clear example of a ramified polymer. Polyethylene is also a prototype of a class of polymers called *homopolymers*. We can define an homopolymer as a polymer in which all the monomeric units are exactly the same, on the other hand, *heteropolymers* are polymers composed by different monomers units. For instance, DNA can be considered as a heteropolymer composed of 4 types of monomers, whereas, proteins are heteropolymers which contain usually up to 20 different kinds of monomers.

Heteropolymers in which there are only two different kinds of monomers are called *copolymers*; if they contain three different types of monomers, *terpolymers*, etc. Copolymers can be additionally classified depending on their internal organization, namely.

- *Statistical copolymers*. The distribution of the two types of monomers in the chain is essentially random **...BAABABBBBBBABBBABAAA...**
- *Alternating copolymers*. Monomers are regularly placed along the chain **...ABABABABAB...**
- *Block copolymers*. Comprised of substantial sequences or blocks of each monomer **...AAAAABBBBBBAAAAABBBBB...**
- *Grafted copolymers*. Polymer blocks of one monomer are grafted onto a backbone of the other monomer forming branches (Figure 2.3).

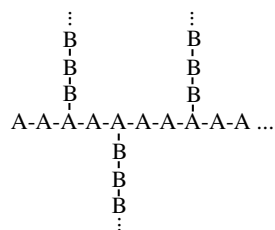


Figure 2.3. Schematic representation of a grafted copolymer molecule.

Both homopolymers and heteropolymers can be synthesized into complex ramified structures. The most usual types of branched polymers are: star polymers, miktoarm star copolymers, star copolymers, comb polymers, and dendrimers (Figure 2.4).

Polymers can be electrically neutral or have charges distributed along their structure. When a polymer contains charged units it is called a *polyelectrolyte*. The charges must be counterbalanced either by the presence of monomers with

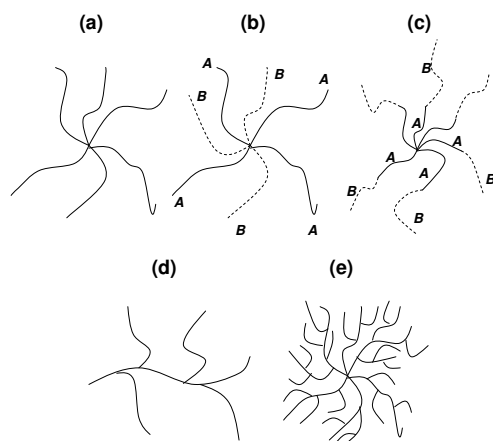


Figure 2.4. Schematic representation of the most usual types of branched homopolymers and heteropolymers: (a) star polymer, (b) miktoarm star copolymer, (c) star copolymer, (d) comb polymer, and (e) dendrimer.

opposite charges in the chain (*polyampholytes*) or by the presence of counter-ions around the chain.

The polymer structure and composition lead to different statistical properties, rising a rich variety of physical behaviors that determine the mechanical and thermal properties of the polymeric materials or how do they interact with other substances or structures.

2.2 Conformations of a polymer chain

A polymer molecule is usually represented in a fully stretched conformation. This representation, although useful in certain cases is definitively misleading in reference to the usual conformations adopted by polymers. In practice, the probability of a molecule to exhibit a fully stretched conformation is extremely low.

Consider, for instance, a fully stretched polyethylene chain as depicted in Figure 2.2. In that conformation the *valence angle* θ and the *dihedral angle* ϕ minimize the steric hindrance (overlap) among the monomers. However, due to the thermal fluctuations, both θ and ϕ are allowed to oscillate around their optimal values. The higher the temperature, the larger the oscillation of θ and ϕ around their optimal values. The slight distortion of one valence or dihedral angle has minimum consequences for the entire chain, but the sum of the effects of many slight distortions leads the chain to adopt conformations very far from the full stretched conformation, developing a random coil structure (Figure 2.5). A chain able to suffer large deviations from the fully stretched conformations is said to exhibit a large degree of *flexibility*.

To simplify still further the model, consider the valence angles and the bond

lengths fixed to their optimal values, so the dihedral angles are the only parameters to consider. As reflected in Figure 2.6, if the carbon C_n rotates, the dihedral angle ϕ changes, however a monomer is not free to rotate because the hydrogen atoms linked to carbon C_n and those linked to the atom C_{n-1} will repel among each other. The repulsions among atoms due to their proximity in space are often called *steric repulsions*. Figure 2.7 shows the energy associated to the dihedral angle ϕ_n . There are three minima (a Trans and two Gauche conformations) separated by two energy barriers. Two essential parameters in determining the polymer conformations are: (1) the energy difference between two consecutive minima $\Delta\epsilon$, and (2) the energy barrier separating the two minima ΔE . If $\Delta\epsilon$ is smaller than the thermal energy, $k_B T$, the relative weight of gauche/trans conformations will be of the order of the unity given rise to flexible chains. In contrast, as the ratio $\Delta\epsilon/K_B T$ increases, the relative weight of gauche/trans conformations tends to zero, the trans state becomes the preferred one leading to a stretched polymer chain. In polyethylene molecules $\Delta\epsilon \sim 3.34 kJ/mol^{-1}$. If we assume that the ratio between the number of *gauche*, n_g , to *trans*, n_t , states is governed by the Boltzmann factor,

$$\frac{n_g}{n_t} = 2 \exp(-\Delta\epsilon/kT) \quad (2.1)$$

we will obtain that n_g/n_t is 0.036, 0.264, and 0.524 for $T=100K$, $T=200K$ and $T=300K$, respectively. These results entails that polyethylene (as well as many other polymer molecules) at room temperature or higher temperatures exhibit a large degree of flexibility since a large number of monomers are in the gauche state. When the temperature is reduced, the number of Gauche conformations n_g reduces and the chain becomes stiffer or less flexible.

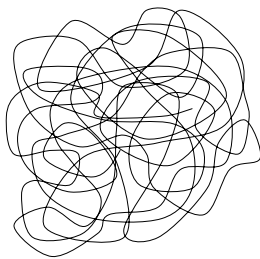


Figure 2.5. Polymers are usually not fully stretched, they resemble a random coil.

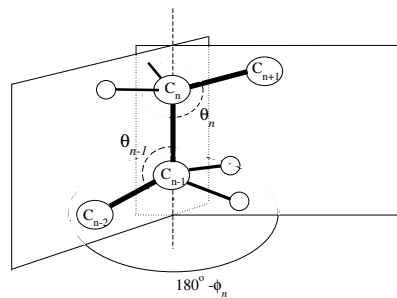


Figure 2.6. Schematic representation of a segment of a polyethylene chain.

A sequence of monomers of a polyethylene molecule maintain an approximately straight path when all their monomers are in the trans state. However,

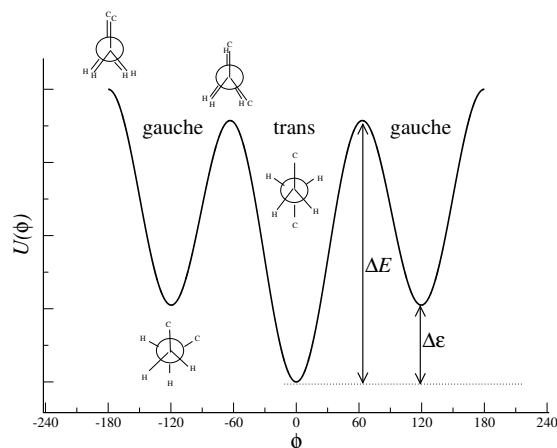


Figure 2.7. Approximate energy landscape associated to a dihedral angle parameter in a carbon backbone polymer. Newman projections are shown in order to illustrate the steric hindrances present at different dihedral angles.

the chain orientation changes dramatically when a gauche conformation occurs. Probability states that given a fixed n_g/n_t ratio, the probability that the $(i+n)$ -monomer has the same orientation in the space that the i -monomer decreases with the distance n . Therefore, a chain can be naively depicted as a succession of rigid rods, each of them composed of monomers in the trans state, separated by monomers in the gauche state. Obviously the length of such rods fluctuates in time, but we can estimate an averaged length l_p for such rods. The quantity l_p is often called *the persistence length*³ and it is a characteristic parameter for a polymer. In the next section it is shown how l_p can be numerically estimated. If we look at a polymer at scales larger than l_p , the polymer behaves as a flexible chain resembling a random coil in which the effective monomers have a size l_p . However, if we look the polymer on scales shorter than l_p , the chain will resemble locally rather stretched. The value of l_p for a real macromolecule depends on the chemical details and the internal structure of the molecule. As an example, the persistence length for polyethylene is about $l_p \sim 0.6nm$, for DNA typical values are of the order of $l_p \sim 50nm$, whereas F-actin⁴ reaches persistence length up to $l_p \sim 10000nm$.

The global behavior of a polymer chain can be considered to be flexible or stiff depending how l_p compares to the full length of the molecule L . If $L \ll l_p$ the chain behaves globally as a rigid rod (fully stretched) at all scales. If $L \gg l_p$ the polymer is considered to be flexible and it looks like a loosely coiled ball (Figure 2.5).

³Formally, we can write l_p as a function of $\Delta\epsilon$: $l_p = l_o \exp(\Delta\epsilon/kT)$, where l_o is a constant.

⁴F-actin is a polymer (or filament) composed by a sequence of linked globular actin proteins. F-Actin as well as myosin filaments are present in myofibrils. Each muscle fiber contains several hundred of thousands of myofibrils.

2.3 Characterization of a single polymer chain

The study and characterization of a single polymer can be done at several levels. In polymer physics we are not usually interested in the very fine chemical polymer details. However, polymer physics looks at the global or coarse properties of the polymers. At this level, it is common to characterize a polymer through the evaluation of the characteristic parameters related to the distribution and orientation of monomers in space. One of these characteristic parameters was found in the previous section when the persistence length l_p was discussed. In the following we will describe other magnitudes used along the thesis to describe the main features concerning the polymer structure.

- The average root mean square end-to-end distance R_{ee} .
- The Kuhn segment length.
- The radius of gyration R_g
- The chain asphericity parameter Δ .
- The non-sphericity parameter A .
- The bond-angle correlation BAC and the persistence length l_p .
- The bond-order correlation function BOC .

2.3.1 The mean square end-to-end distance, and the Kuhn segment length

The mean square end-to-end distance R_{ee}^2 defined as the average (over all chain conformations) of the square distance between the two ends of the polymer chain (Figure 2.8). If the positions of the N monomers of a chain are given by $\vec{r}_1, \vec{r}_2, \dots, \vec{r}_{N-1}, \vec{r}_N$, the mean end-to-end distance is defined as

$$R_{ee}^2 = \langle (\vec{r}_{1N})^2 \rangle^{1/2} = \langle (\vec{r}_1 - \vec{r}_N)^2 \rangle^{1/2} \quad (2.2)$$

where $\langle \dots \rangle$ denotes an average over all the possible chain conformations.

A common parameter intended to measure the degree of flexibility of the polymer is the *Kuhn segment length* l_K defined as,

$$l_K = \frac{R_{ee}^2}{L} \quad (2.3)$$

where L is the length of the chain. The Kuhn length and the persistence length are parameters with close meanings: a large value of l_p or l_K (respect to the size of a monomer) implies a polymer with a low degree of flexibility. In Table 2.1 the Kuhn length for several macromolecules is compared to the size of their monomers, a .

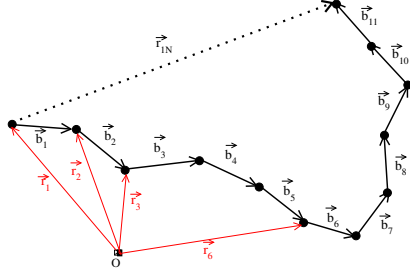


Figure 2.8. Schematic plot of a polymer in which only the position of the center of masses of the monomers are depicted. The position vectors \vec{r} are referred to an arbitrary origin. The vectors that join the center of masses of two consecutive monomers are called bond vectors, \vec{b} . The distance between the two chain ends \vec{r}_{1N} is also shown.

Macromolecule	l_K/a
polypropylene	3
polyvinylchloride (PVC)	4
polystyrene	5
cellulose diacetate	26
polyparabenzamide-benzamide	200
DNA (double helix)	300
polybenzyl glutamate (α -helix)	500

Table 2.1. Comparison between the Kuhn length l_k and the linear size of a monomer a for several molecules ordered with decreasing flexibility.

2.3.2 The Radius of gyration of the chain

Another common way to character the size of a polymer is through the radius of gyration R_g . We define the *radius of gyration tensor* through their elements,

$$R_{\alpha,\beta} = \frac{1}{2N^2} \sum_{i,j=1}^N (r_{i,\alpha} - r_{j,\alpha})(r_{i,\beta} - r_{j,\beta}) \quad (2.4)$$

where α and β denotes de Cartesian components x , y , and z . The tensor can be represented as a diagonalizable 3×3 matrix. The three eigenvalues λ_i ,

$$\begin{pmatrix} \lambda_1 & 0 & 0 \\ 0 & \lambda_2 & 0 \\ 0 & 0 & \lambda_3 \end{pmatrix} \quad (2.5)$$

characterize the size of the polymer along the principal axes. The eigenvectors associated to the eigenvalues point along the directions of the three principal axes of symmetry of the polymer. The square of the gyration radius is defined as the sum of the three eigenvalues λ_i ,

$$R_g^2 = \lambda_1 + \lambda_2 + \lambda_3$$

When the monomers are isotropically distributed, an alternative method can be used in order to compute the radius of gyration,

$$R_g = \langle R^2 \rangle^{1/2} = \langle (\vec{r}_i - \langle \vec{r}_i \rangle)^2 \rangle^{1/2} \quad (2.6)$$

where the outer $\langle \dots \rangle$ implies an average over all polymer conformations, and $\langle \vec{r}_i \rangle$ stands for the position of the center of mass in a given conformation. Debye proved [96] that R_{ee} and R_g are related in the limit $N \rightarrow \infty$ by the equality,

$$R_{ee}^2 = 6R_g^2 \quad (2.7)$$

when no correlations exists among the position of the monomers.

2.3.3 The asphericity and non-sphericity parameters

The eigenvalues $\lambda_1, \lambda_2, \lambda_3$ of the radius of gyration tensor can be used to estimate the "deviation" of the cloud of monomers from a spherical distribution, i.e. to determine the degree of anisotropy of the chain. Thus, the *asphericity* is defined as,

$$\Delta = \frac{(\lambda_1 - \lambda_2)^2 + (\lambda_1 - \lambda_3)^2 + (\lambda_2 - \lambda_3)^2}{2(\lambda_1 + \lambda_2 + \lambda_3)^2} \quad (2.8)$$

When the monomer distribution is perfectly spheric $\Delta = 0$, whereas for very elongated conformations $\Delta \sim 1/4$, and in the limit of a infinite fully stretched chain $\Delta \sim 1$.

In some cases it is possible to know in advance the direction along which the principal axis will lie. Then, a simpler function, the *non-sphericity* A , can be defined in order to measure the degree of anisotropy of the chain [97]. If, for simplicity, we assume the main axis to lie along the eigenvector of λ_2 , the non-sphericity is determined by,

$$A = \frac{1}{2} \left(\frac{2\langle \lambda_2 \rangle - \langle \lambda_1 \rangle - \langle \lambda_3 \rangle}{\langle R_g^2 \rangle} \right) \quad (2.9)$$

where $R_g^2 = \lambda_1 + \lambda_2 + \lambda_3$. $A = 0$ when the monomer distribution is isotropic in the 3d space, and $A = 1$ when all the monomers are perfectly aligned along the eigenvector of λ_2 . When the chain has an isotropic 2d distribution, $A = 1/4$.

2.3.4 The bond-angle correlation function (BAC) and the persistence length l_p

The bond-angle correlation function (BAC) is defined as,

$$BAC(i) = \left\langle \frac{\vec{b}_j \cdot \vec{b}_{j+i}}{|\vec{b}_j| |\vec{b}_{j+i}|} \right\rangle = \left\langle \cos \left(\phi(\widehat{\vec{b}_j \vec{b}_{j+i}}) \right) \right\rangle \quad (2.10)$$

where $\phi(\vec{b}_j, \vec{b}_{j+i})$ is the angle formed by the bond vectors \vec{b}_j and \vec{b}_{j+i} . A bond vector is defined as the difference between the position of two consecutive monomers $\vec{b}_j = \vec{r}_{j+1} - \vec{r}_j$. The *BAC* function measures the degree of correlation between bond angles that are separated i units along the chain. Chains without correlations among monomer positions should have $BAC(i) = 0$ for all i . The *BAC* function can be used in order to estimate of the persistence length l_p of a polymer chain. If we assume the *BAC* function to decay exponentially with the distance between monomers, the persistence length l_p can be defined as the decay length of the *BAC* function,

$$BAC(x) \sim \exp\left(\frac{-x\sigma}{l_p}\right) \quad (2.11)$$

where σ is the monomer size.

2.3.5 The bond orientational correlation function (BOC)

The BOC function measures the correlation in the orientation of polymer bonds between monomers⁵ and is defined as,

$$BOC(i) = \langle \hat{p}_j \cdot \hat{p}_{j+i} \rangle, \quad (2.12)$$

where $\langle \dots \rangle$ represents an average along the chain and over all the polymer conformations. The unitary vector \hat{p}_i is given by

$$\hat{p}_i = \frac{\vec{b}_i \times \vec{b}_{i+1}}{|\vec{b}_i \times \vec{b}_{i+1}|} \quad (2.13)$$

and by definition its perpendicular to the plane containing the bond vectors \vec{b}_i and \vec{b}_{i+1} . The BOC function is expected to be zero when bond vectors are completely uncorrelated in space. Whereas $BOC(i) \rightarrow 1$ if the sequence of bonds between monomers follow a perfect line path.

2.4 Models for ideal chains

Along the XX century, several simplified mathematical models have been proposed in order to gain insight into the statistical properties of polymers. The simplest models were based on the concept of *ideal chains*. An ideal chain represents a similar degree of simplification when compared to the role of the ideal gas

⁵The bond-angle correlation function (BAC) does not describe completely the orientation of bonds. Pairs of bonds with similar bond angles can point into very different orientations in the space.

in the study of gases. An ideal chain is made of immaterial monomers, and correlations among monomers do not exist or do not extend beyond few monomers in the chain sequence. In addition, no interactions with solvent molecules or other polymer chains are taken into account. The different mathematical models developed for ideal chains basically differ in the type of bonding assumed between nearest monomers. The most common models for ideal chains are: the freely jointed chain, the freely rotating chain, the Gaussian chain, and the worm like model.

2.4.1 The freely jointed chain model

The freely jointed chain model is the simplest model describing a polymer: the chain is composed of a sequence of N segments (monomers) of fixed length a (Figure 2.8). Each segment is free to point in whatever direction, and no correlations among their orientations exist. The model is in fact completely equivalent to the mathematical Random Walk problem. The mean square end-to-end distance R_{ee}^2 can be written in terms of the bond vectors \vec{b} as:

$$R_{ee}^2 = \langle (\vec{r}_{1N})^2 \rangle = \left\langle \left(\sum_{i=1}^N \vec{b}_i \right)^2 \right\rangle = \sum_{i=1}^N \langle (\vec{b}_i)^2 \rangle + 2 \sum_{i < j}^N \langle \vec{b}_i \cdot \vec{b}_j \rangle \quad (2.14)$$

Taking into account that bond directions are not correlated $\langle \vec{b}_i \cdot \vec{b}_j \rangle = 0$, and $\langle (\vec{b}_i)^2 \rangle = a^2$, we obtain the very important result,

$$R_{ee} = \langle (\vec{r}_{1N})^2 \rangle^{1/2} = aN^{1/2} \quad (2.15)$$

Thus, an ideal chain composed of freely jointed bonds has a mean size that increases with the square root of the number of monomers in the chain, on the contrary to a fully stretched chain in which the size of the macromolecule increases linearly with N .

The expression 2.15 is a very general result which goes beyond the freely jointed chain model. More realistic models take into account the fact that bond lengths among monomers are not constant, and their values oscillate around an average length following an arbitrary probability bond length distribution function $p(|\vec{b}|)$. It is possible to demonstrate [94] that whatever bond distribution function is taken will lead to the same result 2.15 in the limit $N \rightarrow \infty$.

Thus, the $N^{1/2}$ behavior is *universal* in the limit $N \rightarrow \infty$ for any type of ideal chain without correlations among its bonds. The same result is in fact obtained if correlations among consecutive monomers are present $\langle \vec{b}_i \cdot \vec{b}_j \rangle \neq 0$, but they decrease with the distance $|i - j|$ [94]. When correlations are of finite size, the

chain can be redefined as a sequence of uncorrelated bonds \vec{c} (Figure 2.9) that behaves as predicted by the expression 2.15 in the limit of $N \rightarrow \infty$.

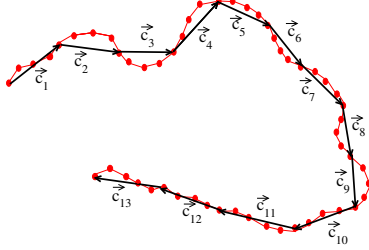


Figure 2.9. A polymer with finite range bond correlations can be redefined in terms of an uncorrelated sequence of bonds \vec{c}_i

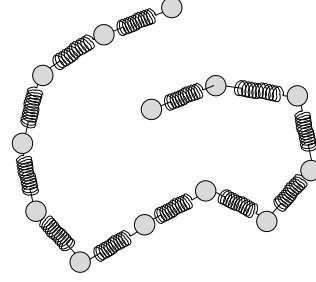


Figure 2.10. A physical representation of a Gaussian chain is a polymer made of $N - 1$ beads in which consecutive monomers are connected by springs obeying Hook's law.

2.4.2 The Gaussian chain model

The *Gaussian chain model* constitutes a particular case of an ideal chain composed of segments of variable length in which the bond length probability distribution function $p(|\vec{b}|)$ is a Gaussian (see Figure 2.10)

$$p(\vec{b}) = \left(\frac{3}{2\pi\langle(\vec{b})^2\rangle} \right)^{3/2} \exp\left(\frac{-3(\vec{b})^2}{2\langle(\vec{b})^2\rangle} \right) \quad (2.16)$$

The limit $N \rightarrow \infty$ also applies to the Gaussian chain model. In fact, whatever bond length distribution is used, it leads to the same $N^{1/2}$ dependence as established in the central limit theorem which states that all distributions tend to become more and more Gaussian if samples are taken over larger and larger sets. The Gaussian model, as the previous models described, do not reproduce correctly the local structure of the polymer, but it describes accurately the statistical properties at large scales. The advantage of using the Gaussian model lies in the fact that is mathematically easier to handle than any other non trivial model and they can be considered as a starting point for more elaborated models. For instance, the bare Gaussian model can be modified to account for monomer correlations, chain stiffness, and energetic interactions among monomers [92].

2.4.3 The freely rotating chain model

In order to characterize chains in more detail, bond lengths and valence angles between contiguous bonds are, in general, restricted to fairly narrow ranges. At room temperature bond length oscillations are typically smaller than a 3% and angle fluctuations are below five degrees. In the *freely rotating chain model* [92] a chain is composed of N bonds of fixed length a , and a constant valence angle θ is specified, however, dihedral angles do not have a fixed value. The constraints of the model lead to the following expression for the correlation between bonds,

$$\langle \vec{b}_i \cdot \vec{b}_{i+k} \rangle = a^2 \cos^k(\theta)$$

the square end-to-end distance in the limit of $N \rightarrow \infty$ is given by [98]

$$R_{ee}^2 = Na^2 \frac{(1 + \cos(\theta))}{(1 - \cos(\theta))}$$

and the relation $R_{ee}^2 = 6R_g^2$ also applies. Improved rotational models tune the correlations among bonds through the introduction of a restricted dihedral angle ϕ . Usually these restrictions are formulated via potentials that depend on θ and ϕ . Calculations become complex and matrix techniques must be used [92]. If we assume a model in which θ and the bond length are constants and the rotational potential only depends on ϕ , it is possible to prove that the mean square end-to-end distance in the limit $N \rightarrow \infty$ is [99]:

$$R_{ee}^2 = Na^2 \frac{[1 + \cos(\theta)] [1 + \langle \cos(\phi) \rangle]}{[1 - \cos(\theta)] [1 - \langle \cos(\phi) \rangle]}$$

2.4.4 The worm like chain model

The models in which valence and dihedral angles are restricted to their characteristic values can be used to describe ideal semiflexible chains, but have the disadvantage of being difficult to study analytically. An easier model for ideal semiflexible chains from the analytical point of view is the *Worm-like chain* continuum model (WLC) also known as the *Kratky-Porod chain* [100]. The WLC hamiltonian of a semiflexible chain with persistence length $l_p = \kappa/(k_B T)$ is:

$$H(\vec{t}(s)) = \frac{\kappa}{2} \int_0^L ds \left(\frac{\partial \vec{t}}{\partial s} \right)^2 \quad (2.17)$$

where $\vec{t}(s)$ is the unit tangent vector to the chain at point s . The partition function of the chain can be formally written as:

$$\int D[\vec{R}(s)] e^{-\beta H(\vec{t}(s))} \quad (2.18)$$

where $\vec{R}(s)$ is the path followed by the chain in space. It is possible to demonstrate that end-to-end distance for a Worm-like chain is [101]:

$$R_{ee}^2 = \frac{l_p^2}{2}(e^{-2L/l_p} - 1 + 2L/l_p) \quad (2.19)$$

that reduces to the behavior of a rigid rod when $l_p \gg L$.

2.5 Real chains: the effect of long-range interactions

The type of interactions that occur in a real chain can be classified in short-range and long-range interactions (see Figure-2.11). Short-range interactions are those due to the bond structure and local interactions between atoms of monomers close in the chain sequence. Long-range interactions involve pairs of units which are remote in the chain sequence but close in space.

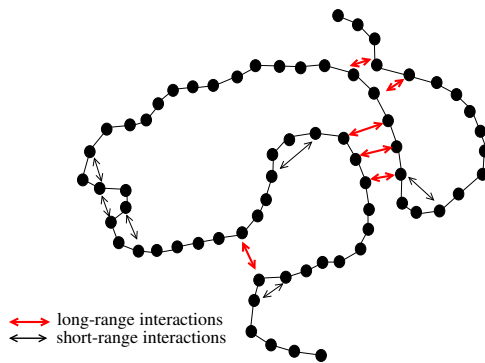


Figure 2.11. Short-range and long-range interactions in a polymer chain.

An example of long-range interactions is the *exclude volume interaction* which manifest the impossibility of two atoms to overlap their domains completely. The exclude volume interaction produces a non zero correlation in the position of two monomers even if they are in opposite ends of the chain. Therefore, the correlations that exclude volume interactions, as well as other long-range interactions (for instance, electrostatic) produce cannot be taken into account by ideal models. Other types of models beyond the ideal ones are needed if we want to mimic the behavior of real chains, although ideal chain models are very useful in describing polymer chains at θ -point (defined below) or polymer melts and semi-diluted polymer solutions.

The monomers in real chains exhibit several types of long-range interactions, just to mention the repulsive steric hindrance of monomers and van der Waals forces, and are responsible of changes in size and structure of the real molecules

respect to ideal chains. It is common to refer the size of a real molecule to an equivalent ideal chain through the *swelling parameter* α ,

$$R_{ee} = \alpha R_{ee}^{(o)}$$

where $R_{ee}^{(o)}$ is the size of an equivalent chain in which long-range interactions are turned off. Experiments show that the value of α is highly dependent on the type of solvent in which the polymer is immersed.

When the interactions among monomers and solvent molecules are thermodynamically favorable the solvent is known as a *good solvent*. In a good solvent the polymer strives to maximize the number of contacts with the solvent by adopting a swelling conformation (Figure-2.12a). A special case of good solvent is the *athermal solvent* in which monomer-monomer and monomer-solvent interactions are of the same strength. The polymer behavior in good solvents is usually modeled through an effective repulsive interaction between monomers. As a consequence, the chain swelling α takes values larger than unity. In fact, experiments show that α is a function of the molecular weight ($\sim N$)⁶. In good solvents the end-to-end distance scales with the chain length as $R_{ee} \sim N^{3/5}$ (in 3d systems) instead of the ideal dependence $N^{1/2}$. A huge amount of work has been devoted to understand the differences between ideal and real chains.

- **The Flory-Fisher theory:** In 1949 Flory devised a simple theoretical scheme to compute the dependence of the molecular size R_{ee} with the molecular weight ($\sim N$) in real chains. The exponent he derived for 3d chains was $\nu = 3/5$. In 1966 M. Fisher generalized the method of Flory to any chain dimensionality obtaining

$$R_{ee} \sim N^\nu \sim N^{\frac{3}{d+2}} \quad (2.20)$$

for chains with exclude volume interactions in a good solvent. The theory [102, 103] is based on a minimization of the free energy of a polymer chain in which two contributions compete: **(a)** a repulsive energy due to the exclude volume interactions, $F_{rep} \sim \langle c^2 \rangle R^d \sim N^2/R^d$, where $\langle c^2 \rangle$ is the monomer concentration in a region of size R^d occupied by the monomers of the chain taken in a mean field approach whose monomer correlations are neglected $\langle c^2 \rangle \sim (N/R^d)^2$ and **(b)**, an elastic free energy $F_{el} \sim R^2/N$

⁶The size of macromolecules can be determined by various experimental methods. For instance, the gyration radius can be inferred from the measurements on scattered light intensity [92]. Another method to estimate the radius of a polymer macromolecule is through the Stokes-Einstein relation and the diffusion coefficient of the polymer that can be obtained using the Photon beat technique.

is introduced to account for the large entropy penalty of stretched configurations. The minimization of $F_{rep} + F_{el}$ leads to Eq. 2.20.

The Flory-Fisher expression (Eq. 2.20) gives results within a percent of the most accurate numerical results. Therefore, for most purposes (Eq. 2.20) can be considered numerically exact. The excellent agreement of Flory-Fisher scheme with the experimental results led to the wrong idea that the method was the correct frame to deal with the exclude volume problem. Lately, other properties calculated with the Flory-Fisher method were observed to not agree so well with experiments on real chains. In fact, the formalism is so successful in calculating the exponent ν because it benefits from a remarkable cancellation of two errors: an overestimation of F_{rep} since correlations among monomers are neglected, and an overestimation of the attractive elastic force F_{el} .

- **Renormalization techniques:**

In 1972 de Gennes showed that a large chain is a critical object and the same methods used in critical systems can be applied to polymer chains [102, 103]. The renormalization technique applied to exclude volume chains proved that polymer chains have, in fact, two universal exponents: ν related to the chain size, and γ related to the chain entropy. All the theoretical formalisms prior to the renormalization implicitly assumed a value of $\gamma = 1$, far from the real value $\gamma \cong 7/6$ in 3d, and $\gamma \cong 4/3$ in 2d.

- **The self avoiding random walk approach:** It constitutes a remarkable fact that the exponents $\nu = 3/5$ and $\gamma = 7/6$ in 3d, as well as $\nu = 3/4$ and $\gamma = 4/3$ in 2d can be obtained if we assume the chain to be a mathematical self avoiding random walk in a lattice. Thus, showing the same universal statistical properties of real chains in good solvents [95].

The temperature is a key factor in determining the net result of the monomer-monomer and monomer-solvent interactions. Common solvents are in general worse "good solvents" at low temperatures because increases the weight of the effective interaction of the attractive forces between monomers, whereas at high temperatures monomers tend to repeal each other. By setting the solvent or the temperature adequately, it is possible to cancel exactly the effects of the repulsion and the attraction among monomers. At this point $\alpha = 1$ and we say that we have reached *the θ -point*. The temperature at which the θ -point is reached is often called the θ -temperature. The θ -point constitutes the right place to test all previous results for ideal chains because real chains behave at the θ -point as if long-range interactions were not present.

If the temperature is reduced below the θ -point, the monomer-solvent interaction becomes less attractive and monomers start to suffer an effective attraction among them. A solvent in which monomers prefer to be in contact with other monomers rather than with solvent molecules is called a *bad solvent*. The attraction among monomers leads the polymer to crunch in order to increase the number of monomer contacts and reduce the interactions with the solvent. The contraction of the chain respect to the ideal size implies a value of $\alpha < 1$. When the chain (coil) becomes compressed, it forms a *globular state* (see Figure-2.12c). Globular states are commonly observed in proteins, DNA and polyelectrolytes. When polymer chains are large, the globules formed in a bad solvent consist of a dense homogeneous nucleus and a thin surface layer. At equilibrium, the globule reaches a size such that attractive and repulsive interactions (that depend on monomer concentration) counterbalance, by means, the osmotic pressure inside the globule is zero. This condition sets the size of a globule to behave as $R_{ee} \sim N^{1/3}$. The transformation from a coil to a globule when the temperature is reduced below the θ -point is a gradual process: the temperature-width of such transformation is proportional to $N^{-1/2}$, and becomes 0 in the limit $N \rightarrow \infty$ as in a true phase transition. The transformation process from coil to globule in stiff chains is sharper and closer to a first-order transition than in flexible chains. If the solvent is extremely poor, the polymer globule precipitates out of the solution to minimize the interactions with the solvent. The solvent is called in this extreme case a "*non-solvent*".

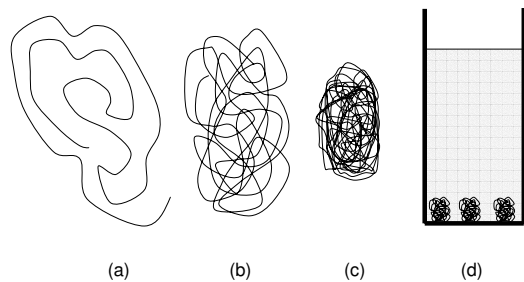


Figure 2.12. The quality of the solvent is a key parameter in determining the swelling parameter of a chain, α : (a) in good solvents, chains tend to be swollen; (b) at the θ -point the chain exhibits ideal behavior; (c) in bad solvents the chain tend to compress and form a globule; (d) when the solvent is extremely poor, polymers precipitate out of the solution ("*non-solvent*" conditions).

2.6 Polymer solutions

In the previous sections we have referred all the discussion to the properties of an isolated chain, but generally we must deal with polymer solutions. In a polymer solution the concentration of monomers c is a key parameter in order to determine

the conformational properties of the individual chains in dissolution as well as the general properties of the solution. The volume fraction of polymer in the solution can be defined as $\phi = ca^3$ where a^3 is the typical size of a monomer. When $\phi = 1$ our solution is really a polymer melt. On the other hand, the limit $\phi \rightarrow 0$ represents the limit of very diluted solutions.

In bad solvents, where monomer-monomer attractions prevail over monomer-solvent attractions, the behavior of polymer solutions is rather easy to explain: the addition of new chains to the solution results in a tendency of chains to stick together. If the polymer concentration is high enough the polymers precipitate out of the solution.

Polymers in good solvents exhibit a behavior by far more complex than polymers in bad solvents. Although it can be surprising at first sight, the regime in which is easier to describe the conformation of single chains is the *concentrated regime* or *melt* $\phi \rightarrow 1$ (in three dimensions). In the concentrated regime all the chains exhibit a structure similar to an ideal chain $R_{ee} \sim N^{1/2}$. This behavior was first understood by Flory, but only long time ahead was recognized by other scientists. The ideal behavior of a polymer chain in a melt can be understood in terms of the fact that the force that tends to self-swollen a chain is compensated by an inward force created by the rest of chains in the melt. Besides, the properties of a single chain in the concentrated regime resemble those of an ideal chain, the global properties of a concentrated solution (as the osmotic pressure) cannot be described through an ideal system. The estimation of the global properties in melts requires the use of realistic interaction potentials and the full theory of liquids.

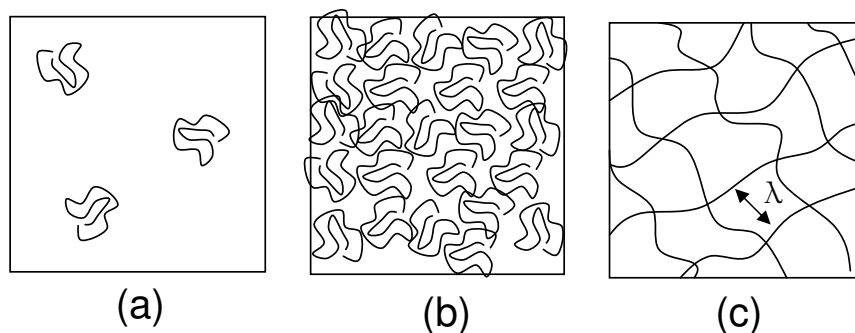


Figure 2.13. When polymer molecules are added to a solvent, several regimes can be observed: (a) diluted regime, (b) crossover from dilute regime to semi-dilute regime, and (c) semi-dilute regime. In the semi-dilute regime, a polymer solution can be considered as a quasi-network with an average mesh size λ .

Unlike melts, diluted solutions display a more complex behavior, but the properties of the solution as a whole have a large degree of universality. When we start to add polymers into a good solvent (suppose $\phi = 0$ initially), chains behave as isolated chains and all the results derived in the previous section applies, i.e. $R_{ee} \sim N^{3/5}$. We call this regime *the diluted regime* (Figure-2.13a). As we add more polymers to the solution we reach a boundary concentration ϕ^* in which polymer chains start to overlap their domains (Figure-2.13b). The addition of more polymers to the solution increases the overlaps and we enter the so-called *semi-diluted-regime* (Figure-2.13c). The value of the boundary concentration ϕ^* depends on the molecular weight of polymers. In good solvents $\phi^* \sim N^{-3\nu+1} \sim N^{-4/5}$ whereas in the θ -point $\phi^* \sim N^{-1/2}$. $\phi^* \rightarrow 0$ when $N \rightarrow \infty$, thus the semi-diluted regime $\phi^* \ll \phi \ll 1$ is observed over a large range of ϕ 's. As it is shown in Figure-2.13c, a semi-dilute polymer solution can be considered as a quasi-network with an average mesh size λ called *the correlation length of the polymer solution*. This length λ can be considered as a mean distance between consecutive contacts of one polymer with another. The dependence of λ with the polymer concentration in good solvents is given by $\lambda \sim \phi^{-3/4}$, whereas the number of monomers g contained in average in a volume of size $\sim \lambda^3$ is $g \sim \phi^{-5/4}$.

In the semi-diluted regime, if we have a segment of chain with a typical size smaller than λ , the segment is expected to behave as an isolated chain, but as the length of the segment becomes of the order of λ the segment is affected by the presence of other chains. Therefore, we can model a polymer chain in the semi-dilute regime as a sequence of blobs of linear size $\sim \lambda$, where each blob is, in fact, statistically independent of the others. As a consequence, the semi-dilute solution can be viewed as a very dense system of ideal chains formed by blobs of size λ with $R_{ee}^2 \sim \frac{N}{g}\lambda^2 \sim N\phi^{-1/4}$, where $\frac{N}{g}$ is the number of blobs per macromolecule. The previous picture of semi-diluted solutions was first derived by Daoud [104, 105] and is often called the *Scaling approach*. The usefulness of the results obtained with the Scaling approach has been verified by neutron scattering experiments. The scaling approach is not the only approach that exists to deal with polymer solutions.

2.6.1 Other theoretical approaches to polymer solutions: the virial expansion, the Flory-Huggins theory, and the des Cloizeaux Law

2.6.1.a The virial expansion

In a diluted solution, the interactions among monomers of different chains are scarce and the global properties can be roughly described through the virial coefficients of an equivalent gas of free monomers. The monomer-monomer and monomer-solvent interactions can be represented though an effective pair-potential $V(r)$. The virial expansion for the pressure of a monomer gas of N particles in a volume V is

$$p = \frac{Nk_B T}{V} \left(1 + \frac{N}{V} B + 2 \frac{N^2}{V^2} C + \dots \right)$$

The second virial coefficient B can be computed as

$$B = \frac{1}{2} \int_0^\infty \left(1 - e^{-\frac{V(r)}{k_B T}} \right) d^3 r \quad (2.21)$$

At temperatures $T \gg \theta$ -temperature, the contribution to the coefficient B of the attractive part of the potential $V(r)$ tends to zero, and B becomes almost constant with temperature: $B = \omega$. The constant ω is often called the *exclude volume of the particle*. Close to the θ -temperature the dependence of B with T can be written as,

$$B(T) = \begin{cases} \frac{\omega(T-\theta)}{\theta}, & \text{for } \frac{T-\theta}{\theta} \lesssim 1, \\ \omega, & \text{for } \frac{T-\theta}{\theta} \gtrsim 1. \end{cases} \quad (2.22)$$

In analogy with the Boyle point for a real gas, the second coefficient vanishes in the virial expansion of the osmotic pressure when T equals the θ -temperature. It is possible to show [106] that third and higher order virial coefficients for a polymer system have a negligible contribution at the θ -point. For this reason when the second virial coefficient becomes zero, the chain behaves as an ideal chain, and the law of van't Hoff is observed up to concentrations of several percent.

2.6.1.b The Flory-Huggins theory for polymer solutions

The former theory which dealt with molecular solutions and melts was developed by Flory and Huggins [93] in the 1940's. Since then, the theory has played a significant role in polymer science and many experimental results have been interpreted in the language of this theory. Flory-Huggins theory is based in a lattice

formalism and assumes a mean field picture in which $\langle c^2 \rangle \rightarrow \langle c \rangle^2$. The free energy F for this model is:

$$\frac{F}{T} = \frac{c}{N} \ln(c) + \frac{1}{2} \omega c^2 + \dots \quad (2.23)$$

where c is the monomer concentration, and ω is the excluded volume that follows

$$\omega = a^3(1 - 2\chi) \quad (2.24)$$

where a is the lattice size, and χ is the Flory-Huggins parameter. The χ parameter is related to the energy of contact polymer-solvent. If $\chi < 0.5$ the solvent is a good solvent, and if $\chi > 0.5$ the solvent is a bad solvent. At the θ -point $\chi = 0.5$. $\chi = 0$ corresponds to an athermal solvent in which $\omega = a^3$. The osmotic pressure predicted by the theory is,

$$a^3 \frac{\Pi}{T} = \frac{\phi}{N} + \ln \left(\frac{1}{1 - \phi} \right) - \phi - \chi \phi^2$$

Notice that for very diluted solutions ($\phi \rightarrow 0$) the ideal gas law $\Pi/T \sim \phi/N$ is recovered. If $\phi \rightarrow 1$ the pressure tends to diverge logarithmically. At intermediate concentrations Π can be expanded in powers of ϕ , being the square term the leading one $\Pi/T \sim \phi^2 + \dots$. This prediction does not agree completely with experimental results where it is observed $\Pi/T \sim \phi^{9/4}$.

2.6.1.c The des Cloizeaux law

Mean field theories are based on neglecting the fluctuations or monomer correlations. The difference between the mean field exponent 2 and the experimental exponent 9/4 in the power law behavior of the osmotic pressure is due to such correlations. The first fluctuation theory was developed by J. des Cloizeaux in 1975 for a semi-diluted solution in athermal solvents. The formalism of des Cloizeaux is based in the formal polymer-magnetic analogy, and predicts the following expression for the osmotic pressure:

$$\frac{\Pi}{T} = a^{-d} N^{-\nu d} \psi(\phi N^{\nu d - 1}) \quad (2.25)$$

where ψ is an universal function with the asymptotic form

$$\psi(x) \sim \begin{cases} x & \text{for } x \ll 1, \\ x^{\frac{\nu d}{\nu d - 1}}, & \text{for } x \gg 1. \end{cases} \quad (2.26)$$

The Eq. 2.25 is often called *the des Cloizeaux law*. Notice that in 3d $\nu d / (\nu d - 1) = 9/4$ consistent with the experimental findings in the semidilute regime. The des Cloizeaux law can be alternatively deduced using the scaling invariance principle without resort to the polymer-magnetic analogy [102, 106].

2.7 Polymers near surfaces. The adsorption process

Until now we have dealt with polymer chains in a free space in which no geometrical constraints are imposed, but polymers are often in contact with surfaces: the surfaces of the vessel that contain the polymer, the surfaces of particles also present in the solution, etc.

When a polymer is close to an impenetrable surface its conformational properties are strongly modified with respect to bulk polymers. A surface can exert an attractive, a neutral or a repulsive interaction onto a polymer close to the surface. When the monomer-surface interactions are repulsive, the polymer tends to be away from the surface. It is common to refer to such situation as a *negative adsorption* because the density of monomers close to the surface is smaller than in the bulk solution. A negative adsorption is also observed by the presence of a neutral but impenetrable surface. In this case, the surface exerts an effective repulsion on the polymer because of the smaller number of allowed chain conformations close to a surface that leads to a reduction of the chain entropy. This phenomenon is known as depletion (see also Section 1.2.2.a).

If the impenetrable surface has an attractive interaction with the monomers a competition between the depletion effect and the possibility of lowering the internal energy arises. It is a well known fact that long polymers can stick more easily onto surfaces than shorter chains even if the monomer-surface interaction is scarcely attractive since long chains can establish a large number of contacts with the surface. When a polymer becomes adsorbed, the gain in energy due to monomer-surface interactions is proportional to $Nk_B T$ whereas the entropic cost of having a chain close to a surface is only of order of $k_B T$.

Nonetheless, polymer adsorption is by far more complex than an on-off state where chains are either negatively adsorbed or fully adsorbed onto the surface. A chain can become only partially adsorbed with adsorbed segments called trains, whereas other segments remain unadsorbed forming the loops and tails (Figure 2.14).

The behavior of a polymer close to a surface is by no means trivial even in the cases in which the enthalpy gained with the monomer-surface interactions would be able to overcome completely the entropic contribution $-TS$. At very low polymer concentrations, a chain under the above conditions spreads over the surface leading to the so-called *pancake conformations* (Figure 2.15a). When the polymer concentration increases, chains must compete for space onto the surface, and the competition leads to the formation of self-organized structures such as *polymer brushes* (Figure 2.15b). A special case of adsorption is related to heteropolymers in which a specific segment of the chain (usually few monomers or

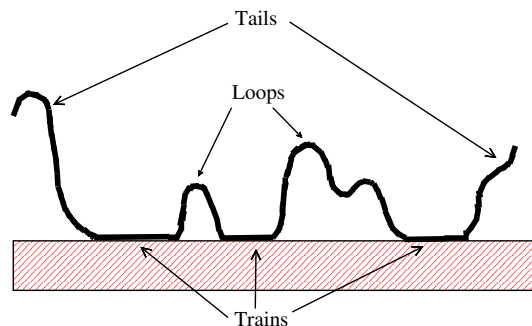


Figure 2.14. When chains are only partially adsorbed it is possible to distinguish loops, trains, and tails.

a chemical group at one end of the chain) has an extreme affinity for the surface whereas the remaining monomers in the polymer has no (or weak) affinity. In such cases it is said that the chain is *attached or grafted* to the surface. At very low solution concentrations, grafted chains tend to develop *mushroom conformations* (Figure 2.15c), whereas at high concentrations *brushes* are formed.

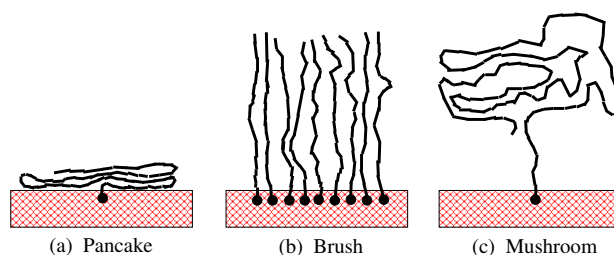


Figure 2.15. Different polymer conformations: pancake, brush, and mushroom.

An even more complex adsorption behavior is observed for polymers that attract each other (self-attracting polymers). These polymers can exhibit a collapse transition in both the desorbed (coil-globule transition) and in the adsorbed states. In turn, self-attractive polymers can also exhibit another state in which the polymeric globule gets attached onto the attractive surface without losing its globular state. This state is known as the surface-attached globular state.

The degree of flexibility of a polymer, and the range of the monomer-surface interactions add extra degrees of complexity to the adsorption problem. For long ranged monomer-surface interactions, an effective adsorption layer exists wherein polymers have a favorable interaction with the surface. If the width of the adsorption layer is large enough new phases are expected [107] depending on the degree of chain stiffness (Figure 2.16): Isotropic weak-adsorbed (IWA), Isotropic strong-

adsorbed (ISA), Nematic weak-adsorbed (NWA), and Nematic strong-adsorbed (NSA). The Nematic phases correspond to chains with a large degree of stiffness.

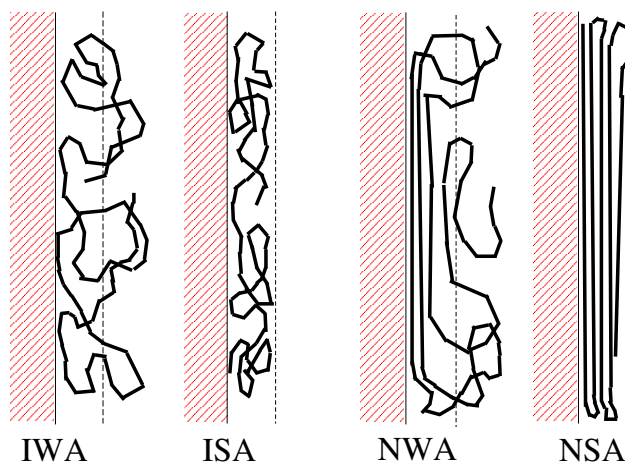


Figure 2.16. When the attractive monomer-surface forces are long-ranged, new possible adsorbed states arise: IWA (isotropic weak-adsorbed state), ISA (isotropic strong-adsorbed state), NWA (nematic weak-adsorbed state), NSA (nematic strong-adsorbed state).

The study of polymers close to a surface far from being a pure academic problem is a very important issue in several technological fields as well as in medical sciences. Applications where polymer adsorption is involved ranges from the classical uses in paints, inks, coatings, lubricants, ceramic processing and adhesives, to the more recent applications for artificial implants, protenomics, DNA separations and recognition chips. Another example of the importance of polymer adsorption is found in the adsorption of proteins onto the walls of devices used in contact with blood such as blood bags, catheters, artificial hearts, renal dialyzers, etc. When fibrinogen or globulin is adsorbed onto the surface of clinical devices becomes denatured. The denatured form activates clotting factors that initiate a cascade of events leading to the formation of a thrombus. Nature also uses polymer coatings in the human body, for instance, the red blood cells are covered by a layer of macromolecules (glykocalix) that regulate their interactions with the walls of blood vessels and with other cells present in the blood. Also in biology is known that polymers interacting with membranes are known to disrupt membranes and produce leaky walls. This is important in the outflow of drugs from vesicles [108] or the inflow of encapsulated DNA into cells [109].

Chapter 3

Numerical Simulations: Basic features of the Stochastic methods

The aim of this chapter is to summarize the common features of the numerical simulation methods used in our studies on polymers and colloids. The use of numerical simulations in science is not a recent issue: history shows that as early as 1777 Buffon [110] made use of random sampling to get an estimation of the number π . Also Lord Kelvin [111] appears to have used stochastic methods to evaluate some difficult integrals as soon as 1901. But it was not before the advent of powerful digital computers that numerical simulations became of common and widespread use in science. Numerical simulations are useful in science for several reasons: they allow to bypass some difficulties inherent to experiments as, for instance, the effects of gravity. Simulations can also measure quantities or behaviors difficult or even impossible to measure with current experimental techniques as, for instance, the measure of forces between two isolated nanoscopic particles without modifying their properties. Furthermore, numerical simulations can provide a first guide to the study of complex systems in laboratory, saving money and time. When compared with theoretical works, numerical simulations can handle usually with less restrictive constraints and can be used to check under which conditions a proposed theory will be valid. Therefore, simulations should be regarded in its own way as a complementary tool to the experimental and theoretical studies.

Although one could be tempted to include all the known chemical and physical details in the numerical models for polymers or colloidal particles, unfortunately the power of calculus of present computers is still rather limited. Usually,

simulations deal with a simplified model of the system in which only the main features are included. A rule of thumb is to include in a numerical model the minimum set of interactions needed in order to describe correctly the properties we want to measure with the level of accuracy required.

By fortune, many generic properties of colloids and polymers can be studied adequately applying statistical methods in which the precise chemical and physical details of the particles can be omitted. Consider a Hamiltonian model H in which the states of the system are denoted by $\vec{x} = (x_1, \dots, x_n)$ where n is the number of degrees of freedom, and the phase space is denoted by Ω . Assume that the states are distributed accordingly to an arbitrary probability distribution function $f(H(\vec{x}))$. Then the mean value of a quantity A is given by what we call the ensemble average,

$$\langle A \rangle = \frac{\int_{\Omega} A(\vec{x}) f(H(\vec{x})) d\vec{x}}{\int_{\Omega} f(H(\vec{x})) d\vec{x}} \quad (3.1)$$

The full enumeration of all possible configurations of the system is not generally possible with present computers because the number of configurations is overwhelming. If we assume that a polymer is modeled as a random walk of $N = 100$ steps in a simple cubic lattice, then the number of possible states is about 10^{78} . If the polymer is modeled as a Self-avoiding random walk, then the number of states is still of the order of 10^{50} . Therefore, even in the simplest models the number of states is far from the capacities of present computers which scarcely can generate of the order of 10^9 conformations per hour in the best cases. Nonetheless, there exist enumeration studies [112] in which the ensemble averages are exactly computed. Present computer power limits the studies to lattice models of polymer chains with $N \lesssim 20$.

A way to overcome the impossibility of computing exact ensemble averages is the estimation of the value of our quantity $\langle A \rangle$ through the evaluation of A along a representative path in the phase space Ω . In fact, laboratory experiments also perform an average over a path in the phase space which involves a very tiny portion of all the states of the phase space. As an example, a rough estimation [113] of the number of states associated to a mol of gas inside a litter bottle at room temperature leads to the formidable number of $(10^{27})^{10^{22}}$ statistical states available to the gas. Lab instruments are estimated to sample about 10^{31} states per second, so we must practically wait an infinity of time in order to perform the whole ensemble average of our litter of gas.

Even if we accept the validity of this approach, a main problem arises: how can we generate numerically paths in the phase space which are statistically representative? The answer is that there are a few methods available for classical

particle-based simulations. Some of these techniques are purely deterministic, others purely stochastic, the remaining techniques can be considered as hybrids. A rough classification of the main groups of techniques available to perform classical numerical simulations of particles could be:

- **Molecular Dynamics (MD).** Newton's equations of motion are solved $m\ddot{x} = -\nabla U$. Depending on the constraints we add to the system we can distinguish between: Micro canonical ensemble MD in which energy is a conserved parameter, Canonical ensemble MD with a constant temperature instead of constant energy, and the Isothermal-Isobaric ensemble MD in which both temperature and pressure are held constant. In all the MD variants, we use the intrinsic dynamics of the model to propagate the system in the phase space.
- **Stochastic dynamics (SD).** Some degrees of freedom are represented only by their stochastic influence on the degrees of freedom that are treated explicitly through MD. For instance the effects of the solvent molecules in a colloidal solution can be mimicked by introducing a frictional force plus a stochastic force into the equations of motion of the solute. As in MD, we use the dynamics to propagate the system in the phase space. In this case, the equations of motion of the particles are a set of Langevin equations. Brownian Dynamics (BD) is a particular case of SD, in fact, it's the most simple case of Stochastic dynamics in which the stochastic force contains no correlations in space or time.
- **Monte Carlo methods (MC).** Although there are many different MC methods, all of them have in common the use of a random sequence of numbers to construct a set of states of the phase space. In most of cases, a straightforward sampling of the phase space leads to very poor results. Most suitable techniques perform an importance sampling, that is, the methods are biased in order to select states that give the dominant contributions to the average. As in the MD case, MC algorithms have been designed to work under many formalisms: micro canonical, canonical, Isothermal-Isobaric, grand canonical, biased Monte Carlo, etc.

A review in detail of all the above techniques and variants exceeds by far the scope of the present chapter. In what follows we are going to summarize the main topics related to the techniques used in our studies, namely: Monte Carlo in the canonical ensemble and Brownian dynamics. Additional information on these methods and their variants can be found in the following books: Newman [113], Allen-Tildesley [114], Heermann [115], and Kalos-Whitlock [116].

3.1 Monte Carlo simulations in the canonical ensemble

In the micro canonical ensemble all the sampled states have the same energy and therefore all them must be sampled with an equal weight. However, in the canonical ensemble we perform the simulation at constant temperature and no restriction exists for the energy of the states. Therefore, in an ensemble average the canonical states do not have equal weights; some states are expected to be visited by the system more frequently than others. The objective is to generate a path in the phase space such that the system visits the different states with the correct probability. In the Monte Carlo method a succession of states is generated through a Markovian process. This Markovian chain of states of the system is designed in such way that when it is run for many steps, it will eventually produce a succession of states which appear with a probability given by the probability distribution function $f(H(\vec{x}))$. The asymptotic regime of the Markov process is independent of the initial state chosen to start the chain. Once the Markov process generates states with probability $f(H(\vec{x}))$, the simulation is said to have reached the "system equilibrium". Before the Markovian chain reaches the "equilibrium", statistical averages must not be performed because system states are sampled with an unknown probability distribution which is surely different from $f(H(\vec{x}))$.

Several conditions must be satisfied in order to ensure the correct asymptotic behavior of the Markovian chain. First of all, the process should satisfy the conditions associated to whatever Markovian process: if we denote $T(A \rightarrow B)$ the transition probability from a given state A to a state B , then $T(A \rightarrow B)$ should not vary over time and should only depend on the properties of the states A and B . In addition, the Markovian process should obey the conditions of "ergodicity" and "detailed balance"¹.

The condition of ergodicity refers to the possibility for the Markov process to reach any state of the system from any other state in a finite sequence of steps. The detailed balance ensures that the rate at which the system makes a transition from A to B is the same than from B to A ,

$$f(A) T(A \rightarrow B) = f(B) T(B \rightarrow A) \quad (3.2)$$

¹In some cases the detailed-balance may be replaced by a less restrictive condition known as the "semi-detailed" balance condition. The semi-detailed balance condition implies that the rate of movements to a given state A , coming from any other state, should be equal to the rate of movements out of A into other states. If one requires only the semi-detailed condition to be satisfied, one must be aware of the fact that the "semi-detailed" condition can lead the Markov chain to an asymptotic limit cycle in which our desired distribution is only one of the many distributions we found to be sampled during the limit cycle. In our simulations we have chosen the detailed-balance condition to be satisfied.

where $f(A)$ and $f(B)$ are the probabilities of the system being in A and B respectively.

In summary, *whatever* Markov process obeying the above rules leads asymptotically to sample the phase space with the desired distribution function f independently of the initial state of the system. It is worthwhile to remark that no other conditions are needed for the Markovian chain to sample states from the distribution f . A consequence of the above statement is that the type of movements we propose to pass from one state to another are not required to mimic any physical motion of the elements of the system. In many cases, the use of unphysical movements to commute among states can be used advantageously to speed up the process of convergence of a Markov chain.

3.1.1 The Metropolis algorithm: general scheme

The first scheme intended to find a suitable Markov process in order to generate a representative path of states was suggested by Metropolis et al [117]. They assumed that the transition probabilities $T(A \rightarrow B)$ can be rewritten as,

$$T(A \rightarrow B) = a(A \rightarrow B) d(A \rightarrow B) \quad (3.3)$$

where $d(A \rightarrow B)$ is the probability of proposing a transition to the state B when we are in the state A , whereas $a(A \rightarrow B)$ is the probability of accepting the proposed transition $A \rightarrow B$. The detailed balance condition requires that

$$a(A \rightarrow B) d(A \rightarrow B) f(A) = a(B \rightarrow A) d(B \rightarrow A) f(B) \quad (3.4)$$

The above equation has many solutions, an example is the so called asymmetrical (or Metropolis) solution,

$$a(A \rightarrow B) = \min(1, z) \quad (3.5)$$

where z is defined as,

$$z = \frac{d(B \rightarrow A) f(B)}{d(A \rightarrow B) f(A)} \quad (3.6)$$

Another solution that satisfies the condition of detailed balance is the symmetrical or Baker solution [118–120],

$$a(A \rightarrow B) = \frac{z}{1+z} \quad (3.7)$$

Both asymmetric and symmetric solutions can be used in the Metropolis Scheme, but it has been found that the asymmetric solution given by Eq. 3.5 gives a

Markov process with a more rapid convergence to the desired distribution function f in some cases [121]. In our Monte Carlo simulations, the asymmetric solution Eq. 3.5 has been the implemented one.

If the n -step of the Markovian sequence of states X_n is known, then a general algorithm to implement the Metropolis Scheme in a Monte Carlo simulation is:

- (a) Propose a possible state X_{n+1}^* as the next step in the Markovian chain. The state X_{n+1}^* is proposed accordingly to the probability function $d(X_n \rightarrow X_{n+1}^*)$.
- (b) Accept the proposed state X_{n+1}^* with a probability $a(X_n \rightarrow X_{n+1}^*)$ given by equation 3.5. The use of the asymmetrical solution implies that: if

$$\frac{d(X_{n+1}^* \rightarrow X_n) f(X_{n+1}^*)}{d(X_n \rightarrow X_{n+1}^*) f(X_n)} > 1$$

we always accept X_{n+1}^* as the new step X_{n+1} in the Markovian chain. Otherwise, we accept the proposal only if

$$\frac{d(X_{n+1}^* \rightarrow X_n) f(X_{n+1}^*)}{d(X_n \rightarrow X_{n+1}^*) f(X_n)} > \xi$$

where ξ is a random uniform number between 0 and 1. If X_{n+1}^* is not accepted accordingly to the above criteria, we set the next step X_{n+1} to be the previous state X_n .

In the next chapters we will refer to the previous algorithm with its common name: *The Metropolis Algorithm*. Up to now the forms of the density probability function f , and the proposal function d remain unspecified. These functions must be set up accordingly to the particular system we want to emulate.

3.1.2 The Metropolis algorithm applied to the canonical collectivity

In the Canonical equilibrium ensemble, we are interested on sampling the states of the phase space accordingly to the Boltzmann probability function,

$$P(X) = \frac{e^{-\beta H(X)}}{Z}$$

where Z is the partition function,

$$Z = \int_{\Omega} e^{-\beta H(X)} dX$$

Therefore we must set $f(X) = P(X)$ in our Metropolis algorithm, and the acceptance probability is

$$a(A \rightarrow B) = \min \left(1, \frac{d(B \rightarrow A)}{d(A \rightarrow B)} e^{-\beta(H(B)-H(A))} \right)$$

It is remarkable that we do not need to know the value of the partition function in order to compute the acceptance probability.

Now, the proposal function $d(A \rightarrow B)$ is the only issue that remains to be specified. In fact, we have a complete freedom for selecting d , provided that ergodicity is satisfied. The most simple and easy option is to use proposal schemes of new states such that the condition $d(A \rightarrow B) = d(B \rightarrow A)$ is guaranteed. Here, we should point out that this may not be the most efficient way to proceed in systems where the acceptance probabilities are very low ². Nonetheless, in the Monte Carlo simulations we have performed for polymer chains, the proposal schemes always satisfy $d(A \rightarrow B) = d(B \rightarrow A)$. Therefore the acceptance probability can be written in our case as

$$a(A \rightarrow B) = \min \left(1, e^{-\beta(H(B)-H(A))} \right)$$

As a consequence of using this acceptance probability, all the states B such that have a minor energy than A will be automatically accepted, whereas all the states B in which the energy is larger than in the state A are subject to a possible rejection. The probability of rejection increases with the energy difference $H(B) - H(A)$ between both states. Thus, our proposal scheme is expected to have acceptance ratios very low for proposals in which $H(B) - H(A)$ is very large. In contrast, large acceptance ratios are expected for proposals in which the difference $H(B) - H(A)$ is minimum. This preference of the Monte Carlo algorithm to better accept states with energies closer to the previous states implies that Metropolis algorithm is expected to generate sequences of states that are strongly correlated.

A sequence of correlated states is not the only problem we must face up on dealing with Monte Carlo simulations. Another drawback of the Monte Carlo methods is that the sequence of states we are generating is only guaranteed to sample the desired Boltzmann distribution in the asymptotic regime. Thus before starting to average any physical quantity, we must ensure that the system has reached "the equilibrium". The number of steps required to arrive at this

²Several proposal schemes in which $d(A \rightarrow B) \neq d(B \rightarrow A)$ has been proposed for some special applications [114] such as high density systems, or systems where directional interactions exist like in proteins and hydrogen-bonded liquids.

asymptotic limit depends on the features of the system as well as on the proposal scheme we use. A common practice to check if the Markovian chain has arrived to the asymptotic regime consists on tracing the evolution of a physical magnitude known to be constant in the equilibrium. As an example, in Figure 3.1, we observe the evolution of the energy of a semiflexible AB-alternating copolymer chain that adsorbs onto a homogeneous surface with the number of Monte Carlo Steps (MCS). In this case, one MCS is equal to the number of monomers of the chain, N . After approximately 15000 MCM's, the energy of the chain reaches a plateau, we can consider that after that point the system is in equilibrium and subsequent steps are suitable to be included in statistical averages. The number of steps needed to reach the equilibrium state is often called the "thermalization period" or the "equilibration period".

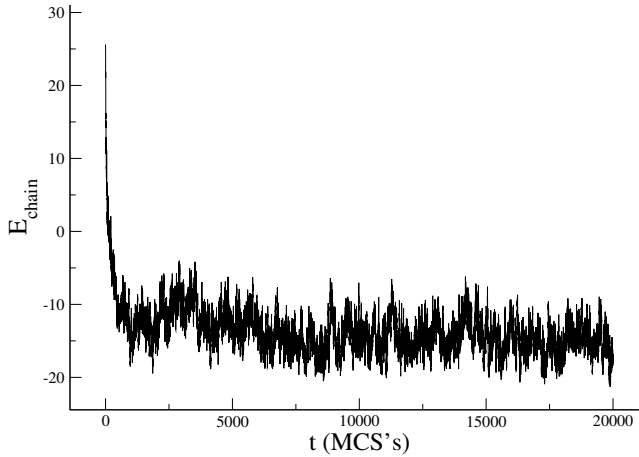


Figure 3.1. Evolution of the energy of a semiflexible AB-alternating copolymer chain with the number of Monte Carlo Steps (MCS's). Chain length $N = 50$, stiffness constant $\kappa = 1.0$, and monomer-surface energy interactions $\epsilon_A = -1k_B T$, and $\epsilon_B = 0$. Temperature is set to $1/T = 3$ in $k_B T$ units. For more details about the meaning of this parameters see Chapter 9.

3.1.3 Statistics from a sequence of correlated states

In the previous section we have seen that after the thermalization or equilibration period the subsequent states produced by the canonical Monte Carlo algorithm are adequate in order to perform physical averages at a constant temperature. Unfortunately, we must accept that the states we obtain have a certain degree of correlation among them. The degree of correlation is as larger as closer are the states in the Markov sequence. In order to minimize the effects that such correlations have on the statistical averages, some extra caution is needed.

Given a set of successive states $X_0, X_1, X_2, \dots, X_n$ generated by a Monte Carlo algorithm, an estimation of the degree of correlation among them can be

obtained by computing the correlation function of a certain magnitude $G(X_i)$,

$$C(\alpha) = (G(X_\alpha) - \langle G \rangle)(G(X_0) - \langle G \rangle)$$

where $\langle G \rangle$ is the averaged value of G along the sequence. Generally $C(\alpha)$ has very long decaying tails. A common practice is to assume the correlation function to be an exponentially decaying function,

$$C(\alpha) \sim e^{-\alpha/\tau}$$

where τ is called the *correlation time*. The Figure 3.2 shows a typical example of the correlation function for a semiflexible AB-alternating copolymer chain that adsorbs onto a homogeneous surface. The magnitude used in order to compute the correlation function C is the energy of the chain. Figure 3.2 shows that the correlation function roughly decays as an exponential function, in which $\tau \sim 3.3$ MCS's.

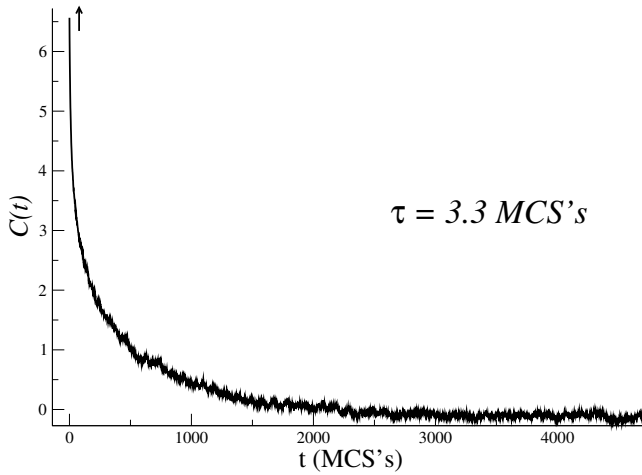


Figure 3.2. Correlation function for a semiflexible AB-alternating copolymer chain. Parameters are the same than in Figure 3.1. The magnitude used in order to compute $C(t)$ is the energy of the chain, where t is measured in units of Monte Carlo Steps.

The long decaying tails of the correlation function tells us that we must wait a large amount of steps if we want two states to be perfectly uncorrelated. Usually, waiting for so long is impractical so the usual procedure is pick another state of the sequence after Δt steps. The optimal value of Δt can be estimated as follows. Once $\langle G \rangle$ is obtained by averaging k -states separated each Δt steps in the Markov chain, it can be demonstrated [122] that the typical deviation of the mean $(\sigma(\langle G \rangle))^2$ (do not confuse with $(\sigma(G))^2$) is

$$(\sigma(\langle G \rangle))_{\text{correlated}}^2 = \frac{1 + 2\tau/\Delta t}{k - 1} (\langle G^2 \rangle - \langle G \rangle^2)$$

It is a common practice in the Monte Carlo techniques to set $\Delta t \sim \tau$ in order to avoid a waste of time in generating idle states, but, at the same time, obtain a value of $(\sigma(\langle G \rangle))^2$ close to that we would obtain for uncorrelated data,

$$(\sigma(\langle G \rangle))_{uncorrelated}^2 = \frac{1}{k-1}(\langle G^2 \rangle - \langle G \rangle^2)$$

This is the criteria we have applied to our Monte Carlo simulations. In an initial simulation we estimate the value of τ which is subsequently used as Δt in the remaining simulations of the system.

3.1.4 Monte Carlo simulations of polymer chains: basic features

We have applied the Canonical Monte Carlo method to mimic the behavior of several systems in which polymer chains are the main element. Here we enumerate the basic features these models have in common. Interactions or additional constraints which are specific to each particular case will be considered in the respective chapters.

3.1.4.a The polymer model

We model polymer chains with exclude volume interactions (see Chapter 2) through the *pearl-necklace model* [123]. Each polymer chain is formed by a sequence of N beads (monomers) of diameter σ . Each bead (monomer) usually represents a set of "chemical monomers". We model the exclude volume interactions among beads through a hard-core potential

$$U_{steric} = \sum_{i,j=1}^N V(r_{ij}), \quad (3.8)$$

where $r_{ij} = |\vec{r}_i - \vec{r}_j|$, and $V(r_{ij})$ is

$$V(r_{ij}) = \begin{cases} 0, & \text{for } r_{ij} > \sigma, \\ \infty, & \text{for } r_{ij} < \sigma. \end{cases} \quad (3.9)$$

3.1.4.b The proposal scheme for polymer chains

The initial state (conformation) of a polymer chain is generated randomly, but preserving the exclude volume constraints. The generated state is introduced into the Monte Carlo algorithm as the first step of the Markovian chain. In the following steps, the proposed conformations are generated from the last accepted

conformation in order to avoid extremely high rejection rates. The particular proposal scheme we have used considers several types of chain movement (see Figure 3.3): the *Kink-Jump* movement involves an arbitrary rotation between 0 and 2π of a monomer along the axis connecting the previous and following monomer in the chain. Obviously this type of movement is not well defined for the two-end monomers. Chain ends just perform random *wiggling motions*: a free rotation of the end-monomer around the previous monomer in the chain.

A monomer rotation of angle θ around an axis given by the unitary vector \vec{u} can be expressed mathematically as,

$$\vec{r}_{new} = \vec{r}_{old} \cos(\theta) + (1 - \cos(\theta)) (\vec{u} \cdot \vec{r}_{old})\vec{u} - \sin(\theta)(\vec{u} \times \vec{r}_{old}) \quad (3.10)$$

where \vec{r}_{new} and \vec{r}_{old} are the position vectors of the monomer that rotates referred to the proposed and the previous monomer position.

When performing chain end wiggling motions, special care must be taken in order to generate true isotropic rotations about the end monomer. A common error is to generate random angles θ (between 0 and π) and ϕ (between 0 and 2π) and substitute them directly into the expressions that translate spherical coordinates into Cartesian ones. The random distribution obtained in that way is non isotropic. Direction cosines can be used to ensure a true isotropic spherical random distribution for the new position of the n -monomer around the position of the previous $(n - 1)$ -monomer [116].

Another type of movement implemented in our simulations for polymer chains is the *reptation* motion. Reptation implies a global movement of the chain which seems to reptate like a snake. Reptation movements can be very useful in order to help the chain to go out faster from pathological conformations like knots. If a reptation movement is proposed (see Figure 3.4) we select randomly one of the two end-monomers of the chain and we try to locate it in a nearest neighbor position of the other chain end preserving the distance between monomers. Once the motion is accepted all monomers are reenumerated accordingly.

3.1.4.c *The link-cell method*

In order to reduce the computer time spent in checking the interactions among particles, a link-cell method [114] has been implemented. Basically, we divide the space into control cells and keep an updated list of the particles inside each cell. The optimal choice for the size of the control cells in our systems is found to be 2.5σ when only exclude volume interactions among monomers are present. When other interactions are taken into account, we set the size of the control boxes to be equal or larger than twice the largest cut off distance of the interactions. In

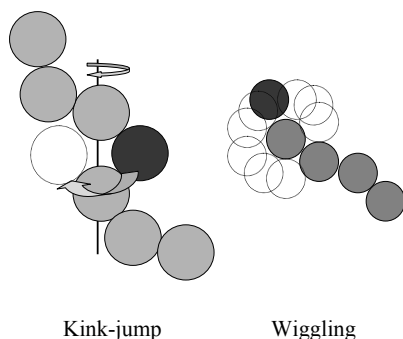


Figure 3.3. Schematic representations of two basic movements for polymer chains: (a) the kink-jump movement for inner monomers, (b) the wiggling motion of a chain end.

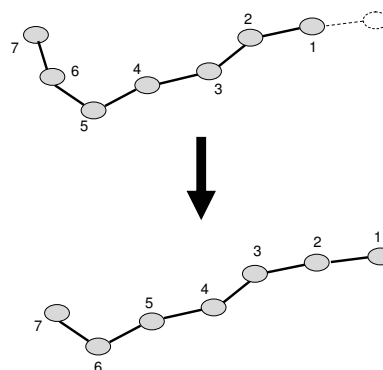


Figure 3.4. Schematic representation of the reptation movement.

this way, instead of checking all pairs of particles, we check only the 26 cubic cells that surround the control cell containing the particle we try to move.

3.1.4.d *The boundary conditions*

We use Periodic Boundary Conditions [114] (PBC) in those systems in which chains can move beyond the limits of the volume controlled by the link-cell method (box system). The use of virtual walls at the borders of the control volume must be avoided because surfaces bias polymer conformations. In the PBC formalism, the space is filled with an imaginary lattice of replicas of the original box system (see Figure 3.5), in all the boxes the molecules mimic the movements that take place in the original box system. When a monomer leaves the original box another monomer from a virtual box enters the original box through the opposite side and takes the role of the former monomer in the system. In order to avoid a polymer chain to interact artificially with itself through PBC and to minimize finite size effects (see Figure 3.6), the length of the box system must be at least twice larger than the full length of the polymer chain.

3.2 Brownian dynamics

Molecular and Stochastic dynamics use the intrinsic dynamics of the model to obtain a sequence of representative states of the phase-space from which averages

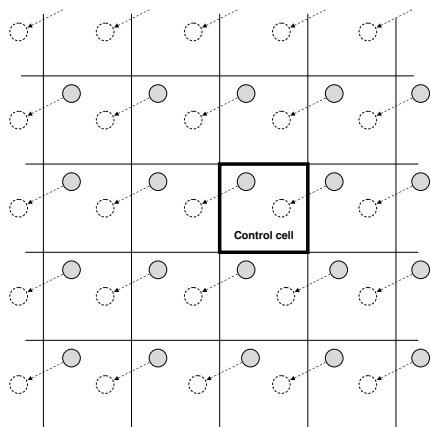


Figure 3.5. When Periodic Boundary Conditions are enforced, a monomer that leaves the control cell is replaced by an equivalent particle entering from a virtual cell.

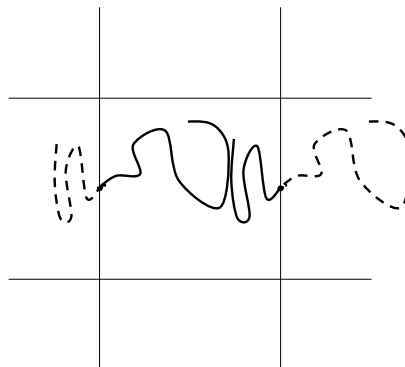


Figure 3.6. When the box length is too small, a chain can interact with itself in an unphysical way.

of physical quantities at the equilibrium can be obtained. In addition, Molecular Dynamics and Stochastic Dynamics give us a natural way to study the relaxation of a system (the dynamics) from an initial state to the equilibrium, as well as the properties of intrinsically non-equilibrium processes³.

In some systems like colloidal suspensions, we observe that some modes of motion in the system are much faster than others. If we use Molecular dynamics to model colloidal suspensions, the presence of these fast motions associated to the solvent molecules would imply the use of very short time-steps and, consequently, long time simulations. In fact, the fast dynamics of the solvent particles is not the interesting part of the problem. To cap it all, the number of solvent particles in a colloidal suspension is usually far larger than the number of colloidal particles. Therefore, the use of direct Molecular Dynamics simulations to mimic colloidal systems is not the optimal way to proceed.

An approach to the true problem may be adopted by representing the elements of the system that are not of fundamental interest through a combination of random forces and frictional terms rather than put them explicitly in the model. Newton's equations of motion are thus replaced by Langevin type equations. This technique is known as *Stochastic Dynamics* (SD).

³Monte Carlo methods can also be used to check behaviors out of equilibrium, although it is usually harder to do because in non-equilibrium studies we cannot choose the type of dynamics to pass from one state to the other.

The *Brownian Dynamics* is the most simple case of SD in which no correlations in time or space are associated with the stochastic force. The equations of motion for a system of N colloidal particles can be approximated by the following set of stochastic differential equations ($i=1,\dots,3N$),

$$m_i \frac{dv_i(t)}{dt} = -m_i \gamma_i v_i(t) + F_i(r_1(t), \dots, r_{3N}(t)) + R_i(t) \quad (3.11)$$

where γ_i are the friction coefficients. In our calculations we will suppose all the friction coefficients to be equal $\gamma_i = \gamma$. These equations are similar to ordinary Langevin equations (see Section 1.1). We require the random force $\vec{R}_i(t)$ to disappear on average,

$$\langle R_i(t) \rangle = 0$$

We assume that colloidal particles follow a Brownian motion when the deterministic forces F_i are zero. The Brownian motion can be enforced by assuming the stochastic forces to be stationary and Gaussian, i.e. their probability distribution is

$$W(R_i) = \frac{1}{\sqrt{2\pi \langle R_i^2 \rangle}} \exp\left(\frac{-R_i^2}{2 \langle R_i^2 \rangle}\right)$$

Furthermore, we must require that the random forces satisfy the fluctuation-dissipation relation,

$$\langle R_i(t) R_j(t') \rangle = 2m_i \gamma_i k_B T \delta_{ij} \delta(t - t')$$

and that stochastic forces are not correlated with systematic forces or prior velocities:

$$\langle R_i(t) v_j(0) \rangle = 0$$

$$\langle R_i(t) F_j(0) \rangle = 0$$

In our simulations, the interactions among colloidal particles have a twofold contribution: a two-body depletion potential based on the Asakura-Oosawa (U_{AO}) (see Section 1.2.2.a) plus a repulsive steric interaction (U_{sc}) given by the following expressions,

$$\frac{U_{AO}(r_{ij})}{k_B T} = \begin{cases} \frac{3\phi_P}{2\zeta^3} \left((1 + \zeta)^2 r_{ij} - \frac{1}{3} r_{ij}^3 - \frac{2(1+\zeta)^3}{3} \right), & \text{for } r_{ij} < (1 + \zeta) \\ 0, & \text{for } r_{ij} > (1 + \zeta) \end{cases} \quad (3.12)$$

ϕ_p	$ U_m /k_B T$
0.1768	2.000
0.2110	3.000
0.2262	3.125
0.2266	3.135
0.2314	3.250
0.2410	3.500
0.2610	4.000
0.2800	4.500
0.2980	5.000
0.3330	6.000
0.3670	7.000

Table 3.1. Relation between non-adsorbing polymer volume fraction, ϕ_p and the absolute value $|U_m|$ of the minimum interacting potential U when $\zeta = 0.1$.

and

$$\frac{U_{sc}(r_{ij})}{k_B T} = r_{ij}^{-n}. \quad (3.13)$$

In Eq. 3.12, ζ is the size-ratio between a polymer chain and a colloidal particle. In our simulations we set $\zeta = 0.1$ as in previous works [124], so the interactions are short ranged with a cut off at $r_{ij} = 1.1$ in units of σ_c . ϕ_P is the reservoir polymer packaging fraction which controls the strength of the depletion interactions in the Asakura-Oosawa model. In the hard-core repulsive interaction given by Eq. 3.13, we have set $n = 36$. Exponents $n < 36$ are reported [125] to lead to anomalies when a hard-core mimic is required in the potential. The total pair-potential $U = U_{AO} + U_{sc}$ passes through a minimum value (U_m) which is related to ϕ_P , (see Table 3.1).

In what follows, we will characterize the strength of the potential in terms of the absolute value of the minimum potential depth, $|U_m|$, instead of ϕ_p . Unless another thing is specified, the friction coefficient of a single colloidal particle is set to $\gamma = 0.5$, and the time step is $\Delta t = 0.005$ in reduced time units of $\sigma(m/U_m)^{1/2}$ with $m = 1$. Figure 3.7 shows tree examples of potentials used in our simulations.

3.2.1 Algorithms for Brownian Dynamics simulations

Several algorithms have been used to solve the set of differential stochastic equations 3.11. A first family of algorithms are those [126, 127] that consider the stochastic force $R_i(t)$ as a constant during each time step Δt . These algorithms

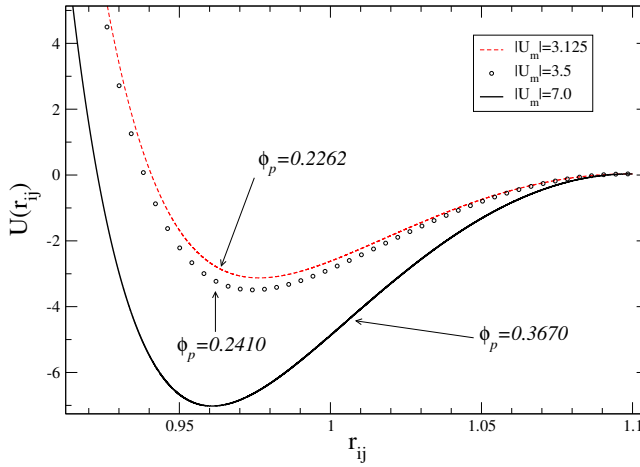


Figure 3.7. Three different examples of typical potentials used in our Brownian dynamics simulations ($k_B T = 1$).

are limited by the condition $\Delta t \ll \gamma^{-1}$ in order to ensure that the correlation time of the stochastic force is much smaller than the velocity relaxation time γ^{-1} . Another family of algorithms [128–130] use in each time step an expansion of the stochastic force in powers of $\gamma \Delta t$. In these algorithms the value of Δt is not limited by γ but it is limited by the rate of change of the deterministic force F_i . Both families of algorithms deal with F_i up to second order in Δt . In order to integrate F_i to higher order, several Runge-Kutta methods [128, 131, 132] have been proposed, but, unfortunately, they are not suitable for large systems due to the large amount of force evaluations required per step. In addition all these Runge-Kutta methods are also to some extent constrained by the condition $\Delta t \ll \gamma^{-1}$, because they improve the treatment of the deterministic part of the force but not the stochastic contribution.

Due to the problems associated to the previous algorithms, we have chosen a different algorithm known as the *Gunsteren-Berendsen* algorithm [133]. It is a third order algorithm in Δt for the deterministic force F_i , and it is not limited by the condition $\Delta t \ll \gamma^{-1}$. In the limit of $\gamma \rightarrow 0$ the famous classical Verlet algorithm is recovered [134]. The use of the Gunsteren-Berendsen algorithm allows us to increase the value of Δt up to 0.005 in reduced units of $\sigma(m/U_m)^{1/2}$ with mass $m = 1$. Large values of Δt allow us to deal with larger systems, and check larger periods of the colloidal dynamics.

3.2.1.a The Gunsteren-Berendsen algorithm for Brownian Dynamics

Eqs. 3.11 are a set of inhomogeneous first order differential equations. A formal solution at time t can be easily obtained if we know the solution for a previous

time t_n ,

$$v_i(t) = v_i(t_n)e^{-\gamma(t-t_n)} + e^{-\gamma(t-t_n)} \int_{t_n}^t e^{+\gamma(t'-t_n)} (F_i(t') + R_i(t')) m^{-1} dt' \quad (3.14)$$

The integral over the deterministic force is obtained by expanding $F_i(t)$ in a power series up to second order,

$$F_i(t) = F_i(t_n) + \frac{dF_i(t_n)}{dt} (t - t_n) + O((t - t_n)^2) \quad (3.15)$$

After performing the integration we arrive at,

$$\begin{aligned} v_i(t) &= v_i(t_n)e^{-\gamma(t-t_n)} + (m\gamma)^{-1} F_i(t_n)(1 - e^{-\gamma(t-t_n)}) \\ &+ (m\gamma^2)^{-1} \frac{dF_i(t_n)}{dt} (\gamma(t - t_n) - (1 - e^{-\gamma(t-t_n)})) \\ &+ m^{-1} e^{-\gamma(t-t_n)} \int_{t_n}^t e^{\gamma(t'-t_n)} R_i(t') dt' \\ &+ O((t - t_n)^3) \end{aligned} \quad (3.16)$$

If we define $\Delta t = t_{n+1} - t_n$, and apply that

$$x_i(t_n + \Delta t) = x_i(t_n) + \int_{t_n}^{t_n + \Delta t} v_i(t) dt \quad (3.17)$$

it is possible to get an expression from which by eliminating $v(t_n)$ and replacing Δt by $-\Delta t$ we obtain the formula we use in the algorithm,

$$\begin{aligned} x_i(t_n + \Delta t) &= x_i(t_n)(1 + e^{-\gamma\Delta t}) - x_i(t_n - \Delta t)e^{-\gamma\Delta t} \\ &+ m^{-1} F_i(t_n)(\Delta t)^2 (\gamma\Delta t)^{-1} (1 - e^{-\gamma\Delta t}) \\ &+ m^{-1} \frac{dF_i(t_n)}{dt} (\Delta t)^3 (\gamma\Delta t)^{-2} [1/2\gamma\Delta t(1 + e^{-\gamma\Delta t}) \\ &- (1 - e^{-\gamma\Delta t})] + X_n^{(i)}(\Delta t) + e^{-\gamma\Delta t} X_n^{(i)}(-\Delta t) \\ &+ O((\Delta t)^4) \end{aligned} \quad (3.18)$$

where $X_n^{(i)}(\Delta t)$ is a random variable defined as,

$$X_n^{(i)}(\Delta t) = (m\gamma)^{-1} \int_{t_n}^{t_n+\Delta t} (1 - e^{-\gamma(t_n+\Delta t-t)}) R_i(t) dt \quad (3.19)$$

It can be demonstrated [135] that $X_n^{(i)}(\Delta t)$ is also stationary and Gaussian with mean zero because it is the result of integrating a random variable with these properties.

One could be tempted to try to simplify the previous formulas by operating the stochastic integrals like in equation 3.19. However, we must remember that stochastic integrals, like Eq. 3.19, are integrals over functions with infinite essential discontinuities, and one must be aware that usual rules for integral calculus do not apply under such conditions. For instance, it would be a mistake to split integral 3.19 in two terms as it would be usual in integral calculus. It is also an error the assumption that $\langle R(t) \rangle = 0$ implies $X_n = 0$ if we try, naively, to compute the integral 3.19 numerically using a $dt \rightarrow 0$ inside an interval of time.

Another remark to be done before applying Eq 3.19 into the Brownian Dynamics algorithm is that the two stochastic random variables $X_n(\Delta t)$ and $X_n(-\Delta t)$ that appear in equation 3.18 are, in fact, correlated. The stochastic values $X_{n-1}(\Delta t)$ and $X_n(-\Delta t)$ obey a bivariate Gaussian distribution [135],

$$\begin{aligned} W(X_{n-1}(\Delta t), X_n(-\Delta t)) &= (4\pi^2 \sigma_1^2 \sigma_2^2 (1 - r^2))^{-1/2} \\ \exp[-(\sigma_2^2 X_{n-1}^2(\Delta t) - 2\sigma_1 \sigma_2 r X_{n-1}(\Delta t) X_n(-\Delta t) \\ + \sigma_1^2 X_n^2(-\Delta t)) / (2\sigma_1^2 \sigma_2^2 (1 - r^2))] & \end{aligned} \quad (3.20)$$

where

$$\begin{aligned} \sigma_1^2 &= \langle X_{n-1}^2(\Delta t) \rangle = \frac{kT}{m\gamma^2} C(\gamma\Delta t) \\ \sigma_2^2 &= \langle X_n^2(-\Delta t) \rangle = -\frac{kT}{m\gamma^2} C(-\gamma\Delta t) \\ r\sigma_1\sigma_2 &= \langle X_{n-1}(\Delta t) X_n(-\Delta t) \rangle = \frac{kT}{m\gamma^2} G(\gamma\Delta t) \\ C(x) &= 2x - 3 + 4e^{-x} - e^{-2x} \\ G(x) &= e^x - 2x - e^{-x} \end{aligned} \quad (3.21)$$

From Eq. 3.18 it is easy to check that in the limit $\gamma \rightarrow 0$ we recover the classical Verlet algorithm. As in the Verlet algorithm we do not need to compute

the velocities in order to solve the differential equations. If velocities are needed for some measurements, then the velocity of the particles can be obtained with accuracy by using,

$$\begin{aligned}
v_i(t_n) = & \frac{H(\gamma\Delta t)}{\Delta t} [x_i(t_n + \Delta t) - x_i(t_n - \Delta t)] \\
& + m^{-1} F_i(t_n) (\Delta t)^2 (\gamma\Delta t)^{-2} G(\gamma\Delta t) \\
& - m^{-1} \frac{dF_i(t_n)}{dt} (\Delta t)^3 (\gamma\Delta t)^{-3} G(\gamma\Delta t) \\
& + X_n^{(i)}(-\Delta t) - X_n^{(i)}(\Delta t)
\end{aligned} \tag{3.22}$$

where $H(x) = x/(e^x - e^{-x})$. The equation 3.22 can be obtained from eliminating $x(t_n)$ after using equation 3.17, and changing Δt by $-\Delta t$.

3.2.1.b Remarks to the implementation of the Gunsteren-Berendsen algorithm in Brownian Dynamics

The Gunsteren-Berendsen algorithm can be implemented in a system of colloidal particles if we know $x(t_n)$, $x(t_{n-1})$, $X_{n-1}(\Delta t)$ and $F(t_{n-1})$ for all the particles. If that is the case, then the next Brownian Dynamics iteration can be performed as follows:

- (1) Evaluate $F(t_n)$ using the $x(t_n)$ positions. In our case, forces are obtained through the derivative of the potentials given by equations 3.12 and 3.13.
- (2) Compute $\frac{dF_i(t_n)}{dt} = \frac{F_i(t_n) - F_i(t_{n-1})}{\Delta t}$
- (3) Generate the random number $X_n(\Delta t)$ from a Gaussian distribution with mean zero and width given by σ_1 (Eq. 3.21). In order to generate the Gaussian random numbers we use a numerical table inversion method developed by Toral and Chakrabarti [136] that is between 3 and 7 times faster than the standard Box-Muller-Wiener algorithm, and has the advantage of being easily vectorizable.
- (4) Generate $X_n^{(i)}(-\Delta t)$. This is the most tricky step of the algorithm because $X_{n-1}^{(i)}(\Delta t)$ and $X_n^{(i)}(-\Delta t)$ are correlated. The conditional distribution of $X_n^{(i)}(-\Delta t)$ given a specific value of $X_{n-1}^{(i)}(\Delta t)$ is

$$\begin{aligned}
W(X_n^{(i)}(-\Delta t) | X_{n-1}^{(i)}(\Delta t)) = & \frac{1}{(2\pi\sigma_2^2(1-r^2))^{1/2}} \\
& \exp[-(X_n^{(i)}(-\Delta t) - r\sigma_2\sigma_1^{-1}X_{n-1}^{(i)}(\Delta t))^2 / (2\sigma_2^2(1-r^2))]
\end{aligned} \tag{3.23}$$

Therefore, we must first generate a Gaussian random number $Y^{(i)}$, from a Gaussian distribution with mean zero and width σ_Y given by,

$$\sigma_Y = \sigma_2^2(1 - r^2) = \frac{kT}{m\gamma^2} \frac{E(\gamma\Delta t)}{C(\gamma\Delta t)} \quad (3.24)$$

where

$$\begin{aligned} E(x) &= 16(e^x + e^{-x}) - 4(e^{2x} + e^{-2x}) \\ &\quad - 24 - 4x(e^x - e^{-x}) + 2x(e^{2x} - e^{-2x}) \end{aligned} \quad (3.25)$$

Once we have $Y^{(i)}$, we obtain the value of $X_n^{(i)}(-\Delta t)$ using

$$X_n^{(i)}(-\Delta t) = X_{n-1}^{(i)}(\Delta t) \frac{G(\gamma\Delta t)}{C(\gamma\Delta t)} + Y^{(i)} \quad (3.26)$$

- (5) Calculate the positions $x(t_{n+1})$ using equation 3.18. If velocities are required, compute them from equation 3.22.

In our simulations on colloidal suspensions, the particles are confined inside a two-dimensional box, usually we use a square box of size 256×256 . The use of powers of 2 as typical lengths of the system will make easier the implementation of Fast Fourier Algorithms when structure factors are computed. Periodic boundary conditions (PBC) are used in the simulations.

In order to obtain an initial condition ready to be used in the Gunsteren-Berendsen algorithm we proceed as follows. We place N colloidal particles randomly inside our two dimensional box; we use a short Monte Carlo simulation with PBC to shake the particles and get rid of possible overlaps. In these initial stages we consider two particles to overlap when they become closer than the cut off associated to the pair-potential. During the shaking process the true potential is turned off. Once we get a set of non overlapping particles, the first step is executed. The values of $x(t_{-1}), X_{-1}(\Delta t), F(t_{-1})$ are unknown so the first algorithm is not applicable yet. The first step is computed as follows: we sample $X_0^{(i)}(\Delta t)$ from a Gaussian with zero mean and width σ_1 , and the positions $x(t_1)$ are obtained by applying,

$$\begin{aligned} x(t_1) &= x(t_o) + v(t_o)\gamma^{-1}(1 - e^{-\gamma\Delta t}) \\ &\quad + m^{-1}F(t_o)\gamma^{-2}(\gamma\Delta t - (1 - e^{-\gamma\Delta t})) + X_o(\Delta t) \end{aligned} \quad (3.27)$$

where the initial velocities $v(t_o)$ are obtained through the Maxwell-Boltzmann distribution.

A final remark in the implementation of the BD Gunsteren-Berendsen algorithm concerns to the numerical accuracy. If $\gamma\Delta t \ll 0.05$ it is advised to expand in power laws the expressions $G(x)$, $G(x)/C(x)$, $1 - e^{-x}$, in order to enforce a good numerical accuracy along the simulation. In our simulations typically $\gamma\Delta t \sim 0.00025$ so we have implemented in our codes the expansions in power series recommended by Gunsteren-Berendsen in their work [133].

Chapter 4

Kinetics of phase transformations in depletion-driven colloids

*Experience is the name everyone gives to their mistakes.
Oscar Wilde, (1854-1900).*

*An expert is a man who has made all the mistakes, which can be made, in a very narrow field.
Niels Henrik David Bohr, (1885-1962).*

So, during these years I have got a lot of experience but I'm still far from being an expert . . .

The present and the next chapter are devoted to the study of 2d depletion-driven colloidal systems. Results from a detailed numerical study using Brownian Dynamics are presented and discussed. A transition from a single dispersed phase to a two-phase coexistence of single colloidal particles and crystalline cluster aggregates is obtained as the strength of the attractive interaction between particles is increased. In this chapter we deal with the results related to the morphology and growth kinetics of the colloidal aggregates obtained when a system is quenched into the two-phase region. Next chapter will be devoted to the study of the dynamical scaling hypothesis for the structure factor $S(q)$ in colloidal systems which in turn will give us opportunity to examine in detail the aggregation mechanisms present during the first steps in the aggregation processes.

4.1 Introduction

The general problem of how a dispersed phase, such as particles in a colloid or molecules in a solution, come together, when destabilized, to form a condensed phase, such as aggregates, gels or precipitated crystalline solids, is of fundamental importance for controlling the assembly of the dispersed phase into a useful

material [137]. Parts of this grand problem have seen considerable previous research such as irreversible aggregation [138] and the formation of fractal aggregates [139], gelation, spinodal decomposition [140], nucleation and early studies of growth during precipitation [141]. However, a general theory that encompasses all these related phenomena is lacking.

Colloidal solutions can display a rich series of phase transitions between gas, liquid and solid phases [80, 142]. The liquid phase can be amorphous or liquid crystalline and the solid phases can be crystalline, amorphous (perhaps fractal) and gel. These possibilities are controlled by the potential between the disperse components and the kinetics of the phase transition. A fluid to crystal transition occurs if the potential is solely hard sphere. Addition of an attractive potential brings on three phase equilibria. A key parameter that causes large changes in the phase diagram is the relative range of the attractive interaction between the colloidal particles. As the relative range of the attractive interaction lessens, the system develops a gas-crystalline coexistence with a metastable liquid-liquid coexistence region.

Theoretical understanding of the colloidal phase diagram leads to a better control of colloidal growth kinetics. For example, colloidal aggregation which is often irreversible, can be made reversible on experimental time scales by tailoring both the strength and range of interaction between colloidal particles. Reversible aggregation of colloids is known to exhibit various intriguing phenomena [80, 142], such as transient gel formation, compactification, and crystallization. Moreover, reversible aggregation has striking similarity with other phase changes such as spinodal decomposition and the formation of precipitated crystalline solids from solutions. A quantitative understanding of reversible aggregation is thus needed for a unifying description of the transition from a general dispersed phase to clusters and for a greater control over the self-assembly and material properties of various colloids.

As we have commented in Section 1.2, the manipulation of the interaction potential between colloidal particles can be achieved in several ways. For a charge stabilized colloidal solution, this can be done by the addition of salt or surfactant solution so that a *secondary minimum* in the interaction potential forms. Another way to control the interaction potential between colloidal particles is to induce a depletion interaction by adding a non-adsorbing polymer (or a different sized colloid [143]) in an otherwise stable colloidal solution. A major advantage of the latter systems is that the strength and range of the depletion interaction can be easily controlled by varying the polymer concentration and the length of the added polymer chains.

Phase behavior of depletion-driven colloids has been studied extensively both

theoretically and experimentally. The equilibrium behavior of these systems being reasonably well understood, much of recent work has been directed to understand kinetics of phase transitions [143, 144] and colloidal gelation [145] (and its relation to glass transition [146] and the more general jamming transition [147]) in these systems. Hobbie [143] has studied growth kinetics of the crystallization process in depletion driven colloids and compared experimental results with mean-field theories of aggregation-fragmentation. Direct observation of crystallization and aggregation has been carried out more recently by de Hoog *et al.* [144] by varying the polymer concentration hence the depth of the depletion potential. Brownian dynamics simulations [124, 148–150] have also been carried out to study transient gel formation and crystallization in these systems. In particular, Soga, Melrose, and Ball [124, 148] (SMB) have observed a variety of non-equilibrium behaviors in their simulations by varying the strength of the depletion potential. Evidences of metastability, homogeneous nucleation, kinetically arrested gel state and density instability were reported by SMB in their simulations. The use of computer simulations to study aggregation kinetics in these systems is particularly useful as one can avoid sedimentation related complications seen in experiments.

In this chapter, we present results from extensive Brownian dynamics simulations¹. We assume that the depletion interaction can be approximately accounted for by an effective two-body interaction between a pair of colloidal particles as suggested by Asakura-Oosawa-Vrij (see Section 1.2.2.a). In contrast to SMB, we focus on lower monomer concentration (far away from the percolation threshold) and restrict ourselves to two-dimensions. This allows us to carry out a detailed comparison of the cluster morphology and aggregation kinetics to traditional models of aggregation and fragmentation. Clusters obtained in the simulations range from dense, faceted crystals to fractal aggregates which shows ramified morphology on large scales but hexagonally-packed crystalline morphology on short length scales. Increasing the depth of the depletion potential well, a transition from dispersed phase to a coexistence of dispersed phase and solid phase is found. Near the transition point, formation of clusters with a round shape is ob-

¹In our Brownian dynamics simulations we consider a 2d system of linear size $L = 256\sigma$ containing $N_m = 13,107$ colloidal particles of mass m and diameter σ . This sets the monomer area fraction to be $f_v \approx 0.157$. We set $m = 1$ and $\sigma = 1$ and measure all distances in units of σ . Periodic boundary conditions are enforced to minimize wall effects. Hydrodynamic interactions, including lubrication forces are ignored in the simulation as they might not be of predominant importance for a study of quiescent colloids [151]. All simulations start from a random initial monomer conformation and the results for the kinetics are averaged over more than 100 runs. For further details about our Brownian dynamics simulations, see Section 3.2.

served. As the well depth is increased further, one first obtains elongated clusters and then fractal clusters form for deep enough well depths. Our simulations also show how growth kinetics evolves from the irreversible limits to systems which come to equilibrium over the simulation time due to fragmentation.

In the following sections we present simulation results and compare them with traditional aggregation, aggregation-fragmentation, and phase separation models.

4.2 Cluster Morphology

Transition from a single dispersed-phase to a state in which the solid phase starts to develop in the two-phase region is observed in the simulations when $|U_m|$ is larger than a critical value U_c . From our simulations, we estimate that $U_c \approx 3.130k_B T$ for our choice of monomer area fraction f_v . For smaller values of $|U_m|$, small *fluctuating clusters* in the dispersed phase form and dissolve over some correlation time. The linear size of these fluctuations increases as one approaches the transition. This is expected as the correlation length in the single phase should increase as a power-law near a critical point. Phase diagram for the model considered here is known accurately in three dimensions [152] but not in two dimensions. For this reason, a quantitative identification of the quench points chosen in our work on the 2D phase diagram is not possible.

For computing cluster properties, we consider two neighboring particles to belong to the same cluster if the distance between their centers is less than or equal to the range of the interaction, i.e., $1 + \zeta$ (or, 1.1 for our choice of ζ) in units of σ . Figure 4.1 shows a snapshot for a system with $|U_m| = 3.125k_B T$. In this case the system is in the single phase as $|U_m| < U_c$ and the largest observed fluctuating cluster has a size less than 100 particles. As shown in the inset of Figure 4.1, these small clusters have amorphous structures. No evidence of crystal formation is found in these clusters. If we set $|U_m|$ close to the critical value but slightly deeper than U_c , nucleation and growth of round clusters occur. Growth of only one round-shape cluster in our finite-sized simulation box is observed in Figure 4.2 for $|U_m| = 3.135k_B T$. This value of $|U_m|$ puts the system barely in the two-phase region.

Increasing the depth of the potential well $|U_m|$ further, nucleation becomes more heterogeneous in our simulation box, as can be seen in the top-left snapshot of Figure 4.3 for $|U_m| = 3.25$ at an early time. For this value of $|U_m|$, large round shaped clusters in a sea of monomers (and small clusters) are observed at late times (left column of Figure 4.3). The average coordination number per particle inside such a cluster is close to six, and as shown in Figure 4.4 (c), hexagonal packing of the particles is clearly present inside the cluster. In Figure 4.4, de-

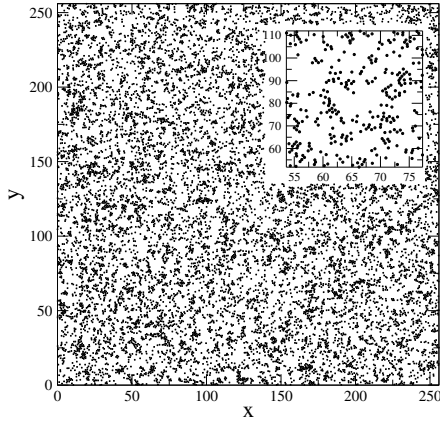


Figure 4.1. Snapshot of the simulated colloidal system at $t = 10000$. Here, well depth is set to $|U_m| = 3.125$. The system is in the single-phase region and the dispersed phase is observed.

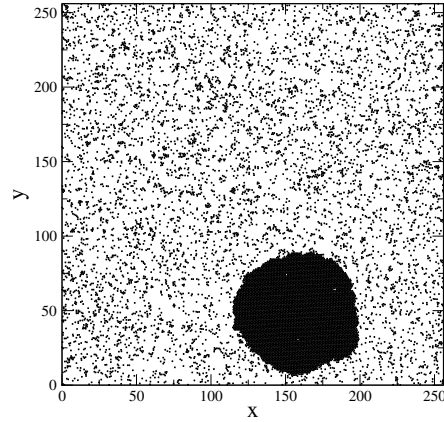


Figure 4.2. Snapshot of the simulated colloidal system at $t = 10000$ for $|U_m| = 3.135$. A single round shaped cluster is growing in the simulated box surrounded by the dispersed-phase.

tails of cluster shapes are shown for several values of the potential well depth. Once two clusters collide with each other, the shape of the newly formed cluster remains anisotropic for some time while it evolves toward a circular shape to reduce interfacial energy. During this course, the resulting cluster bears the history of the collision in its shape (such as in the ordering of single crystal domains inside the cluster as in Figure 4.4e). The timescale for this shape evolution depends critically on the potential well depth $|U_m|$ as we will see shortly.

Increasing the degree of quenching into the two-phase region by setting $|U_m| = 4.0k_B T$, rather elongated clusters that grow with time are seen (Figure 4.3, central column). In this case, the potential well is deep enough to slow down the movement of monomers on a cluster surface which is needed for a reduction of interfacial energy. Therefore, new collisions are produced before anisotropic clusters formed from previous collisions have enough time to reshape themselves into circular clusters. As a result, the clusters seen in this case are elongated even at very late times. For even larger well depth, such as $|U_m| = 7.0k_B T$ (Figure 4.3, right column), fractal clusters are obtained. We speculate that the interfacial tension driven surface reorganization of monomers is almost frozen in this case and the cluster shape results mainly from random cluster-cluster collisions as in a traditional diffusion-limited cluster-cluster aggregation (DLCA) or reaction-limited cluster-cluster aggregation (RLCA) models (see Section 1.3.3.d). However, even for this deep well depth, the aggregates show hexagonal closed-packed crystalline ordering at short length scales (Figure 4.4f) while displaying ramified fractal na-

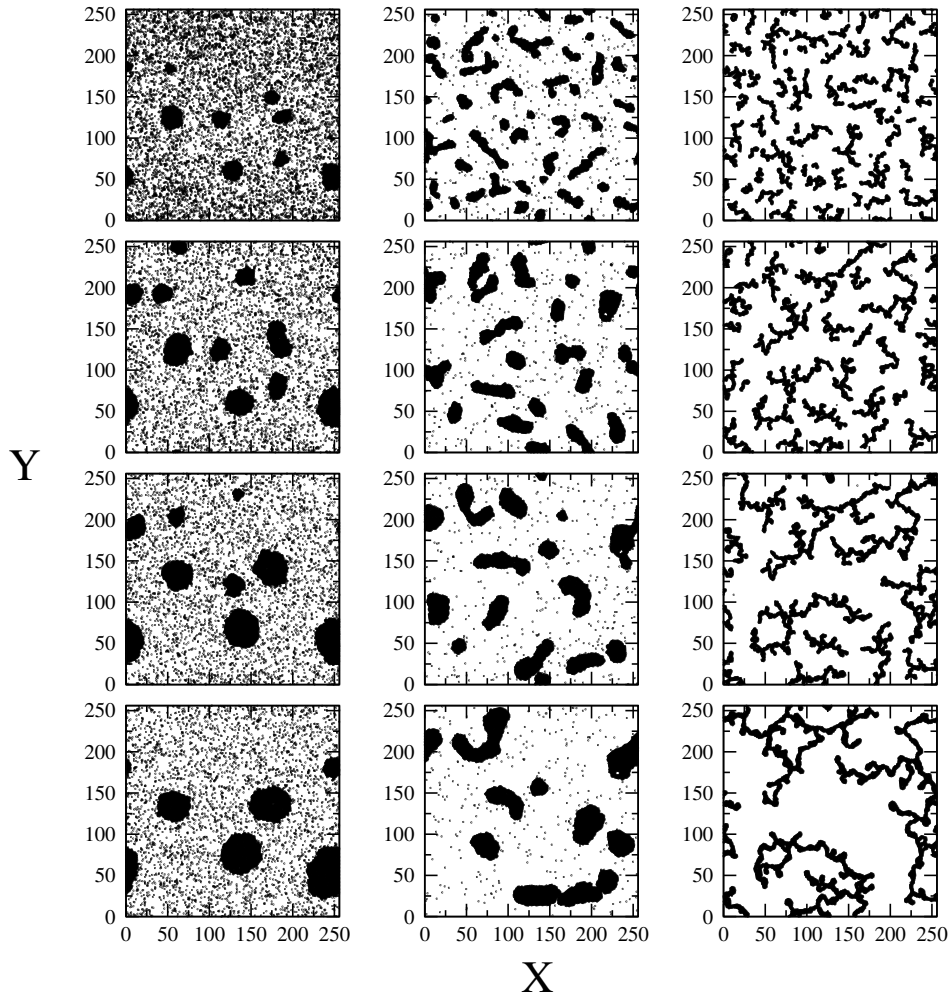


Figure 4.3. Temporal evolution for three different quenches. First column shows snapshots at $t = 3000, 6000, 23000, 40000$ for $|U_m| = 3.25$. Second column shows snapshots at $t = 3000, 20000, 43000, 84000$ for $|U_m| = 4.0$. Third column shows snapshots at $t = 1000, 3000, 10000, 86000$ for $|U_m| = 7.0$. Cluster morphology shows a distinct change as the depth of the potential is varied.

ture at larger length scales. To be specific, this cluster morphology cannot be reproduced by a traditional DLCA modeling for which the typical coordination number of a particle in a cluster is approximately 2. Large-scale morphology of the simulated clusters display close similarities with aggregates observed experimentally by de Hoog *et al.* [144], and Anderson *et al.* [153] in the earlier stages of the aggregation in depletion driven colloids, before sedimentation becomes crucial. It should be noted here that such mixed morphology of aggregating clusters was first observed by Skjeltorp [154] in two-dimensional aggregates of polystyrene spheres attracting via a secondary minimum. In such a system, the superposition of a screened electrostatic repulsion and a van der Waals attraction leads to the formation of a secondary minimum [7, 155] in the potential with a rather high energetic barrier between the primary and the secondary minima. The barrier between these minima prevents irreversible aggregation and these charged colloids can effectively interact through the secondary minima.

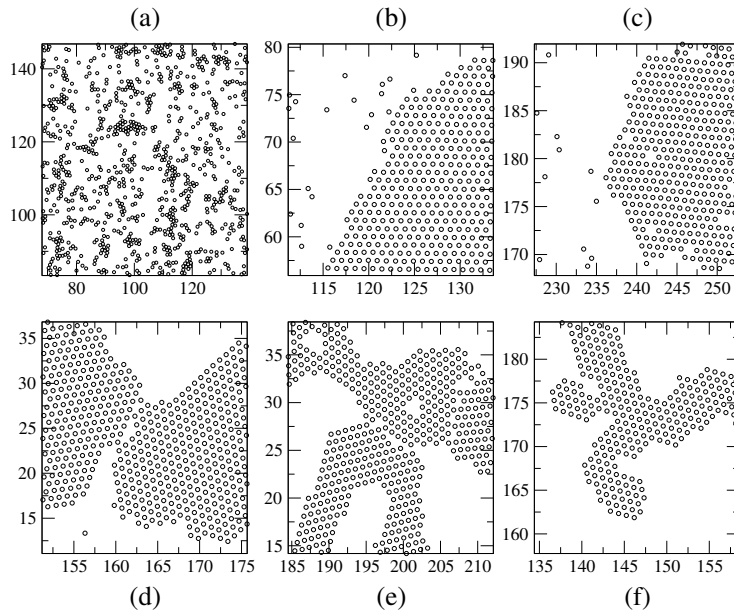


Figure 4.4. Details of cluster morphology for several values of the potential well depth. From top-left to bottom-right, we show results for $|U_m| = 3.125$ (a), 3.135 (b), 3.25 (c), 4.0 (d), 5.0 (e), and $7.0k_B T$ (f), respectively. Cluster morphology for $|U_m| = 3.125$ shows a dispersed phase with non-crystalline structures (a). For well depths larger than the transition value $U_c \simeq 3.130$, particles are arranged hexagonally inside the clusters. When collision between two clusters is recent, history of such a collision can be seen in the resultant cluster shape.

4.3 Comparison with Traditional Models of Aggregation and Phase Separation

4.3.1 Fractal Dimension

The next step in our analysis is to carry out a quantitative comparison of the results from Brownian dynamics simulations with more traditional models such as DLCA and RLCA. These limiting non-equilibrium models have been quite successful in describing aggregation. In DLCA, the rate limiting step is the Brownian diffusion by which the particles meet and stick irreversibly, and in RLCA, the limiting step is the small probability of cluster sticking when they touch. A general feature of such irreversible processes is that the resulting structures are fractals with characteristic fractal dimensions. However, if the magnitude of the interaction potential between colloidal particles is comparable to thermal energy $k_B T$, both rearrangement and fragmentation (hence reversible aggregation) of clusters can take place. In such situations, one needs to compare results of current Brownian dynamics simulations with models that consider both aggregation and fragmentation.

The large length scale cluster morphology obtained in our simulations is quantified by computing the cluster-ensemble averaged fractal dimension D_f (see Sections 1.3.1 and 1.3.2). This is achieved by writing $N \sim R_g^{D_f}$, where R_g is the radius of gyration of an individual cluster containing N particles. Figure 4.5 shows the temporal evolution for fractal dimension in two representative cases. Computation of the fractal dimension confirms a transition from compact clusters with $D_f = 2$ to fractal clusters when we increase the well depth. We find that the fractal dimension for large potential well depth is given by $D_f \simeq 1.4$. Within the statistical error of our data, this value of D_f is the same as the fractal dimension obtained in 2d DLCA models. Thus, Brownian dynamics simulations for a deep well depth reproduce the DLCA limit in terms of the large-scale fractal dimension, even though the short length scale structure of the clusters are totally different in these two models.

4.3.2 Growth Kinetics

Since the potential well depth dictates cluster morphology, it is expected to control cluster growth kinetics as well. We have studied three different regimes (or ‘quench depth’ using terminology of fluid-fluid phase separation) of growth kinetics: deep potential well depth (deep quench in the two-phase region), shallow potential well depth (shallow quench in the two-phase region), and quenches in the single-phase region.

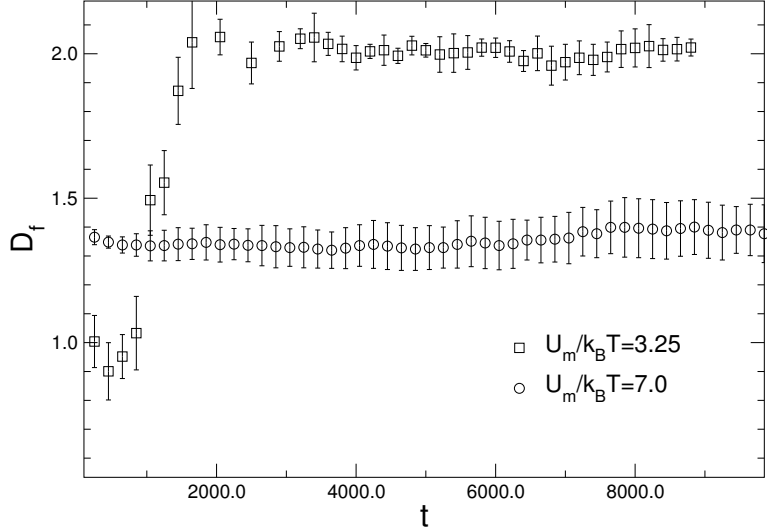


Figure 4.5. Time evolution of the cluster averaged fractal dimension, D_f for well depths $|U_m| = 3.25k_B T$, and $7k_B T$. For the lower value of $|U_m|$, compact clusters are found for which fractal dimension is close to 2. We have calculated the fractal dimension as a function of time including only clusters with a size equal or higher than a 10% of the size of the largest cluster in the system. Inclusion of too small clusters produces a slight bias of the slope which results in D_f being larger than 2. Increasing $|U_m|$ a gradual transition to fractal clusters is observed. Fractal clusters for $|U_m| = 7k_B T$ have a fractal dimension of $D_f \simeq 1.4$, close to 2d DLCA result.

Deep Quench in the Two-Phase Region

We compute the mean-size of clusters $s(t)$ (as number of monomers per cluster) and the cluster-size distribution $n(N)$. Kinetic theory based on Smoluchowski equation predicts that for irreversible aggregation at late times (see Section 1.3.3.a),

$$s(t) \sim t^z \quad (4.1)$$

where z is the kinetic exponent which depends on the homogeneity constant, λ , of the aggregation kernel:

$$z = 1/(1 - \lambda). \quad (4.2)$$

For the DLCA model with a Brownian coagulation kernel, a scaling argument [156, 157] yields $\lambda = (d - 3)/D_f$ in the dilute limit (see also Eq. 1.30). In 3d, this provides $\lambda = 0$ and $z = 1$ as expected [138]. In 2d, however, this leads to $\lambda = -1/D_f = -0.7$ with $D_f = 1.4$ and hence $z = 0.59$ in the dilute limit.

Another factor that influences growth kinetics of fractal aggregates is the *volume fraction occupied by the clusters*, f_v^c . Since the fractal dimension D_f of

the clusters is less than the space dimension d , f_v^c increases throughout aggregation, and evolution to a crowded state takes place. f_v^c can be computed in terms of the perimeter radius of the clusters which is related to the cluster radius of gyration R_g . Thus, cluster crowding can be understood by considering the ratio of the cluster center of mass to cluster nearest-neighbor center of mass separation R_{nn} to the cluster radius-of-gyration R_g which scales with time as, $R_{nn}/R_g \propto t^{-z(d-D_f)/(dD_f)}$. Note that, $R_{nn}/R_g \rightarrow 0$ at late times indicating gelation occurring in the system. In practice, however, the system gels well before this condition is reached as the clusters are ramified. It is known that the kinetic exponent z increases as the system gets dense [158] i.e, as the cluster volume fraction, f_v^c , increases. For an intermediate value of f_v^c , scaling arguments [156] yield $z \simeq 1.28$ in 3d and $z \simeq 0.67$ in 2d.

Our results for $s(t)$ versus t for deep potential wells (such as with $|U_m| = 6.0k_B T$, and $7.0k_B T$) are presented in Figure 4.6 as a log-log plot. The measured kinetic exponent is $z = 0.74 \pm 0.05$ in each case. This value of z is rather similar to the 2d scaling result in the intermediate regime mentioned above [156] and also to the kinetic exponent obtained in large-scale 2d DLCA simulations [159] with a fair degree of cluster crowdedness. This agreement strongly indicates that fragmentation does not play an important role over the simulation time for these choices of the potential well depth.

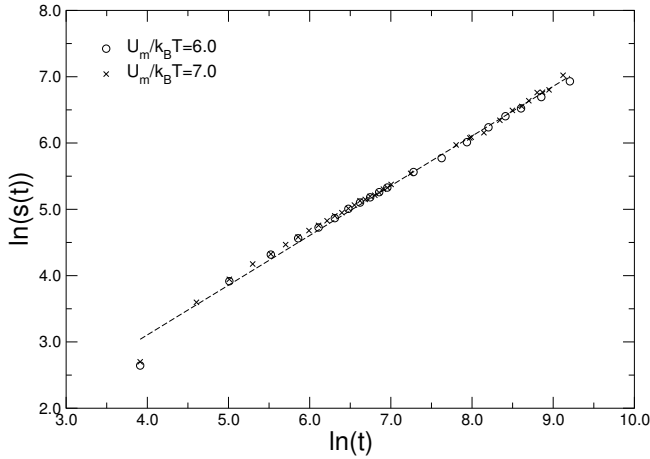


Figure 4.6. Log-log plot for time evolution of the averaged cluster size for deep well depths. The kinetic exponent, z , obtained from linear fits is given by 0.74 ± 0.05 in each case.

The kinetic exponent z can be alternatively obtained by measuring the temporal evolution of the mean cluster radius of gyration, $\langle R_g \rangle$. In the scaling description of DLCA, $\langle R_g \rangle \sim t^a$ with $a = z/D_f$. Therefore, if fractal dimension D_f is known, z can be deduced from a log-log plot of $\langle R_g \rangle$ versus time t . In Figure 4.7 we show such a log-log plot for various values of $|U_m|$. For computing $\langle R_g \rangle$, we only use clusters containing more than four particles. For both $|U_m| = 6.0k_B T$,

and $7.0k_B T$ we obtain $a = 0.52 \pm 0.04$ which yields $z = 0.73$ for $D_f = 1.4$. Thus, both methods of measuring the kinetic exponent z show good agreement with each other for deep well depths.

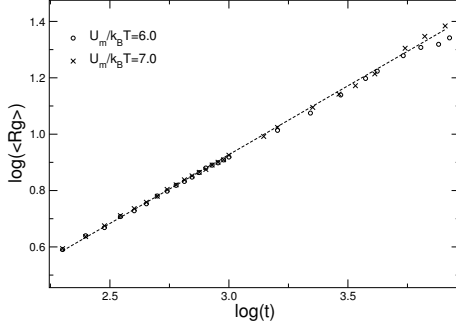


Figure 4.7. Log-log plot of radius of gyration vs time for deep well depths. The exponent, $a = z/D_f$, obtained from linear fits is given by 0.52 ± 0.04 in each case.

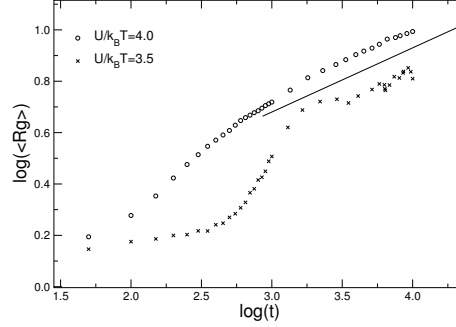


Figure 4.8. Log-log plot of radius of gyration vs time for shallower well depths in the two phase region. The solid line is a guide to the eye with a slope of $1/4$. Cluster growth at intermediate times is consistent with $R_g(t) \sim t^n$ with $n \approx 0.25$.

Shallow Quench in the Two-Phase Region

For shallower well depths in the two-phase region, fragmentation of clusters can take place. However, it is expected that fragmentation predominantly occurs at the surface of the cluster; this is the celebrated evaporation-condensation mechanism behind Ostwald ripening [87]. In addition, surface reorganization of clusters can take place to reduce interfacial tension. One of the most important characteristics of cluster growth under spinodal decomposition is that the clusters are compact and, as a result, both cluster nearest-neighbor separation R_{nn} and the cluster radius-of-gyration R_g grow with the *same* temporal exponent. In other words, there is only one length scale in the system. The growth law in these cases can be generally written as $R_g(t) \sim t^n$. It is well established [140] that $n = 1/3$ at late times in both 2d and 3d, while at intermediate times, dominated by surface diffusion and coalescence of diffusing clusters, the growth law exponent can be characterized [87, 160] by $n = 1/4$. We have plotted a log-log graph of $\langle R_g \rangle(t)$ versus t in Figure 4.8 for two shallower well depths inside the two-phase coexistence. In each case, at intermediate times (when the average radius of gyration of clusters $\simeq 5$ or bigger), we observe growth of clusters characterized by an exponent close to $1/4$. We have checked that both R_g and R_{nn} do increase proportionately with each other at these times. For $|U_m| = 3.5k_B T$, we also observe

a *nucleation induction time* at the very beginning, after which cluster growth and coarsening take place. These last issues will be addressed in more detail in the next chapter.

Quench in the Single-Phase Region

In the presence of fragmentation, as it has already been pointed out in Section 1.3.4.a, Sorensen, Zhang, and Taylor (SZT) arrived at a general expression for the evolution of the mean cluster size in terms of reduced variables $s^* = s/s_o$, and $t^* = t/t_o$,

$$\frac{ds^*}{dt^*} = s^{*\lambda} - s^{*\alpha+2} \quad (4.3)$$

where s_o is the steady-state value of $s(t)$ at long time, and t_o a characteristic time scale for the approach to equilibrium. The exponents λ and α stand for the degree of homogeneity of the aggregation and fragmentation kernels, respectively. It is clear from our discussion above that SZT description of aggregation-fragmentation is not applicable in the two-phase region where the cluster size increases indefinitely in the thermodynamic limit. However, in the single-phase region, where the clusters grow only up to the size of the correlation length, SZT equation might have a limited validity. We numerically solve this first order SZT differential equation (Eq. 4.3) with the initial condition $s^*(t = 0) = 1/s_o$. It is not immediately clear what are the values of λ and α in Eq. (4.3). As we have discussed before, in the dilute limit of DLCA model $z = 0.59$ hence $\lambda = -0.7$, while for a moderate value of cluster crowdedness, z increases to 0.74 in the simulations and the corresponding λ becomes -0.35 . We choose $\alpha = 1/2$ in the mean field model of SZT to roughly incorporate the possibility that cluster fragmentation happens mostly at the surface. As mentioned earlier, we consider two neighboring particles to belong to the same cluster if the distance between their centers is less than or equal to the range of the interaction. A comparison with the SZT prediction in the single-phase is carried out in Figures 4.9 and 4.10 for $|U_m| = 2k_B T$, and $|U_m| = 3.125k_B T$, respectively. In these figures we show SZT predictions along with our simulation results for both $\lambda = -0.35$ and $\lambda = -0.7$ and $\omega = 1/2$. It is clear that $\lambda = -0.7$ shows excellent agreement with the simulation data. This is perhaps due to the fact that the average cluster sizes are relatively small throughout the simulation time and cluster crowding does not substantially modify the dilute limit values of z and λ . Thus, it is appropriate to substitute dilute limit value of $\lambda = -0.7$ in the SZT model for a better comparison with these simulation results.

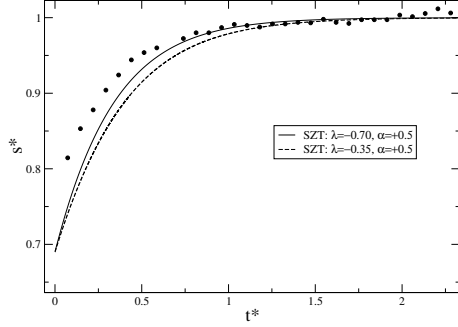


Figure 4.9. Comparison between simulation results for growth kinetics in the single phase and SZT prediction for two sets of parameter values. Here, $|U_m| = 2.0k_B T$.

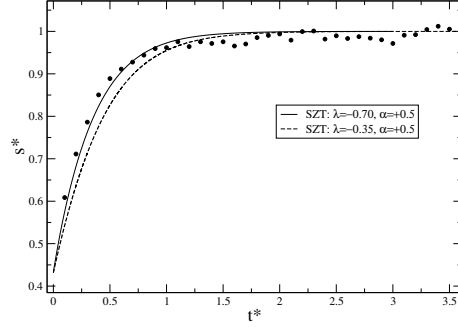


Figure 4.10. The same as in Figure 10 except $|U_m| = 3.125k_B T$ here.

4.3.2.a Cluster Size Distribution

To characterize the cluster size distribution², we invoke a standard scaling ansatz applicable in many physical situations (see Section 1.3.3.b) where cluster distributions are assumed to obey a scaling law given by

$$n(N, t) = \frac{N_m}{s(t)^2} \phi\left(\frac{N}{s(t)}\right) \quad (4.5)$$

where N_m stands for the total number of particles (monomers) in the system, and $\phi(N/s)$ is a general scaling function. The scaling form assumed for the cluster size distribution, (Eq. 4.5) is tested in Figures 4.11 and 4.12 for $|U_m| = 7k_B T$ and $|U_m| = 3.5k_B T$, respectively. Results are averaged over more than 100 runs. The prescribed scaling form seems to work well for $|U_m| = 7k_B T$. For such a deep well depth, one would expect that fragmentation of clusters will be rare and a comparison with DLCA simulations will be meaningful over the simulation time. For irreversible aggregation the scaling function can be expressed as (see Eq. 1.29, and [36])

$$\phi(x) = Ax^{-\lambda} e^{-\eta x} \quad (4.6)$$

for large values of the scaling variable $x = N/s$. Here, $\lambda = 1 - z^{-1}$, and $\eta = 1 - \lambda$. If we consider $z = 0.74$ appropriate for this deep well depth (see Figure 4.6),

²The cluster distribution $n(N, t)$ is normalized as usual

$$\int n(N, t) \cdot N \cdot dN = N_m \quad (4.4)$$

where N_m is the total number of particles in the system.

we find $\lambda = -0.35$ and $\eta = 1.35$. Figure 4.11 shows that Eq. 4.6 with these values of λ and η fit the scaled cluster size distribution quite well for large values of x .

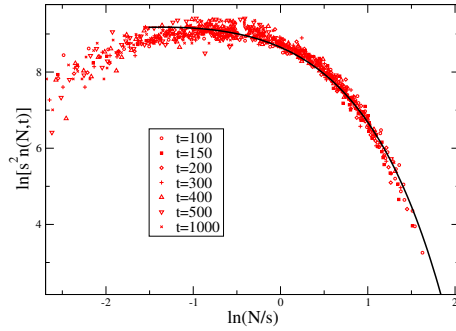


Figure 4.11. Scaling of the cluster size distribution for $|U_m| = 7.0k_B T$. Results are averaged over 150 runs. The solid line is fit to the data according to Eq. 4.6 with $\lambda = -0.35$ and $\eta = 1.35$ for scaling variable $N/s \geq 1$.

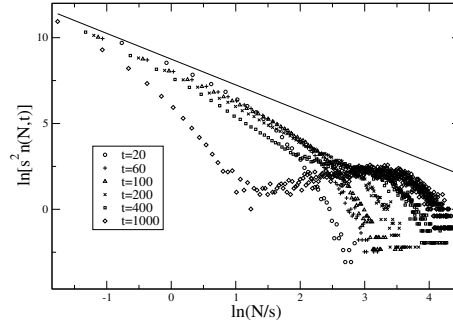


Figure 4.12. Scaling of the cluster size distribution for $|U_m| = 3.5$. Results are averaged over 100 runs. A solid line of slope -1.5 is added to guide the eye.

Scaling does not seem to work so well for $|U_m| = 3.5k_B T$ (Figure 4.12). For small values of the scaling variable and at earlier times, a power law with an exponent close to -1.5 is found in the scaling function. Such power law decay of scaling functions are reminiscent of a RLCA behavior. We should point out that a similar exponent of -1.5 has been observed by Hobbie [143] in the scaling function for a binary colloidal mixture in which depletion forces arise from difference in size between two colloids. The origin of the RLCA type power-law behavior for this shallow well depth is perhaps due to the fact that clusters do not stick the first time they approach each other. There is also a hint of an exponential decay in the size distribution for large x as seen by Hobbie. At later times, the ‘scaling function’ changes appreciably displaying the presence of a broad maximum at an intermediate value of N/s .

4.4 Concluding remarks

To provide a unifying description of the transition from the dispersed phase to the solid phase (which includes both fractal and crystalline aggregates), we have carried out a detailed study of the kinetics of phase transformations in a two-dimensional colloidal system. The interaction among colloidal particles in this work arises from the depletion effect due to the addition of a non-adsorbing polymer and is modeled as an effective two body potential. Although the depletion

force is assumed to be instantaneous in this work, recent work [26] shows that the depletion force will have a time dependence which will in general affect colloidal kinetics. However, this time dependence is quite weak for the size parameter ζ used in our work. Thus, we do not expect this to substantially change our conclusions.

Large-scale morphology of clusters obtained in the simulation show good agreement with those observed by Hoog et al [144] in their experimental work on depletion-driven colloids. We characterize the morphology of clusters for various values of the magnitude of the potential well depth $|U_m|$. There exists a critical value of this well depth (U_c) in the model. When $|U_m| < U_c \simeq 3.130k_B T$, the system remains in a single phase (for our chosen value of monomer area fraction f) characterized by a dispersed phase of monomers and small clusters. A transition from this dispersed-phase to a two-phase coexistence takes place when the system is quenched such that $|U_m| > U_c$. In the two phase region, dispersed and hexagonally packed crystal phase can coexist. Gradual transition from round cluster growth to the formation of elongated clusters is observed as the well depth is increased. Increasing the well depth even more, fractal clusters are observed in the simulation. These fractal clusters have a hybrid nature in the sense that the aggregates show hexagonal closed-packed crystalline ordering at short length scales and a ramified fractal nature at larger length scales. For sufficiently deep potential wells, the large-scale fractal dimension of the clusters are close to those obtained in simulations of DLCA model in 2-dimensions, $D_f \simeq 1.4$.

Further quantitative comparisons with the DLCA model are carried out next in the limit of deep potential well depths. Kinetic exponents obtained from both mean number of particles in a cluster, and average cluster radius of gyration provide strong support that the DLCA limit in the kinetics can be achieved for deep potential wells. In addition, the scaling function for cluster size distribution matches the DLCA scaling form for deep potential well depths. For shallower well depths in the two-phase region, growth kinetics is compared with early-time theories of phase separation. In the single-phase region, comparison of simulation results with a mean-field aggregation fragmentation model shows good agreement.

Our work clearly demonstrates the importance of Brownian dynamics simulations in the study of colloidal aggregation and more generally for studying the transition from a dispersed phase to a solid phase. Past theoretical studies of fractal aggregates in colloids, for example, typically started from the DLCA model which turns out to be the irreversible limits of our simulation and are recovered for a deep well depth. In contrast, aggregates that crossover from fractal to compact crystalline morphology can be easily studied in Brownian dynamics simulations

by changing a simple parameter of the model. More importantly, growth kinetics and aggregate size distributions that evolve from non-equilibrium to equilibrium limits can be accessed in a reasonable amount of computer time.

Chapter 5

Structure factor scaling in colloidal phase separation

In this chapter we continue with the study of the phase separation in depletion-driven colloidal systems. After the study of the morphology and cluster growth kinetics done in the previous chapter, now we focus on the study of the dynamical hypothesis of the structure factor $S(q)$, which in turn will offer us the possibility to discuss the nature of the aggregation mechanisms present in the early stages of the aggregation processes.

5.1 Introduction

Dynamics of phase separation in a quenched system is the subject of many theoretical and experimental investigations in diverse systems [87, 140, 161] such as binary alloys, liquid mixtures, and polymer blends. Subsequent evolution of the quenched system is determined by the location of the quench inside the phase diagram. In the classical picture, a spinodal line divides the phase diagram into two kinds of instabilities that might govern the dynamical processes: nucleation and spinodal decomposition. If the system is quenched between the spinodal and the coexistence lines (nucleation regime), it becomes unstable against localized, strong amplitude concentration fluctuations. In this situation, nuclei of the minority phase are formed. These nuclei evolve with time in the following way: they grow if their size is larger than a certain critical size, otherwise they dissolve. In the spinodal decomposition regime, the system is unstable against long wavelength, small amplitude concentration fluctuations, which generate an interconnected pattern that coarsens with time. Although this simple picture is of general validity, one can not sharply separate the two regimes and the spinodal line

merely serves as a guideline to distinguish which process dominates [162, 163].

The late stages of the phase separation process can be described by a dynamical scaling form with a time-dependent characteristic length, $R(t)$. The fundamental assumption of dynamical scaling is that, in the late stages of the process, only one length scale is relevant. This characteristic length represents a measure of the typical domain size and increases with time. A major feature of this description is that the pair correlation function $g(r, t)$ and the structure factor $S(q, t)$ depend on time through $R(t)$ only, that is,

$$g(r, t) = G(r/R(t)) \quad (5.1)$$

and

$$S(q, t) = R(t)^d F(qR(t)), \quad (5.2)$$

where d is the dimensionality of the system and G and F are time-independent universal scaling functions.

Several years ago, small-angle light scattering experiments in moderately dense colloidal solutions [90, 91, 164, 165] showed a dynamical scaling behavior surprisingly similar to that observed in binary mixtures undergoing phase separation. In particular, the scattered intensity distribution in a concentrated colloidal solution shows a pronounced peak at a finite value of the wavenumber, q_m . Furthermore, the position of the peak moves to smaller values as the aggregation proceeds, while the peak intensity increases. In the later stages of the colloidal aggregation process, the dynamical structure factor, $S(q, t)$, is found to scale according to the following form:

$$S(q, t) = q_m^{-D_f} F^*(q/q_m), \quad (5.3)$$

where $F^*(x)$ is a time-independent scaling function, and D_f is the fractal dimension of the colloidal clusters. This scaling form is characteristic of the physical systems undergoing phase separation (Eq. 5.2), except that, q_m^{-1} is considered a characteristic length in the system, and the spatial dimension d of the system is replaced by D_f , the fractal dimension of the colloidal clusters.

Dynamical scaling of the structure factor in an aggregating colloidal solution is quite unexpected since colloidal aggregation in these experimental systems is irreversible and leads to the formation of fractal aggregates, in contrast to the phase separation processes in binary mixtures. The dynamical evolution of such irreversible colloidal aggregation is well understood in terms of the diffusion-limited-cluster-cluster aggregation (DLCA) model [137], where the initial colloidal monomers execute a Brownian motion until small clusters are formed, and then the clusters themselves diffuse and aggregate to form even larger clusters.

Thus, it is not clear why dynamical scaling with only a single length scale will be appropriate for colloidal aggregation. In fact, Huang, Oh, and Sorensen (HOS) [166] have argued that irreversible colloidal aggregation is characterized by *two different length scales*, namely the mean cluster radius of gyration $R_g(t)$ and the mean nearest-neighbor cluster-cluster separation distance $R_{nn}(t)$. Generally speaking, one can write

$$R_g(t) \sim t^{n_1} \text{ and, } R_{nn}(t) \sim t^{n_2}, \quad (5.4)$$

where n_1 and n_2 are the respective growth exponents. HOS have demonstrated that these two length scales grow with time with two different temporal exponents ($n_1 \neq n_2$) and thus, there is no dynamical scaling of the structure factor in an aggregating colloidal system. This is a direct consequence of the fractal nature of the clusters with a fractal dimension smaller than the space dimension ($D_f < d$). HOS have further concluded that for *monodisperse systems* the total structure factor $S(q, t)$ may be written as the product of two different structure factors, each with its own characteristic lengths. The first component, $S_{cc}(q, t)$, is the cluster-cluster contribution to the total structure factor, for which the cluster nearest-neighbor separation $R_{nn}(t)$ is the associated characteristic length. The second component, $S_{sc}(q, t)$, is contribution from particles inside a single cluster with the cluster radius of gyration R_g as its characteristic length. HOS have claimed that when clusters are compact, as in the case of phase separation in a binary mixture, both characteristic lengths evolve in a same way with time ($n_1 = n_2$). Thus, there would be a single effective length in the system and dynamical scaling will be satisfied. But when clusters are fractals, dynamical scaling might be satisfied at most over a limited window of time when $R_g(t) \approx R_{nn}(t)$, but scaling as a general principle must break down.

In the previous chapter we have shown that a transition from dispersed-phase to a coexistence of dispersed-phase and solid-phase takes place as one increases the depth of the depletion potential well. Near the transition point, formation of clusters with a round shape is observed. As the well depth is increased further, one first obtains elongated clusters and then fractal clusters (with fractal dimension $D_f \simeq 1.4$) form for deep enough well depths. Our simulations also show how growth kinetics and resulting cluster size distributions evolve from the irreversible limit to systems which come to equilibrium over the simulation time due to fragmentation. Thus, depletion-driven colloids, provide us a unique opportunity to study dynamical scaling of time dependent structure factors in a colloidal system which produces *both* fractal and compact clusters as a function of the strength of the depletion potential. Such a study might provide important insight into the validity and applicability of dynamical scaling for various cluster

morphologies. This is one of the motivations behind the work presented in this chapter.

We carry out a detailed simulation of the evolution of the structure factor in depletion-driven colloidal systems, for both shallow and deep quenches into the two-phase region¹. Our results show that true dynamical scaling is reached in a shallow quench (which produces compact clusters) after an initial transient regime. The scaling of the structure factor is confirmed by studying various length scales and by conclusively showing the existence of a single length scale in the system after such transient time. In contrast, the apparent structure factor scaling for a deep quench (which produces long-lived fractal clusters) is found to be only approximate. Two different length scales are found in the system which grow with two different power-law exponents with time. We further study the origin of the peak in the structure factor in this case and compare with theoretical predictions of HOS derived for monodisperse solutions.

5.2 General Features of the Structure Factor

The structure factor $S(\vec{q}, t)$ for a system of N_m monomer particles is defined as (see Section 1.4)

$$S(\vec{q}, t) = \sum_i^{N_m} \sum_j^{N_m} \exp [i\vec{q} \cdot (\vec{r}_i - \vec{r}_j)]. \quad (5.5)$$

The pair-correlation function $g(\vec{r}, t)$ can be obtained from the inverse Fourier transform of $S(\vec{q}, t)$. In order to compute the above quantities we have discretized the system into a $L \times L$ grid of lattice points. We have then calculated the circularly averaged quantities $S(q, t)$ and $g(r, t)$ by using standard fast Fourier transform (FFT) routines.

Figures 5.1a) and 5.1b) show time-dependent structure factors for shallow ($|U_m| = 3.5$) and deep quenches ($|U_m| = 6.0$), respectively. The computed structure factors have been normalized by a factor L^2 , where $L = 256$ is the linear size of system. In each case, we observe a peak in the structure factor. The position of the peak moves to smaller q -values as time progresses and the intensity of the peak increases. In contrast, at short length scales (large q -values), the structure factor does not evolve much at late times. For this reason, the scaling behavior of the structure factors must be examined carefully over appropriate q -values.

¹The numerical model used in this study is similar to the one used in the previous chapter. For further details the reader is referred to Section 3.2 and Chapter 4.

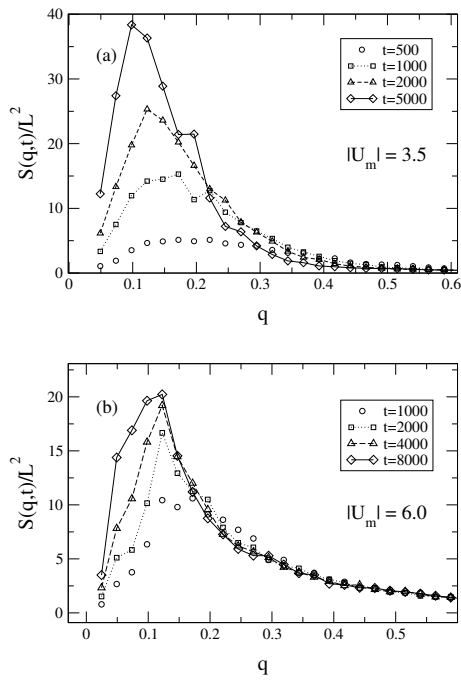


Figure 5.1. Structure factors at several times for (a) shallow $|U_m| = 3.5$, and (b) deep quenched systems, $|U_m| = 6$.

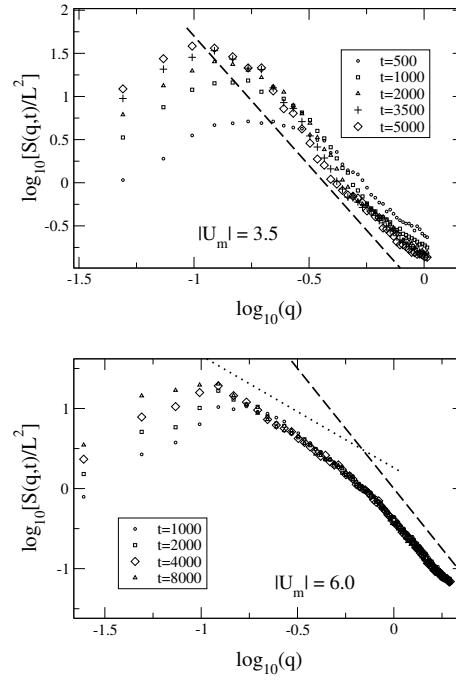


Figure 5.2. Log-log plot of the structure factors at several times for $|U_m| = 3.5$, and $|U_m| = 6.0$. Dashed and dotted lines have been added to guide the eye in the different regimes at large q -values. Dashed lines account for the Porod regime $S(q) \sim q^{-(d+1)}$ ($d = 2$), and the dotted line accounts for the intermediate regime predicted for fractal clusters $S(q) \sim q^{-D_f}$ ($D_f = 1.4$).

For the case of $|U_m| = 6.0$, the overlapping of $S(q)$ data for large q -values at different times is clearly noticeable. This almost frozen structure at short length scales is directly related to the way in which clusters aggregate after the initial transient time (see previous chapter). After an initial period, the small clusters present in the system do not go through any large change of shape or internal rearrangement due to the strong interaction potential. Then, clusters start to collide among themselves and stick in a way similar to the DLCA model without much internal rearrangements. Therefore the main changes in the system should occur at length scales larger than the former cluster size at that time. As the clusters aggregate and increase their size, the overlap of $S(q, t)$ is expected to start at smaller q -values.

Figure 5.2 shows *log-log* plots of the structure factors. Porod regime of $S(q) \sim q^{-(d+1)}$ is observed in the case of $|U_m| = 3.5$ for large q -values (see Section 1.4.1). For deep quenched systems, $|U_m| = 6$, the fractal nature of the clusters (with $D_f \approx 1.4$) exhibit a power law regime at intermediate q -values, $S(q) \sim q^{-D_f}$. With $|U_m| = 6$, we also observe a Porod's regime for larger q values, originating from the short-range crystalline packing of the monomers.

5.3 Scaling of the Structure Factor and Various Length Scales in the System

5.3.1 Growth of Compact Clusters

The time evolution of the structure factor can be characterized by using the standard scaling ansatz, Eq. 5.2. Several quantities can be proposed as representative characteristic length scales of the system: the average cluster radius of gyration $R_g(t)$, the cluster-cluster nearest-neighbor distance $R_{nn}(t)$, the first zero $R_0(t)$ of the *connected part* of the pair-correlation function (a measure commonly used in numerical studies of phase separation in binary mixtures [160]), and the inverse of the location of the peak of the structure factor, $q_m^{-1}(t)$. In order to distinguish the growing clusters from the background sea of monomers and small clusters, our calculations of $R_{nn}(t)$ and $R_g(t)$ are carried out considering only clusters of size > 4 .

Figures 5.3 (a),(b),(c) show scaling plots for time-dependent structure factors for shallow quenched systems ($|U_m| = 3.5$) using R_g , R_0 and $(q_m)^{-1}$ as characteristic length scales, respectively. The three scaling plots show the same trend: after an initial transient period, $t_i \sim 10^3 - 2 \times 10^3$, the data scale nicely onto a master curve. As shown on Figure 5.3(c), the shape of the scaling function agrees quite well with the form predicted by Furukawa [167] for shallow quenches

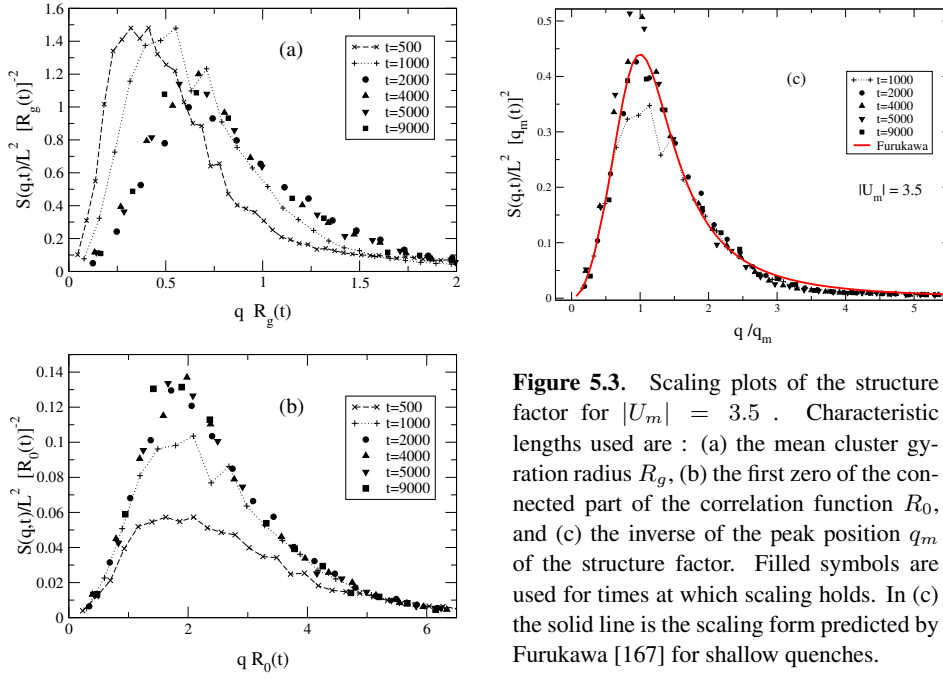


Figure 5.3. Scaling plots of the structure factor for $|U_m| = 3.5$. Characteristic lengths used are : (a) the mean cluster gyration radius R_g , (b) the first zero of the connected part of the correlation function R_0 , and (c) the inverse of the peak position q_m of the structure factor. Filled symbols are used for times at which scaling holds. In (c) the solid line is the scaling form predicted by Furukawa [167] for shallow quenches.

Since scaling seems to work well at late times with various representations of the characteristic length scale, one might conclude that a single effective length scale must exist in the system for the growth of compact clusters. Still a detailed look at the evolution of various length scales is important for a stringent test of the scaling behavior. We must add that we do not expect any deviation from scaling for the evolution of compact clusters at late times, but characterization of the various length scales for this relatively simpler system will provide insight into a more complicated case analyzed later.

In order to make sure of the existence of a single, characteristic length scale in the system, we have plotted in Figure 5.4 the temporal evolution of several *ratios* of various length scales mentioned previously. The behavior of these various ratios is similar in all cases: after the initial transient period t_i , all the length scales in the system evolve in a similar way, and are proportional to each other. In addition, Figure 5.5 shows individual temporal evolution of $R_{nn}(t)$ and $R_g(t)$ in a log-log plot where only clusters of size > 4 are considered. At late times, both quantities are observed to evolve with the same power law exponent (see Eq. 5.4), with $n_1 = n_2 \approx 0.25$. A power-law exponent of $\frac{1}{4}$ indicates that cluster growth at these times is dominated by collisions among large clusters and a corresponding reduction in the interfacial energy by surface diffusion [87].

Now we return to the origin of the breakdown of scaling at earlier times for

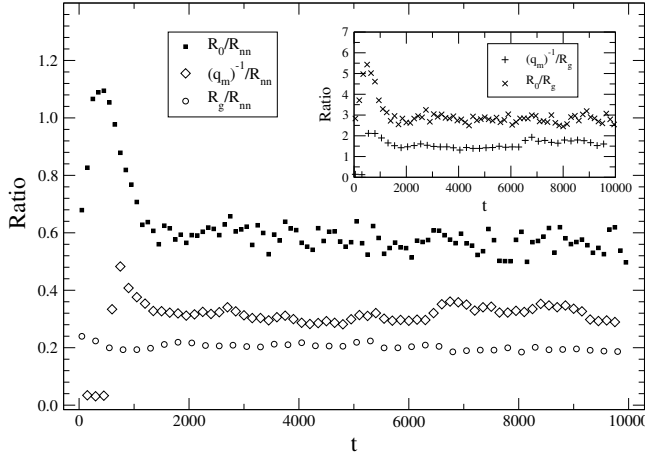


Figure 5.4. A comparison of the temporal evolution of various ratios of possible characteristic lengths: R_g , R_{nn} , R_0 , and $(q_m)^{-1}$ for $|U_m| = 3.5$.

compact cluster growth. To understand this we need to look at the temporal evolution of R_g and R_{nn} carefully. From Figure 5.5, we note that at very early times, $t < t_1 \approx 300$, R_g grows very slowly. In the next stage, $t > t_1$, cluster growth is very fast. This enhanced growth rate lasts up to a second characteristic time $t_2 \approx 1000$ after which a power-law growth of R_g with an exponent $n_1 \simeq 0.25$ is observed. Similarly, three different regimes seem to exist for the growth of the nearest-neighbor cluster distance, R_{nn} . For $t < t_1$, R_{nn} actually *decreases* before reaching a plateau. For $t_1 < t < t_2$, R_{nn} grows very fast and then, beyond t_2 , a power-law growth of R_{nn} with an exponent $n_2 \simeq 0.25$ is observed. It is in this later time regime, $t > t_2$, (i.e., the initial transient time $t_i \approx t_2$) that the system shows scaling behavior with a single, characteristic length scale.

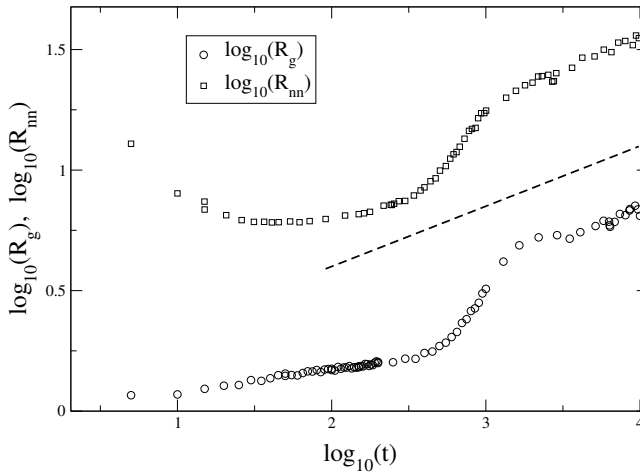


Figure 5.5. The temporal evolution of R_g , and R_{nn} for $|U_m| = 3.5$. After an initial transient period $t_i \sim 10^3 - 2 \times 10^3$, both length measures evolve closely in time as $\sim t^{0.25}$. A line of slope 0.25 has been included to guide the eye.

The three regimes observed in Figure 5.5 can be explained as follows. During

the first stage $t < t_1$, cluster nuclei are formed, and during this initiation period, the mean radius of gyration of clusters remains approximately constant. This value of R_g is expected to be close to the mean critical nucleation radius. During this period, the formation of nuclei leads to a decrease of the mean distance between clusters. This is clearly demonstrated in the observed decrease of R_{nn} at this early stage. Thus, the first regime $t < t_1$ can be identified as a nucleation period in which nucleation of small aggregates takes place. Given the different behavior of R_g and R_{nn} in this first stage, no scaling with a single length scale is possible.

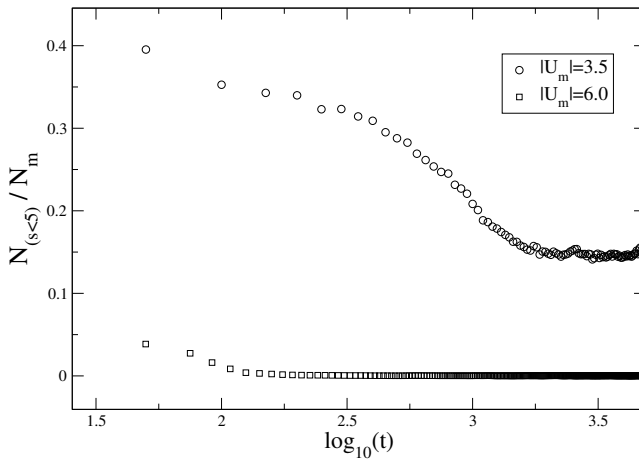


Figure 5.6. Temporal evolution of the fraction of the total number of particles present in clusters of size $N < 5$ for $|U_m| = 3.5$ and $|U_m| = 6.0$.

By plotting the total mass of the small clusters (of size < 5) versus time (Figure 5.6), we find that the characteristic time t_2 of the second stage coincides with the time when the total mass of the population of single particles and small aggregates (i.e. clusters containing less than 5 particles) reaches a steady state. This simulation result suggests that beyond this time t_2 , the net flux of small aggregates becomes roughly zero i.e., the number of small aggregates entering large clusters equals the number of small aggregates leaving large clusters. Thus, for $t > t_2$, the predominant mechanism of cluster growth is due to collision among large clusters and a subsequent reduction of the total interfacial energy as surface area minimizes. On the other hand, at least two different mechanisms contribute to the cluster growth in the intermediate regime $t_1 < t < t_2$. It is easy to show that the mechanism of collision among large clusters leads to the same growth law exponent for R_g and R_{nn} if the clusters are assumed to be compact: the free space that surrounds the new cluster after the collision grows linearly with the new size of the cluster. In contrast, a growth mechanism based on a net flux of single particles and small aggregates towards the large clusters leads to a different temporal evolution of R_{nn} and R_g . This is due to the fact that the

distance between the center of masses of the large clusters remains constant on average, but the radius of gyration grows due to the incorporation of new particles. Therefore, when both growth mechanisms are present in the system as in the intermediate stage $t_1 < t < t_2$, dynamical scaling cannot be expected, even for compact clusters, as R_{nn} and R_g would evolve differently in time. Only beyond a characteristic time t_2 , when the net flux of small aggregates becomes zero, the evolution of R_{nn} and R_g becomes proportional to each other and dynamical scaling of the structure factor holds.

5.3.2 Growth of Fractal Clusters

The scaling behavior of the structure factor for a deep quench into the two-phase region, $|U_m| = 6.0$, is showed in Figures 5.7 *a,b,c* with R_g , R_0 , and q_m^{-1} being used as measures of the characteristic length scale of the system, respectively. For fractal aggregates, the spatial dimension d in the scaling form [Eq. 5.2] is replaced by the fractal dimension D_f ; such a form has been expressed in Eq. 5.2. We note that a scaling description is meaningful only for intermediate values of q since at small length scales (large q -values) an almost frozen hexagonally-packed crystal structure is observed and the structure factor does not evolve much for large q -values at late times [see Figure 5.1b)]. At late times, data for intermediate values of q seems to fall on a master curve indicating a dynamical scaling behavior. Scaling seems to be particularly good when R_0 , and q_m^{-1} are used as characteristic length scales. Such a scaling behavior was observed previously in 2d aggregation of polystyrene colloids [164] and in numerical simulations of the DLCA model [168]. However, as we present shortly, a detailed study of the various length scales in the system suggests that this apparent scaling of the structure factor is not a signature of dynamical scaling in a strict sense.

In Figure 5.8 we show the evolution of R_g and R_{nn} versus time t in a log-log plot. It is clear that these two length scales evolve differently in time with growth exponents $n_1 = 0.52 \pm 0.03$ and $n_2 = 0.36 \pm 0.03$, defined in Eq. 5.4. How does one understand these values of the growth exponents?

As mentioned in the previous chapter, the interfacial tension driven by the surface reorganization of monomers is almost frozen for deep quenches, and the cluster shape results mainly from random cluster-cluster collisions as in a traditional DLCA model. Then, scaling arguments of Ref. [156, 158] for the DLCA model should be applicable here. For DLCA model with a Brownian coagulation kernel one finds that the homogeneity constant, λ , of the aggregation kernel is given by $\lambda = (d - 3)/D_f$ in the dilute limit. The kinetic exponent z , which describes how the mean cluster size $s(t)$ scales with time t , is in turn, related to λ as $z = 1/(1 - \lambda)$. In 3d, this provides $\lambda = 0$ and $z = 1$ as expected [138]. In 2d,

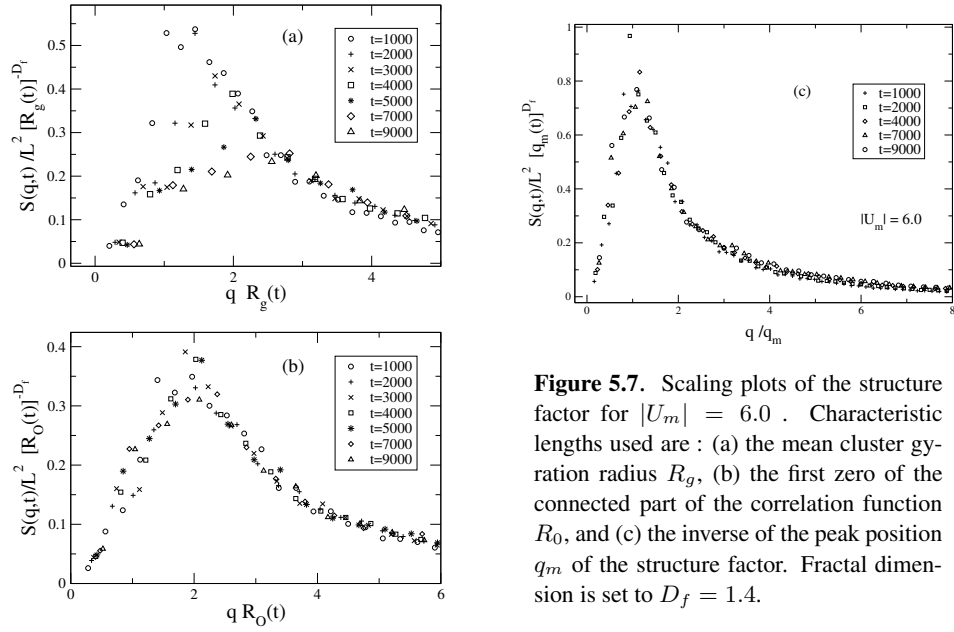


Figure 5.7. Scaling plots of the structure factor for $|U_m| = 6.0$. Characteristic lengths used are : (a) the mean cluster gyration radius R_g , (b) the first zero of the connected part of the correlation function R_0 , and (c) the inverse of the peak position q_m of the structure factor. Fractal dimension is set to $D_f = 1.4$.

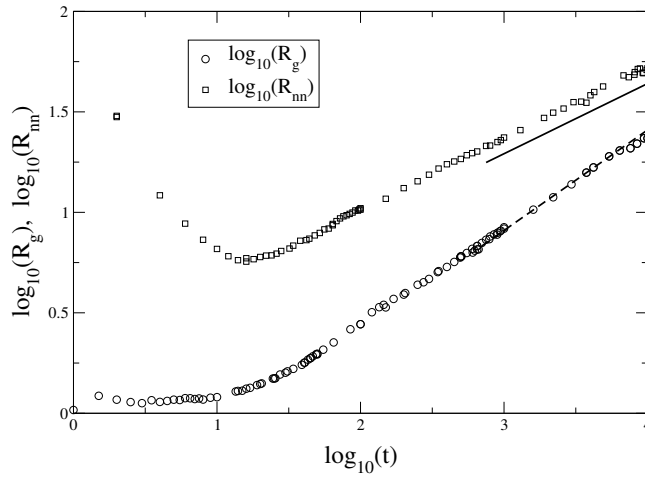


Figure 5.8. The temporal evolution of R_g , and R_{nn} for $|U_m| = 6.0$. For deep quenched systems, the evolution of R_g and R_{nn} is different with time. A solid line of slope 0.36 and a dashed line of slope 0.52 have been included to guide the eye.

however, this leads to $\lambda = -1/D_f = -0.7$ with $D_f = 1.4$ and hence $z = 0.59$ in the dilute limit. However, it is known that the kinetic exponent z increases as the system gets dense [158] i.e, as the *volume fraction occupied by the clusters*, f_v^c , increases. For an intermediate value of f_v^c ($0.1 < f_v^c < 1$), scaling arguments yield $z \simeq 1.28$ in 3d and $z \simeq 0.67$ in 2d. In the previous chapter we have seen how the AO model yield a z -value rather similar to the 2d scaling result in the intermediate regime mentioned above and also to the kinetic exponent obtained in large-scale 2d DLCA simulations with a fair degree of cluster crowdedness [159].

The kinetic exponent z is related to the growth exponent n_1 for the temporal evolution of the mean cluster radius of gyration, R_g . In the scaling description of DLCA, $n_1 = z/D_f$. Following results depicted in the previous chapter, if we consider $z = 0.74$ and $D_f = 1.4$ in 2d, we obtain $n_1 = 0.53$ in excellent agreement with the observation of Figure 5.8. On the other hand, R_{nn} scales as $N_c^{-1/d}$ where N_c is the number of clusters at time t . Since the total number of monomers is constant in the system, one can write $R_{nn} \sim s^{1/d}$ where s is the mean cluster size at time t . As $s \sim t^z$, one obtains $R_{nn} \sim t^{z/d}$. Thus, $n_2 = z/d = 0.37$ in 2d, again in good agreement with the value obtained in Figure 5.8.

Since $n_1 \neq n_2$, it is clear that a single characteristic length does not exist in the system. This is a consequence of the fractal nature of the clusters [166]. The breakdown of scaling is further demonstrated in Figure 5.9 by plotting *ratios* of various length scales in the system. As expected, R_g/R_{nn} is not a constant in time but rather grows with an exponent given by $n_1 - n_2 = 0.16$. Similarly, the ratio R_0/R_g shows clear time dependence. It is interesting to note that both q_m^{-1}/R_{nn} and R_0/R_{nn} show weak dependence on t . This indicates that, both q_m^{-1} and R_0 are closely related to one of the characteristic length scale of the system, namely, R_{nn} . We will address this point further in the next section.

Now that we clearly demonstrate the existence of more than one length scale in the system, why does the structure factor shows scaling as illustrated in Figure 5.7? Note that, as shown in Figure 5.8, the two length scales R_g and R_{nn} approach each other as time progresses. Since their ratio R_{nn}/R_g grows weakly with time t , the relative difference between these two length scales tend to decrease as time increases. This opens up a window in time where these two length scales are of similar magnitude, and scaling over this limited time interval seems to satisfy. Dynamical scaling as a general principle fails to describe the growth of fractal clusters.

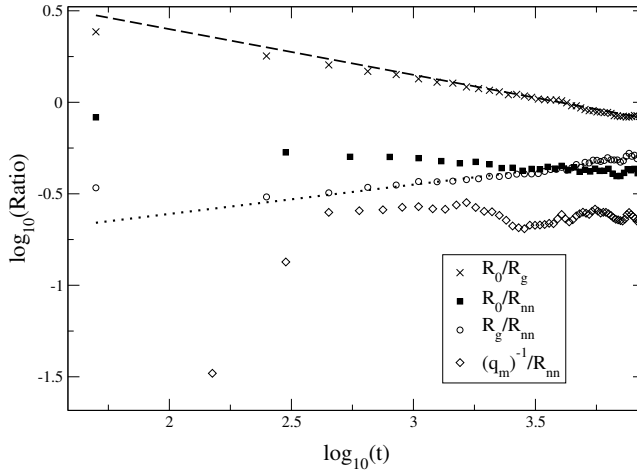


Figure 5.9. A comparison of the temporal evolution of various ratios of possible characteristic lengths: R_g , R_{nn} , R_0 , and $(q_m)^{-1}$ for $|U_m| = 6$. Dashed and dotted lines are guides to the eye with slopes -0.25 and 0.16 , respectively.

5.4 Origin of the Peak in the Structure Factor

HOS has explained the presence of a peak in the structure factor by writing the total structure factor for *monodisperse* systems as a combination of two structure factors: the single-cluster structure factor S_{sc} , which involves the cluster radius of gyration R_g as the characteristic length, and the cluster-cluster structure factor S_{cc} , which involves the mean nearest-neighbor distance R_{nn} as the characteristic length.

Accordingly to HOS, Figure 5.10(a) shows a sketch of the single-cluster structure factor (i.e. as if the cluster was isolated, or the system was very diluted). At low q there is a q -independent Rayleigh regime in which the characteristic length scale of the scattering q^{-1} is much larger than any characteristic size in the cluster, therefore monomers scatter coherently and the structure factor is proportional to the square of the number of monomers contained in the cluster N^2 . This Rayleigh regime ends about $q \sim R_g^{-1}$ because the characteristic length scale of the scattering q^{-1} becomes comparable to the characteristic size of the cluster. When $q > R_g^{-1}$ Porod scattering occurs with a slope of $-(d+1)$ if the cluster is compact and therefore have a definite surface or with a slope $-D_f$ if the cluster has a fractal nature (see Section 1.4.1). Figure 5.10(b) shows a sketch of the cluster-cluster structure factor S_{cc} . For very low q -values, $q < L^{-1}$, where L is the size of the system, the characteristic length scale of the scattering q^{-1} is much larger than any characteristic size in the system and the clusters are considered to scatter coherently. In this regime S_{cc} is expected to be a constant equal to the square number of scatters N_c (the number of clusters in the system). For $L^{-1} \leq q < R_{nn}^{-1}$ the system exhibits the Porod regime of the scattering volume, $S_{cc} \sim q^{-(d+1)}$. When $q \gg R_{nn}^{-1}$ we will have an incoherent addition of N_c

waves that will result in $S_{cc} \sim N_c$. The most tricky regime is the zone in which $q \sim R_{nn}^{-1}$. If the system of clusters were not structured at all, we would also have in this zone $S_{cc} \sim N_c$. In contrast, if the system of clusters were perfectly structured, we would have for $q > R_{nn}^{-1}$ an oscillatory behavior with minima at πR_{nn}^{-1} , $3\pi R_{nn}^{-1}$, \dots , and maxima at $2\pi R_{nn}^{-1}$, $4\pi R_{nn}^{-1}$, \dots . When clusters are neither random positioned nor perfectly correlated, damped oscillations are expected. HOS have shown that in moderately structured systems what remains of the oscillations is a dip below a shoulder near $4.5R_{nn}^{-1}$ which is in the middle of the first minima and the first maxima of the hypothetical oscillations.

Figure 5.10(c) shows the regimes that emerge from the product of S_{sc} and S_{cc} . In moderately structured systems, a peak is expected in the structure factor. But notice that the peak location does not represent any new length scale of the system. HOS claim that q_m^{-1} is not an independent characteristic length scale, but rather can be expressed as a linear combination of R_g and R_{nn} . In addition HOS conjectured that previous explanation applies not only to dense aggregating colloids, but also to other systems like spinodal decomposing fluids. Thus, the use of q_m^{-1} in these systems to infer kinetic information may be dangerous.

Figure 5.11 shows the comparison of the total structure factor with the product $S_{cc} \times S_{sc}$ for deep quenches at $t = 5000$. The inset of Figure 5.11 shows S_{cc} and S_{sc} separately in a log-log plot. The cluster-cluster structure factor S_{cc} , has been computed by considering the centers of mass of the clusters as scattering points. The single cluster structure factor S_{sc} has been obtained by computing the individual cluster structure factors and averaging over all clusters. As it is shown in Figure 5.11, the product $S_{cc} \times S_{sc}$ is a reasonably good approximation for the total structure factor for large q -values. The inset of the Figure 5.11 shows the two power-law regimes for S_{sc} : a regime in which $S_{sc}(q) \sim q^{-D_f}$ and at larger q -values, a regime in which $S_{sc}(q) \sim q^{-(d+1)}$ according to Porod's Law, originating from the short-range crystalline order in the aggregates. S_{cc} on the other hand, flattens out at a q value around $4.5R_{nn}^{-1}$, in good agreement with HOS.

Unfortunately, the measured value of $S_{cc} \times S_{sc}$ does not reproduce the observed peak in the total structure factor from the simulation. Instead, this product shows a monotonically decreasing function. One possible reason for this disagreement at *small* q -values is a larger *polydispersity* of cluster sizes for deep quenches. In contrast, in shallow quenched systems ($|U_m| = 3.5$) one finds polydispersity to be smaller if we do not take into account the sea of small aggregates and single colloidal particles that surround the large clusters. Figure 5.12 illustrates this point by comparing the mass fraction of monomers associated to clusters of size N for $|U_m| = 3.5$ and $|U_m| = 6.0$ when $t = 1000$. Therefore, $|U_m| = 3.5$ seems to be a more suitable system for testing HOS predictions (in-

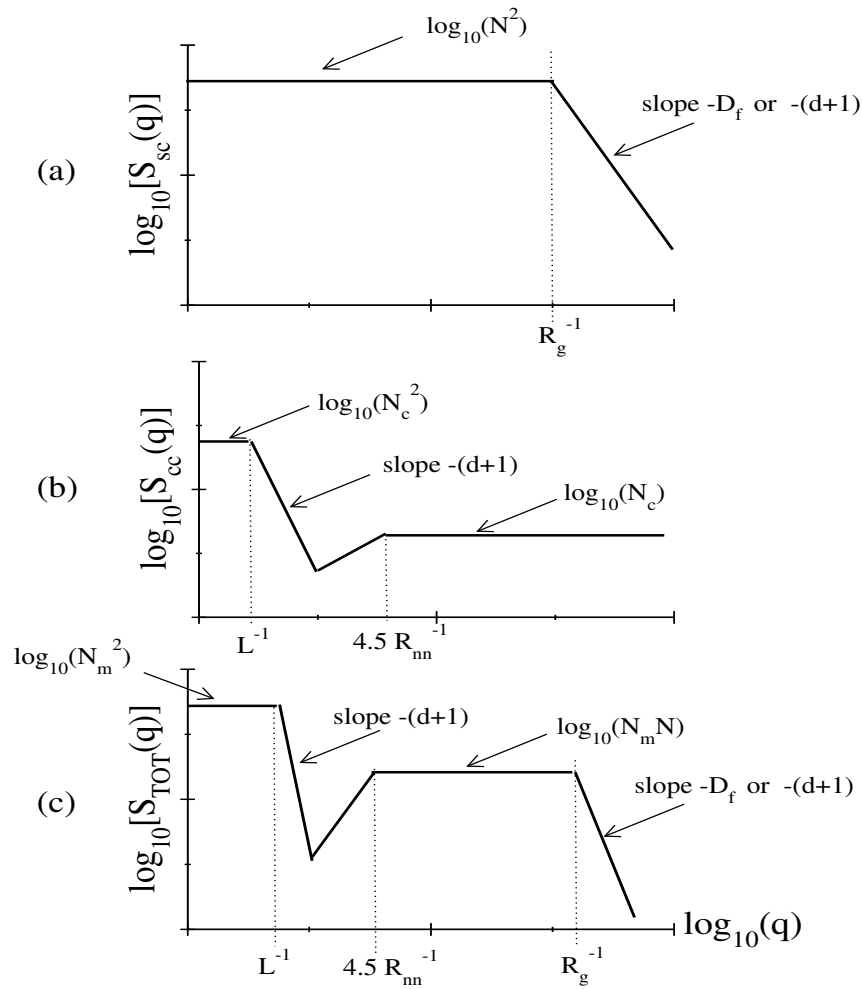


Figure 5.10. Sketch of the different structure factors as a function of wave vector q according to HOS work. (a) Structure factor of an isolated single cluster S_{sc} , (b) cluster-cluster structure factor S_{cc} in which only the centers of masses are considered as scatters, (c) total structure obtained when S_{sc} and S_{cc} are multiplied.

tended to monodisperse systems). Figure 5.13 shows a comparison of the total structure factor for $|U_m| = 3.5$ at $t = 5000$ with the product $S_{cc} \times S_{sc}$ where only clusters larger than $N > 30$ are taken into account. The inset of the Figure 5.13 shows the behavior of S_{cc} and S_{sc} in this case. The dashed line shows the predicted Porod regime for S_{sc} in the case of compact clusters: $S_{sc}(q) \sim q^{-(d+1)}$. S_{cc} again flattens out at a q value around $4.5R_{nn}^{-1}$, in good agreement with HOS. In this case, we observe that the product $S_{cc} \times S_{sc}$ reproduces the peak of the total structure factor. Thus it is quite possible that the absence of the peak in the product $S_{cc} \times S_{sc}$ for $|U_m| = 6$ is due to the polydispersity in the cluster size.

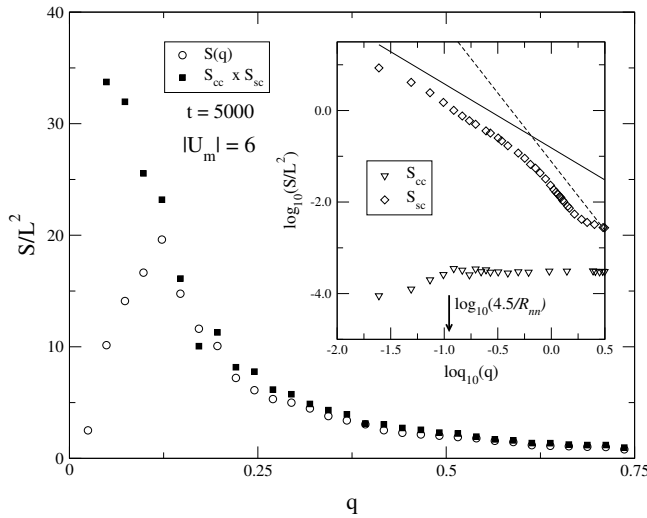


Figure 5.11. The structure factor obtained for $|U_m| = 6.0$ at time $t = 5000$ is compared with HOS prediction $S = S_{cc} \times S_{sc}$. The inset depicts the behavior of S_{cc} and S_{sc} separately in log-log plots. In the inset two lines are plotted to guide the eye for S_{sc} : dashed line stands for a slope equal to $-(d+1) = -3$, and solid line stands for a slope equal to $-D_f = -1.4$. S_{cc} flattens out at a q value around $4.5R_{nn}^{-1}$.

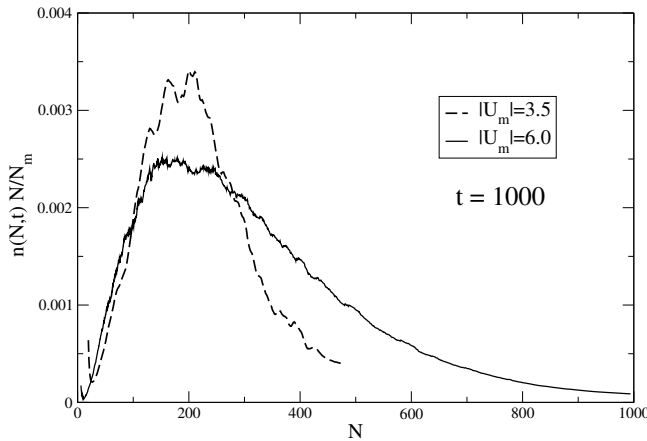


Figure 5.12. Comparison of the mass fraction associated to clusters of mass N , $(n(N,t)N)/N_m$, for $|U_m| = 3.5$ and $|U_m| = 6.0$ when $t = 1000$. The cluster distributions $n(N,t)$ have been presented previously in chapter 4.

In our simulations for both shallow and deep quenches, the peak position q_m^{-1} is found to be closely related to the nearest neighbor cluster-cluster separation

R_{nn} . For compact cluster growth, there is only one length scale in the system and thus q_m^{-1} can also be expressed in terms of the mean radius of gyration of the growing clusters. For fractal cluster growth, there are two independent length scales but over the simulation time, q_m^{-1} is found to be proportional to R_{nn} .

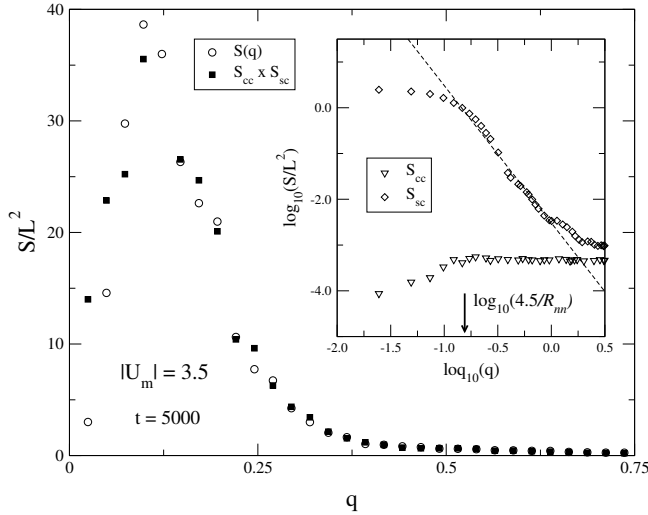


Figure 5.13. The structure factor obtained for $|U_m| = 3.5$ at time $t = 5000$ is compared with HOS prediction $S = S_{cc} \times S_{sc}$ where only clusters larger than $N > 30$ has been taken into account for the calculation of S_{cc} and S_{sc} . The inset depicts the behavior of S_{cc} and S_{sc} separately. A dashed line with a slope equal to $-(d+1) = -3$ is shown to guide the eye. S_{cc} flattens out at a q value around $4.5R_{nn}^{-1}$.

5.5 Concluding remarks

An important result of this chapter is the demonstration that aggregating colloids exhibit a true structure factor scaling only when the growing clusters are compact. This can be achieved for shallow quenches into the two-phase region of a depletion-driven colloid. For such quenches, true scaling occurs after an initial transient time. This transient period covers nucleation of clusters and growth mainly by incorporating monomers and small clusters in the growing nuclei. In this regime, R_{nn} and R_g grow differently with time and scaling does not work. After the transient period, the predominant mechanism of cluster growth is collision among large clusters and the subsequent surface reorganization of clusters to reduce the interfacial tension. This process leads to a similar temporal evolution of R_{nn} and R_g , and a single length scale can be observed in the system. Dynamical scaling is thus satisfied.

For deep quenches, the magnitude of the interaction potential between colloidal particles is much larger than thermal energy $k_B T$. Thus, both rearrangement and fragmentation of clusters are practically frozen and the growing clusters are fractals over long periods of time. Simulation results show that cluster growth in this regime is controlled by two characteristic lengths R_{nn} and R_g that evolve

differently with time. True dynamical scaling is thus not possible although an apparent scaling of the structure factor is observed when these two length scales are comparable in magnitude.

Another important result of this study is to understand the shape of the total structure factor. In this respect, our results are compared with the predictions of HOS. HOS predict that the total structure factor for a monodisperse system can be described as a product of the cluster-cluster and the averaged-single-cluster structure factors, each with its own characteristic length. In the HOS formulation, the peak in the total structure factor arises due to the overlap of these two contributions. Simulation results show that this description works for monodisperse systems but seems to break down for polydisperse cluster size distributions.

Chapter 6

Spherical polymer brushes I: The pair-wise interaction

Spherical polymer brushes (see Figure 6.1) are a particular but extremely interesting case of colloidal particles. The present and the next chapter are intended to increase the knowledge we have about the statistical properties of such colloidal particles. In this chapter we characterize the pair-wise interaction of spherical polymer brushes in the almost unexplored regime in which polymer chains and the brush-core have sizes roughly of the same order of magnitude. Next chapter will focus on the interactions associated with encapsulated spherical polymer brushes.

The objective of this chapter is two fold. First, to check, compare and determine the range of validity of the existing theories; and second, to obtain the interaction profile in the whole range of distances for systems where the curvature effects are relevant. As we have pointed out in previous occasions, besides many applications have been found for spherical polymer brushes, the nature of their interactions is still partially understood. We will show in this chapter, when two particles are brought to a very close distance, the interaction is well described by the Witten and Pincus theory [169], whereas when the particles are far enough apart, the behavior is reproduced by an extension of the Flory theory for dilute polymer solutions. We will compare the overall behavior with the predictions of the phenomenological Doroszowski and Lambourne theory [170]. In addition we will show that the characteristic size of an unperturbed spherical brush follows the same scaling found in the star polymer systems approximation.

6.1 Introduction

The structure and dynamics of polymer brushes have been the subject of considerable experimental and theoretical activity in the last years. Polymer brushes are characterized by a high concentration of end-grafted polymers onto a non adsorbing surface. The constrained geometrical environment limits the available space the polymers can occupy forcing the chains to stretch out, normal to the surface, forming a brush (see Section 2.7). The introduction of curved geometries results in polymer brush structures whose properties differ significantly from those at flat surfaces. This is mainly due to the increased volume available to the stretched polymer as it moves away from the interface. The geometry of the surface determines the particular properties of a curved-brush. Nature, as well as man made objects, offer multiple examples of curved-brush structures that can be roughly approximated by simple geometries like inward/outward cylindrical or spherical brushes as well as onion-skin structures¹ (see Figure 6.2).

Spherical brushes are a case of special interest which have been found to be particularly relevant in many aspects of polymer science and technology [171–176], just to mention:

- The stabilization of colloidal systems². An effective way of stabilization can be achieved by *end-grafting* polymer chains to colloidal particles (spherical brushes), see Figure 6.3. Polymer adsorption is another alterna-

¹There are many examples of curved-brush structures, just to mention: nanotubes with grafted polymers, and amphiphilic brushes made of poly(acrylic acid)-b-poly(n-butyl acrylate) are examples of outward cylindrical brushes. Membrane pores with grafted polymers are examples of inward cylindrical brushes. In reference to spherical brushes, many examples of outward brushes have been given in Chapter 1, in turn the molten liquid core of diblock micelles are examples of inward spherical brushes. Onion-skin structure can be achieved for instance by mixing diblock PVP-PEO molecules with diblock micelles (hydrophobic core plus a PVP outer shell) at moderate and high pH values.

²Stable colloidal systems are desired in a wide range of areas such as paints, glues, food emulsions, and pharmaceuticals. In a paint, for example, a controlled level of aggregation is important in both the application of the paint and its storage in the container. In the case of the application of the paint, the level of aggregations controls the degree of thixotropy of the fluid and permits the paint to "thin" under the shearing influence of the paintbrush or spray gun. Once applied, it thickens, preventing the drip or sag of the paint on the surface. In the case of storage before and during the application, is important that pigments do not sediment eliminating the need to stir the paint continuously. The dispersion and stabilization of small particles in nonionizing media is a question relatively old. As early as 1900, Spring [Spring, M. W. Recl. Trav. Chim. Pays-Bas, **19**, 204, (1900)] speculated that hydrophobic particles are prevented from flocculating by solvated shells on their surfaces.

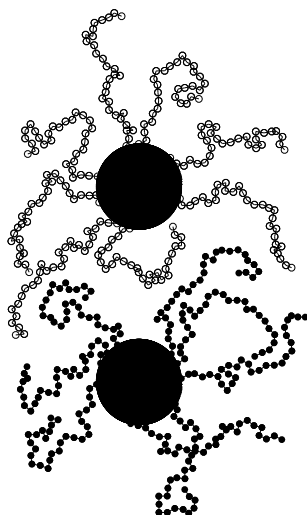


Figure 6.1. Schematic representation of two spherical brushes separated a distance R . Each brush consists on f polymers of length N grafted to a spherical surface of radius r_c .

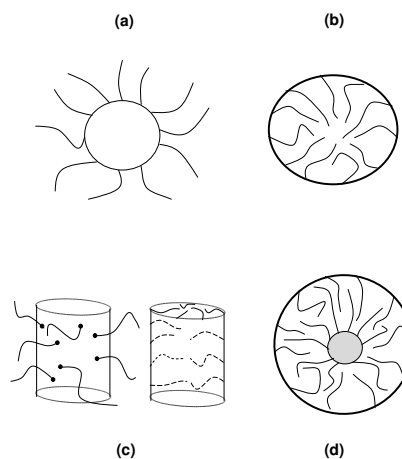


Figure 6.2. Several types of curved-brush structures: (a) outward spherical brush, (b) inward spherical brush., (c) outward/inward cylindrical brushes, and (d) onion-cell brush structure.

tive but as we commented in Chapter 1 it may not have the desired effect of repulsion, indeed, adsorbed polymers can easily produce strong attraction between them [171, 177, 178]. When spherical brushes are used, the chains are chosen to repel both the surface and other chains. This requirement is fulfilled in the presence of a good solvent with a lower surface energy compared to the one of the polymer with the surface. Thus, the effective repulsion between two polymer brushes provides the force required to overcome van der Waals attractive forces.

- Potential drug carriers. Sterically stabilized liposomes are used for drug delivery [176, 179]. Recent experiments have shown that by grafting polymers on liposomes, the circulation time of liposomes in the blood stream can be substantially increased resulting in enhanced drug delivery properties.
- The use of the light-scattering properties of coated spherical particles has been found to be a useful and non-destructive way to probe and size systems ranging from blood cells to paper whiteners [180].
- Chromatography: Alkyl grafted silica particles have been used for gas phase chromatography mainly as stationary phases for high performance liquid chromatography, and it represent about the 80 % of separations.
- Biotechnology: spherical polymer brushes have been found to be useful

in the immobilization of enzymes and antibodies minimizing the adverse effects in their functionality [181].

- Spherical brushes formed by colloidal poly-(methyl methacrylate) spheres with a grafted layer of poly-(12-hydroxy stearic acid) (PMMA-PHSA) has served as a model to emulate hard-spheres minimizing the effect of van der Waals forces [182].

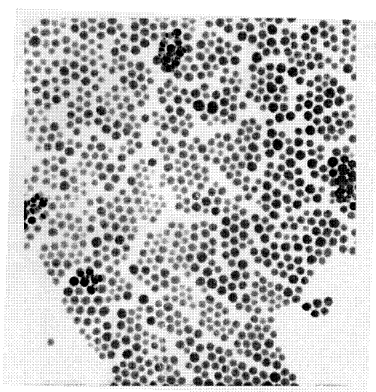


Figure 6.3. Electronic micrograph of sterically stabilized silica. Grafted chains are made from TEPA-terminated polyisobutene ($TEPA = \text{tetraethylenepentamine}$). Polymers are attached to the silica surface that is covered with silanol groups, via its TEPA end group. Taken from H. De Hek and A. Vrij, *Journal of Colloids and Interface Science*, **79**,1,1981.

In addition, spherical polymer brushes are found to display a rich physical behavior, for instance, colloidal silica spheres with grafted alkane chains has been observed to suffer aggregation and cluster formation [183] as well as a sol-gel transition in hexadecane solution [184].

Therefore, the understanding of interactions between brush-polymers are essential for tailoring polymer additives and polymer-induced forces in chemical, medical and materials sciences applications.

From a theoretical point of view, polymer chains anchored onto planar surfaces (flat brushes) were the first type of grafted polymers whose properties were studied in detail by physicists. The scaling properties of planar brushes were initially worked out by de Gennes and Alexander [185, 186]. Immediately after, Semenov [187], Milner-Witten-Cates [188, 189] and Zhulina-Priamitsyn-Borisov [190, 191] developed a self-consistent field theory, predicting a parabolic form for the density profile and obtained an expression for the free energy of two interacting flat brushes. Their predictions were well supported by Monte Carlo [192–195] and molecular dynamics [196] simulations.

Whereas for concave grafting surfaces (a surface that curves towards the polymers) Semenov found that it was possible to use the same interacting potential used for flat brushes, for convex surfaces it was not possible to obtain a self consistent solution under melt conditions [187] that gave a physical distribution of free-ends near the grafting surface. Since then, there have been several attempts to

determine the rheological properties and the effective interaction between spherical brushes. However, the validity of the results obtained were restricted to specific limiting cases.

The monomer concentration profile given by Daoud and Cotton [197] was derived assuming a star shaped polymer. Witten and Pincus [169] (to be referred as WP) derived an expression for the effective interaction potential in the regime where the chains extend far beyond the diameter of the colloidal particles. More recently, Borukhov and Leibler [198] studied the interaction between spherical brushes in the Derjaguin approximation [12], whose validity is limited to systems with small curvature effects.

Numerical models can help us in studying the properties of these systems and test the validity of previous theories. Simulations have been proved to be of confidence in the case of flat brushes, thus, they are expected to be also useful in the case of spherical brushes. But, before presenting our results and the methods used to obtain them, let us review in some detail which theories have been formulated describing those systems and some of the relevant experiments done up to the present. This knowledge will provide a good insight into the topic of spherical brushes and will allow us to better understand the intrinsic difficulties in the study of these systems and to clarify what still remains unclear.

6.2 Theoretical review

In this section we will review in detail the theoretical developments and formalisms designed to deal with end-grafted polymers onto spherical particles. Namely, we shall focus on self-consistent and scaling based theories. The latter will cover the Flory theory for diluted polymer solutions and the phenomenological theory of Doroszkowski and Lambourne.

6.2.1 Self-Consistent Field theories

Self-consistent field (SCF) theories are based on mean field approximations, that is, monomer interactions are emulated by a background potential that depends on the monomer concentration. The mean-field model is known to fail for very dilute solutions [95] and must be corrected when there are strong spatial fluctuations. These fluctuations are expected to be produced near the chain-end of the brush, and also probably near the grafting surface due to the so called wall effects. As a consequence, if the distance between two brushes is large enough, fluctuations in density around the interacting region will turn important, and the force profiles obtained might be erroneous. Furthermore, SCF methods have an

inherent problem. Due to the accumulation of monomers in the space between the two brushes, non linear dependences on the concentration may turn important and change the mean-field potential, this effect will increase as the relative distance between the two brushes decreases.

Basically, all the self consistent field theories and methods applied to spherical brushes can be considered following one of the next development-layouts:

- Taking, as starting point, the flat geometry and apply the Derjaguin approximation.
- On the basis of a lattice model.
- Using analytical approaches (the genuine mean-field).
- On the basis of a diffusion type equation.
- Minimizing the brush free-energy.

6.2.1.a SCF: a flat surface as a starting point

SCF theories have been applied to curved surfaces based on simple corrections to the flat case. One of the most extended corrections is the Derjaguin approximation [12]. This approximation applies when the radius of the colloidal particles is much larger than their relative distance. Let's consider two spheres of radii R_1

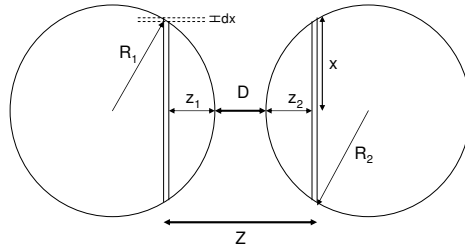


Figure 6.4. Schematic plot of the Derjaguin approximation for the interaction between two colloidal particles.

and R_2 separated a distance D between their surfaces, such as, $D \ll R_1, R_2$ (see Figure 6.4). The force between the two spheres can be obtained by integrating the force between small circular regions of area $2\pi x dx$, ($0 < x < R_i$), perpendicular to the axis that join the two core-centers. The small circular regions have their centers located at a distance z_1 and z_2 from R_1 and R_2 respectively. Thus, their relative distance is $Z = D + z_1 + z_2$. At this distance, both circular regions are taken locally flat, thus:

$$F(D) = \int_{Z=D}^{Z=\infty} 2\pi x f(Z) dx \quad (6.1)$$

where $f(Z)$ is the normal force per unit area between two flat surfaces. Since $x^2 \approx 2R_i z_i$, $Z = D + (x^2/2)(1/R_1 + 1/R_2)$ and we can approximate $F(D)$ as:

$$F(D) = \frac{2\pi R_1 R_2}{R_1 + R_2} W(D) \quad (6.2)$$

where $W(D)$ is the energy per unit area of two flat surfaces at a distance D .

By means of the Derjaguin approximation, Ekaterina et al. [199] found an analytical expression for the interaction of two spherical brushes in the case of cores with radius larger than the polymer layer length. However, only in the case of very weak and very strong compression they found tractable analytical expressions. A mean-field analytical theory was then developed for the interaction between two colloid end-grafted particles. Ekaterina assumed that the equilibrium structure of the grafted polymer is determined by the minimization of its conformational energy. This energy contains volume interactions and elastic chain stretching terms. Ekaterina applied this formalism to the calculus of the density profiles and the conformational free energies of flat brushes. Their results were extended to the case of interacting spherical brushes by making use of the Derjaguin expression. As themselves pointed out, the use of Derjaguin approximation neglects possible chain redistributions from the interaction region to other brush zones (lateral redistributions).

It is also worth to mention the work of Milner and Witten [189] that obtained the mean and Gaussian bending moduli for spherical and cylindrical brushes by expanding in powers of the curvature the free energy of a brush on a curved surface. We might be tempted to use that expansion of the free energy in order to calculate the repulsion between two spherical brushes in the way like Milner Witten and Cates did for two flat brushes. In such case, they first deduced the free energy of a single flat brush and then measured the interaction between two flat brushes. Unlikely, a new problem nonexistent in the flat case arises. In a flat brush all the chains of a brush interact with chains belonging to the other brush due to the flat geometry. But in the spherical case, chains placed in the opposite side of one brush, may weakly interact with the chains of the other brush (and this effect is more relevant when the number of monomers per chain decreases). If calculations are done following this formalism, the force profile of two interacting spherical brushes might differ, at least, in two orders of magnitude from other SCF and Monte-Carlo simulations. Thus, the approximation derived from the free-energy expansion in powers of the curvature gives, in general, very poor results.

6.2.1.b SCF: lattice models

Originally, polymers were modeled with the free-joined step chain model on a lattice, where the generated conformations were weighted with the mean field potential. In these models nor the stiffness nor the correlations among neighbor monomers were taken into account. Chain stiffness was incorporated later in the rotational isomeric state model [200], and correlations between the nearest-parallel-neighbor-bonds were also included in the self-consistent anisotropic field [201]. They found that the chain stiffness effect and the bond correlation effect partly compensate and this fact explained why simple freely-jointed-chains-SCF methods were in a relatively agreement with Monte Carlo and molecular dynamics simulations [202].

These models were first developed for a flat lattice geometry. More recently Wijmans, Leermajers and Fler [203] developed a lattice SCF for two polymer-coated particles. As it uses a formalism based on a diffusion type equation, we will refer to it in the next section.

6.2.1.c SCF: analytical approaches

The first analytical approaches for flat brushes were developed, independently, by Zhulina et al [190, 191] and Milner et al (MWC) [188, 189]. In their formalisms, polymer chain conformations, under the assumption of strong stretching, are approximated by a set of the most likely trajectories. This assumption allows to neglect chain conformation fluctuations about the most probable path between its end points. An exception to the previous assumption may occur at the end of the brush where the concentration is small, and several chain conformations may contribute to the partition sum. In the MWC formalism [188] the action for a grafted chain is analogous to a system in which a particle is forced to follow the path described by the polymer chain from the end-segment to the grafted segment. This particle is supposed to be subject to an equal time potential, (i.e. harmonic potential). Monte Carlo simulations on flat brushes are found in good agreement with the SCF predictions except near the surface and the zone where the brush ends [204].

When these theories were tested on non planar surfaces, Semenov [187] found that the flat-potential no longer gives a self-consistent solution under melt conditions. Thus, for convex surfaces, the flat-potential leads to an unphysical distribution of free-ends (near the grafting surface the density of free ends owe be negative in such case). Semenov suggested that in these geometries, the free chain-ends should be excluded from a zone near the grafting surface in order to keep self-consistency. Following Semenov's suggestions, Ball, Marko, Milner and Witten

(BMMW) [205] developed a quantitative theory under melt conditions introducing an exclusion zone near the grafting surface. By allowing this exclusion zone in their calculus, that increases linearly with the brush thickness, BMMW were able to relate the chain configurations with the free energy in a closed form for convex cylindrical surfaces. However, for the spherical case, BMMW deduced a very complex set of equations that, to our knowledge, still remain unsolved.

Li and Witten [206] have also considered the problem of the exclusion zone in the regime of a marginal solvent. They have implemented a variational approach in order to minimize the free energy with respect to the density of free ends and respect to the polymer trajectories. Their results provide a reasonable density profile, but the free end density is qualitatively different when it is compared with numerical simulations.

6.2.1.d SCF: diffusion type equations

This formalism was first developed by Edwards [207]. In his model a polymer is described as a chain of freely-jointed segments of constant length in the presence of a potential field, where the segment probability distribution function obeys a Schrödinger type equation.

For spherical and cylindrical brushes without external constrictions, Dan and Tirrell [208] solved the Schrödinger equation finding the segment-chain density and the end-chain density profiles for several radius and grafting densities. They also found evidences of an exclusion zone near the interface. Particularly, the results for cylindrical interfaces are in good agreement with the theoretical predictions of BMMW and the exclusion zone seems to change linearly with the brush thickness in the limit of strong curvature. The same result is found for spherical brushes, however, no predictions on the exclusion thickness is done in the BMMW theory. Molecular dynamics simulations for cylindrical brushes under good solvent conditions [209] showed a narrow exclusion zone near the interface, comparable to the theoretical predictions, but only in the case of high surface density of grafted chains.

More recently, another SCF based on the Edwards formalism was applied by Lin and Gast (LG) [210] to calculate the steric repulsion between two spherical particles. To obtain the interaction potential, the density profile for the interacting brushes was calculated assuming a total density equal to the sum of the individual density brushes. Afterwards, volume fraction profiles were calculated self consistently with a mean field potential:

$$U(z) = \frac{\rho_{0S}}{\rho_{0A}} - \ln \phi_S(z) + \chi(\phi_S(z) - \phi_A(z)) \quad (6.3)$$

where ρ_{0S} and ρ_{0A} stands for the bulk number density of solvent molecules and chain segments respectively. χ is the Flory-Huggins interaction parameter. $\phi_S(z)$ and $\phi_A(z)$ are the volume fraction of the solvent and polymer segments in the layer z respectively.

Thus, the free-energy per pair of interacting chains $F(r)$ follows,

$$\frac{F(r)}{k_B T} = -2 \ln(W) - \frac{2\rho_{0S}}{f} \int_{R_{core}}^{r/2} -\ln \phi_S(z') - \chi \phi_A^2(z') dz' \quad (6.4)$$

where f is the number of chains tethered to the surface and W stands for

$$W = \int_{R_{core}}^{\infty} dz' G(z', R_{core}; N) \quad (6.5)$$

being $G(z', R_{core}; N)$ the probability of finding the segment N at the position z' , given that the chain started at the position R_{core} . $G(z', R_{core}; N)$ was, in turn, calculated by solving the diffusion equation taking $U(z)$ as the mean field potential. At this point it is worth to note that Lin and Gast used an expression for the Helmholtz free energy with an extra term in addition to the usual term $-f \ln(W)$. It was argued that this second term corrects partially for an over counting of the segment–segment interaction that arise in mean field theories.

The Helmholtz free energy obtained in this way is measured along the line that joins the two brush centers. Thus, it is possible to determine the free energy per unit area at the midpoint at different relative distances. Afterwards, the total interaction potential can be obtained by integrating over the area of overlap at the midpoint by using the classical Derjaguin approximation,

$$\frac{u(r)}{k_B T} = 2\pi \int_{D/2}^{R_{core}+D/2} (R_{core} - h + D/2) \frac{\Delta F_{mid}(h)}{k_B T} dh \quad (6.6)$$

where D stands for the core surface to surface separation in the direction that joins the two center cores, and $2h$ stands for the separation between the two circular regions.

As Lin and Gast pointed in their article, by making this approximation, they neglected all possible lateral redistributions of polymer segments. As a consequence, their calculation may overestimate the interaction potential specially for small separation of the cores.

On the other hand, Wijmans, Leermajers and Fleer (WLF) [203] developed a lattice SCF based on the Edwards formalism for two polymer-coated particles. WLF proposed a model for particles whose radii is of the same order as the polymer layer thickness. They adopted a cylindrical coordinate system where the z -axis is the axis that links the center of two particles, and the radial coordinate

gives the distance from a point to that axis. This model is a 2d–lattice model in contrast with the 1d–Lin and Gast model.

In their model, the lattice consists in parallel layers of $z=cte$, separated a distance of one polymer segment, each layer being divided in concentric rings of radius R , again separated by one polymer segment. A step probability is defined in order to connect a segment of coordinate (z, R) to a nearest-neighbor point on the lattice:

$$\begin{aligned}\lambda(z, R; z, R - 1) &= \frac{1}{6}\left(1 - \frac{1}{2R-1}\right) \\ \lambda(z, R; z, R + 1) &= \frac{1}{6}\left(1 - \frac{1}{2R-1}\right) \\ \lambda(z, R; z, R) &= \frac{1}{3} \\ \lambda(z, R; z - 1, R) &= \lambda(z, R; z + 1, R) = \frac{1}{6} \\ \lambda(z, R; z', R') &= 0\end{aligned}$$

Assuming the potential energy of a polymer segment $u(z, R)$ to depend on the translational entropy of the solvent molecules, in athermal conditions, it can be written as:

$$\beta u(z, R) = -\ln(1 - \phi_P(z, R) - \phi(z, R)) \quad (6.7)$$

where $\phi_P(z, R)$ is the polymer volume fraction profile, and $\phi(z, R)$ the core volume fraction. WLF results were obtained by solving the composition law recursively using lattice approximations described before and the assumed potential energy. As in the case of Lin and Gast, WLF also obtained predictions about the interaction between two grafted–chains particles. Both SCF results will be compared later with our numerical results.

6.2.1.e SCF: minimizing the brush free-energy

Carignano and Szleifer [211] extended the formalism developed by Ben-Shaul et al. [212], originally devoted to study the micelle formation, to the case of spherical or cylindrical brushes. In the paper of Carignano the probability distribution function of chain conformations is calculated as a function of the local osmotic pressure by minimizing the Helmholtz free energy per unit area of the system, subject to the constraint of the incompressibility of the fluid. In this formalism, the osmotic pressure was introduced as a Lagrange multiplier. They derive a system of nonlinear coupled equations which solution gives the osmotic pressure. In

order to solve such equations, a representative set of chain-configurations allowable to the system has to be generated. Despite Carignano and Szleifer obtained an expression for the free-energy they did not studied the interaction between spherical brushes. Figure 6.5 shows the density profile for a single spherical brush. In this figure we compare our Monte Carlo numerical results (see also [213]) with the Carignano and Szleifer SCF method.

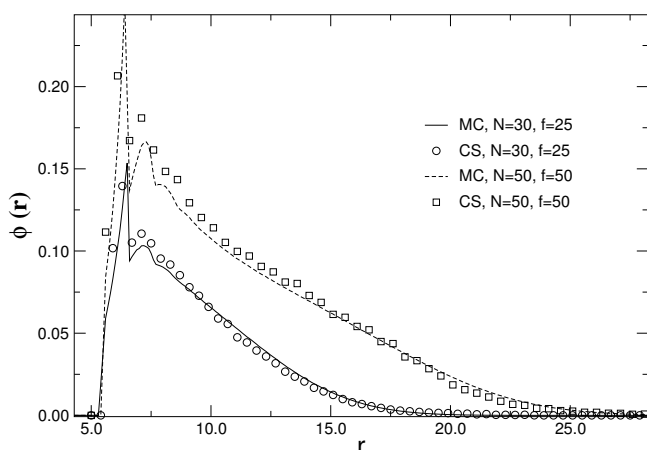


Figure 6.5. Radial monomer density profiles vs. the distance to the core center for different chain lengths N and number of grafted chains f . In this plot we compare the results of our MC simulations with the outcome of the Carignano-Szleifer self consistent field method (CS).

6.2.2 Other related theories to the study of spherical brushes

6.2.2.a The Daoud and Cotton approach

Daoud and Cotton [197] proposed a model for star-polymers. A star-polymer corresponds to the limiting case of a spherical brush in which the core has the size of a monomer. They considered that any given branch of the star can be modeled as a blob which size depends on the local concentration of monomers. Inside the blob the polymer segments are treated as a free self-avoiding chain. Whereas previous theories assumed an uniform swelling of the molecule, i.e. the blobs have all the same size, Daoud and Cotton suggested that the blobs are much more expanded in the outside brush zones than in the region near the core.

Daoud and Cotton defined blobs of increasing size as one goes from the core to the surface of the molecule through a local swelling parameter. They found that, for an isolated star containing f branches and N monomers per branch with a l_b monomer-length and an excluded monomer-volume ν , the variation of the monomer concentration $c(r)$ follows a $c(r) \sim (r/l_b)^{-1}$ variation for $f^{1/2}l_b < r < f^{1/2}\nu^{-1}l_b$, and $c(r) \sim (r/l_b)^{-4/3}$ for $r > f^{1/2}\nu^{-1}l_b$.

Daoud and Cotton found within an accuracy of 10% that their predictions agree with experimental data for star shaped polystyrene. Unfortunately, when

one compares these theoretical predictions for star polymers with the rescaled density profiles for star polymers obtained from Monte Carlo simulations the agreement is much worse [213].

6.2.2.b *Witten and Pincus theory*

Witten and Pincus [169] (WP) proposed a scaling model in which the effective interaction potential of two brushes containing each f long polymers grafted to them, depends logarithmically on the separation between the particles multiplied by an universal coefficient that depends on f . For $f \gg 1$ they calculated the free energy of one spherical brush by using the hypothesis of Daoud and Cotton. Next, they assumed that bringing the two brushes within a close distance, the bulk of the system is similar to a single brush with $2f$ chains. By making that assumption, WP found that the variation of the free-energy when the two brushes are brought from an infinite distance to a very short distance is approximately equal to the free-energy of an isolated brush. Then, by applying scaling arguments, WP found that the interaction potential between two spherical brushes is given by:

$$U(r) \approx \nu f^{3/2} \ln \left(\frac{R_0}{r} \right) \quad (6.8)$$

where R_0 is the characteristic size of an isolated brush and $\nu \cong 3/5$. This logarithmic dependence is found to be valid in the limiting cases of $f \gg 1$, but also for $f = 1$ or 2 . For intermediate values of f , WP do not provide any expression.

6.2.2.c *The theory of Flory for diluted polymer solutions*

The theory of Flory for dilute polymer solutions [93] was developed originally for polymer chains without any core or branching point (see the Flory-Huggins theory on Section 2.6.1.b). We will see later in this chapter, that this result can be used in order to estimate the interaction between two spherical brushes when they are separated a distance large enough. In such case, the effect of the hard-core spherical particle can be neglected, and only the interaction between monomers is of relevance.

A very dilute polymer solution can be regarded as a dispersion of a "clouds" of monomers. Each "cloud" corresponds to a polymer molecule, and the space among those clusters is filled by pure solvent particles. Each polymer chain may be approximated by an spherical object with a density that diminishes with the distance to the center. When we bring two of such molecules close enough; a superposition of their domains takes place. In a good solvent, monomer-solvent interactions are preferred to the pure monomer-monomer interactions. Thus, the

molecules will tend to avoid the overlapping of the domains. Flory calculated the variation of the free energy δF when two of such molecules are brought from the infinity to a distance R . In an overlapping volume δV it is given by:

$$\delta F = 2k_B T \psi_1 \left(1 - \frac{\theta}{T}\right) \rho_k \rho_l \frac{V_m^2}{V_s^2} \delta V \quad (6.9)$$

where ψ_1 stands for the entropy parameter, θ is theta-temperature, V_m is the volume of a monomer, V_s is the volume of a solvent molecule, ρ_k and ρ_l are respectively the monomer density of the brushes labeled k and l in that δV .

Integrating over all the overlapping region, assuming a Gaussian-like monomer density profile in each "cloud", the total free energy is

$$F = k_B T \psi_1 \left(1 - \frac{\theta}{T}\right) \frac{v_p^2}{V_s} \left(\frac{\beta' m^{2/3}}{\pi^{1/2} 2^{1/6}}\right)^3 e^{-R^2 \beta'^2 / 2} \quad (6.10)$$

where v_p stands for the specific molecule volume, $\beta' = 3/\sqrt{\langle r^2 \rangle}$ with $\langle r^2 \rangle$ the mean square of end-to-end distance, and m is the mass of the molecule. $\frac{v_p^2}{V_s} m^2$ is proportional to the number of monomers in the chain and R stands for the distance between the center of mass of the molecules. $\psi_1(1 - \frac{\theta}{T}) = 1/2 - \chi_1$, being $\chi_1 k_B T$ the difference between the energy of a solvent molecule immersed in pure polymer and the energy of that solvent molecule when it is surrounded by other solvent molecules. By differentiation one obtains the repulsive force between that two molecules,

$$f(R) = -\frac{\partial F}{\partial R} = k_B T \psi_1 \left(1 - \frac{\theta}{T}\right) \frac{v_p^2}{V_s} \left(\frac{\beta' m^{2/3}}{\pi^{1/2} 2^{1/6}}\right)^3 \beta'^2 R e^{-R^2 \beta'^2 / 2} \quad (6.11)$$

6.2.2.d The Doroszkowski and Lambourne phenomenological approach

A complete different approach to the study of the interaction between two spherical brushes was given by the phenomenological theory of Doroszkowski and Lambourne (DL) [170]. They assumed that as the two spherical brushes approach, the polymer chains do not interpenetrate resulting in an increase of the local monomer concentration and, as a consequence, in the osmotic pressure. The originated repulsive force is given by the change in the osmotic pressure multiplied by the contact area between the two brushes:

$$f_{DL}(R) = \Delta \Pi \pi \left(R_0 - \frac{R}{2}\right) \left(R_0 + \frac{R}{2}\right), \quad (6.12)$$

where R is the distance between the centers of the cores of both brushes. R_0 is the characteristic radial size of an unperturbed brush measured from the center of its core. $\Delta\Pi$ is the change of the osmotic pressure and it is given by a rather complicated function of the size of the interacting region. In units of $k_B T$ it reads:

$$\Delta\Pi = \frac{1}{v_1} \left(\frac{v_2^{*2} - v_2^2}{2} + \frac{v_2^{*3} - v_2^3}{3} + \mathcal{O}(v_2^4) \right), \quad (6.13)$$

where v_2 is the volume fraction occupied by the Nf monomers in an isolated brush:

$$v_2 = \frac{aNf}{\tau}, \quad (6.14)$$

being a the volume of a single monomer and τ the volume occupied by the monomer chains:

$$\tau = \frac{4\pi}{3}(R_0^3 - r_c^3). \quad (6.15)$$

and v_2^* , defined by

$$v_2^* = v_2(V_R + V_H)/V_H, \quad (6.16)$$

is the volume fraction occupied by the monomers in the compressed state. Monomers initially located inside V_R (half of the overlapping region between the two brushes) are redistributed into the volume V_H since chains are not allowed to interpenetrate (see Figure 6.6). Finally, v_1 is a constant giving the molar volume of the solvent.

The detailed expressions for the geometrical factors V_R and V_H can be easily obtained as:

$$\begin{aligned} V_R &= \frac{1}{3}\pi \left(R_0 - \frac{R}{2} \right)^2 \left(2R_0 + \frac{R}{2} \right) \\ V_H &= \frac{1}{3}\pi \left(R_0 - \frac{R}{2} \right) \left(R_0 + \frac{R}{2} \right) \frac{R}{2} - \frac{2\pi}{3} \left(1 - \frac{R}{2R_0} \right) r_c^3 \end{aligned}$$

The DL theory is, in principle, valid over all relative distances between the two brushes. However, a quantitative analysis of this model involves a truncated expansion of the change in the osmotic pressure and requires the determination of the unperturbed radial size of the brush R_0 which is usually difficult to measure with precision.

6.3 Previous experimental findings

Several papers about the physical properties of terminally attached homopolymer chains on colloidal particles have been published. Experiments on spherical brushes can be classified in three main areas:

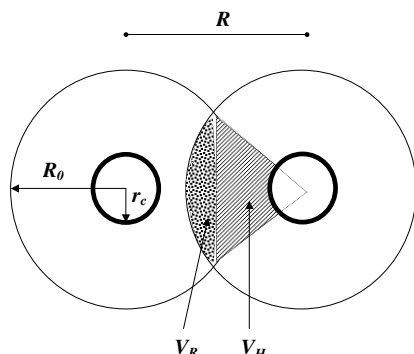


Figure 6.6. Schematic representation of two interacting spherical brushes in the DL model. R_0 is the radial size of an isolated brush; r_c is the core radius. The shadowed regions represent V_H and V_R .

- *Determination of structural properties of a single brush.* Structural properties like density profiles have been elucidated using SANS [214, 215], ESR [216, 217] and NMR [218] experimental techniques. A detailed review can be found in the work of Cohen, Cosgrove and Vincent [219]. For instance, SANS technique has been recently applied to block copolymer micelles [220]: Block copolymer micelles have been found to exhibit a well-defined corona structure, and some close analogies to the Daoud-Cotton model seems to exist.
- *Global properties of solutions containing spherical brushes.* Dispersions of spherical brushes has been observed to exhibit several interesting phenomena: Order-disorder transitions [221], flocculation [222], cluster formation-aggregation processes [183], sol-gel transitions [184], and polymer-driven phase separations [223].
- *Determination of forces among spherical brushes.* There are very few experimental measurements of the force among spherical brushes. These measurements are based on disjoining pressure methods. Disjoining pressure (osmotic pressure) methods are experiments mainly designed to determine the steric interaction between two approaching surfaces. Using such methods it is possible to determine the steric interaction between colloidal particles under compression conditions, or the thickness of a film inside a spherical shell. The compression studies need that particles are packed in some regular array. These arrays may be 2d or 3d. In the case of 2d-arrays, generally a Langmuir surface balance method is used. Particles are spread on a water/organic compound interface and the compression force is usually mechanical, hydraulic, or centrifugal. For 2d arrays, Doroszowski and Lambourne [170, 224] introduced the Langmuir surface balance technique

for latex particles carrying anchored hydrocarbon-miscible polymer chains. They found that, after several cycles of compression-decompression, the particles packed into a 2d hexagonal array on the hydrocarbon side of the interface (see Figure 6.7). In the work of Doroszkowski and Lambourne the core radius is approximately seven times the brush height when the brushes do not interact. The experimental data shows that the repulsion energy increases as the system is compressed, but it does not diverge when the spheres are close to each other, indicating that the maximum packing of the system is not reached.

For three-dimensional arrays of polymers adsorbed onto spherical latex particles, Cairns et al. [225] and Homola et al. [226] measured the particle volume fraction as a function of the applied pressure.

Later on, Evans and Napper [227] assuming an hexagonal array and additive pair potentials, showed how the theoretical free energy can be written in terms of disjoining pressures P_d . The assumption that pair potentials are additive ignores any non additive effect in the many-particle interactions. Nonetheless, there is a way to transform experimental disjoining pressures into pair potentials:

$$P_d = \frac{-1}{\sqrt{2} \left(a + \frac{d_o}{2}\right)^2} \frac{\partial V_T}{\partial d_o} \quad (6.17)$$

where V_T is the total potential energy between pairs of particles, a is the particle radius and d_o is the minimum separation distance between the surfaces of two adjacent particles. The preceding expression does not take into account the disjoining pressure coming from the configurational entropy of the particles, by means the disjoining pressure due to the motion of the centers of mass of the particles. An approximation to that value is done applying the Percus-Yevick equation. Usually this contribution to the disjoining pressures is an order of magnitude smaller than the repulsive pressures, and only in the case of weakly repulsions the configurational entropy of the particles is of relevance.

It is also worthwhile to comment that spherical brushes have been used to emulate specifically hard-spheres [182, 228–232]. Generally, these studies use spheres of colloidal poly-(methyl methacrylate) with grafted chains of poly-(12-hydroxy stearic acid) (PMMA-PHSA) with ratios *Core – radius/Brush – height* ranging from 25 to 60. The core diameter is about $1\mu m$ and the grafted layer about $10nm$ thick. The short grafted layer neutralizes the attractive van der Waals forces among colloids and in turn it provides a short-ranged strong

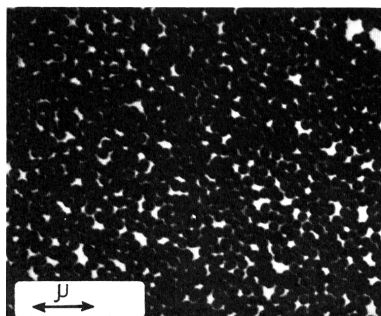


Figure 6.7. Electronic micrography showing the hexagonally close packed particles. The holes are due to the surface friction that suffers the particles that arises from the solvated barriers, which attract one to each other. Taken from [224].

repulsion among particles that mimics the hard-sphere potential. If the ratio $core - radius / chain - length < 5$, then severe deviations from the hard sphere behavior are evident, even selecting properly the chains. When curvature increases, the brush properties change dramatically as for instance the repulsive force they are able to exert.

6.4 Interaction between two spherical brushes

In the previous sections we have reviewed the state of the art of the research on spherical brushes. We have also seen that for convex surfaces the mean field potential used in planar surfaces leads to unphysical results. In cases where the chain extent is much smaller than the core diameter, Ekaterina et al. [199] showed that is possible to obtain tractable expressions for the interaction between two spherical brushes by using the Derjaguin approximation. However, this approximation turns out to be wrong as the core diameter reduces and curvature increases. On the other hand, in the limit of very long chains in comparison to core size $core - radius / chain - length \ll 1$, it has been shown that a good description of such brushes can be done in terms of a star polymer.

None of the previous theories or formalisms has been proven to give a successful description of the interaction in intermediate cases in which the chain extent is of the same order of the core radius. To our knowledge, just the work of Wijmans-Leermakers-Fleer [202] (WLF) studied this intermediate regime. Their results based on lattice SCF calculations have not been contrasted with other results up to now, and we should keep in mind that SCF formalism does not account for the monomer correlations, and therefore, possible deviations from the WLF results can be expected.

In the theoretical review we have presented some promising theories that could model properly the interaction between spherical brushes in the intermediate regime in which the chain extent is of the same size of the core. Namely,

the Witten-Pincus theory (WP) based on the Daoud-Cotton formalism for star polymers, and the Flory theory for diluted polymer solutions. Particularly, the Flory theory, giving the interaction between two globular polymers, is previous to 1953, and no one has previously tried to use these results to study the interaction of spherical brushes. The hypothesis involved in the WP and the Flory theories basically imply that one expects the WP to give a good representation of the interaction profile at short distances, whereas an extension of the Flory theory could work in the case that the two brushes are separated enough that the dilute monomer concentration criteria can be applied. A question that raises is to determine the range of validity of both theories. An answer to this question will be presented here. Worth to consider is the theory of Doroszkowski and Lambourne (DL). The DL theory has been in the forgetfulness for about thirty years, partly due to its complex formalism. However, it has the advantage respect to the WP and Flory theories, to be valid in the whole range of distances separating the two brushes. DL performed in the same work four experiments measuring the interaction between four chemically different kinds of spherical brushes. Unfortunately, DL only reported data at two distances between brushes: at a small separation where the cores were nearly in contact, and at large distances beyond the average brush thickness.

It is convenient for the sake of the comparison with our Monte Carlo results to rewrite the key expressions of Flory and WP theories as follows:

- WP proposes an interaction potential between the two brushes that depends logarithmically on their separation,

$$V_{\text{WP}}(R) = A \ln \left(\frac{R_0}{R - 2r_c} \right). \quad (6.18)$$

being R is the distance between the centers of the colloidal particles, and r_c the core radius. Thus, the force is simply given by:

$$F_{\text{WP}}(R) = \frac{A}{R - 2r_c}. \quad (6.19)$$

The constant A was found to follow a power-law dependence with the number of grafted chains f ,

$$A \sim f^{3/2}. \quad (6.20)$$

- Flory assumed that for very dilute polymer solutions, each polymer can be seen as a collection of monomers forming a rather spherical object characterized by a Gaussian-like monomer density profile. Bringing together two of such polymers might eventually result in an overlapping of the domains.

Hence, in the presence of a good solvent, a repulsive force appears between them. The derived expression for the force in units of $k_B T$ takes the form:

$$F_r(R) = CR e^{-DR^2}, \quad (6.21)$$

where C and D are constants described by:

$$C \sim \frac{M^2}{\langle r^2 \rangle^{5/2}}, \quad (6.22)$$

and

$$D \sim \frac{1}{\langle r^2 \rangle}. \quad (6.23)$$

M is the mass or the total number of segments inside the globular polymer, and $\langle r^2 \rangle$ is the averaged end-to-end square distance of a polymer of length N . We can apply this result to the case of two interacting spherical brushes provided that they are sufficiently apart not to feel the presence of the inner core of the brush. Under these circumstances, we can take $M = Nf$ in the above expression, and $\langle r^2 \rangle$ can be defined as twice the averaged square distance of the monomer chain-ends forming the brush to the core,

$$\langle r^2 \rangle = 2 \frac{\int_0^\infty r^2 \epsilon(r) d^3 \vec{r}}{\int_0^\infty \epsilon(r) d^3 \vec{r}}, \quad (6.24)$$

where $\epsilon(r)$ is the chain-end monomer concentration.

In this chapter, we shall present the results of extensive three-dimensional off-lattice Monte Carlo simulations of two interacting spherical brushes. We have focused our attention in the systems more poorly understood: the interacting forces have been measured in systems where the chain extent is approximately of the same order than the core size and curvature effects are important. The findings we have obtained will be presented after brief descriptions of the numerical model and the formalism used to compute the force between brushes.

6.4.1 Numerical Model

The interaction between two spherical brushes has been simulated by using 3d off-lattice Monte Carlo method (see Section 3.1). A brush is generated by homogeneously distributing f polymer chains onto a colloidal particle modeled by

an impenetrable sphere of radius r_c . Each polymer is represented by the *pearl-necklace model* containing N beads of diameter σ .

Initially, the two spherical brushes are kept sufficiently far away to ensure that during the equilibration process they do not interact. The simulation box is taken to be large enough to avoid any possible boundary effects.

We define one Monte Carlo Step (MCS) as $2 \times N \times f$ trials to move the chains. Initially each individual spherical brush has been equilibrated typically during 10^6 MCS.

6.4.2 Computing the force between spherical brushes

In order to compute the force between the two spherical brushes we have used the numerical technique developed by Toral, Chakrabarti and Dickman [194]. It is worth to remark that this method has no free parameters. We briefly review here this algorithm.

The main idea consists in computing the change in the free energy \mathcal{F} due to an infinitesimal change in the relative positions R of the two interacting spherical brushes. The force, in units of $k_B T$ is given by,

$$F(R) \equiv \frac{\partial \ln Z(R)}{\partial R}, \quad (6.25)$$

where $Z(R) = \exp(-\mathcal{F}/k_B T)$ is the partition function of the system. Due to the hard-core structure of the potential, the partition function

$$Z(R) = \int \prod_{i=1}^{2 \times N \times f} d\mathbf{r}_i \exp \left(- \sum_{j=1}^{2 \times N \times f} V(\mathbf{r}_{ij})/k_B T \right) \quad (6.26)$$

is equal to the volume $\Omega(R)$ of all possible polymer chains configurations compatible with the two spherical colloids separated a distance R .

Let $\Omega_C(R) \subset \Omega(R)$ be the subset of configurations compatible with a movement of one of the spherical brushes towards the other by an amount δR . Similarly, let $\Omega_E(R - \delta R) \subset \Omega(R - \delta R)$ be the set of polymer configurations of $\Omega(R - \delta R)$ in which it is possible to shift the brushes a distance δR apart without overlapping monomers of the two brushes. The compression probability is just $P_C(R) = \Omega_C(R)/\Omega(R)$, and the probability that the expansion can be done is $P_E(R - \delta R) = \Omega_E(R - \delta R)/\Omega(R - \delta R)$. Since the subsets $\Omega_C(R)$ and $\Omega_E(R - \delta R)$ are in one to one correspondence, we have,

$$\frac{Z(R)}{Z(R - \delta R)} = \frac{\Omega(R)}{\Omega(R - \delta R)} = \frac{P_E(R - \delta R)}{P_C(R)}. \quad (6.27)$$

In order to span $Z(R - \delta R)/Z(R)$ two methods are available. First, by direct measurement of the probabilities $P_E(R - \delta R)$ and $P_C(R)$. This can be done by checking whether a virtual displacement $\pm\delta R$ of one brush respect to the other can be carried out preserving the monomer excluded volume criteria. A second method is based on the evaluation of the monomer density pair-correlation function. In the case of two interacting brushes, this second method has been proved to require less computer effort and is the one we have used here. A direct evaluation of probabilities $P_E(R - \delta R)$ and $P_C(R)$ was only performed in a few cases to ensure that the results obtained by computing the monomer density pair-correlation function were correct. Let us to denote the monomer density pair-correlation function as $g_{ij}(r, \theta)$. Thus, $g_{ij}(r, \theta)drd\theta$ is the probability of finding a monomer i of a polymer belonging to brush A and a monomer j of brush B within a distance $(r, r + dr)$ and an angle $(\theta, \theta + d\theta)$, measured respect to the line that joins the two colloids. After compression, particles i and j overlap if $r'^2 = r^2 + (\delta R)^2 - 2r\delta R \cos \theta < \sigma^2$ (see Figure 6.8).

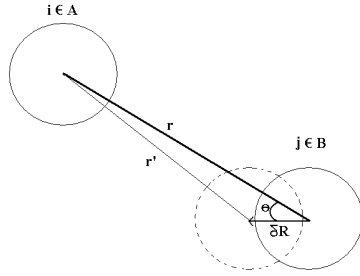


Figure 6.8. Representation of a virtual compression of the two brushes, approaching monomer i belonging to brush A and monomer j of brush B .

In the limit $\delta R \rightarrow 0$ the overlap condition becomes $r < \sigma + \delta R \cos \theta$. Therefore, the probability per MCS that a compression is not allowed is given by

$$\overline{P}_C(i, j) = \int_{-\pi/2}^{\pi/2} \int_{\sigma}^{\sigma + \delta R \cos \theta} g_{ij}(r, \theta) dr d\theta \quad (6.28)$$

$$\approx \delta R \int_{-\pi/2}^{\pi/2} g_{ij}(\sigma, \theta) \cos \theta d\theta \quad (6.29)$$

and the compression probability can be obtained as:

$$P_C(R) = \prod_{i=1}^{N \times f} \prod_{j=1}^{N \times f} [1 - \overline{P}_C(i, j)]. \quad (6.30)$$

In the approximation $\delta R \rightarrow 0$ we obtain:

$$\frac{\partial \ln Z(R)}{\partial R} \approx \frac{1}{\delta R} \ln \frac{Z(R)}{Z(R - \delta R)}, \quad (6.31)$$

and taking the logarithm in Eq. (6.30), expanded up to order δR ,

$$\ln(P_C(R)) = -\delta R \int_{-\pi/2}^{\pi/2} \sum_{i=1}^{N \times f} \sum_{j=1}^{N \times f} g_{ij}(\sigma, \theta) \cos \theta d\theta. \quad (6.32)$$

By defining

$$G(\sigma, \theta) \equiv \sum_{i=1}^{N \times f} \sum_{j=1}^{N \times f} g_{ij}(\sigma, \theta), \quad (6.33)$$

we can rewrite Eq. (6.32) as

$$\ln(P_C(R)) = -\delta R \int_{-\pi/2}^{\pi/2} G(\sigma, \theta) \cos \theta d\theta, \quad (6.34)$$

where $G(r, \theta) dr d\theta$ represents the averaged density of monomers belonging to brush A , separated a distance $(r, r + dr)$ from monomers of brush B , within an angle in the interval $(\theta, \theta + d\theta)$.

In the same way, the expansion probability is given by

$$\ln(P_E(R - \delta R)) = -\delta R \int_{\pi/2}^{-\pi/2} G(\sigma, \theta) \cos(\pi - \theta) d\theta. \quad (6.35)$$

Introducing previous expressions in Eq. (6.27) and Eq. (6.31), the force is given by

$$F(R) = \int_0^{2\pi} G(\sigma, \theta) \cos \theta d\theta. \quad (6.36)$$

This final expression gives the force between the two brushes, separated a distance R apart due to the self-avoid interactions between the monomers of the brushes. Numerically the above integral has been computed by replacing it by the limit when $r \rightarrow \sigma$ of the following averaged sum

$$\left\langle \frac{1}{\Delta r} \sum_{i=1}^{N \times f} \sum_{\substack{j=1 \\ r < r_{ij} < r + \Delta r}}^{N \times f} \cos \theta_{ij} \right\rangle, \quad (6.37)$$

with $\Delta r = 0.001$. The procedure starts by placing the two equilibrated free brushes at distance R far enough to ensure small perturbations to the brush structure. After the force has been computed by using the above expression, the distance R is reduced by an amount $\Delta R = 1$ and the system is let to equilibrate further by 10^5 MCS, before computing the force again. The whole process is repeated until the desired minimum value of the distance R is achieved. Additionally, a similar expression for the interactions between the monomers and the colloidal particle cores has to be considered to compute the whole force between the two brushes. This additional term turns out to be important when the grafted chain density is small and brushes are rather close to each other.

6.4.3 Results and Discussion

The force between two spherical brushes has been computed as a function of their relative distance for different sets of parameters (N, f) . The core radius of the colloidal particle where polymers are grafted is taken to be $r_c = 5\sigma$ and is kept constant throughout all the simulations. The diameter of the monomers is set to $\sigma = 1$. We have varied the number of grafted chains from $f = 5$ to $f = 90$ and we have taken polymer chain lengths in the range $N = 30$ to $N = 100$.

In order to compare the numerical results with the theoretical predictions of the DL theory we need to determine the characteristic radial size of an unperturbed spherical brush R_0 . This quantity is defined as the value of r where the monomer radial density profile $\phi(r)$ drops to zero. $\phi(r)$ is defined as usual:

$$\phi(r) = \frac{\nu(r)}{4\pi r^2 dr}, \quad (6.38)$$

being $\nu(r)$ the number of monomers located within a distance between r and $r + dr$ from the center of the sphere (to this purpose we have taken $dr = \sigma/2$). As an example, in Figure 6.9 we have plotted the volume fraction occupied by the monomers $v(r) = 4\pi/3(\sigma/2)^3\phi(r)$ for different values of chain length N and number of grafted chains f .

In agreement with the results of Toral et al. [213], we have found that $R_0(N, f)$ behaves as in the star-polymer approximation, i.e. it scales as

$$R_0 \sim N^{3/5} f^{1/5}. \quad (6.39)$$

This result supports the previous findings of Daoud and Cotton [197] expected to be valid for large polymer chains ($N \gg r_c$), and a large number of grafted chains. In Figure 6.10 the brush height R_0 is represented as a function of $x = N^{3/5} f^{1/5}$. Observe that all the data fall reasonably well on a straight line of unitary slope.

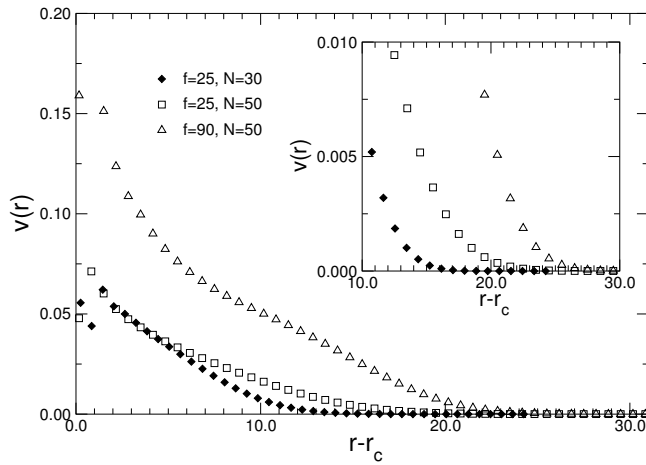


Figure 6.9. Volume fraction occupied by the monomers $v(r)$ plotted against the distance to the surface core $r - r_c$ for different values of the chain length N and number of grafted chains f . Inset: zoom of the region where $v(r)$ drops to zero, defining the characteristic size of the brush R_0 .

As a consequence, since the WP free energy was derived under the assumption of star polymer monomer density profile, we can expect the WP theory to work properly when the two brushes are in close proximity.

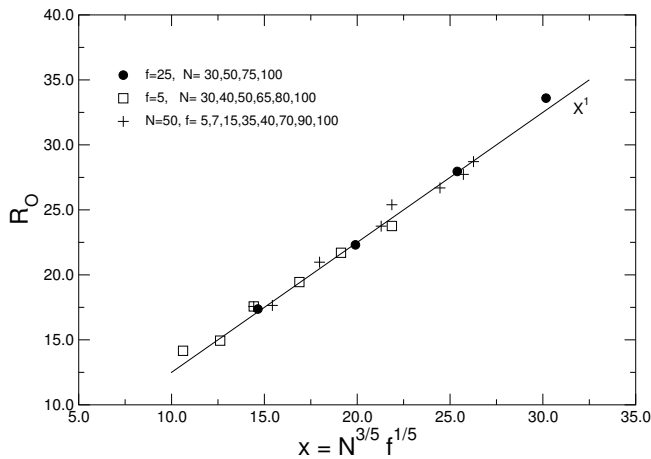


Figure 6.10. Brush height R_0 as a function of $x = N^{3/5} f^{1/5}$. The straight line of unitary slope corresponds to the star polymer approximation.

The computed force between the two brushes versus their relative distance is represented in Figure 6.11. We have taken a chain length of $N = 50$, and varied the number of chains $f = 5, 25, 40, 90$. At short distances the interacting profile can be fitted according to the WP theory (dashed curve), whereas at larger distances the measured data can be adjusted with the Flory theory introduced above for dilute polymer solutions (solid curve). Figure 6.12 shows the results for $f = 25$ and chains lengths $N = 30, 50, 100$. Notice that at small distances the force profile becomes rather independent of N as expected from the WP theory. As it can be seen in the previous plots, and in all the cases studied, it is remarkable

that with the WP and Flory theories, in principle valid in the limiting cases of small and large relative distance between the brushes, we can adjust the whole interacting profile.

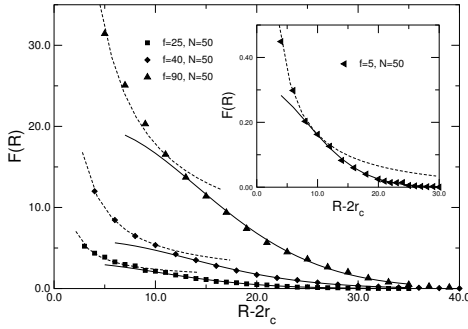


Figure 6.11. Force between two interacting spherical brushes for $N = 50$ and $f = 25, 40, 90$. Inset plot: Case $N = 50, f = 5$. At small relative distance the data is fitted according to the WP theory (dashed curves), whereas at larger distances the force profile is reproduced by the Flory theory (solid lines).

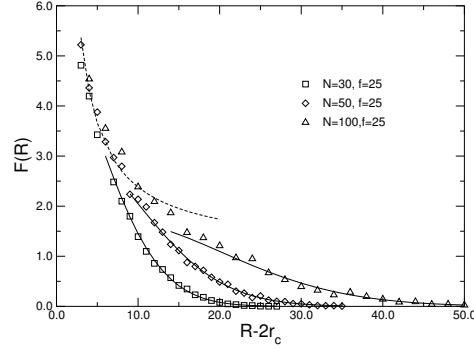


Figure 6.12. Same as Figure 6.11 for $f = 25$ and $N = 30, 50, 100$.

The best fit to the numerical data determine the values of the adjustable constants A , (Eq. 6.19), and C and D (see Eq. 6.21) that appear in the WP and Flory theories respectively. The behavior of A , for $N = 50$, as a function of the number of grafted chains f is represented in a log-log plot in Figure 6.13. The best fit to the data gives a slope of 1.50 ± 0.02 in agreement with the expected power-law dependence $A \sim f^{3/2}$ (Eq. 6.20). We should remark that the WP theory was derived in the limiting cases of $f = 1, f = 2$ and $f \gg 1$. This fact explains the small deviations observed from the expected theoretical behavior for the intermediate values of f ($15 \leq f \leq 25$). In Figure 6.14 we show in a log-log plot of the scaled force $F(R)/f^{3/2}$ as a function of the relative distance between the brushes. We can observe all the data falling into a master curve for small distances where the WP theory is expected to work. Deviations appear as soon as we enter in the Flory regime. For the sake of clarity we have drawn a line of slope -1 that is followed by the numerical data in the WP regime.

In order to analyze the behavior of parameters C and D , we need to compute the averaged square distance of the chain-end monomers $\langle r^2 \rangle$ which is obtained through the chain ends concentration $\epsilon(r)$ (see Eq. 6.24). $\epsilon(r)$ is defined similarly to Eq. 6.38 as:

$$\epsilon(r) = \frac{\mu(r)}{4\pi r^2 dr}, \quad (6.40)$$

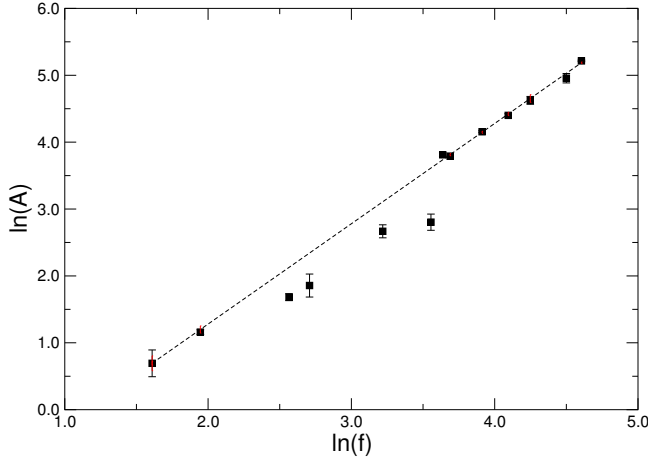


Figure 6.13. Log-log plot of the parameter A vs. the number of grafted chains f . The best fit to the data gives a slope of 1.50 ± 0.02 in agreement with the expected power-law behavior of $3/2$ (Eq. 6.20).

with $\mu(r)$ the number of chain-end monomers within a distance between r and $r + dr$.

The behavior of D as a function of $1/\langle r^2 \rangle$ for all the sets (N, f) studied is shown in Figure 6.15. The best fit to the data gives a slope of 1.06 ± 0.05 in agreement of the expected linear relationship (Eq. 6.23).

Similarly, we have plotted in Figure 6.16 in a log-log scale $C/(Nf)^2$ vs. $1/\langle r^2 \rangle$. For the sake of clarity we have included a solid line of slope $5/2$ corresponding to the theoretical prediction of Flory (Eq. 6.22). Deviations from this behavior are found in systems with large f and small N values, precisely where the assumption of a Gaussian monomer density profile fails. In the first case, large f values force the chains to be strongly stretched, whereas small chain lengths are out of the asymptotic regime where the Gaussian distribution for a globular polymer is found.

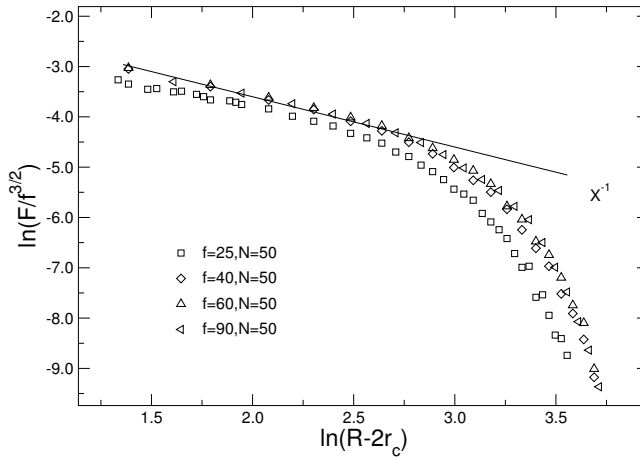


Figure 6.14. Log-log plot of $F/f^{3/2}$ as a function of the relative distance between brushes $R - 2r_c$. A solid line of slope -1 is included to guide the eye and identifies the WP regime.

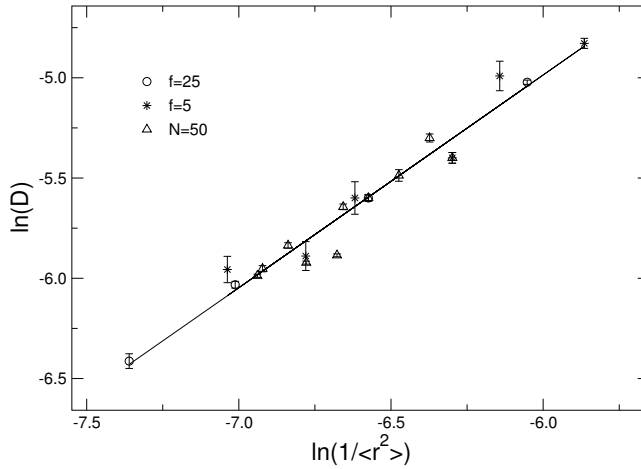


Figure 6.15. Log-log plot of the constant D vs. the inverse of the averaged square distance of the chain-end monomers $1/\langle r^2 \rangle$. The best fit to the data gives a slope of 1.06 ± 0.05 supporting the expected linear relationship of Eq. 6.23.

There are two main reasons for the Flory theory to break down. First, the density profile of end grafted polymer chains is not Gaussian, in general, except for highly curved surfaces. The latter case corresponds to the star polymer approximation where the center-to-end distance is found to reproduce a Gaussian distribution [233]. Furthermore, the theory does not consider the changes induced in the density profile as the polymers interact. Second, when two brushes are far enough the only interaction between them is through the polymer chains, as described by Flory but, as the two brushes approach the interaction of the chains with the core of the colloidal particle becomes relevant and it is not taken into account.

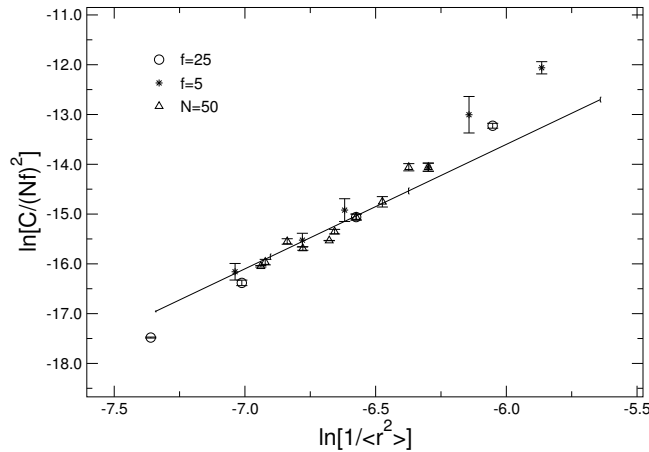


Figure 6.16. Log-log plot of $C/(Nf)^2$ vs. $1/\langle r^2 \rangle$. A solid line of slope $5/2$ is included to guide the eye (Eq. 6.22).

Next, we compare the computed interacting force between the two brushes with the theoretical predictions of the DL theory. In Figure 6.17 we show the results for a fixed chain length ($N = 50$) and different number of grafted chains

f . We separately represent in the inset plot of the figure, the results for a fixed $f = 25$ and different polymer lengths. In all the cases studied, systematic deviations from the DL theory are observed at small separating distances between the two brushes. Whereas the DL theory assumes the interacting polymer chains to recoil and keep inside the domain of its own brush V_H , at small distances this requirement cannot be fulfilled together with the excluded volume criteria, thus chains are forced to interpenetrate. Besides that, we should note that the DL model is an osmotic model, neglecting the change in the free energy associated to the available chain configurations. DL expected the osmotic term to be much larger in comparison with the configurational one as it happens in planar surfaces. The qualitative agreement found with our Monte Carlo simulations confirms this result for spherical and high grafting densities.

Monte Carlo results differ from previous numerical studies based on the self consistent field lattice formalism of Lin and Gast [210] and Wijmans, Leermakers and Fler [202] (to be referred as WLF). WLF developed a two-dimensional SCF-lattice for an athermal system. Their results for $N = 50$ and $f = 31$, using the same core radius as the one used in our simulations ($r_c = 5$), are reproduced in Figure 6.17 (open triangles), and compared with our results for $f = 25$ and $f = 40$. Although the results are of the same magnitude, the WLF model overestimates the interaction at short distances. In Figure 6.18 we compare the results derived from the 1d-SCF method of Lin-Gast with our results. As in the case of WLF, although the results are of the same magnitude, the SCF method of Lin-Gast overestimates the interaction. Since SCF-lattice formalisms do not account properly for monomer correlations, there is a higher monomer concentration in comparison with the one found in Monte Carlo simulations [234]. This higher monomer concentration is responsible for a higher repulsive force.

6.5 Concluding remarks

In this chapter we have presented the results of extensive three-dimensional off-lattice Monte-Carlo simulations of two interacting spherical brushes. We have calculated the force for different values of the chain length N and number of grafted chains f . We have found that the force profile can be divided into two regimes. When the brushes are located within a relative close distance, the measured force is well described by the WP theory, whereas as the separation between the brushes increases, the force is reproduced by extending the theory of Flory for dilute polymer solutions. The overall behavior is qualitatively well adjusted, except at short distances, with the phenomenological DL theory for high density of grafted chains. Finally we should notice that the characteristic radial size of an

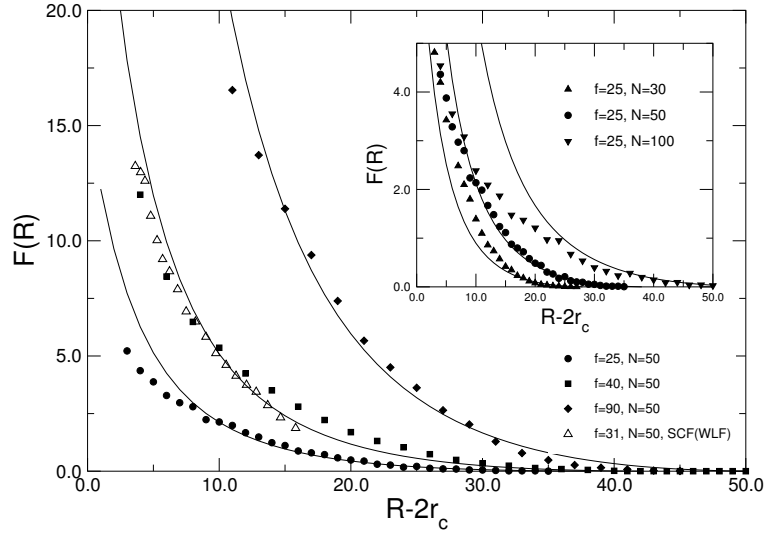


Figure 6.17. Force between two interacting spherical brushes for a fixed chain length $N = 50$ and different number of grafted chains f . Inset plot: Force profile for $f = 25$ and different chain lengths. The solid lines correspond to the theoretical predictions of the DL theory. The open triangles in this figure correspond to the force derived by the WLF SCF-lattice model for $f = 31$ and $N = 50$ (taken from WLF [202]).

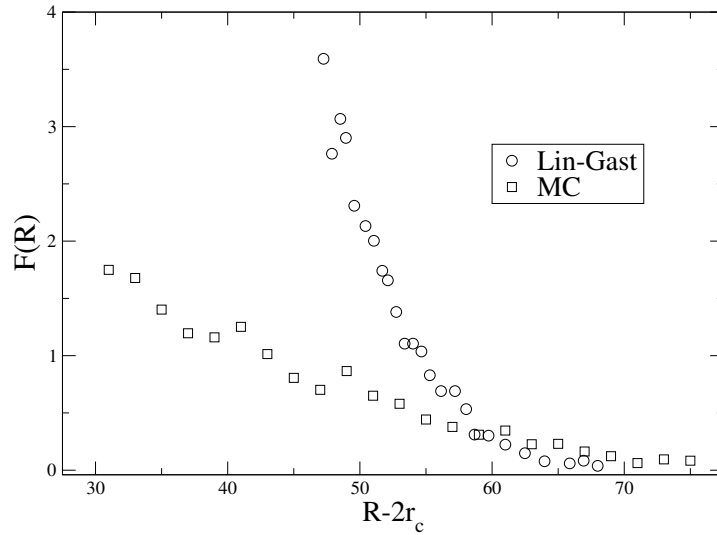


Figure 6.18. A comparison between MC results and the SCF results of Lin-Gast. The open squares represent the force obtained from our MC simulations between two interacting spherical brushes with $f = 38$ (grafting density $\sigma \approx 0.1$), and $N = 200$. The open circles represent the results obtained through the SCF of Lin-Gast for an athermal chain $\chi = 0$, with $N = 200$, $\sigma = 0.1$, and $r_c = 5$ (taken from Lin-Gast [210]).

isolated brush is found to reproduce the scaling relationship for the star polymer's case.

Our results also differ from previous numerical studies based on SCF lattice formalisms of Lind and Gast and Wijmans Leermakers and Fler. This mismatch can be explained by the fact that SCF formalisms cannot account properly for monomer correlations.

It is worth to comment that the Flory theory for dilute polymer solutions and the osmotic theory of DL could be also applied to predict the interaction profile for the case of flat grafted layers. In the case of Flory theory, the Gaussian monomer distribution should be replaced by the characteristic monomer density profile of a flat grafted layer. In the DL theory, expressions for volumes and areas should be rewritten accordingly to the planar geometry and a measurement of the typical height of a free planar brush is also needed.

Finally, as mentioned in the section devoted to the experimental findings, the measure of disjoint pressures by using the expressions derived by Evans and Napper [227], can become a very useful tool in doing further studies towards the understanding of the behavior of sterically stabilized colloidal particles in suspension.

Chapter 7

Spherical polymer brushes II: Encapsulated brushes

Suspensions of colloidal spherical brushes are a complex and interesting problem only studied partially [235–238]. Particularly, in the limiting case of high densities, the colloidal brushes are subject to an isotropic pressure. In such case, the interaction of a colloidal particle with the rest of the system can be modeled, in a first approximation, by a single spherical brush confined inside a spherical cavity. This model has the advantage of reducing the high computer cost. On the other hand, this model turns out to be relevant to the study of the properties of encapsulated dendrimers, liposomes, vesicles containing nanoparticles with grafted chains, and might be of relevance in the synthesis of polymer-grafted metal nanoclusters inside small material cavities or molecular cages.

The purpose of the present chapter is to present the results of extensive MC and SCF simulations of a single colloidal brush confined inside a spherical cavity wall of variable radius. Polymer chains have an extent of the same order of the core size of the colloidal particle such that curvature effects are important. We have measured the monomer density profile and the cavity pressure at different cavity radius. The results using MC and SCF methods have been compared at low and high compression regimes, discussing the advantages of each method.

7.1 Numerical models

7.1.1 Monte Carlo method

In order to simulate the interaction between a spherical brush confined inside a spherical cavity wall, we have used a 3d off-lattice Monte Carlo method (MC) similar to the one used in the previous chapter. We have generated the brush

by homogeneously distributing f polymer chains grafted onto an impenetrable spherical surface of radius r_c . The cavity wall is also impenetrable with a variable radius R (see Figure 7.1).

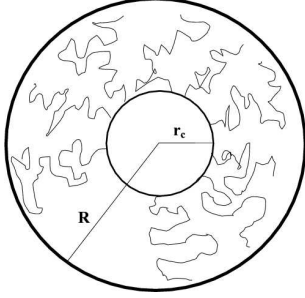


Figure 7.1. Schematic representation of a spherical brush with an impenetrable core of radius r_c inside a spherical cavity of radius R .

Initially, the radius of the cavity wall is set to be larger than the usual extent of the brush to ensure that during the equilibration process no interaction between the brush and the cavity wall occurs. We define one Monte Carlo Step (MCS) as $N \times f$ trials to perform monomer moves. The spherical brush has been equilibrated typically during 5×10^5 MCS. After this initial equilibration time, magnitudes of interest are recorded every 10 MCS. In what follows, the expression for the force and interacting potential are given in units of $k_B T$.

The force that the system exerts to avoid compression is estimated accordingly to Section 6.4.2. In the case of encapsulated brushes the compression probabilities are obtained by spanning directly the probabilities $P_E(R - \delta R)$ and $P_C(R)$ for a given cavity size R . Then, we force to compress the system to a new cavity size $R - \Delta R$. The system is equilibrated again during 10^5 MCS before new measurements are taken.

The monomer radial density ϕ is defined as usual:

$$\phi(r) = \frac{\nu(r)}{4\pi r^2 dr}, \quad (7.1)$$

being $\nu(r)$ the number of monomers located within a distance between r and $r + dr$ from the center of the sphere. The definition of $\phi(r)$ is such that the following normalization holds:

$$\int_0^\infty d^3 r \phi(r) = N f \quad (7.2)$$

In a similar way, we also define the chain-ends monomer density, $\epsilon(r)$, where $\nu(r)$ takes only into account the number of free chain ends.

7.1.2 Self Consistent Field method

In order to compute the probability density function (pdf) for polymer systems, it is customary to deal with a Schrödinger-like equation for the pdf for a single chain [95]. The use of this formalism is a valid approximation for spatial scales much larger than the polymer blob size. However, for encapsulated polymer brushes, and mainly at moderate and high compressions, the spatial scale of the cavity is comparable to the blob size. Thus, the use of the precedent formalism to compute the pdf becomes inadequate. Instead, we compute the pdf of a polymer chain using directly the recurrence law for the pdf from which the Schrödinger-like equation derives [95]. We must be aware that the use of the recurrence law still implies some approximations. It is assumed that on each monomer of the polymer chain acts a potential that only depends on the position of the monomer in the system, $U = U(\mathbf{r})$, therefore, bond correlations are not taken into account. It is also assumed that the potential is a function of the local monomer density, $U(\phi(\mathbf{r}))$, ignoring particle density correlations. Finally, the properties of the whole ensemble of chains are deduced from the pdf of a single chain.

Under the above assumptions, the spherical cavity is discretized in concentric shells of thickness dr and all monomers inside a shell are assumed to be equivalent. A polymer chain composed by N monomers is represented as a path of N segments of length σ . Each segment is labeled by an index τ associated to the spherical shell at which it belongs. The pdf associated to all possible paths composed by n segments, being the first segment inside the shell \mathbf{h}' and the last one inside the shell \mathbf{h} , is defined as

$$G_n(\mathbf{h}', \mathbf{h}) \equiv \sum^A e^{-\sum_{i=1}^n U(\tau_i)} \quad (7.3)$$

in which \sum^A stands for a sum over all the hypothetical n -paths that join the shells \mathbf{h}' and \mathbf{h} . This function verifies $G_n(\mathbf{h}', \mathbf{h}) = G_n(\mathbf{h}, \mathbf{h}')$. Therefore, the pdf associated to a path of $n + 1$ segments may be written as

$$G_{n+1}(\mathbf{h}', \mathbf{h}) = \sum^A \left(e^{-\sum_{i=1}^n U(\tau_i)} e^{-U(\tau_{n+1})} \right) \quad (7.4)$$

Assuming $U(\tau_{n+1})$ to be independent of rest of the segments in the chain and of the starting point of the sequence, the precedent equation reads:

$$G_{n+1}(\mathbf{h}', \mathbf{h}) = \left(\sum_{\mathbf{h}''}^D G_n(\mathbf{h}', \mathbf{h}'') \right) e^{-U(\mathbf{h})} \quad (7.5)$$

where \sum^D implies a sum over all the \mathbf{h}'' shells from which we can get into shell \mathbf{h} using a single segment, therefore, shells \mathbf{h}'' and \mathbf{h} are at a relative distance

less or equal to σ . The above equation stands for the recurrence law needed to calculate the chain pdf once the potential $U(\mathbf{h})$ is given.

We have set the interaction potential $U(i)$ to be proportional to the monomer concentration in shell i , $\phi(i)$:

$$U(i) = \omega \phi(i) \quad (7.6)$$

where w is the excluded volume parameter defined as [207]:

$$\omega = 4\pi \int_0^\infty (1 - e^{-V(r)}) r^2 dr \quad (7.7)$$

and $V(r)$ is in our case the hard-core potential between monomers. For a value of $\sigma = 1$, we obtain $\omega = 4\pi/3 \approx 4.2$

The monomer concentration $\phi(i)$ and the free-end-chain concentration $\epsilon(i)$ are defined as:

$$\phi(i) = \frac{f}{4\pi r_i^2 dr} \frac{e^{U(i)} \sum_{n=0}^{N-n} \sum_{j=i_{r_c}}^{i_R} G_n(i_{r_c}, i) G_{N-n}(i, j)}{\sum_{j=i_{r_c}}^{i_R} G_N(i_{r_c}, j)} \quad (7.8)$$

$$\epsilon(i) = \frac{f}{4\pi r_i^2 dr} \frac{G_N(i_{r_c}, i)}{\sum_{j=i_{r_c}}^{i_R} G_N(i_{r_c}, j)} \quad (7.9)$$

where f is the number of chains and i_{r_c} and i_R are the shell indexes with radius equal to the brush core surface and the cavity wall respectively. The factor $e^{U(i)}$ in the monomer concentration is introduced to avoid double counting of the interaction term $e^{-U(i)}$ at shell i that comes from splitting the pdf into two terms, one that ends at shell i and the other starting at the same shell.

The change in the free energy when we reduce the cavity size, $\Delta\mathcal{F}(i_R)$, is given by

$$\Delta\mathcal{F}(i_R) = \ln \left(\frac{\Omega(i_R)}{\Omega(\infty)} \right) \quad (7.10)$$

being

$$\Omega(i) = f \sum_{j=i_{r_c}}^i G_N(i_{r_c}, j). \quad (7.11)$$

We have set the reference state as a system with a cavity wall at a distance far enough so that no chain can reach this wall. Therefore, the force to compress the brush, given a cavity size R , is:

$$F(R) = -\frac{\partial(\Delta\mathcal{F}(R))}{\partial R} \quad (7.12)$$

Given R , N and f , an iterative process is used to obtain the pdf and the density profiles. We have iterated the process until self-consistency is reached. We set the condition for self-consistency such that the sum of the square differences in the density profiles coming from two consecutive iterative steps is less than 10^{-8} .

The SCF method has the great advantage of being three to four orders of magnitude less expensive in computer time than the MC method. In the next section we will show that SCF and MC calculations give similar results for the density profiles $\phi(r)$ and $\epsilon(r)$ in the case of free polymer brushes. However, SCF predictions for the cavity pressure worsen for highly compressed systems.

7.2 Results and discussion

7.2.1 Density profiles

We have performed extensive numerical calculations for free and encapsulated spherical polymer brushes in order to compute the monomer density profiles and the compression forces for different sets of parameters (R, N, f) . The core radius of the colloidal particle where polymers are grafted is taken to be $r_c = 5\sigma$ and is kept constant through all the simulations. The diameter of the monomers is set to $\sigma = 1$. We have taken polymer chain lengths in the range of $N = 30$ to $N = 70$, and we have varied the number of grafted chains from $f = 5$ to $f = 75$. The range of parameters (N, f) has been chosen in order to obtain chain extents roughly of the same order than the diameter of the core where curvature effects are important. For the SCF method we have used a shell thickness $dr = 0.1\sigma$.

We have first studied the monomer density profiles $\phi(r)$ for an unconstrained spherical brush using our MC simulations and the SCF formalism. In Figure 7.2 we present the results for two different values of the chain length N and number of grafted chains f that correspond to representative values for soft and densely packed brushes. We can observe a good agreement between the MC and SCF calculations. The density oscillations observed at small r , close to the core of the colloidal particle, are originated due to wall-effects of the impenetrable core. For a free spherical polymer brush Cariagno and Szleifer [211] computed the monomer density profile derived from a single-chain mean field theory. A comparison between the Cariagno and Szleifer data (CS) and our results is also included in Figure 7.2. The better agreement of the CS predictions with our MC simulations, in contrast to the SCF calculations, can be understood in the sense that the Cariagno and Szleifer formalism requires a representative sample of chain configurations as an input data to solve the equations that we have generated using our MC method.

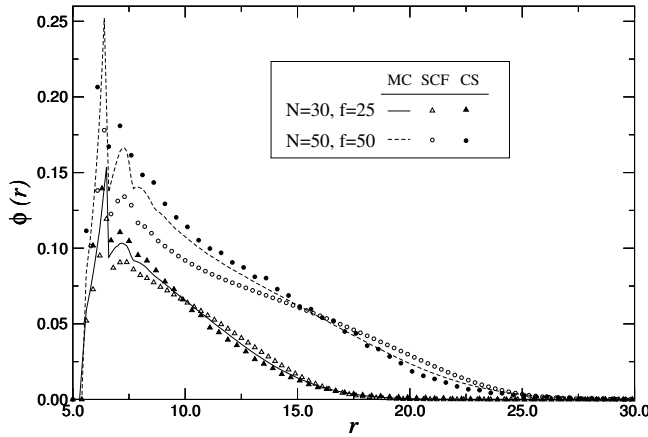


Figure 7.2. Comparison between the monomer density profile $\phi(r)$ for free or uncompressed spherical polymer brushes obtained from our MC simulations (lines) and SCF calculations (symbols) for different values of the chain length N and number of grafted chains f . The results are compared to the predictions of Carignano and Szeifer [211] (CS, filled symbols)

In Figure 7.3 we compare the monomer and chain-end density profiles for unconstrained polymer brushes obtained from our MC and SCF calculations. Figure 7.3(a) stands for $N=30$ and $f=25$, whereas Figure 7.3(b) and Figure 7.3(c) show the results for $(N=30, f=75)$ and $(N=50, f=75)$ respectively. In all cases the profiles are roughly similar. In particular, both methods agree very well in the case of the chain-end density profile $\epsilon(r)$ for short chains in a densely packed brush (see inset of Figure 7.3(b)). This is mainly due to the fact that the chains are forced to be mostly fully stretched out and density correlations, not present in the SCF formalism, are not relevant. On the other hand, the results for the monomer density profiles $\phi(r)$ show systematic differences, although small, between the MC and SCF calculations. Close to the core of the colloidal brush, SCF results display density profiles slightly smaller than those obtained via MC simulations. And vice versa, in an intermediate region, the SCF method gives densities slightly larger than in the MC simulations. The same systematic behavior was found by Cosgrove et al. [239], when comparing MC and SCF density profiles for flat brushes. Cosgrove attributed these differences to the fact that MC simulations accounts explicitly for the excluded volume effect, whereas SCF accounts only approximately for this effect.

7.2.2 Cavity pressure and force profiles

We have measured the force profile exerted by an encapsulated spherical polymer brush onto the external cavity wall through the evaluation of the changes in the free energy due to an infinitesimal change in the radius of the cavity. Within the MC simulations, the force can be calculated by directly measuring the compression probabilities; whereas in the SCF approach, once we have reached self-consistency, we use the pdf in Eqs. 7.10 to 7.12.

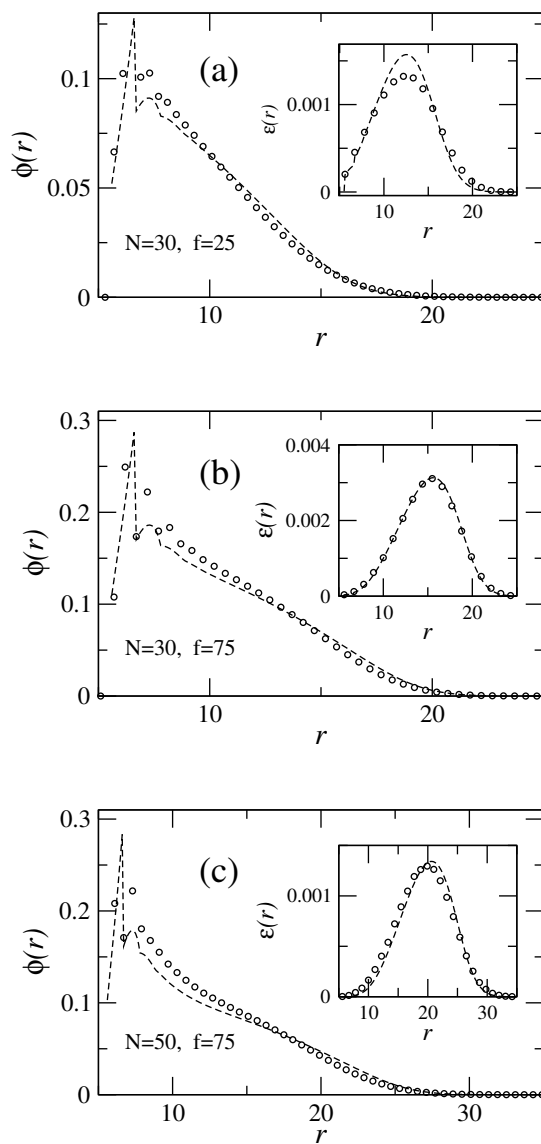


Figure 7.3. Comparison between the monomer density profiles $\phi(r)$ for uncompressed spherical brushes obtained with MC (\circ) and SCF (dashed lines) calculations. Inset: chain-end density profiles. From top to bottom: (a) $N = 30, f = 25$; (b) $N = 30, f = 75$; (c) $N = 50, f = 75$.

Alternatively, we propose another way to compute the force profile and the cavity pressure that is derived from the Flory theory for polymer solutions [93]. This method has the advantage of being computationally inexpensive, and their predictions will be compared with the MC and SCF calculations.

An extension of the Flory theory for polymer solutions

In the Flory theory the osmotic pressure in a polymer solution can be written as (see Section 2.6.1.b):

$$\Pi(R) = \frac{-1}{\mathcal{V}} \left(\ln(1-v) + \left(1 - \frac{1}{N}\right)v + \chi v^2 \right) \quad (7.13)$$

where \mathcal{V} is the molar volume of the solvent, v is the volume fraction of solute, N is the degree of polymerization or chain length, and χ is the Flory parameter. We set $\chi = 0$ which is the condition of a dry-brush. Under this assumption, the contributions to the free energy come only from the entropy associated to all possible configurations of the system. We suppose that the volume of the solvent and the volume fraction of the solute are given respectively by:

$$\mathcal{V} \sim (\tau - aNf) \quad (7.14)$$

$$v = \frac{aNf}{\tau} \quad (7.15)$$

a is the volume of a single monomer. τ is the total available cavity volume between the inner wall, represented by the core of the colloidal particle where chains are grafted and the cavity wall, thus:

$$\tau(R) = \frac{4\pi}{3}(R^3 - r_c^3) \quad (7.16)$$

At variance with the original Flory treatment, the molar volume of the solvent \mathcal{V} refers to the remaining space in the system once we have subtracted the volume occupied by the monomers, thus, it is no longer a constant value.

The force to compress the cavity will be proportional to the area of the cavity wall and to the change in the osmotic pressure, thus:

$$F(R) \sim 4\pi R^2 \Delta\Pi(R) \quad (7.17)$$

In Figures 7.4 to 7.6 we present in log-log plots the force profile $F(R)$ vs. the cavity size R computed for different values of the polymer chain length N and number of grafted chains f . In each figure we include the results coming from the MC simulations (circles), the predictions of the SCF theory (dashed lines) and

results derived from the application of the extended Flory theory (crosses). Figure 7.4 concentrates on the results derived for short polymer chains ($N = 30$); Figure 7.5 for intermediate chain lengths ($N = 50$); and Figure 7.6 for long polymers ($N = 70$). In all the cases studied we have used the same fitting constant to adjust the predictions of the extended Flory theory (see Eq. 7.17), and we have taken, as a reference state, a cavity size R^* at which $\ln(F(R^*)) \rightarrow -\infty$ in the MC simulations.

A direct comparison between SCF and MC force profiles shows a rather good agreement for weakly compressed systems. However, systematic differences are observed for intermediate and high compression values. In the intermediate region we found the SCF forces to be larger than the ones derived from the MC simulations, whereas for high compressions it is the MC force the one that becomes larger than the SCF outcome.

The mismatches observed between the SCF and MC results are due to a twofold effect. For small cavity sizes or highly compressed systems, the assumption in the SCF model of a linear dependence of the mean field potential with the monomer density (see Eq. 7.6) breaks down. In fact, under this assumption, the SCF formalism allows a cavity size smaller than the volume occupied by the polymers without requiring an infinite force. On the other hand, for intermediate compression values, the larger forces obtained with the SCF formalism are originated in an overestimation of the monomer interactions. The SCF method does not include the effect of monomer correlations, thus it allows higher average densities in the system than the ones found in the MC simulations. As a consequence, stronger repulsions between the polymers take place and a higher force is required to compress the brush.

The predictions of the extended Flory theory are found, remarkably, despite its simplicity, to be in a very good agreement with the results of the MC simulations in the intermediate and high compression regimes. However, the force is overestimated for weakly compressed systems. This result is easily explained since the Flory theory was formerly developed for free polymer chains. As the cavity size grows, the difference between a system of grafted chains and a polymer solution becomes evident and, as it is expected, the interaction of the grafted chains with the outer surface is much weaker than the one coming from a polymer solution.

It is worth to notice that the MC data can be fitted remarkably well with the extended Flory theory for intermediate and high compression values, and with the SCF formalism for weakly compressed systems.

We have analyzed the relationship between the monomer volume fraction v (see Eq. 7.15) and the pressure exerted on the cavity wall P defined as the force

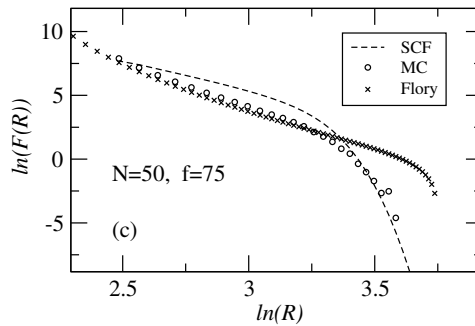
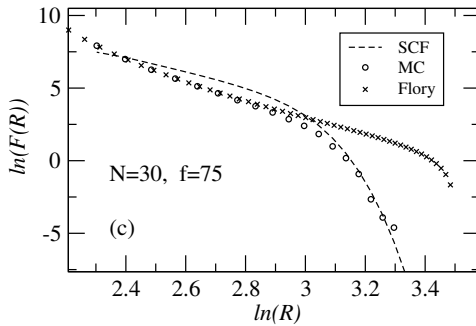
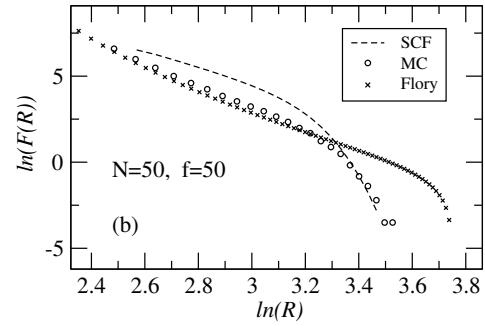
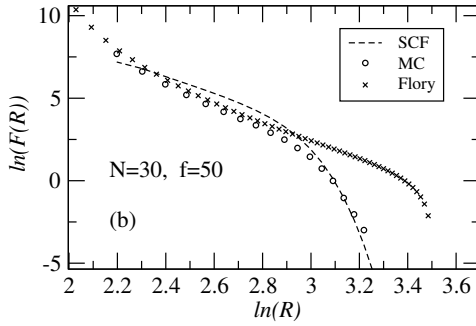
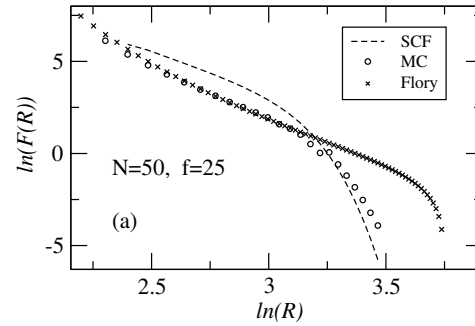
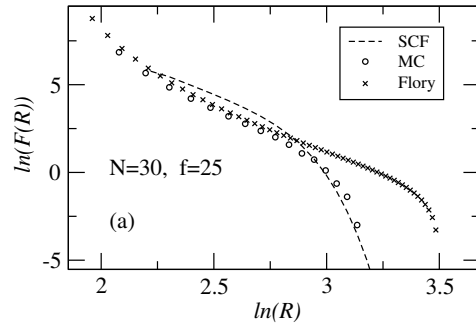


Figure 7.4. Log-log plot of the force profile of an encapsulated spherical polymer brush vs. the cavity size R , for polymer chains of length $N = 30$. MC results are represented by filled circles; SCF data by dashed lines; and the predictions coming from the Flory theory by crosses. Different figures stand for different number of grafted chains f . From top to bottom: (a) $f = 25$; (b) $f = 50$; (c) $f = 75$.

Figure 7.5. Same as Figure 7.4 for polymer chains of length $N = 50$. From top to bottom: (a) $f = 25$; (b) $f = 50$; (c) $f = 75$.

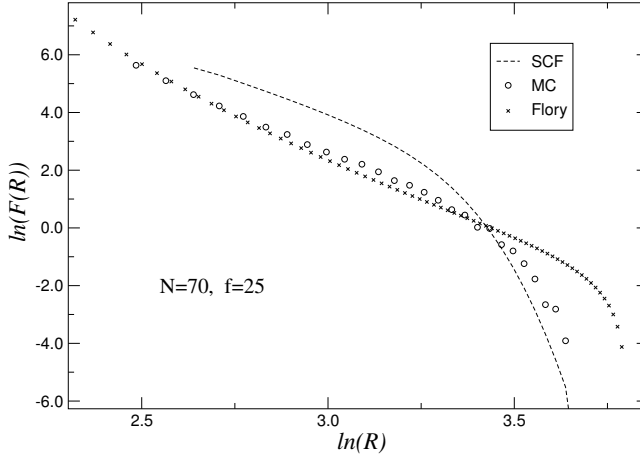


Figure 7.6. Same as Figure 7.4 for the single case of long polymer brushes with $N = 70$ and $f = 25$.

to compress the system divided by the area of the cavity. The results for the MC and SCF calculations are shown in log-log plots in Figure 7.7 and Figure 7.8 respectively. In both cases, we find a complex behavior of the monomer volume fraction with the cavity pressure for weakly compressed systems that depends on the different values of the polymer chain length N and number of grafted chains f . But, for increasing values of the cavity pressure v and P follow a power-law of the form $P \sim v^\alpha$ independent of N and f . The best fit to the numerical data gives a slope of $\alpha = 2.73 \pm 0.04$ for the MC simulations and $\alpha = 2.15 \pm 0.05$ for the SCF results. The exponent obtained for the SCF data is very close to the des Cloiseaux power law ($\alpha = 9/4$) found in semi-dilute polymer solutions [95]. For large monomer concentrations the polymer theory predicts that all thermodynamic properties must reach values that are independent of the degree of polymerization, as we have observed in both MC and SCF methods. We must be aware that des Cloiseaux law is deduced from scaling arguments that neglects non-linear dependences on the concentration. This fact might explain the agreement between SCF and des Cloiseaux law, whereas MC results follows a power law in which a larger exponent can be expected due to large monomer density correlation effects.

Differences between force profiles derived from SCF formalisms, and those obtained from other methods that account for chain interdigitation and correlations between the nearest neighbor bonds are also referenced in several works. For instance, Ruckenstein-Li [240] (to be referred as RL) compared the experimental force profile of two interacting crossed cylinders bearing grafted polymer chains, with the numerical data obtained with a generator matrix formalism and from SCF methods. RL found the matrix formalism to provide a better agreement with the experimental data than the SCF results. In most cases, the force profiles

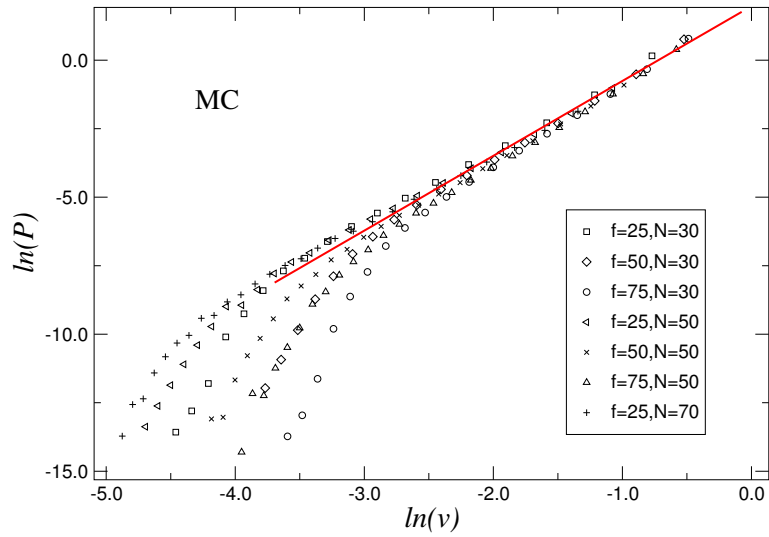


Figure 7.7. Log-log plot of the system pressure P vs. the monomer volume fraction v obtained from MC simulations for different values of the chain length N and number of grafted chains f . A solid line of slope 2.73 is included to guide the eye.

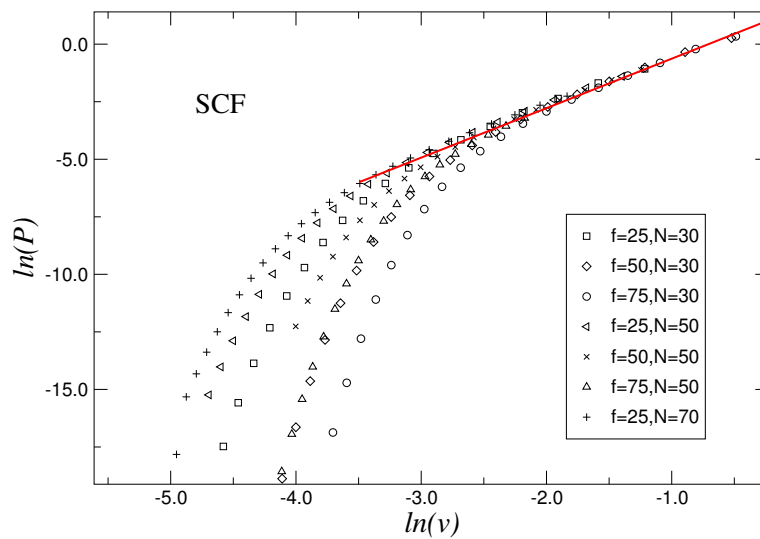


Figure 7.8. Log-log plot of the system pressure vs. the monomer volume fraction v derived from the SCF formalism. A solid line of slope 2.15 is included to guide the eye.

derived by RL with the matrix formalism and the SCF method are rather similar to the ones we found comparing the MC simulations and the SCF calculation. This reinforces our presumption that interdigitation and monomer correlations are responsible of the observed differences between the MC and SCF data. Additionally, the fact that mean field calculations over counts the segment-segment interactions in the evaluation of the free energy, as mentioned above, has already been noticed by Lin and Gast [210].

7.3 Summary and concluding remarks

In this chapter we have studied the behavior of an encapsulated spherical brush inside a spherical cavity. This system is a first approximation to model the interactions in a dense solution of colloidal particles bearing grafted polymer chains onto their surface when chain interdigitation is not favoured. This model is particularly relevant for moderate and high density values where the colloidal brushes are subject to an isotropic pressure, and might be of relevance to the behavior of encapsulated dendrimers, liposomes or vesicles containing polymer brushes as well.

We have measured the monomer density profile and the cavity forces through extensive 3-dimensional off-lattice Monte-Carlo simulations and using a Self-Consistent Field formalism. In the latter case, we have used directly the probability density function recurrence law for the propagator $G_N(r, r')$, avoiding the length scale approximation involved in self-consistent field methods that uses Schrödinger-like equations. Alternatively, we have proposed a theoretical description based on an extension of the Flory theory for polymer solutions to compute the pressure inside the cavity.

A comparison of the predicted forces exerted by the polymer brush onto the cavity surface among the different methods reveals the following: *i*) For weakly compressed systems, MC and SCF data show a rather good agreement. However, the force is overestimated in the extended Flory theory. This difference arises since the Flory theory was developed for free polymer chains and not for polymer brushes, thus, its prediction is not physically relevant when the cavity wall is located at a distance larger than the typical brush extension. *ii*) For intermediate and highly compressed systems the MC data agrees reasonably well with the results derived from the Flory theory. In the intermediate regime, it is the SCF formalism that overestimate the force. This behavior can be easily explained since the SCF method does not account for monomer correlations, allowing higher monomer densities and thus, higher forces are required to compress the brush. On the other hand, for highly compressed systems, the linear dependence of the mean

field potential with the monomer density turns out to be inadequate (the repulsion between monomers allows a volume reduction of the system beyond the own excluded volume of the monomers at a finite energy cost) leading to lower forces than the ones derived from MC simulations.

We have found a power law relationship between the monomer volume fraction and the cavity pressure, $P \sim v^\alpha$. SCF data gives a slope of $\alpha = 2.15$, very close to the des Cloiseaux law derived for semi-dilute polymer solutions. On the other hand, the MC simulations provide a larger exponent $\alpha = 2.73$ that is originated in the monomer correlations not present in the previous models.

Chapter 8

Polymer chains confined to spherical surfaces

In previous chapters we have focused on colloidal systems in which polymers are non-adsorbing or they are grafted chemically by one end onto the surface of the colloidal particles. In the present and the following chapters we will focus on polymers that tend to adsorb onto surfaces. Particularly, in this chapter we study the behavior of semiflexible homopolymer chains fully adsorbed onto spherical colloidal particles. We will see that non-flat geometries induce non trivial behaviors even for simple polymer structures.

8.1 Introduction

Polymers restricted to move on a non-planar surface are a subject of great interest in physics and biology for their exciting fundamental science as well as for their novel technological applications. Adsorption of polyelectrolytes onto colloidal particles [241] and micelles [242] leads to a restricted motion of the polymers on the surface in the limit of strong attractions. Such chain adsorption onto various non-planar surfaces has been studied recently by several authors, both theoretically [243–247] and numerically [248–253]. Polymer adsorption is closely related to the problem of macro ion complexation formation with polyelectrolytes. In particular, formalism used to study adsorption has recently been applied to the study of interesting DNA complexation with proteins like histones [251].

Chain motion onto curved surfaces is also relevant to the problem of a polymer confined inside a cavity [254,255]. Due to entropic effects, flexible polymers tend to fill the available space with the highest concentration in the center of the cavity. Instead, very stiff chains tend to circle near the surface in order to min-

imize the bending energy. Therefore, rigid polymers behave as chains with an effective restricted motion close to the cavity surface. The problem of confined stiff chains turns out to be relevant for DNA packaging into virus capsids and vesicles and its release through nanopores [256–260]. Cryoelectron microscopy experiments for several viruses have shown that DNA molecules arrange within viral capsids in concentric circles involving an helical pitch [261–263]. For instance, Olson et al [263] have observed that T4 bacteriophage genome forms a highly condensed series of concentric layers, spaced about 2.36 nm apart, that follow the general contour of the inner wall of the protein capsid.

Not only DNAs but proteins also can be found encapsulated into nanometer sized vesicles [264,265]. Encapsulation of proteins in reverse micelles dissolved in low viscosity fluids is found to improve *NMR* protein studies by increasing the relaxation times [266]. Again, if a protein is highly confined, an effective restricted motion will take place.

Several recent theoretical works attempt to characterize properties of polymer chains enclosed in shells. Gaussian polymer chains on various types of surfaces in a *D*-dimensional space are studied by Mondescu and Muthukumar (MM) [267]. For spherical surfaces, the averaged mean square end-to-end distance $\langle R_{ee}^2 \rangle$ for large polymer chains has been found to reach a constant value in that study, independent of the space dimensionality. On the other hand, for short chains, a linear dependence with persistence length and chain length has been predicted. Recently, Spakowitz and Wang (SW) [268] have developed a formalism to describe the statistical behavior of a semiflexible worm-like chain confined to a spherical surface and derived a closed expression for $\langle R_{ee}^2 \rangle$. Their model predicts different behaviors for the polymer chain depending on the relative size of the sphere and the chain persistence length.

While the predictions of MM and SW are strictly valid for ideal polymer chains, the study presented in this chapter focuses on confinement of more realistic polymer chains, interacting via excluded volume interactions, onto spherical surfaces. Our results are compared with previously mentioned theoretical predictions and serve as a check on the range of applicability of the ideal chain formalisms. In addition, our study provides insight into new chain conformations not described by the existing theories. To this end, we have performed extensive off-lattice Monte-Carlo (MC) simulations for both flexible and semiflexible chains. For various degrees of rigidity of the chain, we have analyzed confined chain conformations as a function of the chain length and the radius of the sphere. We show that excluded volume chains behave similar to ideal chains and hence, reproduce most of the SW predictions when chains are smaller than the perimeter of the sphere and its degree of stiffness is large enough. For certain choices of the

parameters, however, excluded volume chains show distinctly different behavior from ideal chains. For example, excluded volume chains undergo a disordered to helix transition within a particular range of parameters. This transition is totally absent in the ideal case.

8.2 Theoretical Review

8.2.1 The Mondescu-Muthukumar Theory

Brownian motion and polymer statistics on curved interfaces embedded in a D -dimensional space were studied in detail by Mondescu and Muthukumar [267]. Their work focused on the properties of polymer chains confined to spherical surfaces, cylinders, cones and torus of dimension $D - 1$. Polymers were assumed to behave as Gaussian chains containing N beads. By solving the diffusion equation for the probability distribution function, they derived an expression for the mean square end-to-end distance for a chain confined to a spherical surface:

$$\langle R_{ee}^2 \rangle = 2R^2 \left[1 - \exp\left(-\frac{Ll}{2R^2}\right) \right]. \quad (8.1)$$

Here, R is the radius of the sphere, L is the chain length, and, l is the Kuhn length. This expression is independent of the dimensionality of the system. In the limit of $Ll \ll R^2$ the mean square end-to-end distance is approximately $\langle R_{ee}^2 \rangle \approx Ll$, similar to an ideal random walk. On the other hand, for $Ll \gg R^2$, we get $\langle R_{ee}^2 \rangle \approx 2R^2$. Small chains are expected to increase their mean square end-to-end distance linearly with their size and Kuhn length, whereas long chains are expected to reach a constant value closely related to the radius of the surface.

8.2.2 The Spakowitz-Wang theory

In a more recent work, Spakowitz and Wang [268] introduced a novel representation of the differential geometry of an inextensible curve confined to a spherical surface, and derived a precise description of the chain kinematics for a worm-like chain model. This formalism allows the evaluation of the mean square end-to-end distance in a closed form in a system where the interactions between chain segments are ignored.

In the SW theory, a chain of length L with a persistence length l_p , confined to a spherical surface of radius R has a mean square end-to-end distance given by:

$$\langle R_{ee}^2 \rangle = 2R^2 \{ 1 - e^{-a} [\cosh(ab) + b^{-1} \sinh(ab)] \} \quad (8.2)$$

where $a = \frac{L}{4l_p}$ and $b = \left(1 - \frac{16l_p^2}{R^2}\right)^{1/2}$. An oscillatory behavior is expected for $\langle R_{ee}^2 \rangle$ for $R < 4l_p$, whereas for $R > 4l_p$, different scaling regimes are expected depending on relative values of the sphere radius, the persistence length, and, the chain length. Rigid rod scaling behavior is expected for chains with $L < 2l_p$, yielding $\langle R_{ee}^2 \rangle \sim L^2$. On the other hand, ideal random walk behavior is found for polymer chains that verify $2l_p < L < R^2/(2l_p)$, yielding $\langle R_{ee}^2 \rangle \sim Ll_p$. For large enough chains, $L > R^2/(2l_p)$, SW theory predicts an asymptotic behavior towards the uncorrelated end-to-end value, $\langle R_{ee}^2 \rangle \approx 2R^2$.

Both Mondescu-Muthukumar and Spakowitz-Wang theories predict similar behaviors for large stiff chains. For small chains as well, both theories predict a linear growth of the mean square end-to-end distance with the persistence and chain lengths. For very short chains ($L \ll 2l_p$), however, SW predicts, in addition, a rigid rod regime.

8.3 Numerical model

In order to check the range of validity of previous theories when excluded volume interactions are included in the model, we have performed extensive off-lattice 3d Monte Carlo simulations (see Section 3.1). In our model a single homopolymer chain interacts with an impenetrable spherical surface of radius R . The chain contains N beads of diameter $\sigma = 1$. The distance between consecutive beads along the chain is set to 1.1σ . Therefore the chain length L is equal to $L = 1.1\sigma N$. The total energy of the chain U_{total} is given by

$$U_{total} = U_B + U_{ads} + \sum_{i=1}^N \sum_{i<j}^N V(r_{ij}) \quad (8.3)$$

Here, V is a hard sphere potential:

$$V(r_{ij}) = \begin{cases} 0 & \text{for } |\mathbf{r}_i - \mathbf{r}_j| > \sigma, \\ \infty & \text{for } |\mathbf{r}_i - \mathbf{r}_j| < \sigma. \end{cases} \quad (8.4)$$

U_B is a bending energy term that accounts for the chain stiffness,

$$U_B = \sum_{\theta} \kappa (1 + \cos(\theta))^2, \quad (8.5)$$

θ being the bond angle between any two consecutive bonds, and κ is the stiffness parameter. U_{ads} stands for an attractive interaction with the spherical surface:

$$U_{ads} = n_{ads} \epsilon \quad (8.6)$$

where ϵ is the adsorption energy per monomer and n_{ads} is the number of adsorbed monomers onto the surface. We consider a monomer to be adsorbed when the center of the monomer lies within a distance $(R, R + \sigma)$ from the center of a sphere of radius R . In order to ensure a confinement i.e. a *total adsorption* of the chain on the spherical surface we need to consider a high adsorption energy. We have found that $\epsilon = -10\kappa_B T$ allows such a confinement.

The initial configuration of the self-avoiding polymer is randomly generated onto the surface of the sphere of radius R . One Monte Carlo Step (MCS) is defined, as usual, as N trials to move the chain. The system has been equilibrated for 2×10^6 MCS. Subsequently, chain properties have been evaluated every 10^5 MCS and averaged over 10^5 measurements.

8.4 Results and discussion

8.4.1 Mean square end-to-end distance

In order to compare MM and SW predictions with the MC results for excluded volume chains, we have focused on the mean square end-to-end distance $\langle R_{ee}^2 \rangle$, as a function of the chain length L and stiffness parameter κ for several values of the sphere radius R .

In order to be consistent with the SW work, we first relate the persistence length l_p to a free polymer chain in 3d. The bond-angle correlation function [269] (BAC) has been used in order to calculate l_p (see Section 2.3.4). We have computed the BAC function for free 3d polymer chains composed of N monomers and a stiffness parameter κ , and we have measured the persistence length $l_p(\kappa, N)$. These results are presented in Figure 8.1. We observe that the persistence length is independent of chain length, i.e., $l_p(\kappa, N) = l_p(\kappa)$ as expected. The limiting case of flexible chains corresponds to $\kappa = 0$. In this case, the persistence length is given by the bond length $l_p = 1.1\sigma$.

We have focused, first, on the behavior of flexible polymer chains. The mean square end-to-end distance $\langle R_{ee}^2 \rangle$ as a function of chain length L is studied for different sphere radius R . The results are shown in Figure 8.2. Note that for small enough L/R , $\langle R_{ee}^2 \rangle \sim L^{1.5}$. This exponent is nothing but twice the Flory exponent ($\nu = 3/4$) for a planar 2d self-avoiding random walk (SAW). The observed SAW breaks down for polymer chains that are long enough to feel the curvature of the sphere. This happens when the end-to-end distance becomes of the order of the sphere radius, then a maximum value for $\langle R_{ee}^2 \rangle$ is reached. In between, a transient linear regime is observed due to possible crossover effects. In comparison with the predictions of the SW formalism, a linear regime for chains with

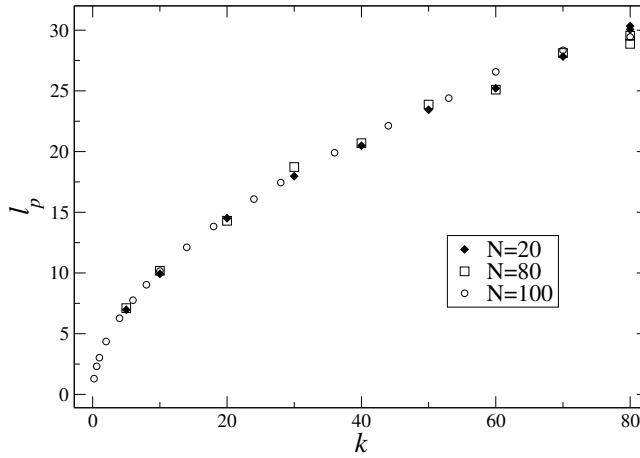


Figure 8.1. Persistence length l_p for a free 3-D polymer chain vs. the stiffness parameter κ and the number of monomers N . The results indicate that the persistence length is independent of the chain length.

length satisfying $L < R^2/(2l_p)$ is found corresponding to our SAW regime but for ideal chains ($\nu = 1/2$). Once the maximum in $\langle R_{ee}^2 \rangle$ is reached, some amount of oscillations appear in the data before we enter the limit of uncorrelated chain ends where $\langle R_{ee}^2 \rangle = 2R^2$.

A comparison between the MC data for flexible polymer chains with the predictions of the MM and SW theories for small sphere radius ($R < 10$) is presented in Figure 8.3. We find MC results to be in better agreement with SW theory (solid lines) than with MM predictions (dashed lines).

For $R = 5$, due to a very small sphere radius, we reach the limit $l_p L \gg R^2$ even for very short chains, and $\langle R_{ee}^2 \rangle \approx 2R^2 = 50$ as predicted by SW and MM theories. An oscillatory behavior is observed in the MC data for all the radius studied for small L . However, the SW theory predicts such oscillations only for $R < 4l_p$. This upper limit is below the range of radius considered for flexible chains ($l_p = 1.1$) and thus, no oscillations can be expected. Finally, the SW and MM formalisms predict, in all the cases studied, a mean square end-to-end distance smaller than MC results. The origin of this disagreement is in the excluded volume interactions between monomers which promote a stretching of the chain and cause an extra degree of orientational bond correlations.

In order to measure such orientational bond correlations we have used the bond orientational correlation function BOC (see Chapter 2.3.5).

In Figure 8.4 we plot the BOC function for short polymer chains ($N = 20$) confined to the surface of a sphere of radius $R = 10$ for several values of the stiffness parameter κ . A comparison between chains with excluded volume interactions (symbols) and ideal chains (lines) is presented. The degree of orientational correlation between bonds decreases as their distance in the chain sequence increases. The largest differences between short ideal and excluded volume chains

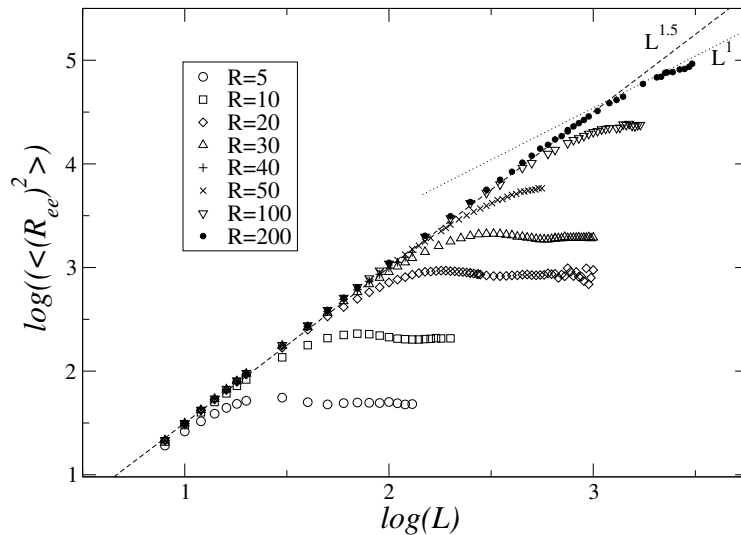


Figure 8.2. Log-log plot of the chain mean square end-to-end distance $\langle R_{ee}^2 \rangle$ as a function of chain length, L , for different values of the sphere radius R for flexible chains ($\kappa = 0$). Symbols depict our MC results. A dashed line of slope 1.5, and a dotted line of slope 1 are included to guide the eye.

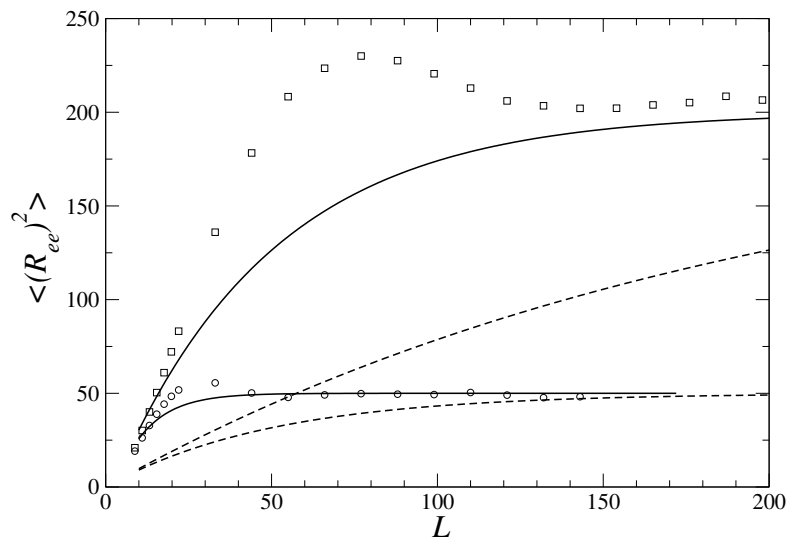


Figure 8.3. Mean square end-to-end distance $\langle R_{ee}^2 \rangle$ as a function of chain length L for $R = 5$ (\circ) and $R = 10$ (\square). The persistence length is set to $l_p = 1$ ($\kappa = 0$). Solid and dashed lines correspond to the predictions of SW and MM, respectively

are observed for flexible chains ($\kappa = 0$, $l_p = 1.1\sigma$). In such a case, the excluded volume effect causes an extra orientational correlation between monomers up to several positions in the chain sequence, whereas an ideal flexible chain loses its bond orientational correlation when bonds are separated more than two positions in the chain sequence. The excluded volume effect is particularly relevant in flexible chains since chain crossovers become banned. The chain monomers act as a steric barrier for other monomers forcing the chain to stretch out and $\langle R_{ee}^2 \rangle$ increases. For ideal chains crossovers take place easily and the monomer distribution is rather isotropic. As the stiffness of the chain increases, the BOC function for both ideal and excluded volume chains display a similar behavior (see Figure 8.4). It is worth to mention that the stiffness contribution to the orientational bond correlations is larger than the excluded volume one for small polymer chains.

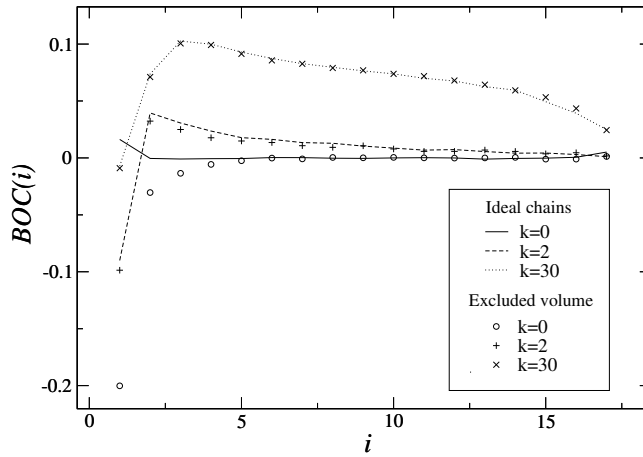


Figure 8.4. Bond orientational correlation function (BOC) vs. the bond position for chains of length $N = 20$ confined to a sphere of radius $R = 10$. A comparison between ideal (lines) and excluded volume chains (symbols) is shown for several values of stiffness parameter $\kappa = 0, 2, 30$ (The corresponding persistence length is $l_p = 1, 4.4, 18.1$, respectively.)

Above results indicate that for increasing value of the chain stiffness, a better agreement between SW theory and MC simulations should be observed. In Figure 8.5 we plot $\langle R_{ee}^2 \rangle$ vs. the chain length L for stiff chains with a persistence length $l_p = 10$ in the regime $R \leq 2l_p$. We can observe a rather good agreement between the MC data (symbols) and the predictions of the SW theory (solid lines), specially for small L values. The position of the local maxima and minima of the oscillatory behavior can be explained in the following way. Local minima appear approximately when the chain length is a multiple of a full revolution around the sphere, that is, $L \approx 2n\pi R$. The conformation of a rather stiff polymer chain merely fluctuates from the one that is fully stretched and follows a maximum circle onto the sphere. On the other hand, the maxima are observed when $L \approx (2n + 1)\pi R$. In fact, chain fluctuations cause the maximum distance to be smaller than the diameter of the sphere $2R$ and the minimum distance to be larger than zero.

As L/l_p increases, the polymer structure can be rescaled to a flexible chain composed of blobs of size l_p . Thus, fluctuations around the conformation that occupies the maximum circle increases and the position of the chain ends become uncorrelated. At this stage $\langle R_{ee}^2 \rangle \rightarrow 2R^2$ for ideal chains. From Figure 8.5 we can observe that the presence of the excluded volume interactions leads to higher asymptotic values for $\langle R_{ee}^2 \rangle$ when compared to the ideal case. Furthermore, when the chain is large enough to complete a full revolution around a maximum circle onto the sphere, the excluded volume leads to an additional separation between successive revolutions. As a consequence, just after the first minimum, the differences between the SW predictions and the MC data are observed to increase.

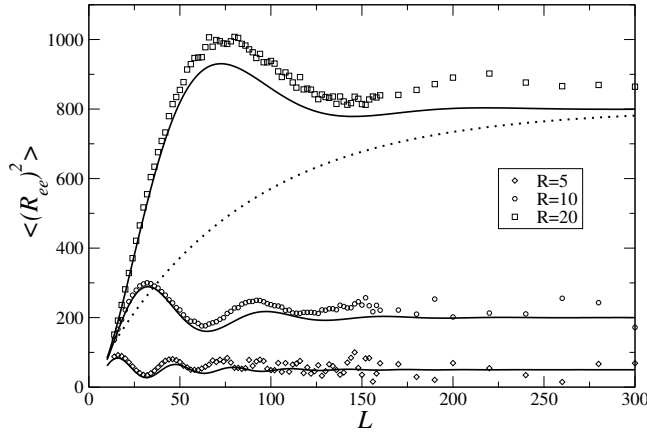


Figure 8.5. Mean square end-to-end distance $\langle R_{ee}^2 \rangle$ vs. the chain length L , for stiff chains with persistence length $l_p = 10$ ($\kappa = 9.8$) and for small values of R/l_p ($R/l_p \leq 2$). Symbols are for our MC data; solid lines correspond to the SW predictions; and dotted line stands for MM solution for a sphere of radius $R = 20$.

The effect of increasing the surface radius is depicted in Figure 8.6. Polymer chains of size such that $L < 2l_p$ exhibit a rigid-rod behavior so that, in the limit of high R/l_p ratio, $\langle R_{ee}^2 \rangle \sim L^2$ (dashed line). The asymptotic value corresponds to a flat surface ($R \rightarrow \infty$). For $L > 2l_p$, the polymer behaves as a flexible chain when rescaled by l_p . In this case, and for large R values, we recover the characteristic 2d-SAW regime with $\langle R_{ee}^2 \rangle \sim L^{1.5}$ (solid line). This result is consistent with the previous simulations for flexible chains shown in Figure 8.2. By increasing the chain length, a transient regime, compatible with possible crossover effects, is observed (dotted line). Finally, a plateau is reached for $L > R^2/(2l_p)$. The size of the chain at which the end-to-end distance reaches its saturation value agrees with the limit predicted by the SW theory in the random walk regime.

For $R/l_p > 4$, the role of the excluded volume interactions is evident in the presence of a maximum in $\langle R_{ee}^2 \rangle$ and subsequent oscillations in it, as shown in Figure 8.7. Such behaviors of $\langle R_{ee}^2 \rangle$ are not predicted by either SW or MM theories. Nonetheless, the comparison shows that the SW results (solid lines) are in much better general agreement with the MC data than the MM predictions (dashed lines).

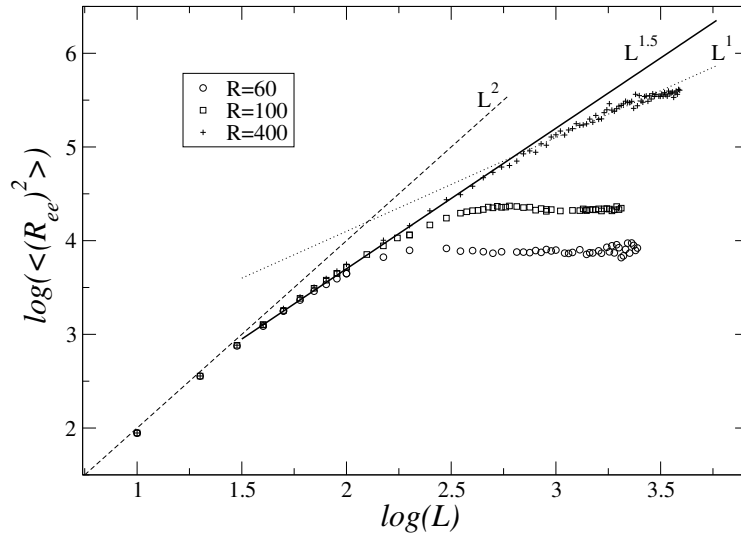


Figure 8.6. Log-log plot of the mean square chain end-to-end distance $\langle R_{ee}^2 \rangle$ vs. the chain length L for high R/l_p ratios ranging from $R/l_p = 3$ to $R/l_p = 10$. The persistence length is set to $l_p = 20$. The dashed line of slope 2, the solid line of slope 1.5, and the dotted line of slope 1 are guides to the eye.

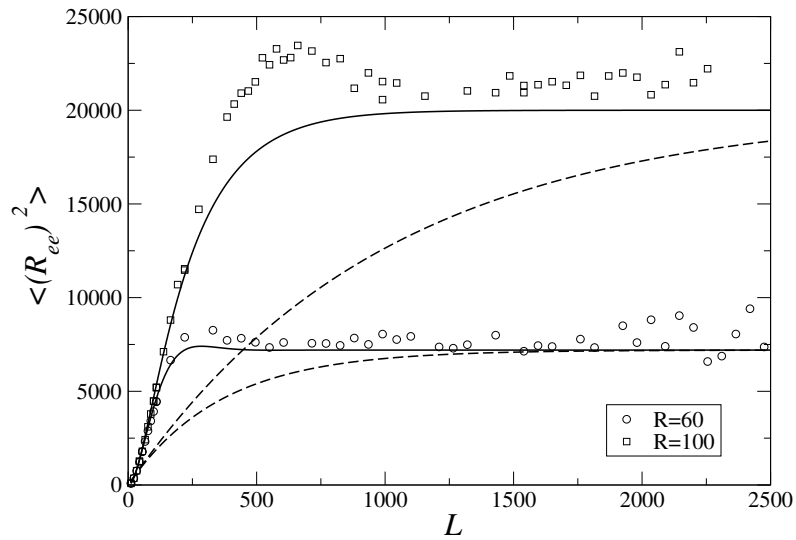


Figure 8.7. Mean square chain end-to-end distance $\langle R_{ee}^2 \rangle$ vs. the chain length L for sphere radius $R = 60$ and $R = 100$. The persistence length is set to $l_p = 20$. Solid lines correspond to the SW predictions and dashed lines are MM results.

The behavior of $\langle R_{ee}^2 \rangle$ with the persistence length l_p has been examined for small and large sphere radius in Figure 8.8 and Figure 8.9 respectively. Our MC data has been compared to the SW formalism for a polymer chain of length $L = 110$. Figure 8.8 shows increasing differences in l_p between the SW predictions and the MC results for various R between $R = 7$ and $R = 15$. These differences have their origin in the transition from disordered to helicoidal polymer conformations (studied in detail in the next section) as the chain stiffness is increased. Such transition is not observed in ideal chains, and thus, are absent in the SW formalism. Nevertheless, SW formalism is still able to qualitatively reproduce the behavior of $\langle R_{ee}^2 \rangle$ with l_p which increases or decreases depending on the value of the sphere radius. It is interesting to mention that the MM formalism predicts a monotonous increase of the mean square end-to-end distance with the persistence length in all cases (see Eq. 8.1). This result does not agree with either SW theory and or with our MC data.

For large sphere radius (Figure 8.9), when the helicoidal state becomes impossible, a gradual recovery of the agreement between the SW predictions and the MC results is observed as l_p increases. In the limit of large l_p values, both SW and MC results match almost perfectly. This agreement is consistent with the fact that BOC functions of ideal and excluded volume chains are observed to be very similar for rigid chains confined to large spheres. Under such conditions, the behavior of an excluded volume chain will approach that of an ideal chain when the probability of contact among non-consecutive monomers decreases and a similar chain stretching is expected in both cases. For $l_p L \ll R^2$ a linear dependence of $\langle R_{ee}^2 \rangle$ with l_p is observed, particularly for large R (see data for $R = 30$ in Figure 8.9). This linear regime agrees with the predictions of the SW and MM theories for $l_p L \ll R^2$.

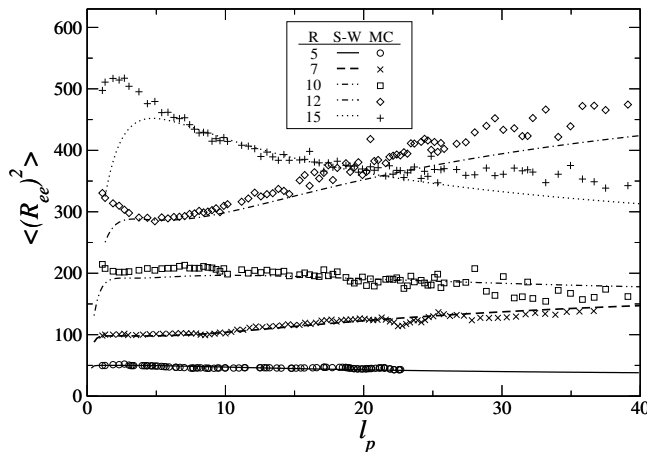


Figure 8.8. Mean square chain end-to-end distance $\langle R_{ee}^2 \rangle$ vs. the persistence length l_p for small and intermediate radius of the sphere R . The chain length is set to $L = 110$. Symbols stand for our MC-data and lines for the SW predictions.

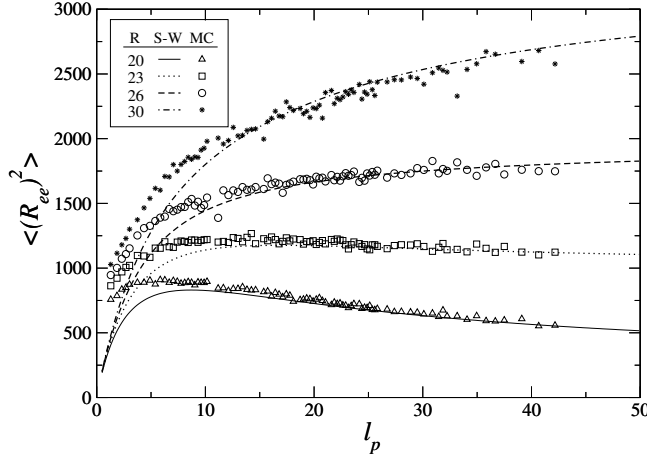


Figure 8.9. Same as Figure 8.8 for large sphere radius.

At first sight, it may seem rather striking that by changing the radius of the sphere only slightly the mean square end-to-end distance changes its tendency to increase or decrease with l_p . This apparent paradox can be easily understood by taking into account the asymptotic value of $\langle R_{ee}^2 \rangle$ in the limit $l_p \rightarrow \infty$. When a polymer has a large degree of stiffness it tends to expand as much as possible and the most favorable energetic configuration is the one that occupies a maximum circle onto the sphere. Thus, the distance between chain ends depends on the ratio between the chain length L and the length of the maximum circle $2\pi R$.

The number of integer circles n_c covered by the polymer is,

$$n_c = \text{Int} \left(\frac{L}{2\pi R} \right),$$

and the arc length that joins the two chain ends is $l_{arc} = L - 2\pi R n_c$. It can be easily seen that the distance between such ends d_{ee} , is given by

$$d_{ee} = 2R \sin \left(\frac{l_{arc}}{2R} \right) \quad (8.7)$$

In Figure 8.10 we plot the behavior of $\langle R_{ee}^2 \rangle$ with the radius of the sphere. We present a comparison between the data obtained in the MC simulations for several l_p value, and for a polymer chain of length $L = 110$, with the geometrical predictions (Eq. 8.7) derived for a chain that follows a maximum circle onto the sphere. We observe that the agreement improves when the chain stiffness is increased, as expected. An almost perfect match between the location of local maxima and minima are obtained. Any residual small differences, are due to the wiggling of the chain and the deviation from the large circle trajectory.

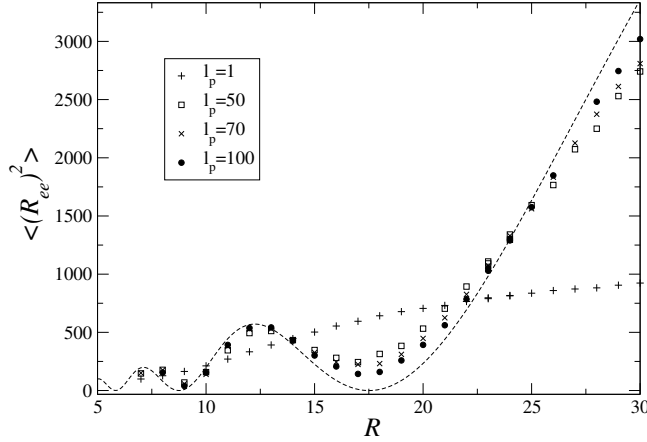


Figure 8.10. Mean square end-to-end distance $\langle R_{ee}^2 \rangle$ vs. the sphere radius R , for several values of the persistence length. Chain length is set to $L = 110$. Symbols stand for our MC-data. The dashed line is the expected behavior from the geometrical calculations based on the maximum circle occupation by the chain (see Eq. 8.7).

8.4.2 Transition from disordered to helicoidal conformations

Although both ideal and excluded volume chains tend to occupy a maximum circle in the limit of $l_p \rightarrow \infty$, a fundamental difference between them arises due to the excluded volume interactions: chains with excluded volume effects are observed to exhibit a transition from a disordered to an helicoidal conformation by increasing the chain stiffness, whereas no such transition to the helicoidal state has been observed for ideal chains. This different behavior between ideal and excluded volume chains as a function of chain stiffness can be probed by measuring the bond orientational correlation function (BOC).

In Figure 8.11(a) and Figure 8.11(b) we have plotted the BOC function for excluded volume and ideal chains, respectively. The polymer chain length has been selected to be $L = 110$ and it is confined to a sphere of radius $R = 10$. We can observe a rather different behavior between them as the stiffness parameter κ is increased. For ideal chains the BOC function decreases monotonically, independent of κ , whereas for excluded volume chains the BOC function displays a local maximum when the beads are separated in the chain by approximately $2\pi R/\sigma$ bond positions. The position of this local maximum is consistent with the fact that approximately $2\pi R/\sigma$ bonds are needed to complete a revolution around the sphere. Figure 8.11(c) shows the subtraction between the BOC function for excluded volume and ideal chains. The differences become evident for a stiffness parameter $k \geq 40$. It is precisely at this point where the transition from a disordered to an helicoidal state takes place. The results for a sphere of radius $R = 7$ are presented in Figure 8.12. The presence of a second maximum (see Figure 8.12(c)) at $i \approx 2\pi R/\sigma$ indicates that the polymer chain, following an helicoidal structure, has completed two revolutions around the sphere ($\kappa \geq 20$). It is worth to note that increasing the L/R ratio the helicoidal state appears at smaller

κ values. Typical conformations for $L = 110$ and $R = 7$ are shown in Figure 8.13. Figure 8.13(a) stands for an excluded volume chain with $\kappa = 2$, below the transition value. In Figure 8.13(b) we have plotted a typical conformation of an excluded volume chain with $\kappa = 50$, where a clear helicoidal structure can be seen. In Figure 8.13(c) a characteristic conformation of an ideal chain with identical rigidity ($\kappa = 50$) is plotted. Observe how, in the latter case, the helicoidal shape is lost and many chain crossovers take place. Such conformations have a smaller entropic penalty than the more ordered helicoidal conformations and, therefore, are preferred. We can conclude that excluded volume interactions are needed for the polymer chain to develop an helicoidal structure.

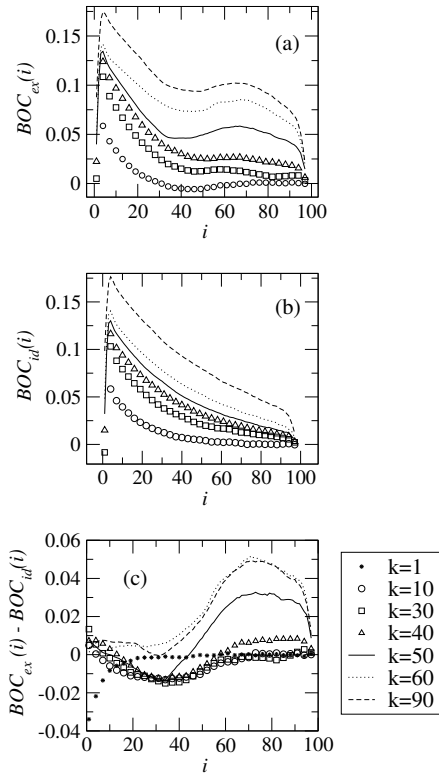


Figure 8.11. Bond orientational correlation function (BOC) as a function of bond position for chains of length $L = 110$ confined to a sphere of radius $R = 10$. (a) excluded volume chains; (b) ideal chains; (c) subtraction (a)-(b). The onset of the helicoidal state is reflected by the appearance of a local maximum at large values of bond position ($\kappa \geq 40$).

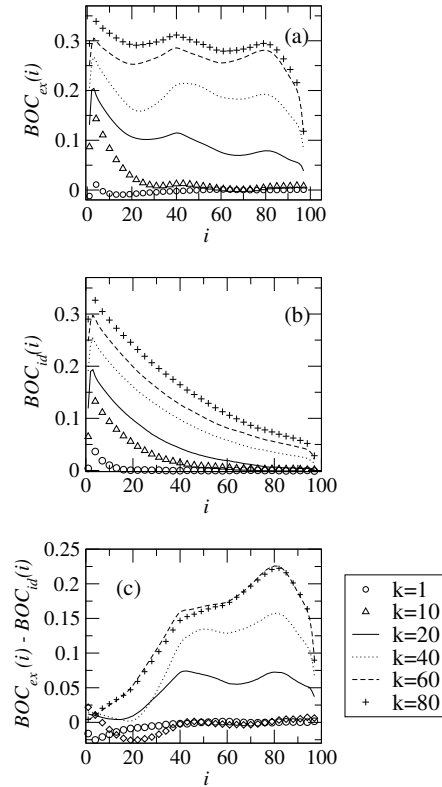


Figure 8.12. Same as Figure 8.11 for a polymer of length $L = 110$ confined to a sphere of radius $R = 7$.

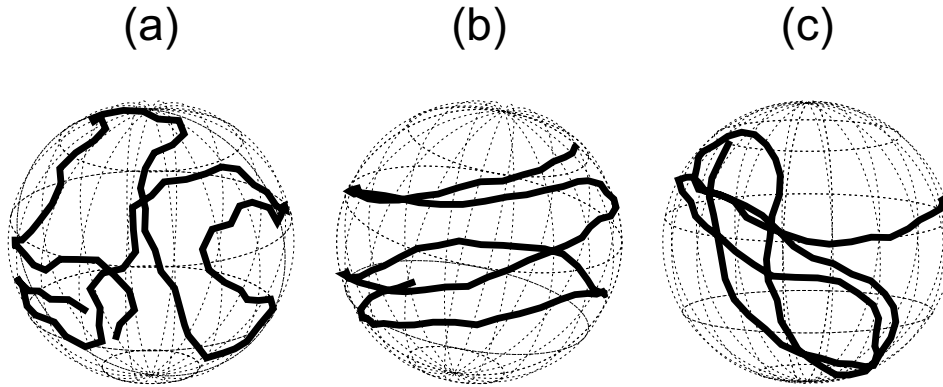


Figure 8.13. Snapshot of a typical conformation of a polymer chain of length $L = 110$ confined to a spherical surface of radius $R = 7$. Figures (a) and (b) correspond to excluded volume chains with a stiffness parameter: (a) $\kappa = 2$, below the transition point; (b) $\kappa = 50$ where the helix is formed. Figure (c) stands for an ideal chain with the same stiffness as in (b). In contrast to the excluded volume chain, no helix structure is found.

To characterize the transition to a helical state, one can try various ways of defining an order parameter [251]. Such effort was unsuccessful in our case where the chain is confined to the surface and did not allow us to probe the change from one configurational state to the other. In contrast, we have found the BOC correlation function to be an extremely useful tool. In fact, one can define an order parameter [249] by integrating the value of our bond correlation function BOC, and normalizing it by the number of monomers. However, it can be deduced from Figures 8.11 and 8.12 that this order parameter will increase for both ideal and excluded volume chains, and the difference between these two cases will be difficult to quantify. In contrast, the complete BOC correlation function contains details of the presence of strong correlations at large distances for excluded volume chains and this information allows us to show the presence of the transition. It also allows one to know whether the new helix state performs one or more revolutions around the sphere.

We should remark that $L > 2\pi R$ is needed to ensure that the chain will circle the sphere at least once. On the other hand, there is also a minimum value of R that makes it possible to accommodate a stable helix. Thus, there is an upper limit to the L/R ratio where helix structures can develop. By increasing L/R we have seen the transition from disordered to helix structures to take place at smaller values of the stiffness parameter κ . For instance, for $L = 110$ the helix forms on a sphere of radius $R = 10$ at a critical stiffness parameter $\kappa_c = 40$, for $R = 7$ at $\kappa_c = 20$ and for $R = 5.5$ at $\kappa_c = 5$. This fact can be easily understood in the following way. A small displacement of a monomer on the surface of the sphere induces a change in the $(1 + \cos(\theta))^2$ term of the bending energy U_B (see

Eq. 8.5) that increases with decreasing the sphere radius. Thus, a smaller value of κ is needed to get the same ΔU_B .

The width of the surface potential that confines the chain to the surface is also expected to play a role in the helicoidal transition [249]. If the range of the attracting potential is large enough, a chain with excluded volume will be able to cross itself at different levels inside the adsorption layer. Eventually, this entails to a situation rather similar to what we observed for an ideal chain. In that case, the chain prefers a disordered conformation in which the entropic penalty is smaller than in an helicoidal state. We thus expect that the helicoidal transition to disappear if the width of the potential is large enough to allow the chain to self-cross at different levels. Note that entropically it is always favorable to have conformations that crosses itself rather than the helical conformation. And if the energetics also allow chain crossings, the helicoidal state must vanish at some point.

Next, we would like to comment on a work by Sakaue et al. (Ref. [249]) who have studied the adsorption of a stiff chain onto a spherical core particle. A direct comparison with these results is not possible as the radius of the spherical surface is only 1.3 times the radius of the monomers in Ref. [249]. In contrast, we have studied systems with a radius of at least 5 or more times the monomers radius. This is necessary in our case since we are considering a totally adsorbed or confined chain and a sphere of too small a radius cannot keep all the monomers of the chain trapped onto the surface. In fact, as we will see shortly, there is a lower limit of a critical radius for the existence of stable helical conformations for a given a chain length. In Ref. [249] a longer range potential is used which allows monomers to fly around without being confined onto the surface. This entails the possibility of having helicoidal conformations that do not affect all the chain. Helicoidal conformations under such conditions of small sphere radius and large width of potentials are not stable and one must speak in terms of a probability for a chain to adopt an helicoidal conformation.

The transition point to the helix state can be roughly estimated if we consider a balance between the bending energy of a polymer chain, that wants to wrap around the sphere along the large circle, and the excluded volume interaction that prevents the chain segments to overlap. On one hand, the bending free energy in the case of a chain forming a helix structure can be written as [270] $F_{bending} \sim l_p L / R^2$. On the other, in order to estimate the steric free energy we have to evaluate the possible number of contacts among monomers that is proportional to the number of monomer units per circle, thus, $F_{steric} \sim L / (2\pi R)$. At the transition point, $F_{bending} \approx F_{steric}$, from which a characteristic persistence length l_{pc} is derived that follows a linear relationship with the sphere radius, $l_{pc} \sim R$.

In Figure 8.14 we have plotted l_{pc} as a function of the radius of the sphere R for different chain lengths. In all the cases studied ($L \gg R$) we have found l_{pc} to grow roughly linearly with the radius of the sphere as predicted.

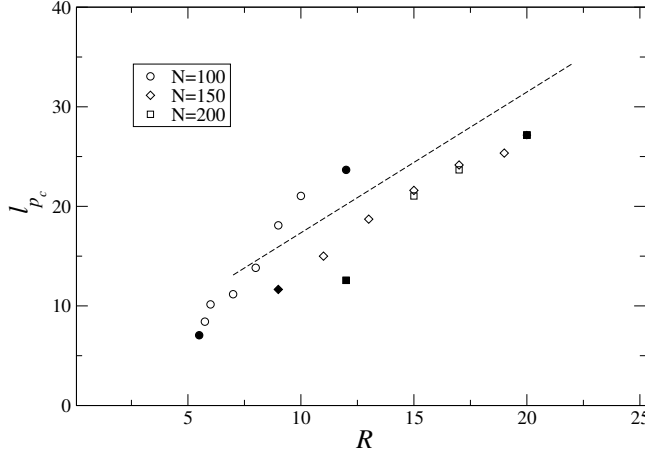


Figure 8.14. Characteristic persistence length l_{pc} for which the helix structure appears vs. the radius of the sphere for several chain lengths. The upper bound and lower bound values of the radius where the helix forms are depicted by filled symbols. The dashed line is a guide to the eye and points out the linear relationship between l_{pc} and R when $L \gg R$.

8.5 Concluding remarks

We have characterized the behavior of excluded volume chains with restricted motion on spherical surfaces using off-lattice Monte Carlo simulations. A comparison with the Mondescu-Muthukumar and Spakowitz-Wang theories developed for non-excluded volume chains has been presented.

We have found that the Spakowitz-Wang theory to be in better agreement with MC results than the Mondescu-Muthukumar formalism. However, we should bear in mind that the MM theory was not intended to account for the stiffness of the chain and deviation from our simulations are expected for large persistence length. This is true for the whole range of parameters studied. We have observed that our numerical data match almost quantitatively with the predictions of the SW formalism when: *i*) chain length is smaller than the length of the maximum sphere circumference; and *ii*) the chain is stiff enough, that is, in the regime $L/(2\pi) < R < 2l_p$. Within this regime, the measurement of the bond orientational correlation function (BOC) for ideal and excluded volume chains provides very similar results. Thus, the behavior of excluded volume chains can be described, in this context, roughly as ideal chains, and the predictions of the SW formalism are reproduced.

The main difference between the SW theory and the MC results, for chains such that $L < 2\pi R$, is found in the measurement of the mean square end-to-end distance $\langle R_{ee}^2 \rangle$. The MC data is characterized by the presence of a maximum and

subsequent relaxation oscillations towards the asymptotic value $2R^2$ for $R/l_p > 4$. The SW theory claims such oscillatory behavior to disappear for sphere radius larger than four times the persistence length, but excluded volume chains are observed to show such damped oscillations in all the cases we have examined.

MC data has shown that both, flexible and stiff excluded volume polymer chains exhibit, in a range of chain lengths, a self-avoiding random walk (SAW) behavior for $R/l_p > 2$ in contrast to the expected ideal random walk predicted by the SW formalism for $R/l_p > 4$. A rigid rod regime is found for $L < 2l_p$. For long polymers, beyond the SAW regime, $\langle R_{ee}^2 \rangle$ reaches a maximum plateau value for $L \geq R^2/(2l_p)$, in agreement with the predictions of the SW formalism.

One exciting feature observed in our MC simulations, is the transition from a disordered to helicoidal polymer conformation. This transition does not exist for ideal chains models, and thus, was not predicted by either MM or SW formalisms. This transition has been studied in detail through the measurement of the BOC function. In the helicoidal state, long-range correlations are observed between bonds displaying local maxima at bond positions that complete a full revolution around the sphere. For a given a chain length, the transition is only found within a particular range of sphere radius. There is a lower bound of persistence length which provides the minimum rigidity required to stretch the chain along the spherical surface. This value decreases with the radius of the sphere. The relation between the characteristic persistence length and the radius of the sphere at the transition point is observed to be consistent with a balance between the bending energy due to deviations of the chain from the large circle trajectory and the excluded volume interactions. Similar behavior has been observed in the study of stiff polyelectrolytes adsorption on an oppositely charged spherical particles. In particular, the simulations carried out by Stoll and Chodanowski [250] show that by increasing the chain stiffness, solenoid conformations at the particle surface are progressively achieved at small or zero values of the ion concentration. The latter corresponds to the case of strong polymer-surface interaction, in agreement with the assumption of polymer confinement implemented in our model.

Chapter 9

Adsorption of stiff copolymers on homogeneous flat surfaces

The adsorption of heteropolymers onto surfaces is a complex problem of the utmost importance. Besides its inherent complexity, many coarse properties of heteropolymers can be obtained through statistical studies. The present chapter is devoted to the study of copolymers, the simplest heteropolymers that exist. In particular, we focus on the role that chain stiffness and chain structure play on the adsorption process of copolymers. We will see that even when only two different types of monomers exist along the chain, the behavior of such polymers exhibit a rich and complex behavior.

9.1 Introduction

Polymer adsorption has been a topic of great experimental and theoretical interest due to its enormous number of applications in science and technology. These applications cover the stabilization of colloidal suspensions, adhesion, gel permeation, chromatography, etc. It is a characteristic feature of all these systems that their physical properties are mediated by the interaction between polymer molecules and an impenetrable surface. The bulk conformational properties of these polymer chains are strongly modified in contact with the surface due to a subtle competition between the loss of entropy at the surface and the gain of internal energy.

In the last decade, a large number of theoretical studies have been devoted to the adsorption of flexible homopolymers [271–277], diblock copolymers [278–

280], *AB*-type alternating copolymers [281–283] and random copolymers [284–286]. In turn, the adsorbing surface has been considered as flat and homogeneous [271–275, 278–286] or heterogeneous [276, 277, 287, 288], including regions with a random distribution of adsorption energies.

However, many polymers are rigid up to a certain extent due to steric and electronic delocalization effects. Few important examples of such stiff chains are found in synthetic macromolecules and specially in biology, just to mention, DNA, collagen, microtubules and actin filaments. On a local length scale, the stiffness is very prominent and it is expected to produce significant changes in the macromolecular properties. Among the many significant phenomena induced by the polymer stiffness we can mention the nematic liquid crystalline ordering of semiflexible polymer segments.

The constrained rotational motions of the monomers about the chain backbone makes inadequate the use of conventional models developed for flexible chains. The statistical mechanics of such chains was first formulated by Kratky and Porod [100], about 50 years ago, and it is still considered as a non trivial problem. In contraposition to flexible chains, the number of studies devoted to stiff polymer chains is scarce and focused on the behavior of homopolymer structures [289–293].

Copolymer adsorption onto surfaces has become recently a topic of great interest. For instance, some copolymers (PLL-g-PEG) are found to spontaneously adsorb from aqueous solutions onto metal oxide surfaces (TiO_2), reducing the adsorption of blood serum and individual proteins, such as fibrinogen, that are known to play a major role in the coagulation process and thrombosis [294–296].

The adsorption of copolymeric chains has also found applications in nanotechnology. For instance, pluronic triblock copolymers is used in order to active external wall carbon nanotubes and, at the same time, to prevent non specific bounding of molecules onto nanotubes surfaces [297]. Such coated nanotubes are the basis for the design of highly specific electronic biosensors. Furthermore, copolymer absorption plays an important role in the design of dynamic polymeric wall coatings for capillary electrophoresis [298]. Polymer properties help to create an ideal wall coating with a notorious impact on the electro-osmotic flow capabilities.

The purpose of the present chapter is to study how the adsorption properties of stiff polymers are modified when the chain structure is changed and to examine whether the universal scaling laws apply in these systems. Besides the block size, we will characterize the adsorption process as a function of the chain rigidity and the chain length. Our simulations are single-chain. Although applications usually involve many interacting chains at the surface, the adsorption of isolated

chains provide a valuable benchmark for studies of many-chain systems and is directly relevant to a number of emerging single-molecule approaches to molecular genomics [299, 300].

9.2 Numerical Model

We have studied the adsorption of a semiflexible block-copolymer chain onto an homogeneous surface using off-lattice Monte-Carlo simulations (see Section 3.1). We have considered the polymer chain to be confined in a box with periodic boundary conditions in the $x - y$ domain. The length of the cell is chosen to be at least twice the chain length N , and an impenetrable planar surface is set at the plane $z = 0$. Chain stiffness is introduced through the bending potential U_{bend} given by:

$$U_{bend} = \sum_{\theta} \kappa(1 + \cos \theta)^2, \quad (9.1)$$

where θ is the bond angle between any three consecutive beads and κ is the bending constant.

Monomer units can be of type A or B and are distributed along the chain of length N according to the selected polymer structure. A diblock copolymer will be denoted by $(A_{N/2}B_{N/2})$ and, in general, a block copolymer formed by α -monomers of type A followed by α -monomers of type B , repeating this sequence along the entire chain, by $(A_{\alpha}B_{\alpha})_{N/2\alpha}$.

Monomers of type A and B interact with the impenetrable surface at $z = 0$ with adsorption energies ϵ_A and ϵ_B , respectively. Thus, we define an adsorption potential U_{ads} as,

$$U_{ads} = n_A\epsilon_A + n_B\epsilon_B, \quad (9.2)$$

where n_A and n_B are the number of A -type and B -type monomers such that their z -coordinate verifies $0 < z < \sigma$. The total energy of the system will contain the above contributions and is written as:

$$U = U_{ads} + U_{bend} + U_{steric} \quad (9.3)$$

where U_{steric} stands for a hard core potential (Eq. 3.9).

The initial configuration of the self-avoiding polymer is randomly generated with one monomer attached to the surface $z = 0$. At very high temperatures, or equivalently at low adsorption energies, the chain has a tendency to diffuse into the bulk. We prevent this by forcing the polymer to have at least one monomer attached to the surface. However, one does not expect any significant change in the statistical properties of the adsorbed chain at low temperatures. We define

one Monte-Carlo Step (MCS) as N trials to move the chain. The system has been equilibrated for 5×10^5 MCS. Subsequently, statistical properties of the chain are evaluated every 10 MCS. The results have been finally averaged over 10^6 measures. For the rest of the chapter we have taken $\sigma = 1.0$. The temperature is given in units of $1/k_B$, hence $T \equiv k_B T$.

9.3 Results and Discussion

9.3.1 Diblock chains

In this section we will focus in the study of the behavior of stiff diblock polymer chains adsorbing onto a planar surface. A diblock chain of length N consists in two segments of equal size $N/2$, the first one composed of monomers of type A , followed by a second block containing monomers of type B . Monomers A and B interact with the surface with energies ϵ_A and ϵ_B , respectively. A negative adsorbing energy stands for an attractive interaction whereas a positive value implies repulsion. Through the simulations we have set $\epsilon_A = -1$ and we have studied the transition towards the adsorbed state as a function of the chain length N , the stiffness parameter κ and the interaction energy ϵ_B .

In Figure 9.1 we have plotted the change in the absolute value of the averaged adsorbing energy per monomer $E/N = \langle n_A \epsilon_A + n_B \epsilon_B \rangle / N$ as a function of the inverse of the temperature $1/T$, for different values of the stiffness κ , and for a fixed adsorbing energy $\epsilon_B = -0.5$. Figure 9.1(a) stands for short polymer chains ($N = 20$), while Figure 9.1(b) is devoted to long chains ($N = 300$).

The behavior observed for stiff diblocks is very similar to the one found for semiflexible homopolymers [290,291]. Stiffed chains adsorb more easily onto the surface with increasing κ and, therefore, they are characterized by a higher critical adsorption temperature T_c . The limiting values observed for $T \rightarrow \infty$ corresponds to a chain completely adsorbed onto the surface with $|E|/N = 1/2|\epsilon_A + \epsilon_B|$. A remarkable difference with respect to the homopolymer adsorption becomes notorious for increasing chain lengths: the adsorption process becomes a two step process. Since A -type monomers interact more strongly with the surface than the B -type monomers, $|\epsilon_A| > |\epsilon_B|$, block- A adsorbs onto the surface at a higher characteristic temperature than the block- B , $T_{cA} > T_{cB}$, as can be seen in Figure 9.1(b). For comparison, we have also included in Figure 9.1(b) the averaged adsorption energy of an homopolymer of equal length, composed with A -type monomers only, and with rigidities $\kappa = 0$ (flexible) and $\kappa = 30$. We can observe that for stiff chains, the characteristic temperature at which the transition to the adsorbed state takes place for the homopolymer (A -type), is very similar to

the one found for the A -type block in the diblock chain.

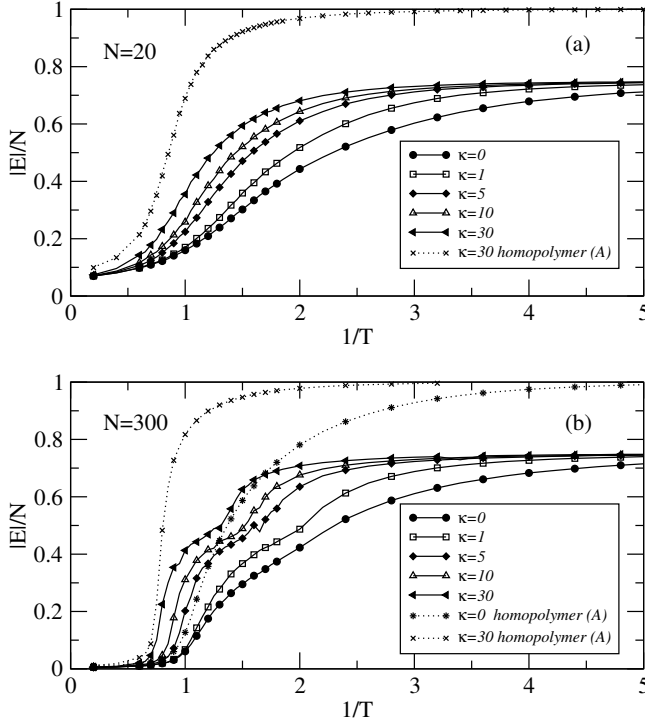


Figure 9.1. Averaged adsorption energy per monomer in diblock chains vs. the inverse of the temperature for different values of the stiffness parameter κ . The interaction energies are set to $\epsilon_A = -1$ and $\epsilon_B = -0.5$. (a) for a short chain $N = 20$; (b) for a long chain $N = 300$. For comparison we include the results for an homopolymer composed of monomers of type A for flexible ($\kappa = 0$) and stiff chains ($\kappa = 30$). Note how for increasing the chain length the adsorption becomes a two step process.

The effect of changing ϵ_B on the adsorption process is shown in Figure 9.2. The rest of parameters are set to $N = 200$ and $\kappa = 30$. Observe that for $\epsilon_B \geq 0$ the adsorption becomes independent of ϵ_B . This fact is due to the repulsive interaction with the surface in addition to the entropic effect. In these cases, the block- B does not adsorb at all. On the other hand, for an attractive interaction ($\epsilon_B < 0$) the block- B adsorbs onto the surface at a characteristic temperature that increases with the intensity of the interaction, as expected.

The characteristic adsorption temperatures at which the chain adsorbs onto the surface can be determined from the position of the maximum in the specific heat. The results for $N = 150$ and $\kappa = 30$, for different values of ϵ_B , are presented in Figure 9.3. A single peak appears for $\epsilon_B > 0$ corresponding to the characteristic adsorption temperature of block- A alone. For an attractive interaction we can observe two maximums related to T_{cA} and T_{cB} . It is also clear that the adsorption transition becomes sharper as $|\epsilon_B|$ increases. We should remark that at a constant chain length and stiffness, the characteristic adsorption temperature for the block- A is practically unaffected by tuning ϵ_B . To make clear the dependence of the transition temperature with the chain stiffness and the intensity of the interaction with the surface, we have plotted in Figure 9.4 $T_c(N, \kappa, \epsilon)$ as a function of the

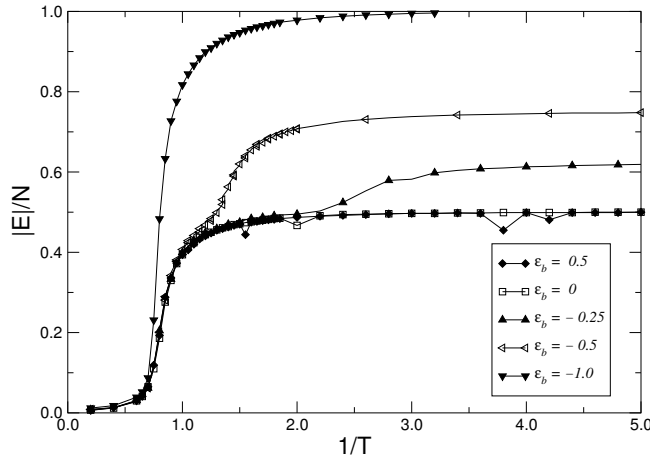


Figure 9.2. Averaged adsorption energy per monomer vs. the inverse of the temperature for different values of ϵ_B . The other parameters are set to $N = 200$, $\kappa = 30$ and $\epsilon_A = -1$. Note how the adsorption process becomes independent of ϵ_B for $\epsilon_B \geq 0$.

chain length N . The characteristic adsorption temperature is found to increase with the chain length and rigidity, as expected, and specially with the interaction with the surface, where the differences between T_{cA} for $\epsilon_A = -1$ and T_{cB} with $\epsilon_B = -0.5$ are remarkable even for the same stiffness κ .

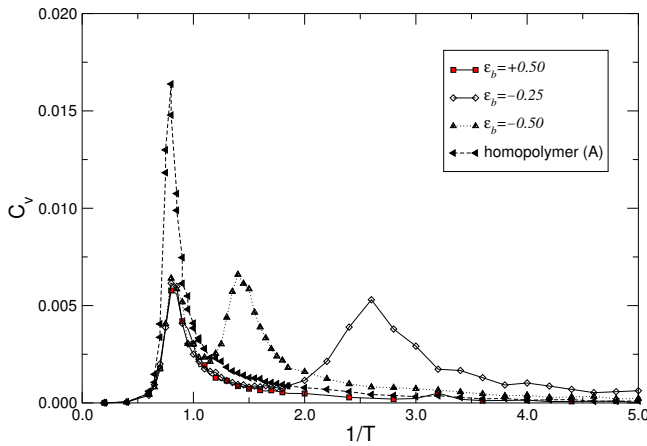


Figure 9.3. Specific heat of a stiff diblock chain vs $1/T$ for different adsorption energies ϵ_B . The other parameters are set to $N = 150$, $\kappa = 30$ and $\epsilon_A = -1$.

In order to examine the critical adsorption properties of semiflexible block-copolymers, we will assume initially the scaling *ansatz* proposed by Kramarenko et al. for flexible homopolymers [291]. We have determined the critical adsorption temperature for $N \rightarrow \infty$, $T_c(\infty, \kappa, \epsilon)$, and using these values we have done a scaling analysis of the data for the fraction of adsorbed monomers $\chi \equiv n/N$ as a function of the scaling variable τN^ϕ . n is the number of adsorbed monomers; N the chain length; and $\tau = (T - T_c(\infty, \kappa, \epsilon))/T_c(\infty, \kappa, \epsilon)$ is the temperature distance to the critical temperature. For a given value of the stiffness and the interaction energy, the crossover scaling for the fraction of adsorbed monomers can

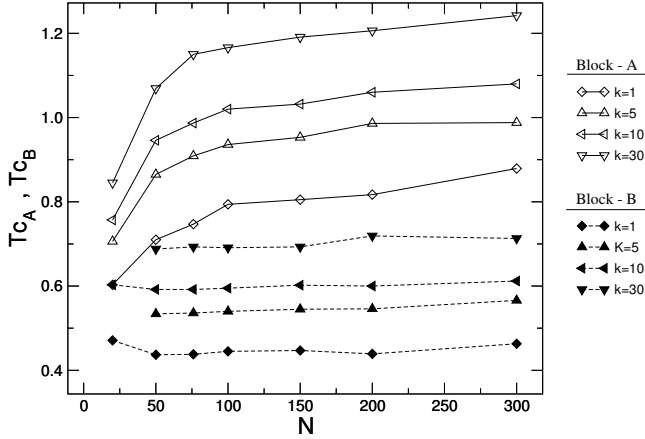


Figure 9.4. Transition temperatures for the block-*A* $T_{cA}(N, \kappa, \epsilon_A)$ (opened symbols) and for the block-*B* $T_{cB}(N, \kappa, \epsilon_B)$ (filled symbols), vs. the chain length, N . $\epsilon_A = -1$ and $\epsilon_B = -0.5$.

be expressed as:

$$\chi/N^{\phi-1} = h(\tau N^{\phi}) \quad (9.4)$$

In order to test our Monte-Carlo method, we have derived first the results for flexible homopolymers. In this case, we found an exponent $\phi = 0.59 \pm 0.02$ in agreement with the well known scaling exponent predicted by Kramarenko et al. [291]. This result is shown in the inset plot of Figure 9.5. However, for homopolymers with a large degree of stiffness we were unable to find the same scaling exponent. The best scaling exponent we have found for $\kappa = 30$ is $\phi = 0.85 \pm 0.05$ (Figure 9.5), far from the expected value for flexible chains. The fact that there is a range of values of ϕ that do not change appreciably the scaling has been observed in the paper of Moghaddam et al. [282] studying the behavior of a SAW copolymer onto a cubic lattice, thus, for small values of κ one could even scale the data with $\phi \approx 0.59$ with no appreciable differences [290]. The situation changes completely for large κ . In this sense, Kuznetsov and Sung [275] showed that the transition deadsorbed-adsorbed for semiflexible polymers is an outcome of the interplay between the shape of the surface attraction, including the thickness of the adsorption layer, the thermal fluctuations, and the chain stiffness. This non-universal scaling behavior has been also evidenced in the work of Gompper [301], where three distinct sub-regimes were expected due to the dependence of the scaling exponent ϕ with the potential shape acting on the monomers. Thus, a good scaling relation for semiflexible polymer chains must be a function of stiffness parameter κ , and the adsorption energy ϵ . In general, in our simulations we observe that as the degree of stiffness increases, the best value for the critical exponent ϕ in order scale the data also increases.

For diblock copolymers we were unable to find a single exponent ϕ for the whole chain, however, we observed that we could scale the data separately for

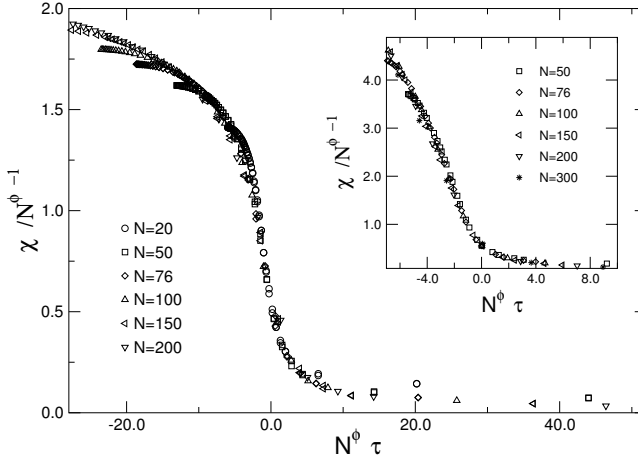


Figure 9.5. Scaling function $\chi/N^{\phi-1}$ vs. the scaling argument τN^ϕ for a semiflexible homopolymer with an adsorption energy $\epsilon = -1$ and a chain stiffness $\kappa = 30$. The best scaling exponent found is $\phi = 0.85$. Inset plot: The same scaling function for flexible homopolymers ($\kappa = 0$) with $\phi = 0.59$.

each block introducing two different exponents, ϕ_A and a ϕ_B , corresponding to the blocks with adsorbing energies ϵ_A and ϵ_B , respectively. In Figure 9.6 we show the scaling of stiff diblock chains ($\kappa = 30$) with $\epsilon_A = -1$ and $\epsilon_B = -0.5$. For the A -block we found an exponent $\phi_A = 0.80 \pm 0.05$ similar to the one found for an homopolymer of the same rigidity and adsorbing energy. This result indicates that there is a small effect of the B -block as long as the difference in the adsorbing energies is not too large. For the B -block we found a rather worse scaling with an exponent $\phi_B \approx 0.1$ (inset of Figure 9.6).

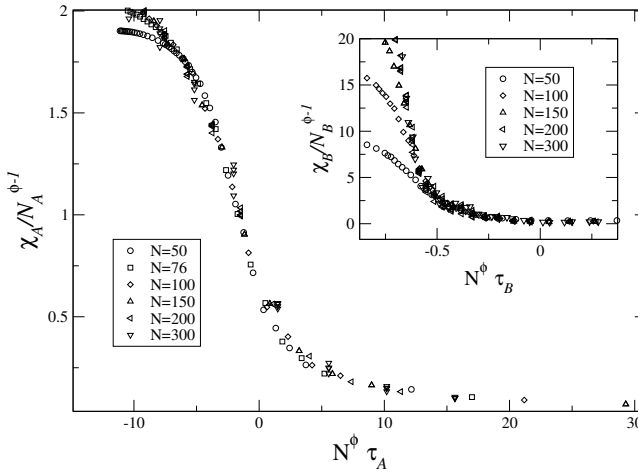


Figure 9.6. Scaling function $\chi/N^{\phi-1}$ vs. the scaling variable τN^ϕ for block- A of a semiflexible diblock chain with adsorption energies $\epsilon_A = -1$ and $\epsilon_B = -0.5$. The chain stiffness is set to $\kappa = 30$. The best scaling exponent for the block- A is $\phi_A = 0.8$, similar to the one found for semiflexible homopolymers with the same rigidity and adsorption energy. Inset plot: Same as before for the block- B . The best scaling exponent found is $\phi_B = 0.1$.

In comparison to our results, a recent study of Whittington [281] deduced analytically for a lattice-flexible SAW, in the limit $N \rightarrow \infty$, that an homopolymer

of N_A monomers has the same critical adsorbing temperature T_c than a block copolymer of N_A monomers in which the B -type monomers interact with the surface with an energy $\epsilon_B = 0$. This result is in agreement with the outcome of Figure 9.2. Moreover, the value of T_{cA} is practically unaffected by the presence of the B -block in any case, and it is very close to the corresponding T_c for an homopolymer composed of A -type monomers (see Figure 9.3). As a result, Whittington et al. expected a same value of ϕ for these chain structures, only AB -alternating chains were an exception. This result is also in agreement with our findings (Figure 9.6). Thus, our numerical results suggest that the findings of Whittington et al., derived for flexible chains, could be extended to stiff polymer chains, with a scaling exponent that depends on the interaction parameters, $\phi(\kappa, \epsilon)$, even in the case where $\epsilon_B \neq 0$.

In order to characterize the behavior of semiflexible polymer chains, another magnitude of interest is the radius of gyration. In Figure 9.7 we show the components of the radius of gyration parallel and perpendicular to the adsorbing surface for chains with different rigidities. The adsorbing energies have been selected to be $\epsilon_A = -1$ and $\epsilon_B = -0.5$. It is clear from the picture that increasing κ , the parallel component reaches to its maximum value and, accordingly, the perpendicular component drops to zero (the polymer is fully adsorbed), at earlier times, that is, at a higher temperature. The two different blocks also display a different behavior due to the different adsorbing energies. The higher $|\epsilon|$ the higher is the temperature at which the block adsorbs. In Figure 9.8 we show the effect of ϵ_B on the components of the radius of gyration associated to the A -block for a fixed chain stiffness. The less adsorbing B -block hampers the A -block to be completely adsorbed at its characteristic adsorbing temperature. A complete adsorption of the A -block only takes place when the whole chain is adsorbed.

The behavior of the radius of gyration with the chain stiffness can be easily explained. Assume that a semiflexible diblock chain has a persistence length given by:

$$l_p \sim \left(\frac{\kappa}{T}\right)^\alpha \quad (9.5)$$

where $\alpha \rightarrow 0.5$ in the limit $\kappa/T \rightarrow \infty$ [290]. Thus, we can model the chain as an ideal rod-like polymer of N/l_p units which radius of gyration is proportional to

$$R_g \sim l_p \left(\frac{N}{l_p}\right)^\nu \sim N^\nu \left(\frac{\kappa}{T}\right)^{\alpha(1-\nu)} \quad (9.6)$$

where $\nu = 3/(d+2)$ is the Flory exponent that depends on the space dimensionality d . In Figure 9.9 we analyze the scaling of $R_g N^{-\nu}$ vs κ/T . For semiflexible

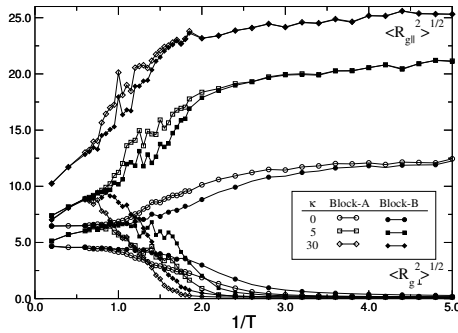


Figure 9.7. Parallel and perpendicular radius of gyration for the A -block (open symbols) and the B -block (filled symbols) of a diblock polymer chain for several degrees of stiffness κ . The chain length is set to $N = 100$, $\epsilon_A = -1$, $\epsilon_B = -0.5$.

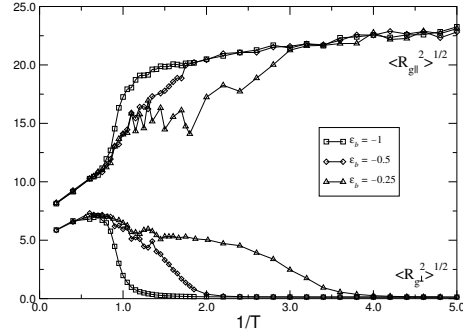


Figure 9.8. Comparison between the parallel and perpendicular radius of gyration for the A -block for different adsorption energies for the B -type monomers ϵ_B . Diblock chains have stiffness $\kappa = 10$, chain length $N = 100$, and $\epsilon_A = -1$.

diblock chains in the unadsorbed state, a slope of $\alpha(1 - \nu) = 0.2$ is expected; whereas in the adsorbed state (inset of Figure 9.9), the system becomes 2d, and $\alpha(1 - \nu) = 0.125$. Both regimes have been confirmed by our numerical data.

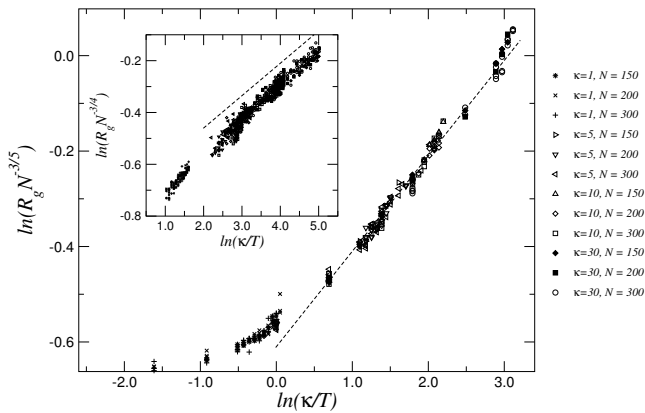


Figure 9.9. Scaling plot for semiflexible diblock chains in the unadsorbed state. $\kappa = 10$, $\epsilon_A = -1$ and $\epsilon_B = -0.5$. A dashed line of slope 0.2 is included to guide the eye. Inset: Same scaling plot in the adsorbed state (the system is now 2d). A dashed line of slope 0.125 is included to guide the eye.

9.3.2 Block copolymer chains

In this section we shall study the adsorption process of block copolymers formed by a repeated sequence of $N/(2\alpha)$ units $A_\alpha B_\alpha$. In Figure 9.10 we have plotted the averaged adsorbed energy per monomer for different stiff copolymer structures generated by changing the value of α . The rest of the parameters for this figure are fixed to $\kappa = 10$, $N = 200$, $\epsilon_A = -1$ and $\epsilon_B = -0.5$. In order to compare with previous results, the diblock structure and an homopolymer formed by A -

type monomers are also included. As in the diblock case, $|E|/N \rightarrow 1/2|\epsilon_A + \epsilon_B|$ in the limit $1/T \rightarrow \infty$, corresponding to a fully adsorbed chain. It is remarkable to note that the two-step adsorbing process observed in the diblock case, that determines the existence to two characteristic adsorbing temperatures T_{cA} and T_{cB} , vanishes for small values of α . As a result, a single peak in the specific heat data is expected.

The corresponding specific heat for the same polymer structures analyzed in Figure 9.10 is shown in Figure 9.11. For $A_{100}B_{100}$ (diblock) we can clearly observe two peaks which location identifies the characteristic adsorbing temperatures of blocks A and B . Particularly, $T_{cA} > T_{cB}$ since $|\epsilon_A| > |\epsilon_B|$. By reducing the value of α , T_{cA} becomes smaller and, at the same time, T_{cB} increases. For $\alpha = 20$ the peak associated to T_{cB} is residual, and for the A_5B_5 copolymer structure there is only a single peak which location is clearly dominated by the monomers with higher adsorption energy. The adsorption becomes then a single step process like the one observed in homopolymers. At this stage, the block structure is lost and the polymer chain could be replaced by a collection of blobs containing each 2α monomers with an adsorbing energy $\epsilon = (\epsilon_A + \epsilon_B)/2$.

The characteristic adsorption temperature for the A -block, T_{cA} , as a function of the block size α for different chain rigidities is plotted in the inset of Figure 9.11. As expected, T_{cA} increases with the chain stiffness κ and with α . The position of the arrows indicate the value of T_{cA} for an homopolymer of the same length, composed of A -type monomers with the same rigidity. For completeness, we have also included the results for random AB -copolymers (we have assigned to them, arbitrarily, $\alpha = -5$ in the inset of Figure 9.11). We can conclude that random AB -copolymers behave similarly as A_1B_1 copolymers.

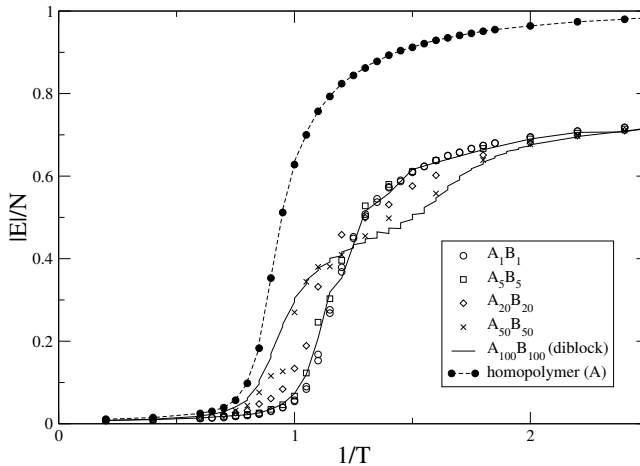


Figure 9.10. Averaged adsorption energy per monomer for several block copolymer structures vs. $1/T$. The rest of the parameters are set to $\kappa = 10$, $N = 200$, $\epsilon_A = -1$ and $\epsilon_B = -0.5$. For comparison an A -type homopolymer is also included.

Another magnitudes of interest in order to characterize the behavior of block-

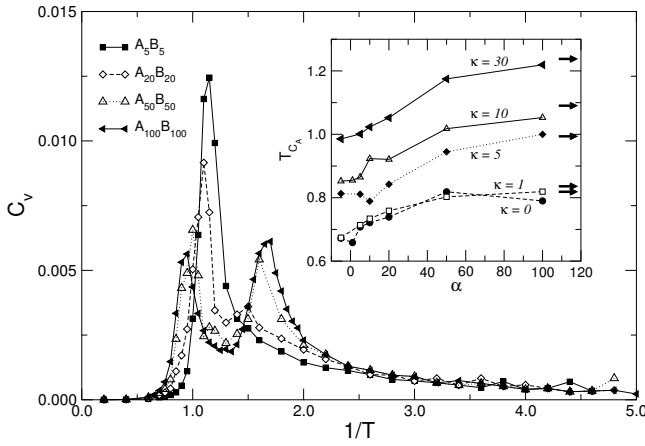


Figure 9.11. Specific heat vs $1/T$ for different copolymer structures with $\kappa = 10$, $N = 200$, $\epsilon_A = -1$, and $\epsilon_B = -0.5$. Inset: Characteristic adsorption temperatures for the A -block, T_{cA} , vs. the block size α for different chain rigidities κ . We have assigned, arbitrarily, $\alpha = -5$ to random AB -copolymers. Arrows indicate the value of T_{cA} for an A -type homopolymer of the same length and rigidity.

copolymers are the number and length of *chain trains* (see Section 2.7). The typical train length, L_t , is obtained as the averaged number of monomers within a train; and the number of trains, N_t , is the averaged number of trains within a chain. In Figure 9.12 we have plotted L_t vs. $1/T$ for different block-copolymer structures and rigidities. The rest of parameters have been fixed to $N = 200$, $\epsilon_A = -1$ and $\epsilon_B = -0.5$. As expected, a reduction in temperature increases the train length. In addition, as it was pointed out by Kramarenko [291] in his study on homopolymer chains, a stiffed chain has high disadvantage of bending, thus, the neighboring monomers of an adsorbed monomer increase their probability of being adsorbed. Therefore, we must expect that stiff chains will contain less number of trains but of major length (see Figure 9.12). At first sight, the change in L_t is apparently barely affected by the chain structure and it seems to be dominated only by the stiffness. However, if we look in detail into what happens within the desorbed-adsorbed transition region (see inset of Figure 9.12), we realize that the chain structure does matter. The fact is that by increasing the block size α , the length of the train, at a given temperature, is also increased.

Whereas, L_t is a monotonous increasing function of $1/T$, N_t must display a completely different behavior. At high temperatures ($1/T \rightarrow 0$) the chain is nearly desorbed and $N_t \rightarrow 0$. Below the characteristic adsorption temperature ($T \ll T_c$) the chain becomes almost fully adsorbed and $N_t \rightarrow 1$. Thus, N_t must have a maximum value. This maximum takes place at $T = T_c$ as it is shown in Figure 9.13. Thus, while cooling the system the number of adsorbed monomers increases generating new trains of small length. The number of trains becomes maximal at the characteristic adsorbing temperature and, a further reduction in temperature, promotes the new adsorbed monomers to link trains rather

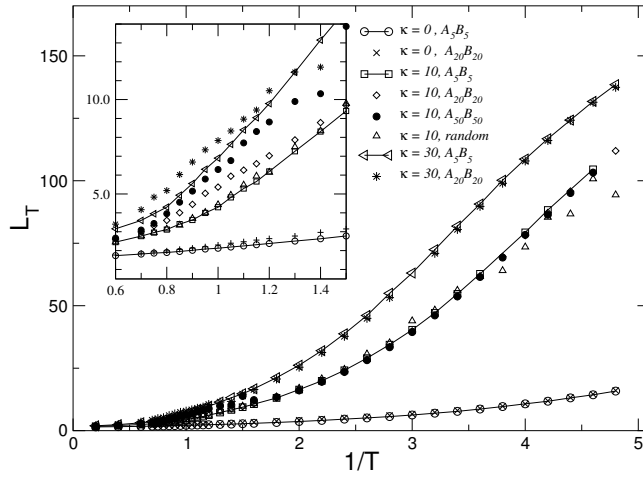


Figure 9.12. Train length L_t vs. $1/T$ for different copolymer structures and rigidities. The rest of parameters are set to: $N = 200$, $\epsilon_A = -1$ and $\epsilon_B = -0.5$. Inset plot: zoom of the deadsorbed-adsorbed transition region.

than generating new ones, thus reducing its number but increasing their length. Figure 9.13 also shows that the maximum number of trains at T_c increases for copolymers with smaller block size α . This result is expected to be even more pronounced as the difference in the adsorbing energies $|\epsilon_A - \epsilon_B|$ increases. In Figure 9.13 we can observe clearly two peaks in the curve corresponding to the copolymer $A_{50}B_{50}$ in agreement with the two maximums found in the specific heat data (Figure 9.11). This result is another indication that the adsorption process takes place in two steps. The inset plot of Figure 9.13 shows the behavior of N_t for a given structure (A_1B_1) but with two different rigidities. The maximum for the stiffer chain shifts to higher temperatures and smaller values in agreement with the previous results. This maximum in the number of trains has been also observed in the case of flexible homopolymers [284].

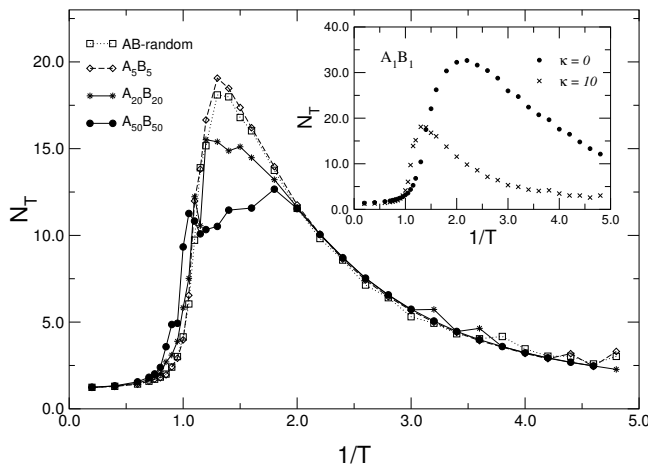


Figure 9.13. Averaged number of trains N_t vs. $1/T$ for different copolymer structures. The rest of the parameters are set to $\kappa = 10$, $N = 200$, $\epsilon_A = -1$ and $\epsilon_B = -0.5$. Inset: Dependence of N_t with the chain stiffness for the A_1B_1 structure.

If we set one of the adsorbing energies to be repulsive, for instance, $\epsilon_B \geq 0$, the polymer does not adsorb completely for a temperature small enough. In fact, B -type monomers are repelled from the surface and trains are composed basically by A -monomers. As a result, for copolymers with a small block size, N_t reaches a plateau value that depends on α and the chain stiffness κ . Results for $\epsilon_B = 0$, and copolymer structures A_1B_1 and A_5B_5 with different rigidities, are shown in Figure 9.14. This behavior is similar to one found by Zheligovskaya et al. [284] for flexible A_1B_1 copolymers.

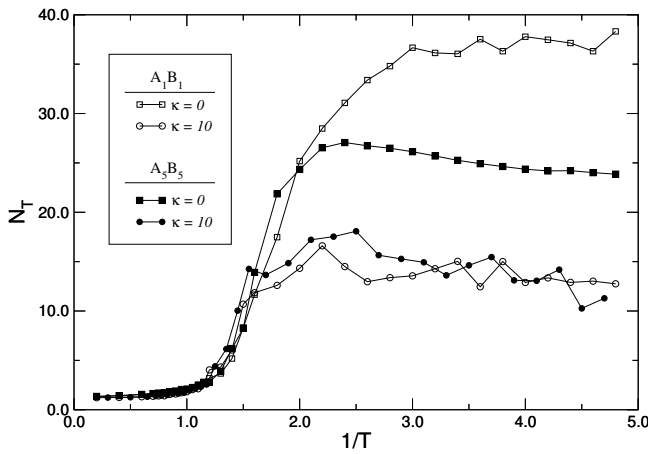


Figure 9.14. N_t vs. $1/T$ for block-copolymers of small block size with the B -type monomers having a neutral interaction with the surface, $\epsilon_B = 0$. The other parameters are $N = 200$ and $\epsilon_A = -1$.

9.4 Concluding remarks

In this chapter we have presented the results of extensive off-lattice Monte-Carlo simulations of the adsorption of semiflexible block copolymers onto flat homogeneous surfaces.

The adsorption process has been analyzed under different chain lengths (N), degrees of stiffness (κ), adsorption energies for the two types of monomers (ϵ_A, ϵ_B), and sizes of the block structure (α).

We have focused first in the adsorption of diblock structures. As expected, stiffer chains adsorb at a higher temperatures onto the surface, similarly to what is observed for semiflexible homopolymers [290]. However, long diblock chains are found to exhibit a well defined two-step adsorption transition, characterized by two typical adsorption temperatures that depend on the corresponding adsorption energies $T_c(\kappa, \epsilon)$. The critical adsorption properties have been analyzed assuming the scaling *ansatz* proposed by Kramarenko et al. [291], originally developed for flexible homopolymers. The scaling works nicely when applied to each block separately, but the critical exponent is no longer $\phi = 0.59$. This non-universal

behavior was already expected by Kuznetsov and Sung [275] and Gomper [301], suggesting $\phi = \phi(\kappa, \epsilon)$. The adsorption behavior of each block is barely disturbed by the presence of the other, independently of the adsorption energies. This result indicates the possibility to extend the analytical predictions of model of Whittington [281] to stiff diblock chains even in the case where none of the adsorbing energies is equal to zero. The radius of gyration has been computed in the adsorbed and non-adsorbed state and we have verified that it follows the expected scaling behavior (Eq. 9.6).

For stiff block-copolymer structures we have found that the separation between the two peaks in the specific heat data, identifying the characteristic adsorption temperatures, narrows for smaller values of the block size α . For α small enough we found a single peak and adsorption becomes a single step process like in homopolymers. We have measured the length and the number of chain trains during the adsorption transition. The train length is found to increase monotonically with the block size α and with $1/T$, whereas the number of trains has a maximum value (previously observed in the adsorption of flexible homopolymers [285]) located at $T = T_c$. We found the maximum number of trains to decrease with increasing α . The observed effects of the chain stiffness over the chain trains may be of interest for further studies related to pattern recognition.

Chapter 10

Stiff polymer adsorption onto striped surfaces

The study of polymer adsorption onto heterogeneous surfaces is at present a challenging issue which is directly related to the pattern recognition problem. As in the case of copolymers, beside the enormous complexity of the general problem, many coarse properties of these systems can be derived through the use of statistical methods. In this chapter we study the adsorption and the pattern recognition processes of semiflexible homopolymers onto striped surfaces. We will see that it exist an optimal stripe width that maximizes the chain stretching in the adsorbed state. Furthermore, adsorption and recognition processes are observed to occur at different temperatures generally.

10.1 Introduction

Polymers physically adsorbed onto solid surfaces has found a wide range of applications such as, protective coatings of electronic devices, lubricants, stabilization of colloidal suspensions, adhesion and, more recently, for biological and medical purposes. Particularly, the generation of surfaces that are able to withstand protein adsorption is a major challenge in the design of blood-contacting materials for medical implants and bio-affinity sensors. It is also of great interest the study of the polymer adsorption onto heterogeneous surfaces that are characterized by a fluctuating polymer-surface interaction [288]. Real biomolecules carry a pattern encoded in their sequence distribution, and a properly chosen functionalized surface may be able to recognize this information and adsorb it strongly [287]. In this sense, a major effort is concentrated in adsorption of flexible polyelectrolytes onto heterogeneously charged surfaces [302–304].

Random heteropolymers are known to be the simplest physical models for proteins or DNA and, like many biological macromolecules, are rigid to a certain extent due to electronic delocalization and steric effects. Since the free rotations about the chain backbone are restricted, the chain statistics cannot be described accurately by conventional models for flexible polymer chains, and only few recent developments have been done in the area of semiflexible polymers at surfaces [290, 291, 305].

The purpose of the present Chapter is to investigate the role of the polymer structure in the adsorption process onto a patterned surface consisting in stripes of variable width. Such structure has been found particularly relevant to the DNA adsorption on charged membranes [306].

By measuring the fraction of monomers adsorbed onto the surface, the degree of stretching and the non-sphericity, as a function of the system temperature, we have analyzed the adsorption characteristics in terms of the chain length and rigidity. We have found that a higher degree of stiffness and an increasing chain length enhances the surface pattern recognition. Our results also indicate that the adsorption transition foregoes the surface recognition and that chains, in the adsorbed state, find an optimal stripe width that maximizes their stretching.

10.2 Numerical Model

We have simulated the adsorption of a semiflexible polymer chain made of N beads onto a planar surface using off-lattice Monte-Carlo methods. The chain model is identical to the one used in the previous chapter (see Sections 3.1 and 9.2). In this case, the surface is composed of heterogeneities in the form of stripes oriented along the y -axis with a characteristic width ω . The polymer has an attractive interaction with alternate stripes and a neutral one with the others. A schematic view of the system is presented in Figure 10.1. We must note that for $\omega \ll 1.1\sigma$ the polymer will not feel the heterogeneities of the surface and will not be relevant for pattern recognition. All the monomer units have an attractive interaction with the stripes on the surface with adsorption energy $\epsilon < 0$. We again define one Monte Carlo Step (MCS) as N trials to move the chain. The system has been in this case equilibrated for 10^6 MCS. Subsequently, measurements are taken every 10 MCS. The results have been finally averaged over 10^5 measures.

10.3 Results and Discussions

We have studied the adsorption process of a stiff homopolymer chain onto an attractive striped surface. We have investigated the behavior for different chain

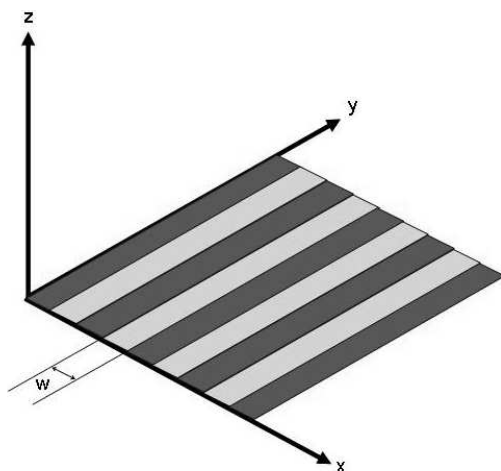


Figure 10.1. Schematic representation of a striped surface. Dark stripes have an attractive interaction with the polymer chain whereas clear ones are neutral.

lengths $N \in [25, 250]$ and chain rigidities $\kappa \in [0, 30]$ for several values of the stripe width ω . The flexible chain limit corresponds to $\kappa = 0$.

In previous studies it has been clearly established that a polymer chain adsorbs strongly onto a planar homogeneous surface at a characteristic temperature that increases with the chain length and stiffness [290]. Thus, we are interested to see how the adsorption process is influenced by structure of an heterogeneous attractive surface that, in our case, is controlled by the stripe width. In Figure 10.2 we have plotted the fraction of monomers adsorbed onto the surface $\chi \equiv n_c/N$ vs the inverse of the temperature $1/T$ for $N = 250$ and $\kappa = 30$. The results for different widths are compared with those corresponding to an homogeneous attractive surface. We can observe that the transition towards a complete adsorbed state takes place at higher temperatures with increasing the stripe width ω , and that the highest characteristic adsorbing temperature is found for an homogeneous surface. This result can be easily understood since for an homogeneous surface the polymer chain does not need to accommodate to a particular surface pattern once it has been adsorbed.

The transition temperatures to the adsorbed state, $T_c(N, \kappa, \omega)$, are determined from the temperature corresponding to the maximum of the specific heat data, that is directly derived from the measure of the fluctuations of the internal energy. The characteristic temperatures T_c as a function of the stripe width ω , for $\kappa = 30$ and for different chain lengths N , are represented in the inset plot of Figure 10.2. We can observe that for a given chain length T_c increases with increasing ω , and that at a particular stripe width T_c also increases with N , as expected. Data represented at $\omega = 0$ corresponds to an homogeneous attractive surface from which the highest values of T_c are obtained. This characteristic temperature provides a

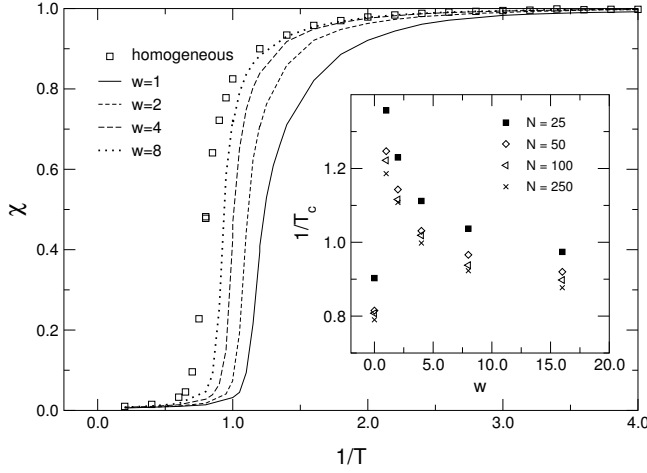


Figure 10.2. Fraction of monomers adsorbed onto the surface χ vs $1/T$ for different values of the stripe width ω . The chain length is set to $N = 250$ and its bending parameter $\kappa = 30$. Inset: Characteristic adsorbing temperatures as a function of ω for different chain lengths ($\kappa = 30$).

valuable information in order to identify the transition point towards the adsorbed state, however, does not account for pattern recognition yet. One expects that, once the chain is adsorbed onto the surface, then it has to accommodate to the specific pattern, and this process may take place at a lower temperature than T_c .

10.3.1 Degree of stretching

Since our pattern is composed of stripes oriented along the y -axis we introduce a parameter that will measure the degree of stretching of the polymer chain, in its adsorbed state, along the y -axis.

A fully stretched chain of length $L = N\sigma$ has a radius of gyration respect to its center of mass equal to $R_g = L/\sqrt{12}$, thus, we define the degree of stretching of a polymer chain Q , as the ratio between the y -component of its radius of gyration (computed as referred in Eq. 2.6) and the radius of gyration of a fully stretched chain:

$$Q = \frac{\sqrt{12}}{N\sigma} \langle R_{gy}^2 \rangle^{1/2} \quad (10.1)$$

The degree of stretching Q as a function of the stripe width ω for different chain lengths is plotted in Figure 10.3. The chain rigidity is set to $\kappa = 30$ and measures are taken at a temperature of $1/T = 4$ where the chain is almost completely adsorbed. For the sake of comparison, the results corresponding to an homogeneous attractive surface are included in the $\omega = 0$ data. Remarkably, we can observe that, independently of the chain length, there is an optimal value for the stripe width ($\omega = 2$) that maximizes the stretching Q . The introduction of an attractive striped pattern onto the surface increases notably the degree of stretching, and this stretching is enhanced by the introduction of even small quantities of chain stiff-

ness. The existence of an optimal stripe width is due to a competition between the entropy, that tends to spread the chain over the surface almost isotropically, and the internal energy that accounts for the bending energy and the interaction of the polymer with the surface, that tends to concentrate all the monomers along the major axis of a single stripe.

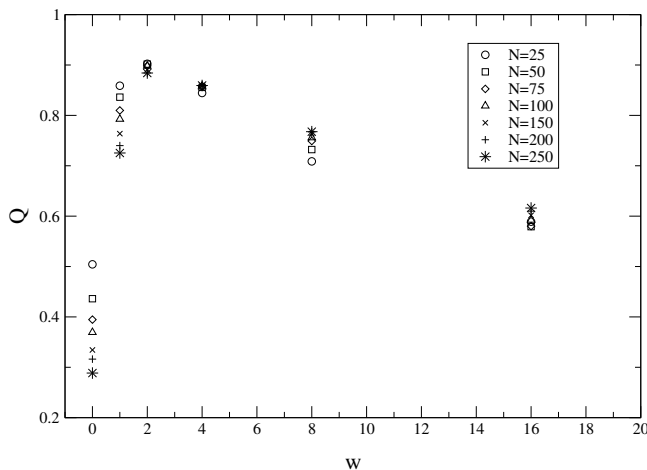


Figure 10.3. Measure of the degree of stretching Q vs. the stripe width ω for different chain lengths. The stiffness of the chain is set to $\kappa = 30$. Q has been evaluated for a completely adsorbed chain $1/T = 4$.

The polymer chain avoids costly jumps between neighboring stripes by passing over non-adsorbing zones that will rise the internal energy of the system. However, if the stripe width is small enough, the chain can spread over many different stripes without exposing too many monomers to the non-adsorbing regions. A clear snap-shot of this situation is shown in Figure 10.4. We have plotted a typical conformation of a flexible polymer chain ($\kappa = 0$) of length $N = 200$ at $1/T = 4$ adsorbed onto a striped surface of width $\omega = 1$ (left picture) and $\omega = 2$ (center picture). However, by increasing the stiffness of the chain it will align along the y -axis as it is shown in the right picture of Figure 10.4, where a typical conformation of a rigid chain at its optimal stripe width is plotted.

From Figure 10.3 we can also observe that for narrow stripes ($\omega \leq 2$) the higher degree of stretching is obtained for short chains, whereas, for increasing ω long chains are the ones that provide the best Q values. This behavior can be easily explained since short chains, even for small values of the bending parameter κ , tend to behave rod-like and can easily adjust to thin stripes, furthermore, jumps among neighboring attractive stripes will expose a large percentage of monomers to non-adsorbing zones. On the other hand, as ω increases, short chains find more lateral space to try to accommodate more isotropically and thus, reducing the value of Q .

In Figure 10.5 we have plotted the behavior of the degree of stretching as a function of the chain stiffness κ for different values of the stripe width. The chain

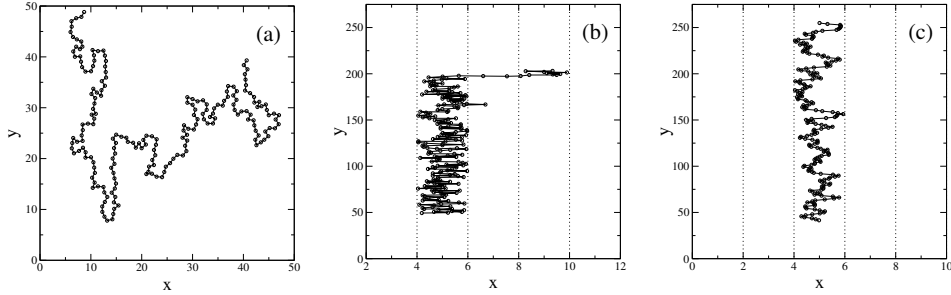


Figure 10.4. (a) Snap shot of a typical configuration of a flexible polymer chain adsorbed onto a striped surface with a stripe width $\omega = 1$. The chain length is set to $N = 200$. (b) same as before for a stripe width $\omega = 2$. (c) Same as (b) for a stiff chain with $\kappa = 30$.

length is selected to be $N = 150$ and the measures are done at $1/T = 4$. We can observe that increasing the chain rigidity the degree of stretching increases and, at the same time, the optimal stripe width switches to smaller values. Under these circumstances, the bending energy dominates the entropic contribution.

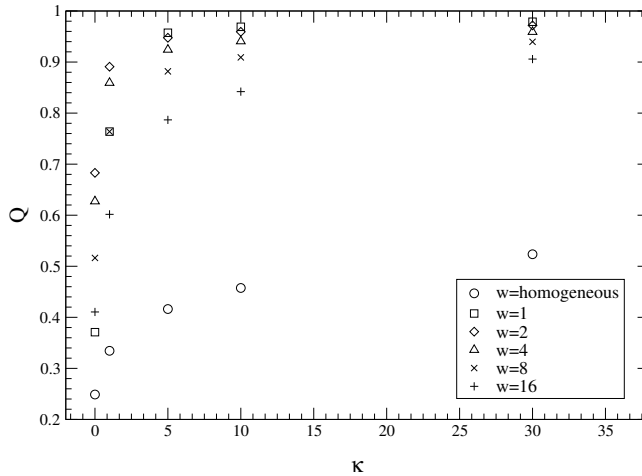


Figure 10.5. Degree of stretching Q vs. the chain stiffness κ for different values of the stripe width at $1/T = 4$ and $N = 150$. For the sake of comparison we include the results corresponding to an attractive homogeneous surface (\circ).

The behavior of the y -component of the radius of gyration of the polymer chain $\langle R_{gy}^2 \rangle^{1/2}$ with the temperature for different stripe widths is shown in Figure 10.6. The chain length is chosen to be $N = 100$ and the bending parameter $\kappa = 1$. The initial values of $\langle R_{gy}^2 \rangle^{1/2}$ (at high temperatures) correspond to a free non-adsorbed polymer chain. By reducing the temperature, the polymer adsorbs onto the surface and $\langle R_{gy}^2 \rangle^{1/2}$ grows until it reaches a plateau value that depends on ω . For homogeneous surfaces or wide attractive stripes this plateau is reached earlier (meaning at higher temperatures) but has a smaller value. The maximum value for an almost completely adsorbed chain ($1/T \rightarrow 4$) is obtained at the optimal stripe

width. While reducing the temperature the maximum degree of stretching shifts from wider to narrower stripe widths as an indication that the polymer needs a further reduction of the entropic contribution in order to adjust to thinner attractive stripes. By increasing the chain stiffness the transition towards the plateau value becomes sharper suggesting the existence of a characteristic temperature T_r at which the surface pattern is recognized by the polymer chain. T_r is expected to be lower than the characteristic adsorbing temperature, T_c , since the polymer chain first adsorbs onto the surface rather isotropically, and a further reduction in the temperature will reduce the number of jumps between neighboring stripes until the chain aligns along the major axis of a single stripe.

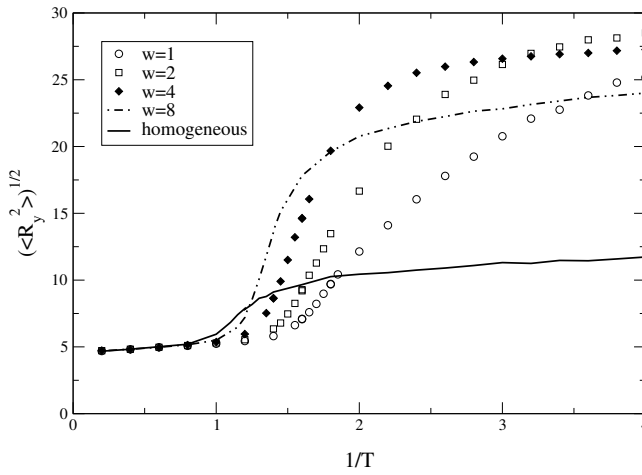


Figure 10.6. Variation of the y -component of the radius of gyration $\langle R_{gy}^2 \rangle^{1/2}$ vs. $1/T$ for several stripe widths. $N = 100$ and $\kappa = 1$.

10.3.2 Non-sphericity

In order to identify the characteristic temperature at which the recognition takes place T_r we measure the non-sphericity of the polymer chain (see Section 2.3.3). Since the polymer adsorbs onto the surface before it adjusts to the specific pattern we assume $\langle R_{gz}^2 \rangle = 0$. We define the characteristic recognition temperature, T_r , as the temperature at which the chain adjusts to an specific pattern. Thus, if the stripe width is ω , the polymer chain must adjust to the stripe width and then align along the major axis of the stripe.

Given a chain of length N with a bending parameter κ , it is easy to estimate the expected non-sphericity value A_{th} of chain adsorbed onto a single stripe. The polymer will form blobs of diameter ω , containing each N_b monomers. The radius of gyration of a blob with radius $r = \omega/2$ is $R_{gb} = r/\sqrt{2}$ that, for an excluded-volume chain, is related to N_b through the Flory expression [93]:

$$R_{gb} = l_p(\kappa)^{1/4} N_b^{3/4}$$

where $l_p(\kappa)$ is the persistence length of a stiff polymer chain. It has been found that $l_p = \gamma\kappa^{1/2}$ [290]. Our best fit to the data gives $\gamma = 0.55 \pm 0.01$. Now, it is possible to know the number of monomers containing each blob:

$$N_b(\omega, \kappa) = \left[\frac{\omega}{2\sqrt{2}} \left(\frac{1}{\gamma\kappa^{1/2}} \right)^{1/4} \right]^{4/3}$$

The total number of blobs is nothing but N/N_b , and the polymer will cover an extension along the major axis of the stripe of $L_y = \omega N/N_b$. Then, the radius of gyration along the y -axis follows: $\langle R_{gy}^2 \rangle = L_y^2/12$, and in its perpendicular direction: $\langle R_{gx}^2 \rangle = \omega^2/12$.

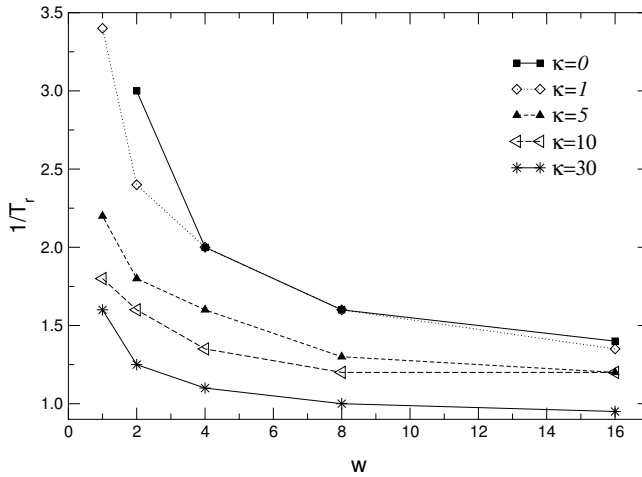


Figure 10.7. Characteristic pattern-recognition temperatures T_r vs. the stripe width ω for different values of the chain rigidity. $N = 250$.

We have evaluated the non-sphericity of the polymer chain $A(T)$, and its value has been compared to the expected $A_{th}(N, \kappa, \omega)$. We have defined the temperature at which the pattern recognition takes place when the following criteria is satisfied:

$$T = T_r(N, \kappa, \omega) \quad / \quad \frac{A(T)}{A_{th}} \geq 0.99$$

In Figure 10.7 we have plotted $1/T_r$ as a function of the stripe width ω for different chain rigidities. The chain length is selected to be $N = 250$. Observe how wider stripes are recognized earlier (at higher temperatures) than narrower ones, and that by increasing the stiffness parameter κ , T_r is also raised. The dependence of T_r on the chain length N is shown in Figure 10.8. In this case we have selected $\kappa = 30$. Observe how T_r increases with increasing the chain length. For the sake of comparison, we have over plotted the corresponding characteristic adsorbing temperatures T_c for $N = 25$ and $N = 250$. Note that $T_c > T_r$ in all the cases

studied supporting the assumption that the polymer first adsorbs onto the surface and then the chain adjusts to the specific pattern.

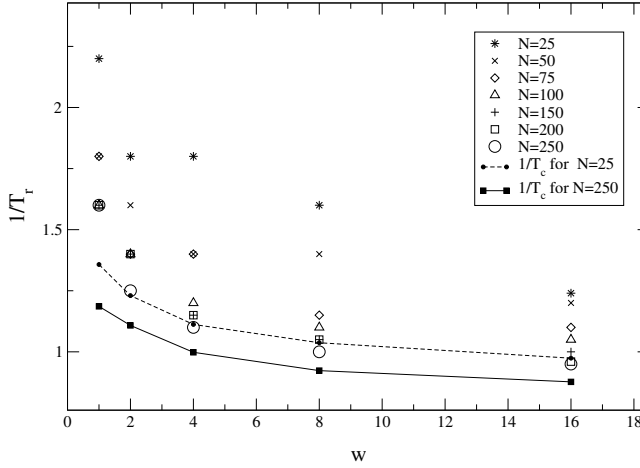


Figure 10.8. Characteristic pattern-recognition temperatures T_r vs. the stripe width ω for different chain lengths. The stiffness is set to $\kappa = 30$. For the sake of comparison we include the characteristic adsorbing temperatures T_c for $N = 25$ and $N = 250$.

10.4 Summary and Conclusions

In this Chapter we have presented extensive numerical off-lattice Monte-Carlo simulations of a stiff polymer chain adsorbing onto a structured surface consisting in alternated attractive and neutral stripes. We have analyzed, in terms of the chain length and rigidity, the adsorption and the pattern recognition process as a function of the stripe width. We have seen that this process is twofold. During the cooling sequence, the polymer chain first adsorbs onto the surface at a characteristic temperature T_c , and then, a further reduction in the temperature is needed for the chain to reorganize and adjust to the specific pattern. The characteristic adsorbing temperature T_c is found to increase with the stripe width ω .

In order to study the pattern recognition process we have evaluated the *degree of stretching* Q and the *non-sphericity* A of the polymer chain. We have found an optimal value of the stripe width that maximizes Q . This optimal width reduces with increasing the chain stiffness. The measure of Q also indicates that short chains accommodate better to narrow stripes at low and moderate chain rigidities, however this fact does not necessarily implies recognition. We have defined a criteria to estimate the characteristic temperature at which the chain recognizes the pattern T_r . We have verified $T_c > T_r$ in all the cases studied and that T_r increases with the stripe width and the chain length and rigidity.

Despite the simplicity of this model, it might serve to extract useful information on the most relevant chain and surface parameters that are able to enhance the

polymer adsorption onto specific patterns. Furthermore, lateral heterogeneities might require the proper selection of lengths scales, including the chain length N and its persistence length l_p , that must be commensurate quantities with the domain size of the pattern. At the same time, heterogeneous surfaces represent a unique means of manipulating the size and the orientation of polymer morphologies over a large range of length scales that are of great interest in bio and nanotechnologies.

Chapter 11

General conclusions

This thesis has focused on the study of particularly interesting aspects concerning the kinetics and phase transformation of depletion driven colloids and the polymer-surface interaction under complex structures, from the interaction of spherical micelles or colloids with grafted polymer chains, to the polymer adsorption on patterned surfaces and polymer packaging in capsids. Numerical simulations based on Brownian Dynamics and off-lattice Monte-Carlo techniques are compared to mean field and self-consistent field theoretical approaches, as well as scaling analysis. The main results we have obtained are summarized in the following lines.

Depletion driven colloids

The study of 2d-depletion-driven colloidal systems presented in Chapters 4 and 5 shows a transition from a single dispersed phase to a two-phase coexistence of monomers and clusters as the depth of the interaction potential among the colloidal particles is changed. Increasing the well depth further, fractal clusters are observed in the simulation. These fractal clusters have a hybrid structure in the sense that they show hexagonal closed-packed crystalline ordering at short length scales, and a ramified fractal nature at larger length scales. For sufficiently deep potential wells, the diffusion-limited cluster-cluster aggregation (DLCA) model is recovered in terms of the large-scale fractal dimension D_f of the clusters, the kinetic exponent z , and the scaling form of the cluster size distribution. For shallower well depths inside the two-phase coexistence region, a comparison of the kinetics of cluster growth with intermediate-stage phase separation in binary mixtures shows close similitude between both phenomena. In the single phase region, growth kinetics agrees well with a mean-field aggregation-fragmentation model

of Sorensen, Zhang, and Taylor (SZT) [71].

The study of the dynamical scaling hypothesis for the structure factor, $S(q)$, in depletion-driven colloidal phase separation presented in Chapter 5 shows that a true dynamical scaling is observed for shallow quenches into the two-phase gas-solid coexistence region. Our results show that for shallow quenches, after an initial transient period, there is only one characteristic length scale in the system and, therefore, conditions required for dynamic scaling to hold are satisfied. The initial transient period covers nucleation of clusters and growth mainly by incorporating monomers and small clusters in the growing nuclei. In this regime, the cluster-cluster nearest-neighbor distance, R_{nn} , and the average cluster radius of gyration, R_g , grow differently with time and the scaling does not work. After the transient period, the predominant mechanism of cluster growth is the collision among large clusters and the subsequent surface reorganization in order to reduce the interfacial tension. The processes that remain after the transient period leads to a similar temporal evolution of R_{nn} and R_g , and therefore a single length scale can be observed in the system.

In deep quenches the growth process leads to fractal clusters and the system is controlled by two characteristic lengths that evolve differently in time. True dynamical scaling thus cannot be expected to hold. However, an apparent scaling for the structure factor is observed over some period of time when these two characteristic length scales become comparable to each other. A partial agreement is observed when results are compared with the theoretical predictions by HOS [166]. HOS assume that in monodisperse systems the structure factor can be write as a product of cluster-cluster and the averaged single-cluster structure factors, each with its own characteristic length. Simulations point out that HOS can account for the origin of the peak for shallow quenches in the two-phase region. In contrast, HOS fails to explain the origin of the peak for deep quenches in the two-phase region. A plausible explanation for the breakup of HOS theory is the fact that large clusters are observed to be more polydisperse in deep quenches than in shallow quenches.

The studies done along Chapters 4 and 5 for depletion-driven colloids clearly demonstrate the importance of Brownian dynamics in the study of colloidal aggregation, and more generally, for studying the transition from a dispersed to a solid phase. Aggregates that cross over from fractal to compact crystalline morphology can be easily studied in Brownian Dynamics simulations by just changing a parameter.

Polymer-surface interactions

Spherical polymer brushes

In Chapters 6 and 7 we have focused on the study of a particular kind of colloidal particles known as spherical polymer brushes. Simulations have focused on systems in which curvature effects are important. In Chapter 6 we have measured the interacting force between two spherical brushes. Our results support a description of the force profile divided into two regimes. At short separating distances between the brushes the force is well described by the theory of Witten and Pincus [169], whereas at larger distances the interaction is reproduced by extending the theory of Flory for dilute polymer solutions. The overall behavior is qualitatively well adjusted, except at short distances, with the phenomenological theory of Doroszkowski and Lambourne [170] for a high density of grafted chains. The characteristic radial size of an unperturbed brush is found to follow the same scaling relationship with the chain length N and number of grafted chains f as in the star-polymer systems $R_0 \sim N^{3/5} f^{1/5}$. Results have been also compared with SCF formalisms of Lin-Gast [210] and Wijmans-Leermakers-Fleer [202]. Strong discrepancies are found between SCF and MC formalisms for systems with large curvature. SCF methods are observed to overestimate the interactions at short distances between spherical brushes because they cannot account adequately for monomer correlations.

In Chapter 7 we have studied the behavior of a spherical brush confined onto a spherical cavity. The monomer density profile and the cavity pressure have been measured. In addition to MC technique we have used a Self-Consistent Field formalism in which we have used directly the probability density function recurrence law for the propagator $G_N(r, r')$, avoiding the length scale approximation involved in self-consistent field methods that uses Schrödinger-like equations. A direct comparison between the SCF and MC methods reveals the SCF calculation to be a valuable alternative to MC simulations in the case of free and softly compressed brushes. In the case of strongly compressed systems we have proposed an extension of the Flory theory for polymer solutions, whose predictions are found to be in good agreement with the MC simulations and has the advantage of being computationally inexpensive. In the range of high compressions, we have found the monomer volume fraction v to follow a scale relationship with the cavity pressure P , $P \sim v^\alpha$. SCF calculations give $\alpha = 2.15 \pm 0.05$, close to *des Cloiseaux law* ($\alpha = 9/4$), whereas MC simulations lead to $\alpha = 2.73 \pm 0.04$. We conclude that the higher value of α obtained with MC comes from the monomer density correlations not included in the SCF formalism.

Polymers confined onto spherical surfaces

Results for flexible and semiflexible excluded-volume polymer chains confined to impenetrable spherical surfaces have been presented in Chapter 8. Results are compared with the theoretical predictions for ideal chains by Mondescu and Muthukumar (MM) [267], and Spakowitz and Wang (SW) [268], respectively. The SW prediction is found to be in better agreement with our simulation results than the MM prediction in all the cases studied. Conformation of chains of length L , and persistence length l_p restricted to move on a sphere of radius R , can be reasonably described by the SW formalism in the regime $L/(2\pi) < R < 2l_p$. For $R/l_p > 2$, the mean square end-to-end distance, as a function of the chain length, evolves from a two-dimensional (2d) self-avoiding random walk behavior to a saturation value. A rigid rod behavior is recovered in the limit of short and stiff chains. Unlike ideal chains, excluded volume chains confined to a spherical surface of large enough radius display a transition from a disordered to an helicoidal state as chain stiffness is increased. We have characterized this transition through the bond orientational correlation function and the Monte Carlo results reflect a balance between the bending energy and the excluded volume interactions.

Polymer adsorption

The adsorption processes of semiflexible polymers onto flat surfaces have been studied in Chapters 9 and 10. Chapter 9 presents the results for the adsorption of block-copolymers onto homogeneous surfaces. The behavior of several copolymer chain structures, such as homopolymers, diblocks, $(A_\alpha B_\alpha)$ block copolymers, and random heteropolymers have been compared. In all the cases studied, we have found the adsorption process to be favored with an increase of the chain rigidity. Particularly, the adsorption of diblock structures becomes a two-step process characterized by two different adsorbing temperatures that depend on the chain stiffness, the chain length and the adsorbing energies ϵ_A and ϵ_B . This twofold adsorbing process changes to a single one for copolymers of reduced block size α . Each block of the stiff copolymer chain is found to satisfy, independently, the classical scaling laws for flexible chains, however, we found the scaling exponent ϕ to depend on the chain stiffness and the adsorbing energies. The measurement of the radius of gyration exhibits a typical behavior of a polymer chain composed of N/l_p blobs which persistence length follows $l_p \sim (\kappa/k_B T)^{0.5}$ for large stiff chains.

Chapter 10 presents the results for the adsorption process of homopolymer chains onto a sticky periodic stripe like pattern of variable width. We have analyzed, in terms of the chain length and rigidity, the adsorption and the pattern

recognition process as a function of the stripe width. We have seen that this process is twofold: *i*) the chain adsorbs rather isotropically onto the surface at a characteristic temperature T_c and, *ii*) a further reduction in the temperature is needed for the chain to reorganize and adjust to the specific pattern. Such polymer reorganization has been studied through the evaluation of the chain *degree of stretching* Q and the *non-sphericity* A . We have found an optimal stripe width that maximizes the stretching. We have introduced a criteria to estimate the characteristic temperature at which the pattern recognition takes place $T_r < T_c$ and we have studied its dependence with the chain and surface relevant parameters.

Bibliography

- [1] Einstein, A., *Investigations on the theory of the Brownian Movement*, Methuen, 1926. ; Einstein, A., *Investigations on the theory of the Brownian movement*, Dover Publications: New York, 1956.
- [2] Doi, M. ; and Edwards, F. S., *The theory of Polymer Dynamics*. Oxford Science, 1986.
- [3] Cukier, R. I; and Deutch, J. M., *Phy. Rev.* **177**, 240, (1969).
- [4] Bocquet, L.; and Hansen, J. P. J., *Stat. Phys.* **76**, 505 and 527, (1994).
- [5] Wilemski, G., *J. Stat. Phys.* **14**, 153-169, (1976).
- [6] Evans, D. F.; and Wennerstroöm, H., *The colloidal domain: where physics, chemistry and biology meet*, second edition; Wiley-VCH: New York, 1999.
- [7] Israelachvili, J., *Intermolecular and Surface Forces*; Academic Press, SanDiego, 1994.
- [8] Hamaker, H. C., *Physica (Utrecht)*,**4**, 1058, (1937).
- [9] Lifshitz, E. M., *Soviet Physics JETP (Engl. Transl)*, **2**, 73, (1956).
- [10] Dzyaloshinskii, I. E.; Lifshitz, E. M.; and Pitaevskii, L. P., *Adv. Phys.*, **10**, 165, (1961).
- [11] Everaers, R., and Ejtehadi, M. R., *Phys. Rev. E*, **67**(4), 041710, (2003).
- [12] Derjaguin, V. B., *Kolloid-Zeitschrift*, **69**, 155-164, (1934).
- [13] Verwey, E. J. W.; Overbeek, J. Th. G.; van Nes, K. *Theory and Stability of Lyophobic Colloids: the interaction of Sol particles having an electric double layer*. New York, 1948.
- [14] van Roij, R., *J. Phys.: Condens. Matter*, **12**, A263, (2000).
- [15] Boström, M.; Williams, D.R.W.; and Ninham, B. W., *Phy. Rev. Lett.*, **86** (16), 168103, (2001).
- [16] Grasso, D.; Subramaniam, K.; Butkus, M.; Strevett, K.; and Bergendahl, J., *Reviews in Environmental Science and Bio/Technology*, **1**, 17, 2002.
- [17] Asakura, S., and Oosawa, F. *J. Chem. Phys*, **22**, 1255, (1954).

- [18] Asakura, S., and Oosawa, F, J. Polym. Sci., **33**, 183, (1958).
- [19] Vrij, A., Pure appl. Chem., **48**, 471, (1976).
- [20] Meijer, E. J.; and Frenkel, D. J., Chem Phys., **100**, 6873, (1994).
- [21] Bolhuis, P. G.; Louis, A. A.; and Hansen, J. P., Phys. Rev. Lett, **89**, 128302, (2002).
- [22] Dijkstra, M.; and van Roig, R., Phys. Rev. Lett., **89**, 208303, (2002).
- [23] Gast, A. P.; Hall C. K.; and Russell, W. B., J. Coll. Int. Sci., **96**, 251, (1983).
- [24] Lekkerkerker, H. N. W.; Poon, W. C. K.; Pusey, P. N.; Stroobants, A.; and Warren, P. B., Europhys. Lett., 559, **20**, (1992).
- [25] Brader, J. M.; Evans, R.; and Schmidt, M., Molec. Phys., **101**, 3349, (2003).
- [26] Vliegthart, G. A.; and van der Schoot, P., Europhys. Lett., **62**, (4), 600, (2003).
- [27] Fuchs, M.; and Schweizer, K. S., J. Phys. Condens. Matter, **14**, R239, 2002.
- [28] Poon, W. C. K., J. Phys.:Condens. Matter., **14**, R859, (2002).
- [29] Jullien, R; and Botet, R., *Aggregation and fractal aggregates*. World Scientific: Singapore, 1987.
- [30] Mandelbrot, B., *Les objects fractals, forme, hasard et dimension*. Flammarion, France, 1975. Mandelbrot, M., *The fractal geometry of nature*, Freeman, 1982.
- [31] Vicsek, T., *Fractal Growth Phenomena* (second edition). World Scientific, Singapore 1992.
- [32] Meakin, P., *Fractals, scaling and growth far from equilibrium*. Cambridge University Press, Cambridge, 1998.
- [33] Rogers, C. A., *Hausdorff Measures* 2nd Ed. Cambridge, England: Cambridge University press, 1999.
- [34] West, B. J., *Fractal Physiology and Chaos in Medicine*. World Scientific, Singapore, 1990.
- [35] Bunde, A.; and Havlin, S., *Fractal in Science*. Springer, Heidelberg, 1994.
- [36] van Dongen, P.G.J.; and Ernst, M.H., Phys. Rev. Lett., **54**, 1396, (1985).
- [37] Ball, R. C.; Weitz, D. A.; Witten, T. A.; and Leyvraz, F., Phys. Rev. Lett, **58**, 274, (1987).
- [38] Friedlander, S. K.; and Wang, C. S., J. Colloid Interface Sci., **22**, 126, (1966).
- [39] Lai, F. S.; Friedlander, S. K.; Pich, J.; and Hidy, G. M., J. Colloid Interface Sci., **39**, 395, (1972).
- [40] Leyvraz, F., Physics Reports, **383**, 95-212, (2003).
- [41] T. Vicsek, and F. Family, Phys. Rev. Lett, **52**, 1669, (1984).
- [42] Meakin, P; Vicseck, T.; and Family, F., Phys. Rev. B, **31**, 564, (1985).

-
- [43] Family, F.; Meakin, P.; and Vicsek, T., J. Chem. Phys., **83**, 4144, (1985).
- [44] Meakin, P.; and Ernst, M. H., Phys. Rev. Lett., **60**, 2503, (1988).
- [45] Meakin, P.; and Family, F., Phys. Rev. A, **38**, 2110, (1988).
- [46] Ziff, R. M.; McGrady, E. D., J. Chem. Phys., **82** (11), 5269, (1985).
- [47] Botet, R.; and Jullien, R., J. Phys. A, **17**, 2517, (1984).
- [48] Leod, J. Mc., Quart. J. Math. Oxford Ser. (2), **13**, 119, (1962).
- [49] Leyvraz, F.; and Tschudi, H., J. Phys. A, **14**, 3389, (1981).
- [50] Lushnikov, A., Izv. Akad. Nauk SSSR, Ser. Fiz. Atmosfer. i Okeana, **14**, 738, (1978).
- [51] Ziff, R., J. Stat. Phys., **23**, 241, (1980).
- [52] Kang, K.; and Redner, S., Phys. Rev. A, **30**, 2899, (1984).
- [53] Vicsek, T.; Meakin, P.; and Family F. Phys. Rev A, **32**, 1122, (1985).
- [54] Gillespie, D. T, J. Comp. Phys., **22**, 403, (1976).
- [55] Gillespie, D. T. *Exact Stochastic simulation of coupled chemical reactions*, J. Phys. Chem., **81**, 2340, (1977).
- [56] Thorn, M.; and Seebelberg, M., Phys. Rev. Lett., **72**, 3622, (1994).
- [57] Odriozola, G.; Jordá, A. M.; Schmitt, A.; Callejas Fernández, J.; Martínez García, R.; and Hidalgo Álvarez, R., Europhys. Lett., **53**, 797, (2001).
- [58] Witten, T. A.; and Sander, L. M., Phys. Rev. Lett., **47**, 1400, (1981).
- [59] Eden, M. in Proc. 4-th Berkeley Symp. on Math. Statistics and Probability, vol. 4, Ed. F. Neyman (Berkeley, University of California Press), (1961).
- [60] Meakin, P., Phys. Rev. Lett., **51**, 1119, (1983).
- [61] Kolb, M.; Botet, R.; and Jullien, R., Phys. Rev. Lett., **51**, 1123, (1983).
- [62] Several reaction-limited models were designed without a defined time scale and therefore do not allow the study of the dynamical properties: Jullien, R.; and Kolb, M., J. Phys., **17**, L639, (1984). Brown, W. D.; and Ball, R. C., J. Phys., **A18**, L517, (1985).
- [63] Lamb, W., Math. Meth. Appl. Sci., **27**, 703, (2004).
- [64] Family, F.; Meakin, P.; Deutch, J. M, Phys. Rev. Lett., **57**, 727, (1986).
- [65] Blatz, P. J.; and Tobolsky, A. V., J. Phys. Chem, **49**, 77, (1945).
- [66] Ziff, R. M.; J. Stat. Phys., **23**, 241, (1980).
- [67] Barrow, J. D.; J. Phys A, **14**, 729, (1981).
- [68] Ball, J. M.; and Carr, J., J. Stat. Phys., **61**, 203, (1989).
- [69] Costas, M. E.; Moreau, M.; and Vicente, L., J. Phys. A:Math. Gen., **28**, 2981,

- (1995).
- [70] Ernst, M. H.; and van Dongen, P. G. J., *Phys. Rev. A*, **36**, 435, (1987).
- [71] Sorensen, C. M.; Zhang, X. H.; and Taylor, T. W., *Phys. Rev. Lett.*, **59**, 363, (1987).
- [72] Vigil, R. D. ; and Ziff, R. M., *Phys. Rev. Lett.*, **61** (12), 1431, (1988).
- [73] Elminyawi, I. M.; Gangopadhyay, S.; and Sorensen, C. M., *J. Colloid Interface Sci.*, **144**, 315-323, (1991).
- [74] Odriozola, G.; Leone, R.; Schmitt, A.; Callejas Fernández, J.; Martínez-García; and Hidalgo-Álvarez, R. , *J. Chem. Phys.*, **121** (11), 5468, (2004).
- [75] Odriozola, G.; Schmitt, A.; Callejas Fernández, J.; Martínez-García, R.; Leone, R. ; and Hidalgo-Álvarez, R., *J. Phys. Chem. B*, **107**, 2180, (2003).
- [76] Odriozola, G.; Schmitt, A.; Moncho-Jordá, A.; Callejas Fernández, J.; Martínez-García, R.; Leone, R. ; and Hidalgo-Álvarez, R., *Phys. Rev. E*, **65**, 031405, (2002).
- [77] Weitz, D. ; and Pine, D., *Diffusing-wave spectroscopy in Dynamics Light scattering: The Method and Some applications*. Ed. W. Brown, vol 49 of *Monographs on the physics and chemistry of Materials*. pp 652-720. Oxford: Oxford University Press, (1993).
- [78] Sorensen, C. M., *Aerosol Science and Technology*, **35**, 648, (2001).
- [79] Pine, D. J. in *Soft and fragile matter: Nonequilibrium dynamics, Metastability and Flow. Proceedings of the Fifty Third Scottish Universities Summer School in Physics, St. Andrews*. Editors M. E. Cates and M. R. Evans. Institute of Physics Publishing, Bristol, 2000.
- [80] Poon, W.C.K; and Haw, M. D., *Adv. Coll. Int. Sci.*, **73**, 71, (1997).
- [81] Hiemenz, P. C. ; and Rajagopalan, R., *Principles of colloid and surface chemistry (Third edition)*. Marcel Dekker Inc, New York, 1997.
- [82] Guinier, A., *Ann. Phys.*, **12**, 161, (1939).
- [83] Guinier, A.; Fournet, G.; Walker, C. B.; and Yudowitch, K. L., *Small angle scattering of X-rays*. Wiley, New York, (1955)
- [84] Teixeira, J. in *On Growth and Form, Fractal and non-Fractal patterns in Physics*. Edited by H. E. Stanley, and N. Ostrowski; Nijhoff, Dordrecht, pp. 145-165, (1986).
- [85] Schaefer, D. ; Martin, J. ; Wiltzius, P.; and Cannell, D., *Phys. Rev. Lett.*, **52**, 2371, (1984).
- [86] Axelos, M. ; Tchoubar, D.; Bottero, J.; and Fiessinger, F., *J. de Physique (France)*, **46**, 1587, (1985).
- [87] Gunton, J. D.; San Miguel, M.; and Sahni, P. S. in *Phase Transition and Critical Phenomena vol. 8*. Edited by C. Domb, and J. L. Lebowitz. Academic, London, (1983).

-
- [88] Porod, G. in *Small-Angle X-ray Scattering*. Edited by O. Glatter and O. Kratky. Academic, London, (1983).
- [89] Porod, G., *Kolloid Z.*, **124**, 83, (1951).
- [90] Carpineti, M.; and Giglio, M., *Phys. Rev. Lett.*, **68**, 3327, (1992). Carpineti, M., and Giglio, M., *Phys. Rev. Lett.*, **70**, 3828 (1993).
- [91] Bibette, J.; Mason, T. G.; Gang, H.; and Weitz, D. A., *Phys. Rev. Lett.*, **69**, 981, (1992).
- [92] Flory, P. J., *Statistical mechanics of chain molecules*; Hanser Publishers: New York, 1969.
- [93] Flory, P. J., *Principles of polymer chemistry*; Cornell University Press: London, 1971.
- [94] Cloizeaux, J. des; and Jannink G., *Les polymères en solution: leur modélisation et leur structure*; Les éditions de physique: Paris, 1987.
- [95] de Gennes, P. G., *Scaling Concepts in Polymer Physics*; Cornell University Press: London, 1988.
- [96] Debye, P., *J. Chem. Phys.*, **14**, 636, (1946). The proof of the relation between R_{ee} , and R_g can be also found in many books. For instance: [92].
- [97] Haslam, A. J.; Jackson, G.; and McLeish, T. C. B., *Macromolecules*, **32**, 7289, (1999).
- [98] Kuhn, W., *Kolloid-Z.*, **68**, 2, (1934).
- [99] Oka, S., *Proc. Phys. Math. Soc. Japan*, **24**, 657, (1942).
- [100] Kratky, O.; and Porod, G., *Rec. Trav. Chim.*, **68**, 1106, (1949).
- [101] Liverpool, T.B in *Annual reviews of computational physics VIII*. Ed. Stauffer, D. World Scientific, Singapore 2001.
- [102] de Gennes, P. G., *Phys. Lett.*, **38A**, 339, (1972).
- [103] des Cloizeaux, J., *Phys. Rev.*, **A10**, 1665, (1974); *J. Physique*, **42**, 635, (1981).
- [104] Daoud, M.; Cotton, J.P.; Farnoux, B.; Jannink, G.; Sarma, G.; Benoit, H.; Duplessix, R.; Picot, C.; and Gennes, P.G.D., *Macromolecules*, **8**, 804, (1975). See also Okano, K.; Wada, E.; Taru, Y.; and Hiramatsu, H.; *Rep. Prog. Polym. Sci. Japan*, **17**, 141, (1974).
- [105] Daoud, M., Ph. D. Thesis. Available from Laboratories Léon Brillouin, CEN Saclay, 91, Gif s/ Yvette, France.
- [106] Grosberg, A. Yu.; Khokhlov A. R. in *Statistical Physics of Macromolecules*; American Institute of Physics: New York, 1994.
- [107] Kuznetsov, D. V. ; and Sung, W., *J. Phys. II France*, **7**, 1287-1298, (1997).

- [108] Mayer, L. D.; Krishna, R.; Webb, M.; and Bally, M., *J. Lipid Res.*, **10**, 99, (2000).
- [109] Nair, R. R. ; Rodgers, J. R.; and Schwarz, L. A., *Mol. Ther.*, **5**, 455, (2002).
- [110] Buffon, G., *Essai d'arithmétique morale, Supplément à l'Histoire Naturelle*, vol. 4, (1777).
- [111] Lord Kelvin, *Phil. Mag.*, series 6, **2**, 1, (1901).
- [112] Kremer, K.; and Binder, K., *Comput. Phys. Rep.*, **7**, 259, (1988).
- [113] Newman, M. E. J.; and Barkema, G. T., *Monte Carlo Methods in Statistical Physics*. Clarendon Press: Oxford, 1999.
- [114] Allen, M. P.; Tildesley, D. J., *Computer simulation of liquids*. Clarendon Press, Oxford, 1999.
- [115] Heermann, D. W., *Computer simulation methods*. Springer-Verlag, New-York, 1990.
- [116] Kalos, M. H.; Whitlock, P. A., *Monte Carlo Methods, volume 1: basics*. Wiley, New York, 1986.
- [117] Metropolis, N.; Rosenbluth, A. W.; Rosenbluth, M. N.; Teller, A. H.; and Teller, E., *J. Chem Phys.*, **21**, 1087-92, (1953).
- [118] Wood, W. W.; and Jacobson, J. D., *Monte Carlo simulations in statistical mechanics*. Proceedings of the Western Joint Computer Conference, pp 261-9. San Francisco, (1959).
- [119] Flinn, P. A.; and McManus, G. M., *Phys. Rev.*, **124**, 54-9, (1961).
- [120] Barker, A. A., *Aust. J. Phys.*, **18**, 119, (1965).
- [121] Valleau, J. P.; and Whittington, S. G., *A Guide to Monte Carlo for Statistical Mechanics*, Modern Theoretical Chemistry Series, vol. 5, B. Berne, Ed., Plenum, New York, 1976.
- [122] Müller-Krumbhaar, H.; and Binder, K., *J. Stat. Phys.*, **8**, 1, (1973).
- [123] Baumgärtner, A., *Applications of the Monte Carlo Method in Statistical Physics*, 2nd ed; Edited by K. Binder. Topics in Current Physics 36; Springer-Verlag: Berlin, 1987.
- [124] Soga, K. G., Melrose, J. R., and Ball, R. C., *J. Chem. Phys.*, **110** (4), 2280, (1999).
- [125] Melrose, J. R., *Europhys. Lett.*, **19**, 51, (1992).
- [126] Turq, P.; Lantelme, F.; and Levesque, D., *Molec. Phys.*, **37**, 223, (1979).
- [127] Hynes, J. T.; Kapral, R.; and Torrie, G. M., *J. Chem. Phys.*, **72**, 177, (1980).
- [128] Helfand, E., *J. Chem. Phys.*, **69**, 1010, (1978).
- [129] Helfand, E.; Wasserman, Z. R.; and Weber, T. A., *Macromolecules*, **13**, 526, (1980).

-
- [130] Ermak, D. L.; and Buckholtz, H.; J. Comput. Phys., **35**, 169, (1980).
- [131] Pear, M. R.; and Weiner, J. H., J. Chem. Phys., **69**, 785, (1978).
- [132] Weiner, J. H.; and Pear, M. R., Macromolecules, **10**, 317, (1977).
- [133] van Gunsteren, W. F.; and Berendsen, H. J. C., Molecular Physics, **45**, 637, (1982).
- [134] Verlet, L., Phys. Rev., **159**, 98, (1967).
- [135] Papoulis, A., *Probability, Random Variables and Stochastic Processes*. McGraw Hill, 1965.
- [136] Toral, R. ; Chakrabarti, A., Comp. Phys. Comm., **74**, (3), 327, (1993).
- [137] *Kinetics of Aggregation and Gelation*, edited by F. Family and D. Landau, (North-Holland, Amsterdam, 1984).
- [138] Friedlander, S. K., *Smoke, Dust and Haze*, (Oxford, New York, 2000).
- [139] Meakin, P., J. of Sol-Gel Sci. and Tech., **15**, 97, (1999).
- [140] For a review, see, for example, Bray, A. J., Adv. Phys., **43**, 357, (1994).
- [141] Walton, A. G., *The Formation and Properties of Precipitates*, Interscience, New York (1967). Nielsen, A. E., *Kinetics of Precipitation*, Pergamon, Oxford (1964).
- [142] For a review, see, Anderson, V. J.; and Lekkerkerker, H. N. W., Nature, **416**, 811, (2002).
- [143] Hobbie, E. K., Phys. Rev. Lett., **81**, 3996, (1998).
- [144] de Hoog, E. H. A.; Kegel, W. K.; van Blaaderen, A.; and Lekkerkerker, H. N. W., Phys. Rev. E, **64**, 021407, (2001).
- [145] Segrè, P. N.; Prasad, V.; Schofield, A. B.; and Weitz, D. A., Phys. Rev. Lett., **86**, 6042, (2001).
- [146] Puertas, A. M.; Fuchs, M.; and Cates, M. E., Phys. Rev. Lett., **88**, 098301, (2002).
- [147] Liu, A. J.; and Nagel, S. R., Nature (London), **396**, 21, (1998).
- [148] Soga, K. G.; Melrose, J. R.; and Ball, R. C., J. Chem. Phys., **108**, 6026, (1998).
- [149] d'Arjuzon, R. J. M.; Frith, W.; and Melrose, J. R., Phys. Rev. E, **67**, 061404, (2003).
- [150] Costa, D.; Ballone, P.; and Caccamo, C., J. Chem. Phys., **116**, 3327, (2002).
- [151] Nguyen, N. Q.; and Ladd, A. J. C., Phys. Rev. E, **66**, 046708 (2002); J. F. Brady, J. Chem. Phys. **99**, 567, (1993); Riese, D. O.; Wegdam, G. H.; Vos, W. L.; Sprik, R.; Fenistein, D.; Bongaerts, J. H. H.; and Gerhard Grübel, G., Phys. Rev. Lett., **85**, 5460, (2000).
- [152] Dijkstra, M.; Brader, J. M.; and Evans, R., J. Phys:Condens. Matter., **11**, 10079, (1999).
- [153] V. J. Anderson, V. J.; de Hoog, E. H. A.; and Lekkerkerker, H. N. W., Phys. Rev.

- E, **63**, 011403, (2001).
- [154] Skjeltorp, A. T., Phys. Rev. Lett., **58**, 1444, (1987).
- [155] Victor, J. M.; and Hansen, J. P., J. Phys. Lett., **45**, L -307,(1984).
- [156] Chakrabarti, A.; Fry, D.; and Sorensen, C. M.; Phys. Rev. E, **69** (3), 031408, (2004).
- [157] Kolb, M., Phys. Rev. Lett., **17**, 1653, (1984).
- [158] Fry, D.; Sintès, T.; Chakrabarti, A.; and Sorensen, C. M., Phys. Rev. Lett., **89**, 148301, (2002).
- [159] Fry, D., PhD Thesis, Kansas state University, (2003).
- [160] Huse, D. A., Phys. Rev. B, **34**, 7845, (1986).
- [161] Binder, K.; and Fratzl, P. in *Phase Transformations in Materials*, G. Kostorz (ed.), Wiley-VCH, Weinheim (2001).
- [162] See, for example, Binder, K. in *Materials Science and Technology, Vol. 5: Phase Transformations in Materials*, P. Haasen (ed.), Wiley-VCH, Weinheim (1990).
- [163] Chakrabarti, A., Phys. Rev. B, **45**, 9620, (1992).
- [164] Robinson, D. J.; and Earnshaw, J. C., Phys. Rev. Lett., **71**, 715, (1993).
- [165] Earnshaw, J. C.; Harrison, M. B. J.; and Robinson, D. J., Phys. Rev. E., **53**, 6155, (1996).
- [166] Huang, H.; Oh, C.; and Sorensen, C. M., Phys. Rev. E, **57** (1), 875, (1998).
- [167] Furukawa, H., Phys. Rev. B., **33**, 638, (1986); Physica A, **123**, 497, (1984).
- [168] Sintès, T.; Toral, R.; and Chakrabarti, A., Phys. Rev. E (Rapid Commun.), **50**, R3330, (1994).
- [169] Witten, T. A.; and Pincus, P. A., Macromolecules, **19**, 2509, (1986).
- [170] Doroszkowski, A.; and Lambourne, R., J. Poly. Sci: Part C, **34**, 253, (1971).
- [171] Napper, D. H. *Polymeric Stabilization of colloidal dispersion*; Academic: London, 1983.
- [172] Russel, W. B.; Saville, D. A. ; and Schowalter, W. R. *Colloidal Dispersions*; Cambridge University Press: Cambridge, 1989.
- [173] Meyer, R. A., Appl. Opt., **18**, 585, (1979).
- [174] van Zanten, J. H.; and Monbouquette, H. G., J. Colloid Interface Sci., **146**, 330, (1991).
- [175] Hsu, W. P.; Yu, R.; and Matijevic, E., J. of Colloid Interface Sci., **156**, 36, (1993).
- [176] Kuhl, T. L.; Leckband, D. E.; Lasic, D. D.; and Israelachvili, J. N., Biophys. J., **66**, 1479, (1994).
- [177] Yethiraj, A.; Hall, C. K.; Dickman, R., Journal of Colloid and Interface Science,

- 151**, 102,(1992).
- [178] Scheutjens, J. M. H. M.; and Fleer, G., *J. Colloid Interface Sci.*, **16**, 361, (1982). de Gennes, P.-G., *Macromolecules*, **15**, 492, (1982). Klein, J.; and Pincus, P., *Macromolecules*, **15**, 1129, (1982). Israelachvili, J.N.; Tirrell, M.; Klein, J.; Almog, Y.; and Klein, J., *J. Colloid Interface Sci.*, **106**, 33, (1985).
- [179] Woodle, M.; and Lasic, D. D., *Biochim.Biophys.Acta*, **171**, 1113, (1992).
- [180] Quirantes, A.; and Delgado, A. V., *J. Phys. D: Appl. Phys.*, **30**, 2123, (1997).
- [181] Wittemman, A; and Ballauff, M., *Analytical Chemistry*, **76**, (10), 2813, (2004).
- [182] Phan, S.; Russel, W. B.; Cheng, Z.; Zhu, J.; Chaikin, P. M.; Dunsmuir, J. H. ; and Ottewill, R. H., *Phys. Rev. E*, **54**, 6633, (1996).
- [183] Hansen, P. H.; and Bergstrom, L., *J. Colloid Interface Sci.*, **218**, 77, (1999).
- [184] Grant, M. C. ; and Russel, W. B., *Phys. Rev. E*, **47**, 2606, (1993).
- [185] de Gennes, P. G., *J. Phys.(Paris)*, **37**, 1443, (1976). *Macromolecules*, **13**, 1069, (1980). *C. R. Acad. Sci. (Paris)*, **300**, 839, (1985).
- [186] Alexander, S. J., *Phys.(Paris)*, **38**, 983, (1977).
- [187] Semenov, A. N., *Sov. Phys. JETP*, **61**, 733, (1985).; *Zh. Eksp. Teor. Fiz.*, 88, 1242, (1985).
- [188] Milner, S. T.; Witten, T. A.; and Cates, M. E., *Macromolecules*,**21**, 2610, (1988). *Europhys. Lett.*, **5**, 413, (1988); *Macromolecules*, **22**, 853, (1989).
- [189] Milner, S. T.; and Witten, T. A., *J. Phys.(Paris)*, **49**, 1951, (1988).
- [190] Zhulina, E. B.; Priamitsyn, V. A. ; and Borisov, O. V., *Polym. Sci. USSR*, **31**, 205, (1989).
- [191] Zhulina, E. B.; Borisov, O. V.; and Priamitsyn, V. A., *J. Coll. Interf. Sci.*, **137**, 495, (1990).
- [192] Chakrabarti, A.; and Toral, R., *Macromolecules*, **23**, 2016, (1990).
- [193] Lai, P. Y.; and Binder, K., *J. Chem. Phys.*, **95**, 9288, (1991).
- [194] Toral, R.; Chakrabarti, A.; and Dickman, R. *Phys. Rev. E*, **50**, 343, (1994).
- [195] Chakrabarti, A.; Nelson, P.; and Toral, R. *Phys. Rev. A*, **46**, 4930, (1992); *J. Chem. Phys.*, **100**, 748, (1994).
- [196] Murat, M.; and Grest, G. S., *Macromolecules*, **22**, 4054, (1994). *Phys. Rev. Lett.*, **63**, 1074, (1989).
- [197] Daoud, M.; and Cotton, J. P., *J. Physique*, **43**, 531, (1982).
- [198] Borukhov, I.; and Leibler, L., *Phys. Rev. E*, **62**, R41, (2000).
- [199] Zhulina, E. B.; Borisov, O. V.; and Priamitsyn, V. A., *Journal of Colloid and interface science*, **137**, 495, (1989).

- [200] Leermakers, F. A. M.; and Scheutjens, J. M. H. M., *J. Chem. Phys.*, **89**, 3264, (1988).
- [201] Leermakers, F. A. M.; and Scheutjens, J. M. H. M., *J. Chem. Phys.*, **89**, 6912, (1988).
- [202] Wijmans, C. M.; Leermakers, F. A. M.; and Fleer, G. J., *J. Chem. Phys.*, **101**, 8214, (1994).
- [203] Wijmans, C. M.; Leermakers, F. A. M.; and Fleer, G. J., *Langmuir*, **10**, 4514, (1994).
- [204] Lai, P-Y; and Zhulina, E. B., *J. Phys (II)*, **2**, 547-560, (1992).
- [205] Ball, R. C.; Marko, J. F.; Milner, S. T.; and Witten, T. A., *Macromolecules*, **24**, 693, (1991).
- [206] Li, H.; and Witten, T. A., *Macromolecules*, **27**, 449, (1994).
- [207] Edwards, S. F., *Proc. Phys. Soc.*, **85**, 613, (1965).
- [208] Dan, N.; and Tirell, M., *Macromolecules*, **25**, 2890, (1992).
- [209] Murat, M.; and Grest, G.S., *Macromolecules*, **24**, 704, (1991).
- [210] Lin, E. K.; and Gast, A. P., *Macromolecules*, **29**, 390, (1996).
- [211] Carignano, M. A.; and Szleifer, I., *J. Chem. Phys.*, **102**, (21), 8662, (1995).
- [212] Ben-Shaul, A.; Szleifer, I.; and Gelbart, W. M., *J. Chem. Phys.*, **83**, 3597, (1985).
- [213] Toral, R.; and Chakrabarti, A., *Phys. Rev. E*, **47**, 4240, (1993).
- [214] Cosgrove, T.; Crowley T. L.; Vincent, B.; Barnett, K. G.; and Tadros, Th. F., *Faraday Discussions*, **16**, 101, (1982).
- [215] Beaufile, J. P.; Hennion, M. C.; and Rosset, R., *J. de Physique*, **44**, 497, (1983).
- [216] Hommel, H.; Legrand, A. P.; Balard, H.; and Papirer, E., *Polymer*, **24**, 959, (1983).
- [217] Hommel, H.; Legrand, A. P.; Courtier, J.; and Desbarres, J., *Eur. Polym. J.*, **15**, 993, (1979).
- [218] NMR experiments are based on the assumption that monomers far from the surface have smaller relaxation times than segments near the surface. By grafting ^{13}C labels at a location of interest in the polymer chain, is it possible to estimate the monomer concentrations at various distances from the surface. For NMR technique applied to spherical brushes see for instance Cosgrove, T.; Vincent, B.; Cohen Stuart, M.; Barnett, K. G.; and Sissons, D. S., *Macromolecules*, **14**, 1018, (1981); and Gilpin, D. K.; and Geindoga, E., *J. Chromatogr. Sci.*, **21**, 352, (1983).
- [219] Cohen Stuart, M. A.; Cosgrove, T.; and Vincent, B., *Advances in Colloid and Interface Science*, **24**, 143, (1986).
- [220] Forster, S.; Wenz, E.; and Linder, P., *Phy. Rev. Lett.*, **77**, 95, (1996).

-
- [221] McConnell, G. A.; Gast, A. P.; Huang, J. S.; and Smith, S. D., *Phys. Rev. Lett.*, **71**, 2102, (1993).
- [222] Edwards, J.; Everett, D. H.; O'Sullivan, T.; Pangalou, I.; and Vincent, B., *Journal of the chemical Society. Farady Transactions*, **80**, 2599, (1984).
- [223] de Hek, H.; and Vrij, A., *Journal of Colloid and Interface Science*, **84**, 409, (1981).
- [224] Doroszowski, A.; and Lambourne, R., *J. Colloid Interface Sci.*, **43**, 97, (1973).
- [225] Cairns, R. J. R.; Ottewill, R. H.; Osmond, D. W. J.; and Wagstaff, I., *J. Colloid Interface Sci.*, **54**, 45, (1976).
- [226] Homola, A.; and Robertson, A. A., *J. Colloid Interface Sci.*, **54**, 286, (1976).
- [227] Evans, R.; and Napper, D. H. J., *Colloid Interface Sci.*, **63**, 43, (1978).
- [228] Pusey, P. N.; and van Meegen, W., *an Exxon Monograph: Physics of Complex and Supermolecular Fluids*, edited by S.A.Safrar and N.A.Clark; Wiley-Interscience, New York, 1987, p.673.
- [229] Paulin, S. E.; and Ackerson, B. J., *Phys. Rev. Lett.*, **64**, 2663, (1990).
- [230] Mewis, J.; Frith, W. J.; Strivens, T. A.; and Russel, W. B., *AIChE J.*, **35**, 415, (1989).
- [231] Underwood, S. M.; Taylor, J. R., and W. van Meegen, *Langmuir*, **10**, 3550, (1994).
- [232] Pusey, P. N., *Liquids, Freezing, and the Glass Transition* edited by J.P. Hansen, D. Levesque, and J.Zinn-Justin; Elsevier, Amsterdam, 1991.
- [233] Wijmans, C. M.; and Zhulina, E. B., *Macromolecules*, **26**, 7214, (1993).
- [234] Cosgrove, T.; Heath, T.; van Lent, B.; Leermakers, F.; and Scheutjens, J. *Macromolecules*, **20**, 1692, (1987).
- [235] Nommensen M. H. G. D.; van den Ende, D.; and Mellema, J., *Phys. Rev. E*, **59**, 3147, (1999).
- [236] Dzubiella, J.; Likos, C. N.; and Löwen, H., *J. Chem. Phys.*, **116**, 9518, (2002).
- [237] Schaink, H. M.; Nommensen, P. A.; Jongschaap, R. J. J., and Mellema, J., *J. Chem. Phys.*, **113**, 2484, (2000).
- [238] Watzlawek, M.; Likos, C. N.; and Löwen, H., *Phys. Rev. Lett.*, **82**, 5289, (1999).
- [239] Cosgrove, T.; Heath, T.; van Lent, B.; Leermakers, F.A.M.; and Scheutjens, J. M. H. M., *Macromolecules*, **20**, 1692, (1987).
- [240] Ruckenstein, E.; and Li, B., *J. Chem. Phys.*, **107**, 3, (1997).
- [241] Sukhorukov, G. B.; Donath, E.; Davis, S.; Lichtenfeld, S.; Caruso, F.; Popov, V. I.; and Möhwald, H., *Polym. Adv. Technol.*, **9**, 759, (1998).
- [242] McQuigg, D. W.; Kaplan, J. I.; and Dubin, P. L., *J. Phys. Chem.*, **96**, 1973, (1992).
- [243] Birshtein, T. M.; and Borisov, O. V., *Polymer*, **32**, 916, (1991); Birshtein, T. M.;

- and Borisov, O. V., *Polymer*, **32**, 923, (1991).
- [244] Schiessel, H.; Widom, J.; Bruinsma, R. F.; and Gelbart, W. M., *Phys. Rev. Lett.*, **86**, 4414, (2001).
- [245] Netz, R. R.; and Joanny, J.-F., *Macromolecules*, **32**, 9026, (1999).
- [246] von Goeler, F.; and Muthukumar, M. J. *Chem. Phys.*, **100**, 7796, (1994).
- [247] Odijk, T., *Macromolecules*, **26**, 6897, (1993).
- [248] Laguecir, A.; Stoll, S.; Kirton, G.; and Dubin, P. L., *J. Phys. Chem. B*, **107**, 8056, (2003).
- [249] Sakaue, T.; Yoshikawa, K.; Yoshimura, S. ; and Takeyasu, K., *Phys. Rev. Lett.*, **87**, 078105, (2001).
- [250] Stoll, S.; and Chodanowski, P., *Macromolecules*, **35**, 9556, (2002).
- [251] Kunze, K.-K.; and Netz, R. R., *Phys. Rev. Lett.*, **85**, 4389, (2000).
- [252] Kong, C. Y.; and Muthukumar, M., *J. Chem. Phys.*, **109**, 1522, (1998).
- [253] Nguyen, T.T.; and Shklovskii, B.I., *Physica A*, **293**, 324, (2001).
- [254] Pais, A. C.; Miguel, M. G.; Linse, P.; and Lindman, B., *J. Chem. Phys.*, **117**, 1385, (2002).
- [255] Marenduzzo, D. ; and Micheletti, C., *J. Mol. Biol.*, **330**, 485, (2003).
- [256] Purohit, P. K.; Kondev, J. ; and Phillips, R., *Proc. Nat. Acad. Sci.*, **100**, 3173, (2003).
- [257] Muthukumar, M., *J. Chem. Phys.*, **118**, 5174, (2003).
- [258] Arsuaga, J.; Tan, R. K.-Z.; Vazquez, M.; De Witt Summers; and Harvey, S. C., *Biophysical Chemistry*, **101**, 475, (2002).
- [259] Kindt, J.; Tzlil, S.; Ben-Shaul, A.; and Gelbart, W. M., *Proc. Nat. Acad. Sci.*, **98**, 13671, (2001).
- [260] Kiran Kumar, K.; and Sebastian, K. L., *Phys. Rev. E*, **62**, 7536, (2000).
- [261] Richards, K. E.; Williams, R. C.; and Calendar, R., *J. Mol. Biol.*, **78**, 255, (1973).
- [262] Cerritelli, M. E.; Cheng, N.; Rosemberg, A. H.; McPherson, C. E.; Booy, F. P.; and Steven, A. C., *Cell*, **91**, 271, (1997).
- [263] Olson, N. H.; Gingery, M.; Eiserling, F. A.; and Baker, T. S., *Virology*, **279**, 385, (2001).
- [264] Colletier, J.-P.; Chaize, B.; Winterhalter, M.; and Fournier, D., *BMC Biotechnology*, **2**, 9, (2002).
- [265] Zhou, H.-X.; and Dill, K. A., *Biochemistry*, **40**, 11289, (2001).
- [266] Wand, A. J.; Ehrhardt, M. R.; and Flynn, P. F., *Proc. Nat. Acad. Sci.*, **95**, 15299, (1998).

-
- [267] Mondescu, R. P.; and Muthukumar, M., *Phys. Rev. E*, **57**, 4411, (1998).
- [268] Spakowitz, A. J.; and Wang, Z-G, *Phys. Rev. Lett.*, **91**, 166102, (2003).
- [269] Micka, Uwe; and Kremer, Kurt, *J. Phys.: Condens. Matter*, **8**, 9463, (1996).
- [270] Sakaue, T.; and Löwen, H., *Phys. Rev. E*, **70**, 021801, (2004).
- [271] P.G. Khalatur. In *Mathematical Methods in Contemporary Chemistry* ;S.I. Kuchanov; Gordon and Breach: New York, 1996.
- [272] De'Bell, K.; and Lookman, T., *Reviews of Modern Physics*, **65**, 87, (1993).
- [273] Vrbova, T.; and Prochazka, K., *J.Phys.A: Math.Gen.*, **32**, 5469, (1999).
- [274] Ponomarev, A. L.; Sewell, T. D.; and Durning, C. J., *Macromolecules*, **33**, 2662, (2000).
- [275] Kuznestov, D. V.; and Sung, W., *Macromolecules*, **31**, 2679, (1998).
- [276] Sumithra, K.; and Sebastian, K. L., *J.Phys.Chem.*, **98**, 9312, (1994).
- [277] Muthukumar, M., *J.Chem.Phys.*, **103**, 4723, (1995).
- [278] Orlandini, E.; Seno, F.; and Stella, A. L., *Phys. Rev. Lett.*, **84**, 294, (2000).
- [279] Singh, Y. ; Kumar, S.; and Giri, D., *J. Phys. A: Math. Gen.*, **32**, L407, (1999).
- [280] Marques, C. M.; Joanny, J. F.; and Leibler, L., *Macromolecules*, **21**, 1051, (1998).
- [281] Whittington, S. G.; *J.Phys. A: Math Gen.*, **31**, 3769, (1998).
- [282] Moghaddam, M. S.; Vrbova, T.; and Whittington, S. G., *J. Phys. A: Math. Gen.*, **33**, 4573, (2000).
- [283] Clancy, Th. C.; and Webber, S. E., *Macromolecules*, **26**, 628, (1993).
- [284] Zheligovskaya, E. A.; and Khalatur, P. G., *J. Chem. Phys.*, **106**, 8598, (1997).
- [285] Zheligovskaya, E. A.; Khalatur, P. G.; and Khokhlov, A. R., *Phy. Rev. E*, **59**, 3071, (1999).
- [286] Khokhlov, A. R.; and Khalatur, P. G., *Phys. Rev. Lett.*, **82**, 3456, (1999).
- [287] Srebnik, S.; Chackraborty, A. K.; and Shakhnovich, E. I., *Phys. Rev. Lett.*, **77**, 3157, (1996).
- [288] Sumithra, K.; and Baumgärtner, A., *J. Chem. Phys.*, **109**, 1540, (1998).
- [289] Chen, Z. Y.; and Cui, S. M., *Phys. Rev. E*, **52**, 3876, (1995).
- [290] Sintès, T.; Sumithra, K.; and Straube, E., *Macromolecules*, **34**, 1352, (2001).
- [291] Kramarenko, E. Y.; Winkler, R. G.; and Khalatur, P. G., *J. Chem. Phys.*, **104**, 4806, (1996).
- [292] Van der Linden, C. C.; Leermakers, F. A. M.; and Fleer, G. J., *Macromolecules*, **29**, 1000, (1996); **29**, 1172, (1996).
- [293] Joanny, J. F.; and Johner, A., *J.Phys.II (France)* , **6**, 511, (1996).

- [294] Kenausis, G. L.; Volrofs, J.; Elbert, D. L.; Huang, N.; Hofer, R.; Taylor, L. R.; Textor, M.; Hubbell, J. A.; and Spencer, N. D. J., *Phys. Chem. B*, **104** (14), 3298, (2000).
- [295] Huang, N.-P.; Michel, R.; Voros, J.; Textor, M.; Hofer, R.; Rossi, A.; Elbert, D. L.; Hubbell, J. A.; and Spencer, N. D., *Langmuir*, **17** (2), 489, (2001).
- [296] Ruiz-Taylor, L. A.; Martin, T. L.; Zaugg, F. G.; Witte, K.; Indermuhle, P.; Nock, S.; and Wagner, P., *Proc. Natl Acad. Sci, USA*, **98**, 852, (2001).
- [297] Chen, R. J.; Bangsaruntip, S.; Drouvalakis, A.; Wong Shi Kam, N., Shim, M.; Li, Y.; Kim, W.; Utz, P. J; and Dai, H., *PNAS*, **100** (9), 4984, (2003).
- [298] Doherty, A. S.; Berglund, K. D.; Buchholz, A.; Kourkine, I. V.; Przybycien, T. M; Tilton, R. D.; and Barron, A. E., *Electrophoresis*, **23**, 2766, (2002).
- [299] Schwartz, D. C.; and Samad, A., *Curr. Opin. Biotechnol.*, **8**, 70, (1997).
- [300] Wang, W. N.; Lin, J. Y.; and Schwartz, D. C., *Biophys. J.*, **75**, 513, (1998).
- [301] Gompper., G. In *Biologically Inspired Physics*, L. Peliti ed. Plenum Press: New York, 1991.
- [302] de Vries, R.; Weinbreck, F.; and de Kruif, C. G., *J. Chem. Phys.*, **118**, 4649, (2003).
- [303] McNamara, J.; Kong, C.; Muthukumar, M., *J. Chem. Phys.*, **117**, 5354-5360, (2002).
- [304] Semler, J.; Genzer, J., *J. Chem. Phys.*, **119**, 5274-5280, (2003).
- [305] Kuznetsov, D. V.; Sung, W., *Macromolecules*, **31**, 2679-2682, (1998).
- [306] Clausen-Schaumann, H.; Gaub, H. E., *Langmuir*, **15**, 8246-8251, (1999).

ERRATUM

This section is intended to enumerate and correct the errors made when the thesis manuscript was written. We thank very much people who has contributed to point out some of the errors and we encourage everybody who has read the thesis and found other mistakes to contribute to this section. The last update of this section is October, 2005.

- **Page 3, first paragraph** In the manuscript we say '*In 1905, Einstein [1] proposed the following theory to explain the Brownian (colloidal) motion: ...*'. This lines are inaccurate and could be misleading in the sense that they only gives credit to Einstein and neglects Langevin's contribution who is in fact responsible for equation (1.1) on the same page. These lines should be replaced as follows: '*In 1905, Einstein [1] applied both thermodynamics and statistical mechanics to a collection of Brownian particles and related the diffusion constant D to: (a) the mean square displacement in time $\langle (x(t) - x(t_o))^2 \rangle = 2Dt$, and (b) the viscosity η , and temperature T , $6\pi\eta r_p D = RT/N_A$ where N_A is the Avogadro Number, R is the ideal gas constant, and r_p is the radius of the particle. The above formula constituted one of the former ways to measure the Avogadro number accurately. In 1908, Langevin [^{*1}] presented a different approach to the Brownian movement by writing an equation of motion for an individual Brownian particle: the displacement $\vec{x}(t)$ of a colloidal particle of mass m is governed by the equation*

$$m \frac{d^2 \vec{x}}{dt^2} = -\frac{1}{\mu} \frac{d\vec{x}}{dt} - \nabla U + \vec{f}_{random}(t)$$

that assumes ...', where [^{*1}] refers to 1908 Langevin paper: '*Sur la théorie du mouvement brownien*', Comptes Rendus de l'Academie des Sciences (Paris), **146**, 530-533, (1908).

- **Page 25, after eq. (1.29)** Where it says '*For $\omega < 0$* ' should be replaced with '*For $\lambda < 0$* '.
- **Page 36, eq. (1.63)** Notice that the function $g(\vec{r})$ defined in eq. (1.63) and related to the structure factor $S(\vec{q})$ through eq. (1.65) is not the pair correlation function which is usually depicted as $g(\vec{r})$. Equation (1.63) defines the 'space density-density correlation function' which is usually depicted as $G(\vec{r})$ instead of $g(\vec{r})$ as we did. In fact, if we use as notation $G(\vec{r})$ to refer to the 'space density-density correlation' function, and $g(\vec{r})$ for the pair correlation function, it is possible to write the following relation: $G(\vec{r}) = \delta(\vec{r}) + \Phi g(\vec{r})$, where $\Phi = \langle \Phi(\vec{r}) \rangle$ is the average density.

- **Page 188, in the last paragraph** The sentence '*The limiting values observed for $T \rightarrow \infty$ correspond to a chain ...*' should be replaced by '*The limiting values observed for $1/T \rightarrow \infty$ correspond to a chain ...*'.
- **Page 193, after eq. (9.5)** The sentence '*Thus, we can model the chain as an ideal rod-like polymer ...*' should be replaced by '*Thus, we can model the chain as a flexible rod-like polymer ...*'.

ADDENDA

This section is intended to include comments, cites, and reviews about issues which were not included formerly in the manuscript, but are very close related to the topics reviewed in the thesis. We encourage everybody who has read the thesis and knows interesting information about issues related to the thesis to contribute to this section. The last update of this section is October, 2005.

- **About the Brownian motion:** it seems that Brownian motion was observed before Robert Brown studied it in 1828. In 1785, the scientist Jan Ingenhousz reported the movement of carbon dust particles on alcohol.
- **About EPID's, e-paper, and REED's:** additional information about Electrophoretic Image Displays, and the so called e-paper can be found for instance in the following web-pages: <http://www.sipix.com/technology/epaper.htm>, <http://www.eink.com/index.html>. Information about REED's, Reverse Emulsion Electrophoretic Crystals, which could be an alternative to EPID's, can be found on <http://zikon.com/reed.htm>.
- **About other applications of spherical brushes:** Magnetic nanoparticles with grafted antibodies onto their surface have made available an ultrasensitive method for detecting proteins. Conventional assays for detecting the same proteins are reported to be six orders of magnitude less sensitive than this method. For more information, see Jwa-Min Nam, C. Shad Thaxton, and Chad A. Mirkin, *Science*, **301**, 1884, (2003).
- **Encapsulated polymer brushes (Chapter 7):** the study of encapsulated brushes can be also of relevance for the behavior of polymer brushes (like sterically stabilized liposomes) when trapped by macrophages in the body. For more information, see for instance S.M. Moghimi, A.C. Hunter, and J.C. Murray, *Pharmacological Reviews*, **53**, 283, (2001). The study can be also relevant for polymer nanoparticle-brushes encapsulated into composite materials, see for instance: M.Z. Rong, M.Q. Zhang, H.B. Wang, H.M. Zeng, *J. of Poly. Sci. B*, **41**, 1070, (2003); A. Pucci, N. Tirelli, E.A. Willneff, et al., *J. of Materials Chemistry*, **14**, 3495, (2004).

Camina caminaràs i cap endant te
faràs, braç sonant i orella fumant, a la fi
de la tesi som arribats.

I els polimers i els col·loids in En
Juanet amb ells visqueren contents i ale-
gres anys i més anys.

I si no són vius són morts; i si no
són morts són vius; i al cel mos vegem
tots plegats.

Amèn.

Ciutat de Mallorca. Maig de 2005.

Curriculum vitae



Joan J. Cerdà was born in Palma of Mallorca, in 1975. He is currently an Assistant Instructor at the Physics Department of the Universitat de les Illes Balears. His research topic is biophysics, and physics of polymers and colloids.

Personal Information

Date of birth: 29/11/1975
Place of birth: Palma de Mallorca
Private address: C./ Des Tord n.42, E-07009 Marratxí (Illes Balears)
E-mail: jcerda@imedea.uib.es
Phone: +34 971 173207
Fax: +34 971 173 426

Education

- (June 1998) Master Degree in Physics. Universitat de les Illes Balears, Palma de Mallorca.
- (June 2003) Master Degree in Chemistry. Universitat de les Illes Balears, Palma de Mallorca. Premi extraordinari de llicenciatura (First Class Honors distinction award).
- (August 2003) Ph.D. Science Exams, qualification: excellent.

Current Position

- Assistant Instructor (Ajudant Universitat) at the Departament de Física de la Universitat de les Illes Balears (since Oct. 2003).

Visit to Other Institutions

- Kansas-State University, Manhattan, KS, (USA). Under the supervision of Dr. A. Chakrabarti. (July-August, 2003) and (June-August, 2004).

Publications

1. “*Pair Interaction between End-grafted Polymers onto Spherical surfaces: a Monte Carlo Study*”. Juan J. Cerdà, Tomás Sintés, and Raúl Toral, *Macromolecules*, **36**, 1407-1413, (2003). [A]
2. “*Interaction of colloidal particles bearing grafted polymer chains onto their surfaces*”. Juan J. Cerdà, Tomás Sintés, and Raúl Toral. In *Coloides e interfases*, Editors L. M. Liz, M. Arzán, P. Hervés. Servicio de Publicaciones de la Universidad de Vigo, 2003. ISBN: 84-8158-242-5.[C]
3. “*Kinetics of phase transformations in depletion-driven colloids*”. Juan J. Cerdà, Tomás Sintés, C. M. Sorensen, and A. Chakrabarti, *Phys. Rev. E*, **70**, 011405, (2004). [A]
4. “*Structure factor scaling in colloidal phase separation*”. Juan J. Cerdà, Tomás Sintés, C. M. Sorensen, and A. Chakrabarti, *Phys. Rev. E*, **70**, 051405, (2004). [A]
5. “*Excluded Volume Effects on Polymer Chains Confined to Spherical Surfaces*”. Juan J. Cerdà, Tomás Sintés, and A. Chakrabarti, *Macromolecules*, **38**, 1469-1477, (2005). [A]
6. “*Stiffed polymer adsorption. Onset to pattern recognition*”. Juan J. Cerdà, and Tomás Sintés, *Biophysical Chemistry*, **115**, 277-283, (2005). [A]
7. “*Adsorption of Semiflexible Block-Copolymers on Homogeneous Surfaces*”. Juan J. Cerdà, Tomás Sintés, and K. Sumithra. Submitted to *Journal of Chemical Physics*. [A]
8. “*A Monte Carlo and Self-Consistent Field calculations of encapsulated spherical polymer brushes*”. Juan J. Cerdà, Tomás Sintés, and Raúl Toral. Submitted to *Journal of Chemical Physics*. [A]

[A] = Article, [C] = Chapter Book

Conference Presentations

1. Juan J. Cerdà, Tomás Sintés, and Raúl Toral, “*Polímeros anclados sobre superficies esféricas por uno de sus extremos*”, II reuions de la xarxa temàtica d’estructures espacio-temporals de la Generalitat de Catalunya. Barcelona, Feb. (2002). [O]
2. Juan J. Cerdà, Tomás Sintés, and Raúl Toral, “*Interaction between colloidal particles with polymers grafted onto their surfaces*”, Congreso de Física Estadística, FISES 2002. Tarragona, May (2002). [P]
3. Juan J. Cerdà, Tomás Sintés, and Raúl Toral, “*Estudio de las interacciones en sistemas de partículas coloidales con polímeros anclados sobre su superficie*”, V Reunión del grupo especializado de Coloides e interfases (GECI) de la Real Sociedad Española de Química y Real Sociedad Española de Física. Vigo, Jul. (2003). [O]
4. Juan J. Cerdà, Tomás Sintés, and Raúl Toral, “*Adsorción de cadenas poliméricas semiflexibles sobre superficies homogéneas y heterogéneas.*”, Congreso de Física Estadística, FISES 2003. Pamplona, Oct. (2003). [P]
5. Juan J. Cerdà, and Tomás Sintés, “*Stiff polymer adsorption: onset to pattern recognition*”, Biology after the Genome: a physical view, BIFI 2004, I International Conference. Zaragoza, Feb. (2004). [P]
6. Juan J. Cerdà, Tomás Sintés, and Amitabha Chakrabarti “*DNA packaging into virus capsids*”, Jülich Soft Matter Days 2004. Kerkrade, Holland, Nov.(2004). [P]
7. Juan J. Cerdà, Tomás Sintés, and Amitabha Chakrabarti “*Monte Carlo Study of semiflexible polymer chains confined to spherical surfaces*”, II Congreso Nacional BIFI 2005. Zaragoza, Feb. (2005). [P]

[O] = Oral presentation, [P] = Poster presentation

Participation in research projects:

- Fenómenos cooperativos y emergentes en sistemas complejos entre la física y la biología. FIS2004-05073-C04-03.

